THE DEACTIVATION OF SINGLET MOLECULAR OXYGEN IN THE GASEOUS PHASE.

by

D. S. Richards M.Sc.

A thesis submitted to the University of Keele in partial fulfilment of the requirements for the Degree of Doctor of Philosophy.

Department of Chemistry

University of Keele

August 1985

TO MY FAMILY

ACKNOWLEDGEMENTS

In presenting this thesis I would like to thank the following people:

Dr. Peter Borrell for his guidance and encouragement, not only in the laboratory but in all aspects of my postgraduate training.

My co-workers Dr. Razmik Boodaghians, Dr. Patricia Borrell and Mr. Andrew Billington for many helpful discussions.

Professor I. T. Millar and Professor G. Jones for the facilities in the Department of Chemistry.

The technical staff of the Chemistry and Computing Science Departments, particularly Mr. P. Holbrook, Mr. J. Wilcox, Mr. R. Pattison, Mr. P. Callaghan, and Mr. I. Marr, who are always willing to help with any task. Special thanks go to the glassblower Mr. C. Cork, whose skill we all rely upon to a great degree.

Mrs. M. Furnival for typing the tables and Mr. T. Bolam who is responsible for the graphic and photographic work.

My wife for reading the drafts of each chapter and advising on the grammatical quality of this thesis. Also for her patience and encouragement over the past four years.

The University of Keele for a Departmental Studentship, without which this study would not have been possible.

Last but not least my family for their help and encouragement throughout my education.

The work reported in this thesis was carried out by the candidate under the supervision of Dr. P. Borrell. The majority of the experimental results in the study of HCl as a deactivator were obtained in collaboration with Dr. R. Boodaghians; those run numbers are designated with the prefix R. All other experimental work (designated D or DSR) and the analysis of all data was carried out by the candidate.

ABSTRACT

A study of the deactivation of singlet molecular oxygen by HCl, HBr, H_2, and D_2 has been made, paying particular attention to the temperature dependence.

The rate constants for the deactivation of $O_2(a^1\Delta_g)$ at 295K were found to be:

$$k_d^{HCl} = (8.00 \pm 0.34) \times 10^4 \ \text{mol}^{-1}\ \text{dm}^3\ \text{s}^{-1}$$

$$k_d^{HBr} = (4.2 \pm 2.8) \times 10^4 \ \text{mol}^{-1}\ \text{dm}^3\ \text{s}^{-1}$$

$$k_d^{H_2} = (2.22 \pm 0.26) \times 10^4 \ \text{mol}^{-1}\ \text{dm}^3\ \text{s}^{-1}$$

$$k_d^{D_2} = (2.56 \pm 1.30) \times 10^3 \ \text{mol}^{-1}\ \text{dm}^3\ \text{s}^{-1}$$

and those for the deactivation of $O_2(b^1\Sigma^+_g)$ were found to be:

$$k_q^{HCl} = (1.60 \pm 0.20) \times 10^7 \ \text{mol}^{-1}\ \text{dm}^3\ \text{s}^{-1}$$

$$k_q^{HBr} = (1.42 \pm 0.07) \times 10^8 \ \text{mol}^{-1}\ \text{dm}^3\ \text{s}^{-1}$$

$$k_q^{H_2} = (2.76 \pm 0.06) \times 10^8 \ \text{mol}^{-1}\ \text{dm}^3\ \text{s}^{-1}$$

$$k_q^{D_2} = (5.27 \pm 0.18) \times 10^6 \ \text{mol}^{-1}\ \text{dm}^3\ \text{s}^{-1}$$

The determination of the deactivation rate constants over the temperature range 500 to 1200K was carried out using a discharge flow - shock tube apparatus. The temperature dependence of the

deactivation of $O_2(a^1\Delta_g)$ may be described by the following Arrhenius expressions:

$$k_d^{HCl} = (2.76\pm1.70) \times 10^7 \exp[-(1750\pm190)/T] \quad mol^{-1}\ dm^3\ s^{-1}$$

$$k_d^{H_2} = (1.32\pm1.08) \times 10^8 \exp[-(2600\pm180)/T] \quad mol^{-1}\ dm^3\ s^{-1}$$

$$k_d^{D_2} = (2.75\pm0.75) \times 10^7 \exp[-(2740\pm90)/T] \quad mol^{-1}\ dm^3\ s^{-1}$$

It was not possible to obtain data for the deactivation of $O_2(a^1\Delta_g)$ by HBr above 295K.

The deactivation of $O_2(b^1\Sigma^+_g)$ by HCl was nearly independent of temperature, although the deactivation of $O_2(b^1\Sigma^+_g)$ by H_2 and D_2 showed a positive temperature dependence. These temperature dependences could not be fitted to a simple function of temperature.

The results of this study are discussed in terms of the deactivation probabilities. Where possible, the temperature dependence is compared with the predictions of the short range interaction theory of Kear and Abrahamson and the long range interaction theory of Braithwaite, Ogryzlo, Davidson and Schiff. Comparisons with the Landau-Teller theory of vibrational to vibrational energy transfer are also made.

CONTENTS

INTRODUCTION

1.1 Background

In recent years there has been a considerable amount of interest shown in the chemical and physical behaviour of the first two electronically excited states of molecular oxygen, in the gaseous phase. The areas in which there has been most activity are atmospheric chemistry, air pollution and laser technology.

(a) Atmospheric Chemistry

Studies of the airglow and the aurora can be traced as far back as 1788 when nights of unusual brightness appeared on record. However, it was not until 1909 that Yntema obtained photometric evidence of the airglow. The subject became intensely studied and more diversified. In 1961 there were more than 1600 references considered currently significant [1].

The first electronically excited species of oxygen, $O_2(a^1\Delta_g)$, is the most important and is produced in the atmosphere primarily by photolysis of ozone at wavelengths below 300nm. The main losses are due to collisional quenching and radiation to the ground state at 1270nm. This infrared emission is present in the twilight glow and provides a measure of the ozone distribution above 80km, hence those workers concerned with ozone depletion and atmospheric modelling require a knowledge of the reactions of $O_2(a^1\Delta_g)$ with other atmospheric species. There have been many investigations of the $O_2(a^1\Delta_g)$ distribution, involving both terrestrial [2] and rocket borne [3] measurements.

The second electronically excited species, $O_2(b^1\Sigma^+_g)$, is a companion of $O_2(a^1\Delta_g)$ in the atmosphere and gives rise to the

infrared day glow at 762nm. Its removal is almost entirely through quenching by atmospheric gases. This species is present in lower concentrations than $O_2(a^1\Delta_g)$ and is considered to be much less significant in atmospheric chemistry.

(b) Air Pollution

Although the reactions of singlet molecular oxygen are now known to be less important in atmospheric pollution than was once thought, they are still of interest because of the uniqueness of the products which may also have adverse biological effects.

In the presence of alkenes, it has been shown to oxidize nitric oxide in photochemical smogs, leading to the production of several eye irritants [4]. One such irritant is peroxyacetylnitrate (PAN). This is a water soluble substance which can be hydrolysed in the lung. In situ generation of $O_2(a^1\Delta_g)$ in this manner can cause cell damage, leading to lung cancer, via the formation of peroxides in the living cell. Indeed, singlet molecular oxygen has been studied in connection with blood disease, some forms of cancer and the ageing process in man [5].

(c) Laser Technology

The development of the oxygen-iodine laser was made possible due to the discovery of a practical $O_2(a^1\Delta_g)$ generator [6] utilizing chlorine and hydrogen peroxide, the overall reaction being:

$$Cl_2 + H_2O_2 + 2NaOH \longrightarrow O_2(a^1\Delta_g) + 2NaCl + 2H_2O \qquad (1.1)$$

This reaction was first observed by Mallet [8] in 1927 as a weak red chemiluminescence, which was later found to be due to the $O_2(a^1\Delta_g)$ 'dimol' emission. The $O_2(a^1\Delta_g)$ generator of McDermott and co-workers was able to produce about 40% $O_2(a^1\Delta_g)$ in pure oxygen, at about 1 torr. I_2 was injected in an argon carrier gas at 90°C prior to entrance into the laser cavity. In this way, the first oxygen-iodine continuous wave laser was manufactured. Run times of several minutes were obtained with a measured laser output of 4 milliwatts. This laser system relies on the transfer of energy from chemically generated $O_2(a^1\Delta_g)$ to produce an energy inversion in the spin-orbit states of atomic iodine, and has become known as the chemically pumped oxygen-iodine laser (COIL).

Recently, there has been intense interest in this laser system, with a view to producing a hybrid version capable of operating in a pulsed mode. Many workers [7,9,46] have been involved in studying the kinetics of this system. One result of these studies has been to identify the need for an iodine atom precursor, stable in electronically excited oxygen but which is also an inefficient quencher of $O_2(a^1\Delta_g)$, $O_2(b^1\Sigma^+_g)$, and $I(^2P_{1/2})$, together with the capability to manufacture $O_2(a^1\Delta_g)$ in high concentration.

In each case, it is helpful to have a sound knowledge of the processes by which singlet molecular oxygen is both produced and removed under a variety of conditions. To this end, elucidation of the mechanisms of such processes would be a great advantage. In a thorough investigation of the subject, one of the most important pieces of information is the functional dependence of the rate constants of the various processes with respect to temperature , which can provide information about the intermolecular potentials involved.

Although there have been major developments in the theoretical approaches to understanding these processes, there remains a lack of convincing correlation with experimental observation. The reactions and quenching of singlet molecular oxygen have been studied by a variety of methods at room temperature. Temperature dependence studies have been restricted by attempts to raise or lower the temperature through the use of thermostatted jackets. This approach has limited the study to temperatures between 200K and 400K. While this temperature range is adequate for most purposes, the reactions of singlet molecular oxygen, particularly the deactivation of $O_2(b^1\Sigma^+_g)$, show little temperature dependence and so a much wider range is desirable.

The approach in this study has been to combine the high temperature advantages of a shock tube with those of the lower temperature flow tube apparatus. The result has been the discharge flow-shock tube which allows reactions to be studied over a temperature range of 500K to 2000K, as well as at room temperature.

1.2 The Temperature Dependence Of Reaction Rates

The study of chemical reactions at high temperatures provides a considerable amount of information about the nature of a chemical reaction. With rare exceptions, the rate of a chemical reaction increases with temperature. In 1889, Arrhenius made the general observation that a plot of the natural logarithm of the rate constant versus reciprocal temperature for a series of reactions was linear. Recalling that Van't Hoff (1884) found that the same was true for equilibrium constants, because of the relationship:

$$d\ln K/dT = \Delta H/RT^2 \qquad (1.2)$$

Arrhenius proposed that:

$$k = Ae^{-Ea/RT} \qquad (1.3)$$

This equation* assumes that both the pre-exponential factor and the activation energy are independent of temperature.

For the majority of gas phase rate constants, this simple form is adequate. However, for a small group of reactions this is not the case. One example is the termolecular recombination of atoms or atoms with diatomics. In such cases, it is found that the pre-exponential factor is temperature dependent and the equation must be modified to:

$$k = A'T^n e^{-Ea'/RT} \qquad (1.4)$$

where $Ea' = Ea + CT$ and $A' = A/T^n$. Note that $n = C/R$. If n is considerably less than unity, which is usual for gas reactions, the

value of the T^n term approaches unity and Ea' approaches Ea, since C/R will be very small.

The pre-exponential factor is related to the collisional frequency of the reactant molecules. Simple Collision Theory [10], predicts the following relationship between rate constant and temperature:

$$k = \pi r_{AB}^2 (8RT/\pi\mu)^{1/2} e^{-Ea/RT} \qquad (1.5)$$

where r_{AB} is the collision cross-section and μ the reduced mass. This equation may be expressed as,

$$k = CT^{1/2} e^{-Ea/RT} \qquad (1.6)$$

which is also a similar expression to the Arrhenius equation.

Simple Collision Theory assumes that collisions are simple and does not allow for the existence of transition states and activated complexes, nor does it allow the activation energy to be calculated or steric effects to be taken into account.

Transition state theory [11] takes into account the formation of an activated complex, which has a transient existence at the top of a potential energy barrier between reactants and products, and predicts the following equation for the relationship between rate constant and temperature:

$$k = k_B T/h.\ e^{+\Delta S/R}.e^{-\Delta H/RT} \qquad (1.7)$$

where k_B is the Boltzmann constant, h is Plancks constant, ΔH the enthalpy and ΔS the entropy of the activated complex. ΔH may be related to Ea by $Ea = \Delta H + (n-1)RT$, where n is the order of reaction. The overall equation becomes,

$$k = k_B T/h.\ e^{n}.\ e^{+\Delta S/R}.\ e^{-Ea/RT} \qquad (1.8)$$

Therefore, with a few assumptions about the nature of the activated complex , the pre-exponential factor may be estimated, from a consideration of the partition functions. It is also possible to estimate the activation energy for small molecules, however this involves a complex quantum mechanical treatment. Again, this is very similar to the Arrhenius equation but incorporates a temperature dependence in the pre-exponential factor.

$$k = BTe^{-Ea/RT} \qquad (1.9)$$

Other temperature dependences are known. For example, the Landau-Teller Theory [12] of vibrational energy transfer predicts that the probability of energy transfer per collision, P, will be related to temperature by:

$$\text{Ln } P \alpha T^{-1/3}$$

(1.10)

The rate constant is related to P by:

$$k = ZP(1-e^{h\nu/kT})$$

(1.11)

where Z is the collision rate, hence $k \alpha T^{-1/3}$ [13].

If the Landau-Teller Theory is approached from a quantum mechanical stand point, then several temperature dependent terms are found to play a part. The most widely applied approach is that of Schwartz, Slawsky and Hertzfeld, [12] sometimes called SSH Theory. It is a three dimensional quantum mechanical treatment which yields a prediction for the relaxation time. The most dominant of the temperature dependent terms is $T^{-1/3}$ which results in a linear Landau-Teller plot. In general, most quantum mechanical approaches lead to:

$$\text{Ln}(1/k) = A + BT^{-1/3}$$

(1.12)

In a few cases other temperature dependent terms become important. For example, some polar molecules show an inverse dependence due to the dominance of attractive forces in interactions.

* In all equations given in this section the units of k will depend upon the overall order of reaction . For zero order , mol dm^{-3} s^{-1} , for first order, s^{-1} ; and for second order, mol^{-1} dm^3 s^{-1}.

1.3 The Discharge Flow - Shock Tube

The combination of a flow discharge apparatus and a shock tube provides a powerful tool for the study of the high temperature reactions of unstable species, such as electronically excited molecules, atoms and radicals, which must be generated in situ.

This thesis is concerned with the study of singlet molecular oxygen in a discharge flow - shock tube. A brief history of the technique is given in this section.

Although the first shock tube was developed by Vieille in 1899 [14], it was not until the early 1960's that Hartunian, Thompson and Hewitt [15] constructed the first discharge flow - shock tube. They used an RF discharge to study the chemiluminescent recombination reactions of atomic oxygen with carbon monoxide and also with nitric oxide. Gross and Cohen [16], working in the same laboratory, used the technique with a microwave discharge to study further chemiluminescent reactions.

The discharge flow - shock tube used in this study was developed from an apparatus constructed in 1969 by Borrell, Borrell and Brittain [17] to study active nitrogen. Later the technique was developed to allow singlet molecular oxygen to be studied. The system differs from those used previously in the direction of the flow; the facilities for pre-shock analysis of the concentration gradient along the tube; and the use of whole post-shock regime for analysis.

In some respects singlet molecular oxygen facilitates the use of a discharge flow tube since reactions which remove $O_2(a^1\Delta_g)$, generated in the microwave discharge, are slow enough to produce an appreciable concentration of $O_2(a^1\Delta_g)$ along the tube at room temperature. In other respects the same property is a disadvantage, when at high temperature a measurable change is required during the hot flow time of the experiment.

In the case of $O_2(b^1\Sigma^+_g)$, which is produced from $O_2(a^1\Delta_g)$ in the energy pooling reaction [18,19] establishing a steady state concentration, study is also relatively easy at room temperature. Potential problems arise at high temperatures when the analysis depends upon relaxation to a new steady state. For this to be observed the rate constants for the formation and removal of $O_2(b^1\Sigma^+_g)$ must have different temperature dependences.

The apparatus and experimental techniques involved in this study are described in Chapter 2.

1.4 Singlet Molecular Oxygen

This section describes the electronic structure, spectroscopy, and reactions of singlet molecular oxygen together with methods of generating and detecting these species. It is not intended to be a comprehensive literature survey. The discovery and early work on singlet molecular oxygen is described, as well as the most recent work.

1.4.1 Electronic Structure

The electronic configuration of molecular oxygen may be written as:

$$KK(2s\,\sigma_g)^2(2s\,\sigma_u)^2(2p\,\sigma_g)^2(2p\,\pi_u)^4(2p\,\pi_g)^2$$

Figure 1.1 shows the corresponding molecular orbital diagram. Since the two degenerate π antibonding orbitals contain only two electrons, it is possible to rearrange these electrons and write three electronic states for molecular oxygen; $^3\Sigma^-_g$, $^1\Delta_g$, $^1\Sigma^+_g$, (Table 1.1).

The ground state, which has the lowest energy, occurs when the two electrons are unpaired and have parallel spins. The first two excited states occur when the spins are opposed. In the case of the first electronically excited state, $O_2(a^1\Delta_g)$, the electrons are paired, therefore their orbital angular momentum is in the same direction, $\Lambda=2$, giving rise to a doubly degenerate state. The second electronically excited state, $O_2(b^1\Sigma^+_g)$, has these electrons in different orbitals and thus their orbital angular momentum is opposed, $\Lambda=0$. This gives rise to one unique state for $O_2(b^1\Sigma^+_g)$, which is higher in energy than $O_2(a^1\Delta_g)$ since it is more energetically unfavourable for electrons of opposite spin to be unpaired.

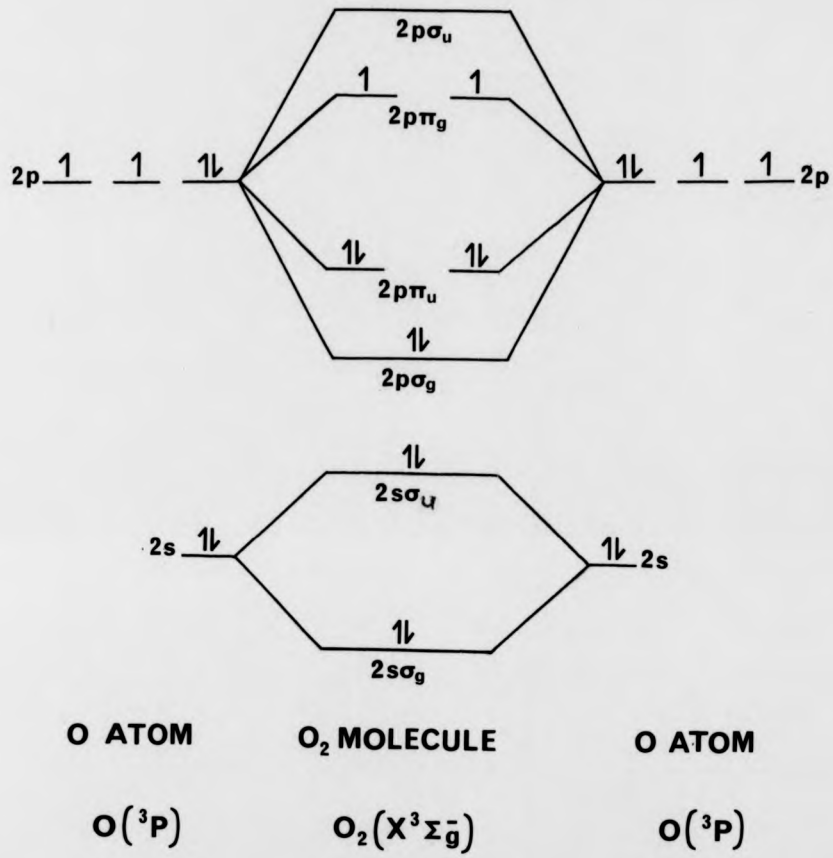

Figure 1.1 Molecular orbital diagram for Oxygen

State	Occupancy of $2p\pi g$		Orbital Angular Momentum	Spin Angular Momentum	Symbol	Energy Above Ground State
2nd Excited	$\underline{\uparrow}$	$\underline{\downarrow}$	$\Lambda = 0$	$S = 0$	$b^1\Sigma_g^+$	157 kJ
1st Excited	$\underline{\uparrow\downarrow}$	$\_$	$\Lambda = 2$	$S = 0$	$a^1\Delta_g$	94 kJ
Ground	$\underline{\uparrow}$	$\underline{\uparrow}$	$\Lambda = 0$	$S = 1$	$X^3\Sigma_g^-$	0 kJ

Table 1.1 Electronic States of Molecular Oxygen

Hund's rule may be applied to confirm the energetic sequence of the states. The rule specifies that the state with maximum multiplicity lies lowest in energy and states of equal multiplicity, the one with the greatest Λ lies lowest. Therefore in order of increasing energy the electronic states for molecular oxygen are: $^3\Sigma_g^-$, $^1\Delta_g$, $^1\Sigma_g^+$.

Figure 1.2 shows the potential energy - internuclear distance diagram for some of the lower electronic states of molecular oxygen [20]. The two lowest excited states are often produced together and so they are frequently referred to collectively as singlet molecular oxygen or simply singlet oxygen.

A detailed explanation of the state symbols may be found in several texts, such as Herzberg [21]. A brief summary of the main points is given here.

The symbols X, a, and b designate the ground state and the first and second electronically excited states of a molecule respectively.

The main state symbol describes the total orbital angular momentum (integer values of Λ from zero) around the symmetry axis as Σ, Π, Δ, Φ, etcetera.

The main symbol is preceded by superscript 1, 2, 3 indicating the spin multiplicity of the state, (S = 0, 1/2, 1, etcetera, respectively).

Σ symbols are followed by a superscript which indicates whether the wave function does (-) or does not (+) change sign on reflection in any plane passing through the nuclei.

Linear molecules which have a centre of inversion (e.g. O_2) have a symmetry element which defines the inversion of the wave function at the centre of the molecule (g for even, or u for odd). This notation is given as a subscript.

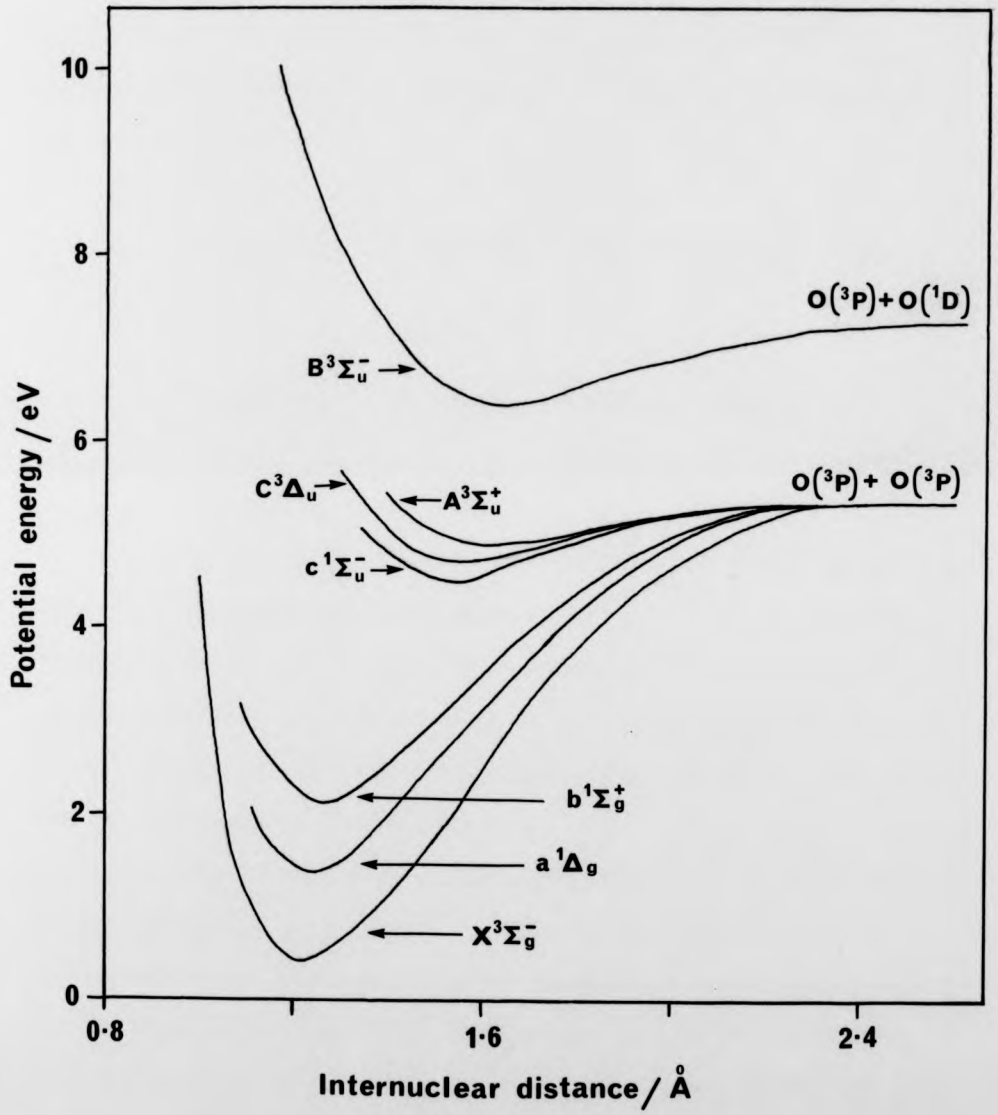

Figure 1.2 Potential energy diagram for Oxygen

1.4.2 The Spectroscopy of Singlet Molecular Oxygen

The optical transitions of singlet molecular oxygen to the ground state are well known [21]. These are forbidden transitions, hence their radiative lifetimes are long and their intensities correspondingly low. The radiative lifetime of $O_2(a^1\Delta_g)$ is approximately 44 minutes [22] and that of $O_2(b^1\Sigma^+_g)$, approximately 7 seconds [23].

$$O_2(a^1\Delta_g) \text{ ----> } O_2(X^3\Sigma^-_g) + h\nu\ (\lambda = 1270\text{nm}) \qquad (1.13)$$

$$O_2(b^1\Sigma^+_g) \text{ ----> } O_2(X^3\Sigma^-_g) + h\nu\ (\lambda = 762\text{nm}) \qquad (1.14)$$

The electric dipole transitions from the excited singlet states to the ground state are spin, symmetry, and in the case of $O_2(a^1\Delta_g)$, orbitally forbidden. The transitions occur as magnetic dipole transitions which have considerably smaller probabilities ($\sim 10^{-5}$) than those for allowed electric dipole transitions [21,48], and are consequently much weaker.

Electric dipole transitions may be induced by a perturbation of the dipole during collision with another molecule. Such perturbations are normally small and result in a radiative life-time of the order of seconds for collision complexes. $O_2(b^1\Sigma^+_g)$ is essentially unaffected by such processes because its life-time is already of this order of magnitude. The radiative life-time of $O_2(a^1\Delta_g)$ may be shortened in the presence of O_2, N_2, and CO_2 at high pressures (4 atmospheres) as demonstrated by Badger, Wright and Whitlock [49].

Simultaneous transitions [24] can occur when singlet oxygen -

singlet oxygen collisions are more probable. The spin inversion restriction upon the single molecule transition is removed when simultaneous transitions occur since the total electron spin may be conserved. The emission in such cases occurs as a single photon.

$$2O_2(a^1\Delta_g) \longrightarrow 2O_2(X^3\Sigma^-_g) + h\nu \ (\lambda = 634nm) \qquad (1.15)$$

$$O_2(a^1\Delta_g) + O_2(b^1\Sigma^+_g) \longrightarrow 2O_2(X^3\Sigma^-_g) + h\nu \ (\lambda = 476nm) \qquad (1.16)$$

$$2O_2(b^1\Sigma^+_g) \longrightarrow 2O_2(X^3\Sigma^-_g) + h\nu \ (\lambda = 381nm) \qquad (1.17)$$

Other 'dimol' emissions have also been observed when one of the electronic states is vibrationally excited. In this work only one 'dimol' emission has been studied (equation 1.15). This emission was monitored in order to observe the temperature dependence of the deactivation of $O_2(a^1\Delta_g)$, as an alternative to monitoring the single molecule transition (equation 1.13) which would have required the use of an infrared detector.

1.4.3 Generation of Singlet Molecular Oxygen

There are five main methods of producing singlet molecular oxygen, in the gaseous phase, under laboratory conditions. A brief description of these methods is given in this section.

(a) Electric Discharge

Electric discharges (microwave, RF and DC) passed through molecular oxygen have been found to be the most convenient method of

generating singlet molecular oxygen in a flowing gas. Microwave discharges are the most commonly used.

Purified oxygen is passed through a microwave discharge either on its own or diluted in an inert carrier gas at a pressure of 1 - 10 Torr. Downstream, the gas contains a fraction of $O_2(a^1\Delta_g)$. Estimates of the proportion of $O_2(a^1\Delta_g)$ to $O_2(X^3\Sigma^-_g)$ produced in the discharge have varied from 5 - 20% [25,26,27].

The mechanism of formation of singlet molecular oxygen by this method is uncertain. It has been suggested that atom recombination is involved [13] but a more probable explanation is an electron impact mechanism [28]. While $O_2(a^1\Delta_g)$ is mainly formed in the discharge, $O_2(b^1\Sigma^+_g)$ is mainly produced outside the discharge from $O_2(a^1\Delta_g)$ via the energy pooling reaction [17,18]. The concentration of $O_2(b^1\Sigma^+_g)$ in our apparatus is estimated to be 0.02%.

$$2O_2(a^1\Delta_g) \longrightarrow O_2(b^1\Sigma^+_g) + O_2(X^3\Sigma^-_g) \qquad (1.18)$$

Atomic oxygen is also a product of the discharge. If it is allowed to remain in the gas flow, this impurity will lead to an unnecessarily complex set of possible reactants and products particularly if quenching gases are also added to the flow. Atomic oxygen can be removed by the introduction of mercury vapour to the stream of gas. This serves not only to remove the oxygen atoms but also appears to catalyse their recombination and results in an increase in the concentration of $O_2(a^1\Delta_g)$ and $O_2(b^1\Sigma^+_g)$. This has been reported to be due to the following sequence of reactions [29].

$$Hg + O \longrightarrow HgO \qquad (1.19)$$

$$HgO + O \longrightarrow Hg + O_2^* \qquad (1.20)$$

Slanger and Black have also observed the production of $O_2(a^1\Delta_g)$ via the recombination of oxygen atoms on a pyrex surface [30].

There are other approaches to the oxygen atom problem; one is to remove the oxygen atoms on a silver oxide or silver oxide / mercuric oxide surface; another to dilute the discharged oxygen sufficiently to ignore the oxygen atom concentration. The latter method carries with it the disadvantage that the $O_2(a^1\Delta_g)$ and $O_2(b^1\Sigma^+_g)$ concentrations are also lowered, which decreases both the reaction rates and the accuracy with which they may be measured.

In our apparatus, the use of a microwave discharge to produce singlet molecular oxygen and mercury vapour to remove oxygen atoms is favoured. A detailed description is given in Chapter 2.

(b) Laser Excitation

This technique is particularly suitable for the production of either $O_2(a^1\Delta_g)$ or $O_2(b^1\Sigma^+_g)$ in the absence of the both each other and atomic oxygen. The narrow band width of a laser source allows particular vibrational levels of an electronically excited molecule to be selectively populated. The problem of overcoming the small absorption coefficient for direct excitation of molecular oxygen, due to the forbidden nature of the transitions, is solved by using the high intensities of radiation produced by laser action.

$O_2(a^1\Delta_g)$, in the v=1 vibrational state, has been produced using neodymium glass and neodymium YAG lasers [31,32]. Tunable dye

lasers have been used [33,34] to produce $O_2(b^1\Sigma^+_g)$ in both the v=0 and v=1 vibrational states. More recently Kohse-Hoinghaus and Stuhl have used the photolysis of $O_2(X^3\Sigma^-_g)$, by a vacuum ultraviolet hydrogen laser, to generate $O_2(b^1\Sigma^+_g)$, indirectly, via energy transfer from $O(^1D)$.

(c) Photolysis of Ozone

Ozone photolysis at wavelengths below 300nm [35] produces only two products, $O_2(a^1\Delta_g)$ and $O(^1D)$.

$$O_3 + h\nu\ (\lambda < 300nm) \longrightarrow O(^1D) + O_2(a^1\Delta_g) \qquad (1.21)$$

The quantum efficiency of this reaction is approximately unity. Energy transfer from the $O(^1D)$ fragment produces $O_2(b^1\Sigma^+_g)$ if $O_2(X^3\Sigma^-_g)$ is present as an acceptor. This method also suffers from the same problems, of oxygen atom impurity, which arise in the electrical discharge technique.

(d) Photosensitization

Photosensitization is well documented as a method of producing singlet molecular oxygen in solution [36] but has not received much attention in the gas phase. A triplet sensitizer is used as a vehicle for the transfer of energy to $O_2(X^3\Sigma^-_g)$ and thus produce singlet molecular oxygen.

Findlay and Snelling [37] have used triplet benzene to produce $O_2(a^1\Delta_g)$, in the gas phase, while other workers have had success using triplet sulphur dioxide to produce $O_2(a^1\Delta_g)$ [38] and $O_2(b^1\Sigma^+_g)$ [39].

Reactions of this type are thought to be responsible for the

presence of singlet molecular oxygen in polluted atmospheres.

(e) Chemical Reaction

The use of chemical reactions as a source of singlet molecular oxygen for gas phase studies has been somewhat neglected. However a practical $O_2(a^1\Delta_g)$ generator has been built [6] using a basic solution of chlorine and hydrogen peroxide, which was described in section 1.1 .

Murray and Kaplan [40] have devised a method for preparing a solid ozone - triphenylphosphite complex in dichloromethane at -70°C.

$$(C_6H_5O)_3P + O_3 \text{ ----> } (C_6H_5O)_3P(O_3) \qquad (1.22)$$

When heated to -35°C this complex decomposes to produce $O_2(a^1\Delta_g)$.

$$(C_6H_5O)_3P(O_3) \text{ ----> } (C_6H_5O)_3P{=}O + O_2(a^1\Delta_g) \qquad (1.23)$$

1.4.4 Detection of Singlet Molecular Oxygen

There are several methods of detecting singlet molecular oxygen in the gaseous phase. For the most part these methods are physical rather than chemical, though a combination of the two can often prove useful. A detailed review of the possible methods of detection has been prepared by Wayne [28].The account given here of the detection of singlet molecular oxygen deals only with the methods used in this work.

Emission spectroscopy is used to monitor both $O_2(a^1\Delta_g)$ and $O_2(b^1\Sigma^+_g)$. Single molecule bands occur at 1270nm (equation 1.13) and

762nm (equation 1.14). Since the use of a microwave discharge to produce singlet molecular oxygen results in a high concentration of $O_2(a^1\Delta_g)$, the 'dimol' emission band at 634nm (equation 1.15) is sufficiently intense to be observed using a visible/near infrared photomultiplier. The same photomultiplier may then be used to observe both excited species simply by changing the filter.

A chemical method was used to calibrate a particular photomultiplier - filter combination with respect to the $O_2(a^1\Delta_g)$ concentration. The reaction of 2,3 dimethylbut-2-ene with $O_2(a^1\Delta_g)$ is rapid and involves no side reactions with $O_2(X^3\Sigma^-_g)$ and $O_2(b^1\Sigma^+_g)$.

$$(CH_3)_2C{=}C(CH_3)_2 + O_2(a^1\Delta_g) \longrightarrow H_2C{=}C(CH_3){-}C(CH_3)_2{-}OOH \qquad (1.24)$$

This reaction was used as a titration reaction, giving an end point when the 634nm emission is extinguished. A full description is given in Chapter 2.

1.5 Aims Of This Study

The aim of this work was to study further the temperature dependence of the deactivation of both $O_2(a^1\Delta_g)$ and $O_2(b^1\Sigma^+_g)$.

It was hoped that the study of pairs of quenchers, in this case HCl and HBr as well as H_2 and D_2, would yield more useful information than was obtained from previous studies [13,44] in which the quenchers varied considerably in nature. A further reason for the temperature dependence study of the quenching of singlet molecular oxygen by these additives was that some theoretical work had already been carried out on the quenching of $O_2(b^1\Sigma^+_g)$, by HBr and H_2, by Ogryzlo and co-workers [41,42]. Although temperature dependence determinations were carried out, by Ogryzlo and co-workers and also Kohse-Hoinghaus and Stuhl [43] on HBr, HCl, H_2, and D_2, they were over a comparatively short temperature range of about 200 degrees Kelvin around room temperature. Clearly, the greater the temperature range over which such reactions are studied, the better is the test of the proposed theories. A wide temperature range also allows one to be much more certain of the form of the observed temperature dependence.

Very little work has actually been carried out on the temperature dependence of $O_2(a^1\Delta_g)$. Previous work in this laboratory indicated that the temperature dependence of the quenching of $O_2(a^1\Delta_g)$ was Arrhenius in nature. It was also an aim of this work to expand these studies to include the quenching gases already mentioned.

This work may also be seen as part of the continual improvement and adaption of the discharge flow - shock tube for the study of the chemical kinetics of transient species in the gaseous phase. Indeed a brief study of the nitrogen atom recombination reaction has also been carried out, which is part of a preliminary

examination of the reactions leading to the production of oxygen atoms via the reaction of nitric oxide with atomic nitrogen.

EXPERIMENTAL

2.1 Introduction

This chapter serves to describe the discharge flow - shock tube apparatus. It is first described as a whole and then each of its component parts (flow tube, shock tube, gas handling and detection systems) is considered individually.

The test and calibration procedures carried out on the instrumentation are also described. An outline is given of the experimental routine, developed so that each measurement is performed under as near identical conditions as possible.

Finally, there is an appraisal of the safety aspect of operating the discharge flow - shock tube and handling the chemicals involved.

2.2 Discharge Flow - Shock Tube Apparatus

The apparatus (Figure 2.1) includes a conventional microwave discharge flow tube, which may be used to make kinetic measurements at ambient temperatures. The flow tube has been constructed to allow shock waves to be propagated along its length to raise the temperature of the flowing gas instantaneously. The shock wave is produced by increasing the pressure of the gas in the driver section until it is high enough to burst the diaphragm. The shock heated test gas, previously moving at approximately one metre per second towards the driver section, is pushed back along its path by the contact surface, travelling past the photomultiplier detectors up to three orders of magnitude faster.

The advantage that this has over a conventional shock tube is that transient species may be produced in the flowing gas by a method which is independent of the shock heating. Thus, transient species can be studied at temperatures below those required for their production by purely thermal means.

The combination of a shock tube with a flash photolysis technique has been investigated by Burns and Hornig [62] and also by Bradley and Tuffnell [63], in an attempt to provide a means of generating transient species prior to shock heating. Such an apparatus requires the shock to be produced very rapidly after the transient species is generated; even then the onset of the decay may be missed. Another disadvantage is that there is little or no time to establish the pre-shock conditions and compare them with the post-shock conditions in the same experiment, as a result pre-shock conditions may have to be inferred from separate room temperature measurements.

The discharge flow-shock tube has advantages over the flash photolysis-shock tube approach, since the transient species produced

FIGURE 2.1 DISCHARGE FLOW-SHOCK TUBE APPARATUS

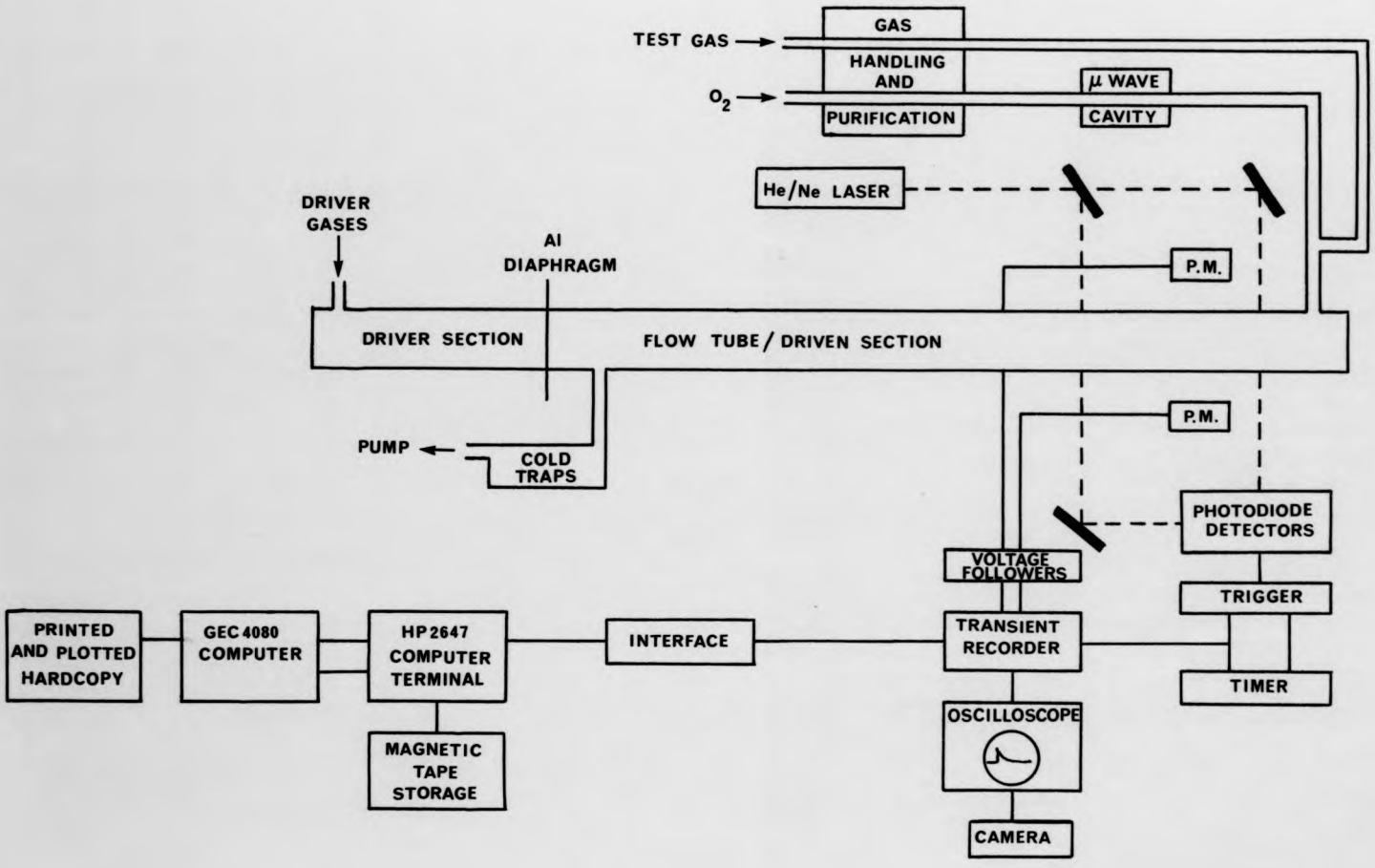

in the flowing gas have a static concentration gradient. Consequently, time may be taken to determine this gradient accurately before the high temperature measurements are made.

A view of the apparatus is presented in Plates 2.1 and 2.2 .

2.2.1 Discharge Flow Apparatus

Continuous flow tubes were among the first techniques devised [64] to follow fast reactions. Although originally designed to study reactions in the liquid phase, they were later utilized in gas phase studies as well. The principle is quite simple: one measures the concentration of reactants as a function of distance along a tube from the point of mixing.

With a continuous flow system, the distance is related to time by the linear flow velocity. One must assume that mixing reaches homogeneity very rapidly. Such tubes have been very successful in measuring the rate constants for a variety of gaseous processes at room temperature and other temperatures over a limited range using thermostatted jackets.

Figure 2.2 shows the flow tube component of the apparatus, together with the microwave cavity and gas handling system.

Singlet molecular oxygen is produced by passing purified oxygen over a mercury reservoir and then through a microwave discharge. The discharge is produced in a quartz tube by a 2450 MHz microwave generator (EMS Microtron 200), with a maximum power output of 200W. The microwave cavity (EMS 214L) is a 1/4 wave radial type, cooled by a jet of compressed air, which may be tuned to minimize the reflected power. Under normal operating conditions (100W generator output) the reflected power is about 1-2% when the cavity is well tuned. The cavity is shielded by a Faraday Cage and is located 1.3

Plate 2.1

The discharge flow-shock tube, looking towards the driver section. The flow tube is covered with black cloth and is located behind the test gas handling system.

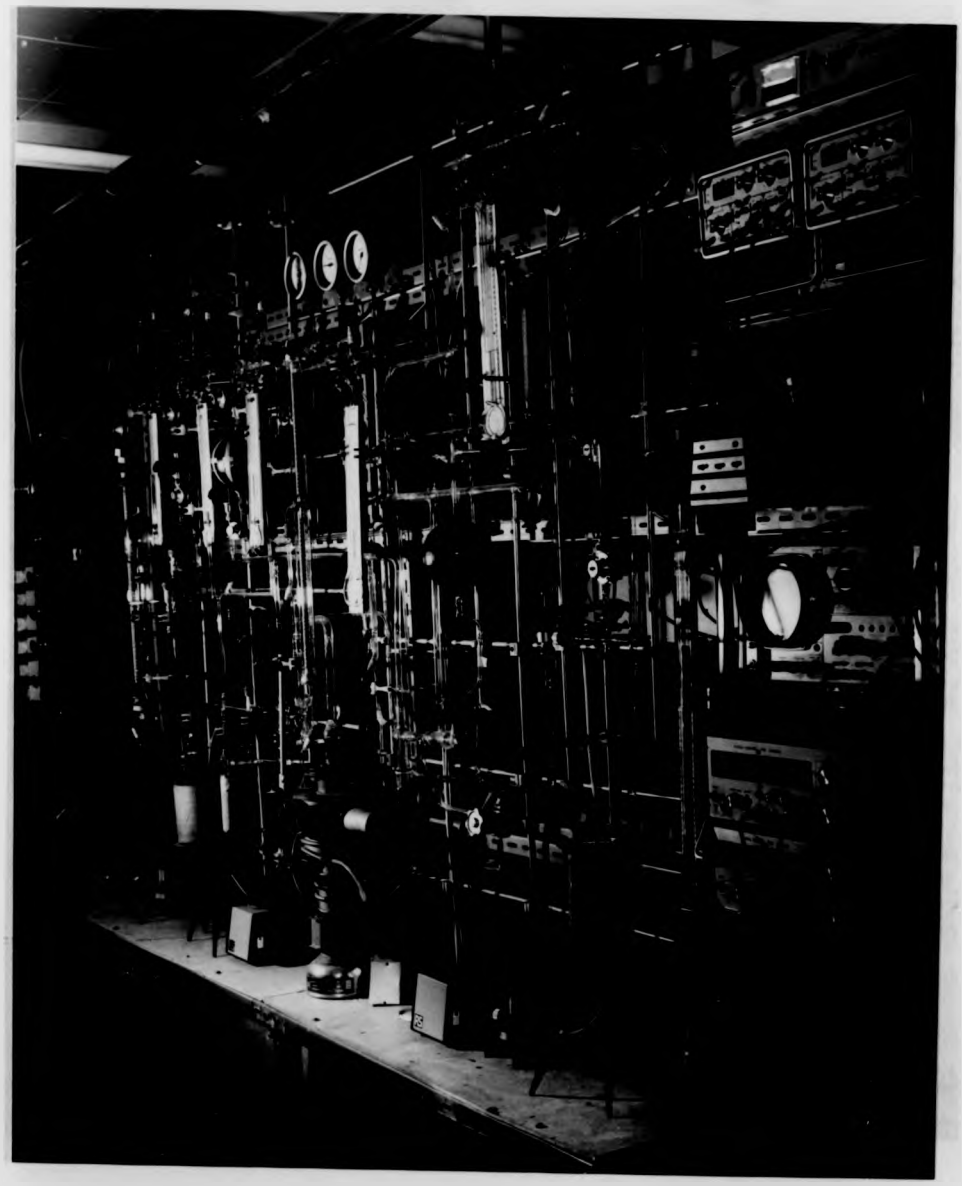

Plate 2.1

The discharge flow-shock tube, looking towards the driver section. The flow tube is covered with black cloth and is located behind the test gas handling system.

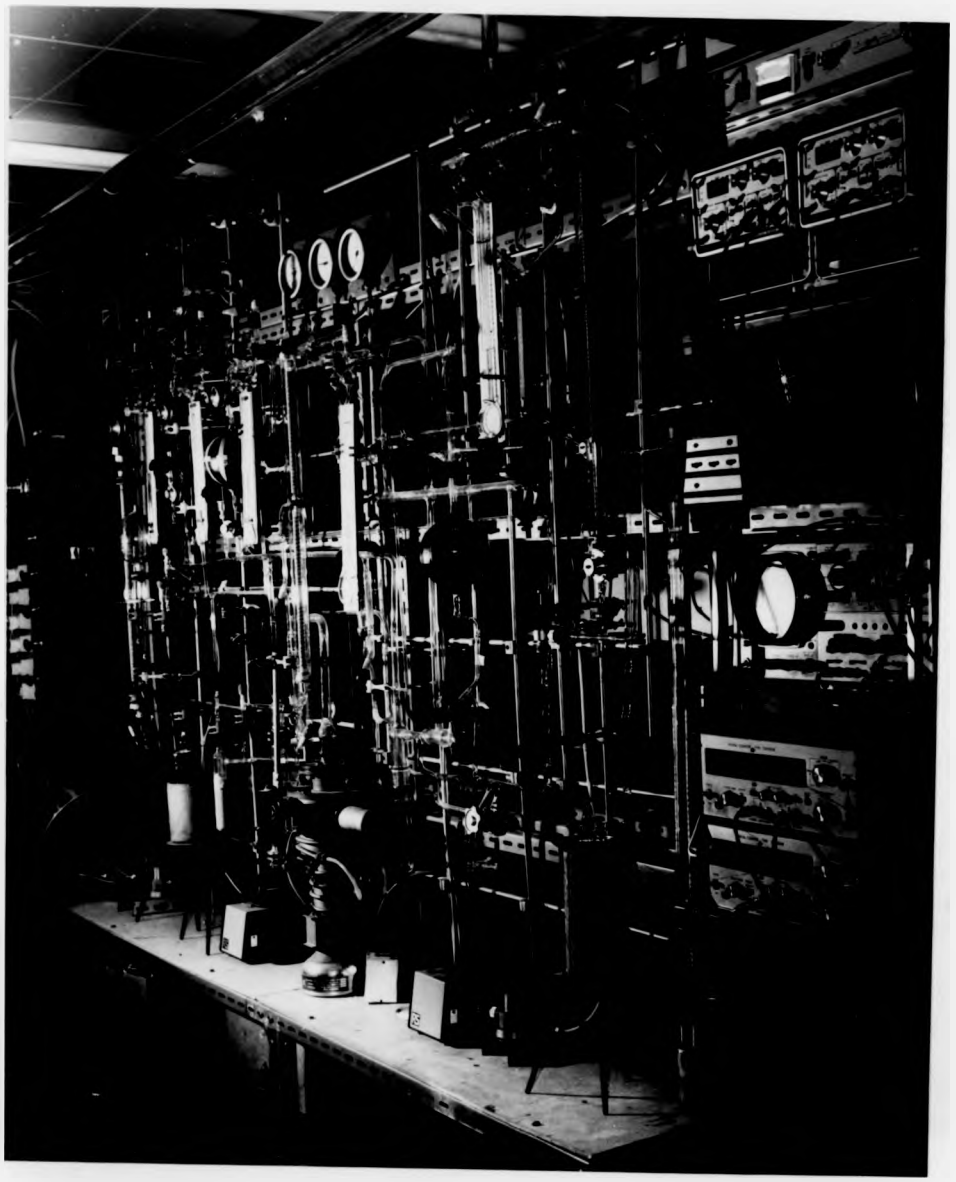

Plate 2.2

The discharge flow-shock tube, looking towards the discharge. The console on the right houses the light screen detectors.

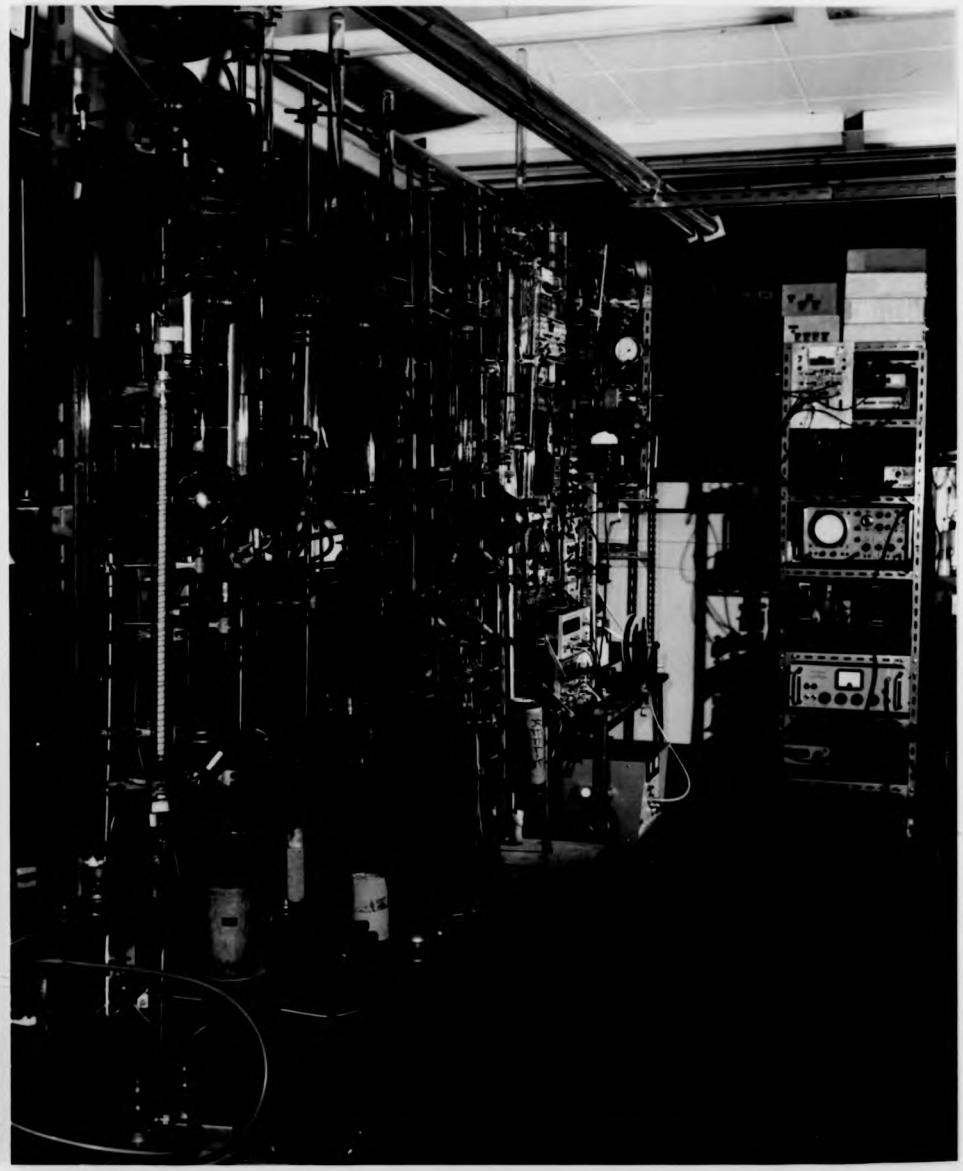

Plate 2.2

The discharge flow-shock tube, looking towards the discharge. The console on the right houses the light screen detectors.

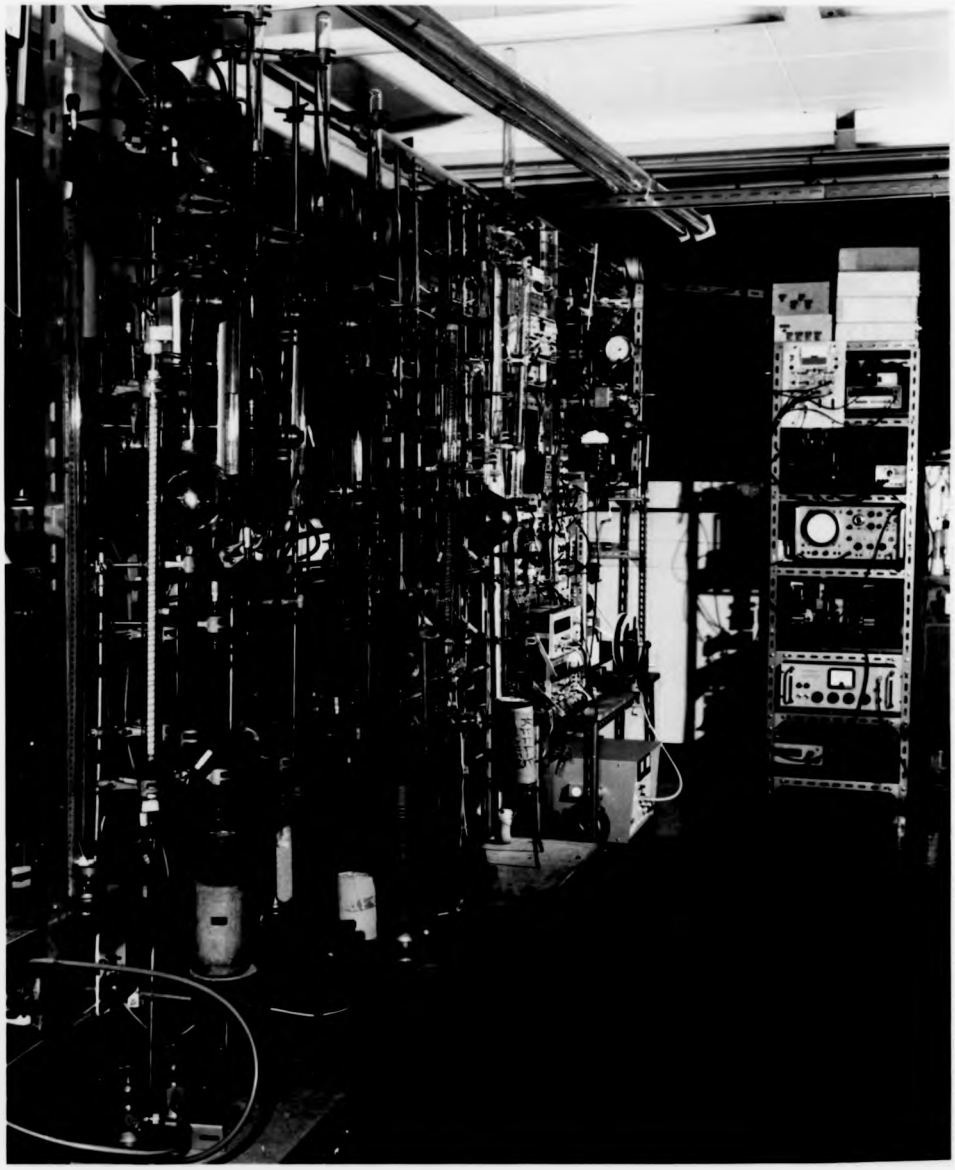

FIGURE 2.2 FLOW TUBE AND GAS HANDLING SYSTEM

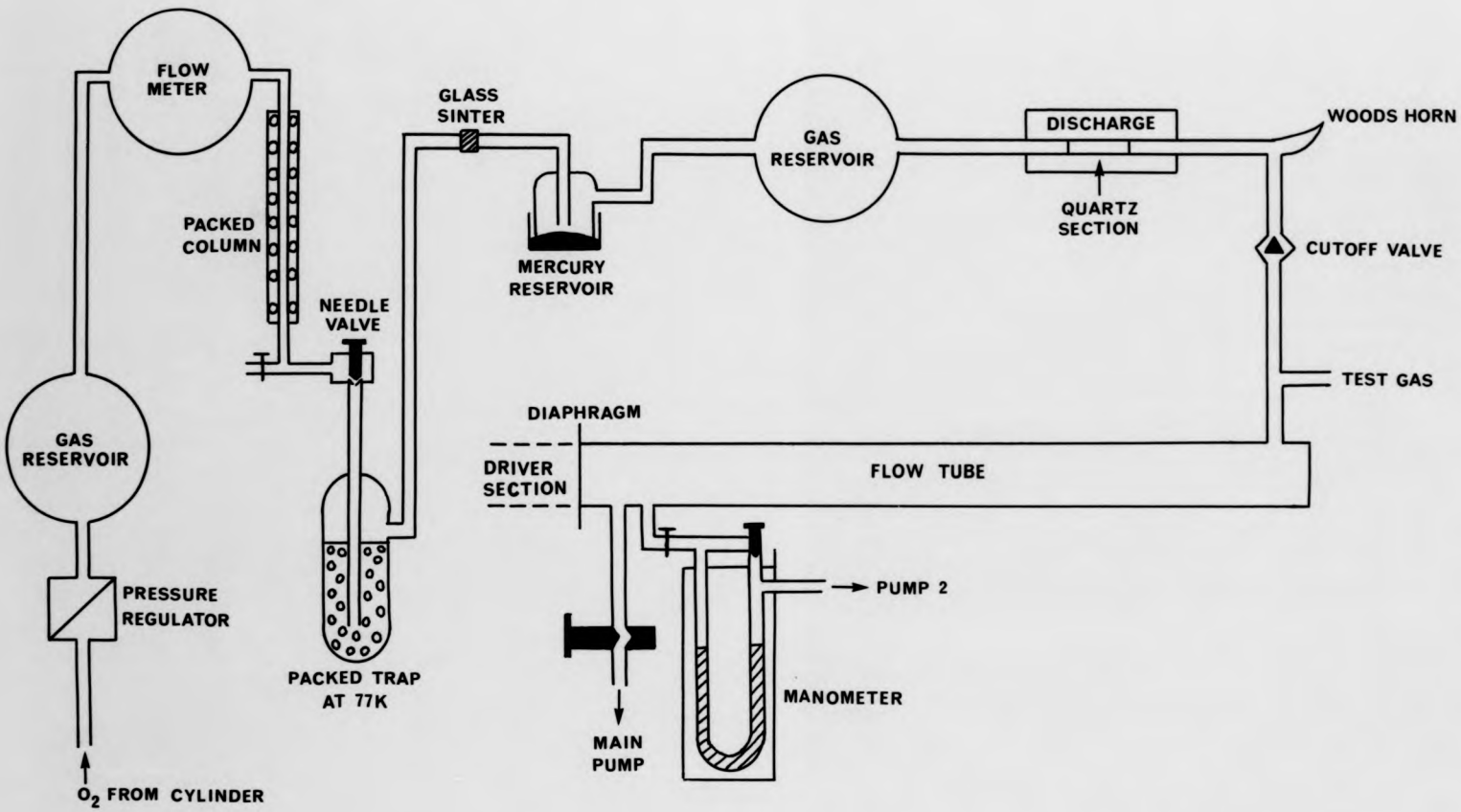

metres upstream of the main flow tube.

After passing through the discharge the mercury laden oxygen contains $O_2(a^1\Delta_g)$, $O_2(b^1\Sigma^+_g)$, and $O_2(X^3\Sigma^-_g)$ together with Hg and O atoms. The atomic oxygen is removed by reaction with the atomic mercury. A film of mercuric oxide is deposited in the 0.8 metres of tube following the discharge. Mercuric oxide is also active in removing oxygen atoms [29], producing $O_2(a^1\Delta_g)$ and regenerating atomic mercury, as described in section 1.4.3 (a) . The absence of atomic oxygen at the O_2-test gas mixing point may be demonstrated by adding nitric oxide as a test gas. When this was done no air afterglow was detected, indicating the absence of oxygen atoms.

The microwave cavity and mercury reservoir are protected from the shock wave and the piston of high pressure gas by a PTFE cut-off valve, which is closed by the arrival of the shock wave. This prevents fragments of diaphragm material from lodging in the cavity and also stops the mercury being blown back into the gas handling system.

The main flow tube consists of a 5 m length of pyrex tubing (Corning Ltd.) with an i.d. of 50.8 mm. The tube is pumped by a large rotary pump (Edwards HISC 3000). The flow rate and the pressure in this tube can be controlled by a PTFE screw valve located between the flow tube and the pump.

The pressure in the flow tube is measured using a diethylphthalate manometer separately pumped by a smaller rotary pump (Edwards Speedivac ED35). The density of the diethylphthalate was measured as 1.1176×10^3 kg m^{-3}, giving a factor for the conversion of mm DEP (diethylphthalate) to torr of 0.08251.

2.2.2 Shock Tube Apparatus

In its simplest form the shock tube [65] consists of a long straight tube, of uniform cross-section, divided into two sections by a thin diaphragm. Each section is filled with a gas (not necessarily the same gas) at different pressures. The diaphragm is rapidly removed either by pricking it with a needle or by increasing the pressure on one side until it bursts.

As the diaphragm bursts, the driver gas expands into the test section (low pressure) in the manner of a piston accelerating to a constant velocity. The resulting pressure step generates a shock wave which travels in front of the expanding gas (contact surface), along the axis of the tube, parallel to the walls. Meanwhile a rarefaction wave is propagated in the opposite direction at the velocity of sound. The shock wave heats the test gas, on which observations are made before the arrival of the contact surface. The time available for such observations can be of the order of microseconds or milliseconds depending on the length of the tube and the difference in velocity between the shock wave and the contact surface [66].

Figure 2.3 is a diagram of the shock tube component of the apparatus used in this work. The driver section is 1.3 m long , with an i.d. of 50.8 mm, and is constructed from stainless steel. This is separated from the 5 m long, 50.8 mm i.d., pyrex driven section (flow tube) by an aluminium diaphragm.

A wide range of shock speeds may be obtained, from 0.7 km s^{-1} to 1.6 km s^{-1} in this tube. This is achieved by:

(a) changing the thickness of the diaphragm (0.051 or 0.102 mm) which results in bursting pressures of 2.3 and 6.5 atmospheres.

FIGURE 2.3 SHOCK TUBE

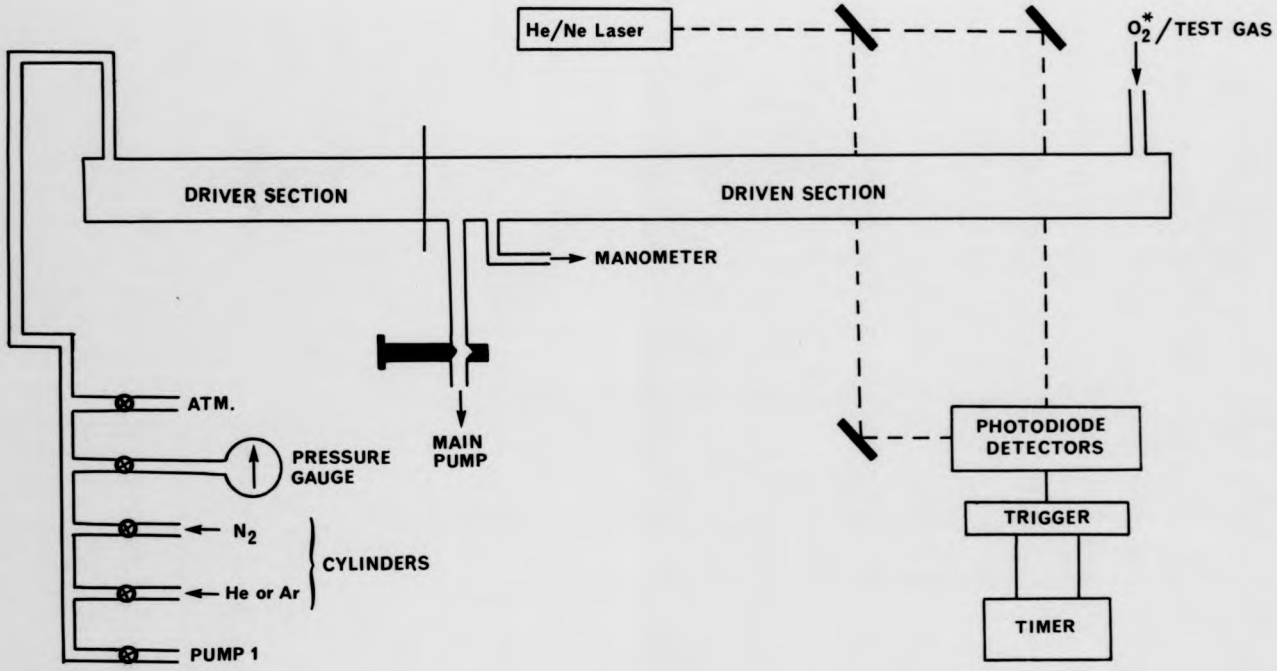

(b) varying the composition of the driver gas ($Ar/N_2/He$)

An argon driver gas with a bursting pressure of 2.3 atmospheres, produces a shock wave with a speed of 0.7 km s^{-1}. The upper limit, 1.6 km s^{-1}, is produced using a helium driver gas at a bursting pressure of 6.5 atmospheres.

The observation station at which the photomultipliers are located is 4.4 m from the diaphragm, to maximize the time elapsed between the passing of the shock wave and the arrival of the contact surface, without interference from the reflected shock wave produced when the shock wave reaches the end of the tube. The speed of the shock wave is measured using the laser light screen arrangement described in section 2.3 .

When not in use both driver and flow sections are left under vacuum to avoid unnecessary adsorption of water vapour by the system. The system is pumped down through liquid nitrogen traps for one hour, prior to experiments being carried out, in an attempt to remove as much water vapour as routinely possible.

2.2.3 Gas Handling System

The system for handling the driver gases is shown in figure 2.3. The gases are used as supplied (Table 2.1) without further purification. The gases are taken from the supply cylinders by 10 mm nylon tubing to a manifold which also contains outlets to the atmosphere, a Budenberg dial gauge, and a small rotary pump (Edwards Speedivac ED 35).

Mixing of the driver gases may be achieved by introducing one gas into the driver section at a chosen pressure and then increasing the pressure of the driver section to the diaphragm bursting point using the second gas.

The handling of the test gas requires a more complicated

Table 2.1. Gases Used

Gas	Usage	Supplier	% Purity
Argon	Driver	B.O.C.	99.996
Helium	Driver	Gas & Equipment	99.995
Nitrogen	Driver & Test	B.O.C.	99.99
Oxygen	Test	B.O.C.	99.80
Hydrogen	Test	B.O.C.	99.996
Hydrogen Chloride	Test	B.O.C.	99.6
Hydrogen Bromide	Test	B.O.C.	99.8
Deuterium	Test	B.O.C.	99.70
Nitric Oxide	Test	B.O.C.	99.2

system because of the need for further purification and accurate flow control, together with the handling requirements of both non-corrosive and corrosive gases

Figure 2.2 shows the framework of the oxygen gas handling system from the supply cylinder to the flow tube. The handling of the test gas is carried out in a similar system, up to the point where the oxygen enters the mercury reservoir. Each unit in each system can be isolated from its neighbours by a Rotaflow tap (Corning Quickfit).

Oxygen and the non-corrosive test gases are passed from their cylinders through a pressure regulator (Edwards VPC1) which maintains a pressure of 740 torr in the first gas reservoir. Corrosive gases were found to attack the pressure regulator and thus required special handling through a unit (Figure 2.4) which bypassed the regulator. This unit consisted of a Teflon Sampling Bag (Alltech Associates 41302) with an inlet/outlet port connected to the supply cylinder and the gas reservoir by PTFE tubing. The inflation of the bag by the test gas was maintained between 3/4 and 1/2 full, to ensure a steady flow of gas to the reservoir at atmospheric pressure. The reservoir (1 dm^3) is present to help steady the flow of gas to the flow meter.

In the first experiments, when HBr and HCl were studied, both flow meters were of the capillary type (Figure 2.5(a)). These flow meters were made in the laboratory and required calibration. The calibration was performed by flowing pure oxygen into a previously evacuated closed system, of known volume (15.3 dm^3) [46], at a constant flow rate. The length of time for this operation was chosen so that the pressure rise in the closed system did not have an observable effect upon the flow rate. By measuring the final pressure of the closed system and knowing the volume and flow time provided that there is no change in temperature during the operation, the flow rate is calculated from:

FIGURE 2.4 CORROSIVE GAS PRESSURE REGULATION UNIT

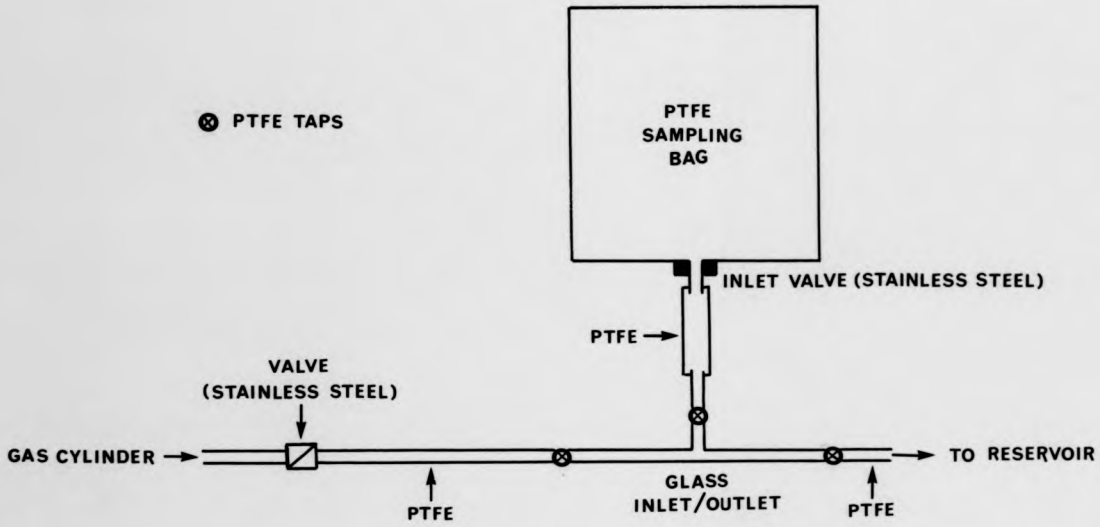

FIGURE 2.5

a) CAPILLARY FLOW METER

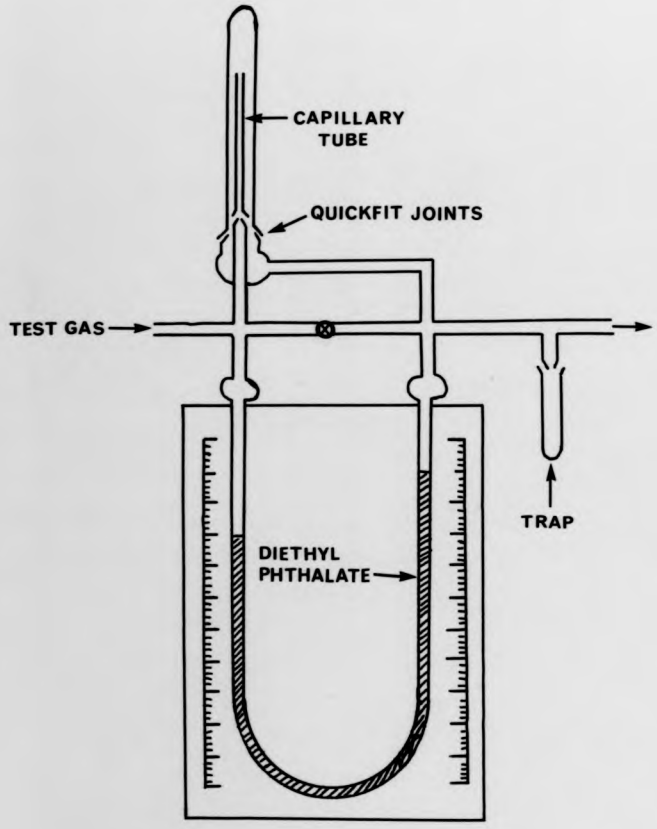

b) THERMAL MASS FLOW METER

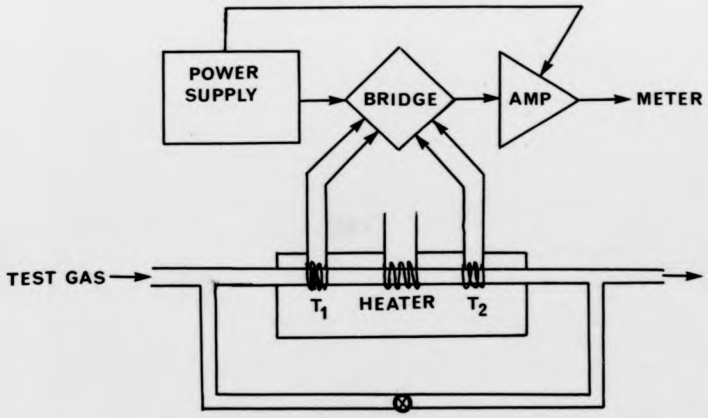

T_1 UPSTREAM TEMPERATURE SENSOR

T_2 DOWNSTREAM TEMPERATURE SENSOR

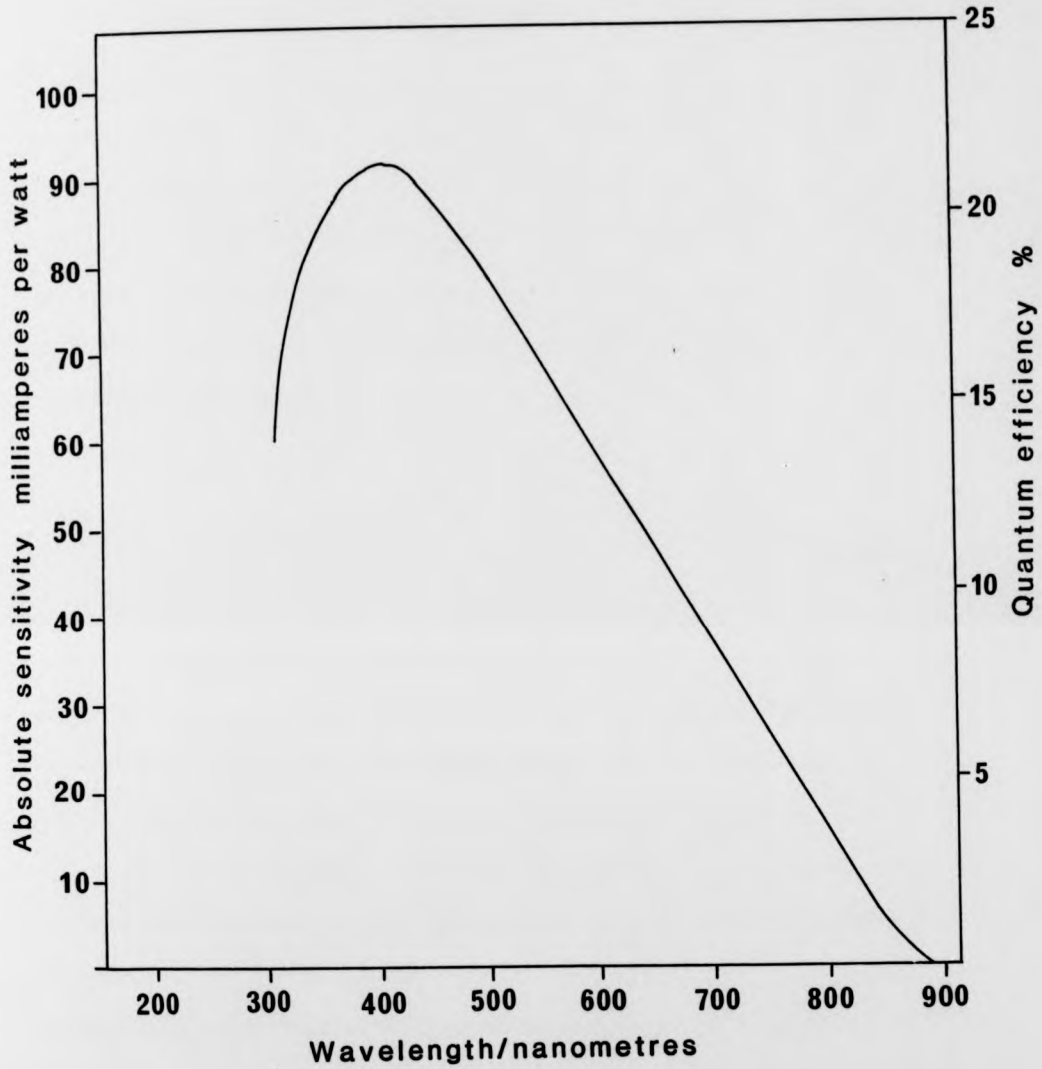

FIGURE 2.6 SPECTRAL RESPONSE OF PHOTOMULTIPLIERS

$$\text{FLOW RATE} = V_1 P_1 / P_2 t \qquad (2.1)$$

where V_1=volume of the closed system, P_1=pressure of the closed system, P_2=pressure of the gas in the gas handling system, and t=flow time. This procedure was carried out for several different flow rates measured as mm of diethylphthalate on the meter. The calibration of the flow meters may then be corrected for the test gas by applying Poiseuille's Law [45].

$$\Phi_m / \Phi_o = \eta_o / \eta_m \qquad (2.2)$$

where Φ_m and Φ_o are the flow rates of the test gas and oxygen respectively, and η_m and η_o are the viscosities at the operating temperature (295K). The calibration graphs for the flow meters calibrated by the author are given in Figures 2.7 and 2.8

The disadvantage of capillary flow meter method is that daily fluctuations in pressure and temperature have an adverse effect upon the accuracy of the calibration. Corrections must be made constantly, particularly when the Teflon bag regulating unit is in use.

When H_2 and D_2 were studied, thermal mass flow meters (Brooks 5810) were introduced to replace the capillary models. These flow sensors operate on the basis of a temperature difference rather than a pressure difference (Figure 2.5(b)). A heating coil uniformly heats the gas flow stream. As a result, both upstream and downstream sensor coils are heated by the flowing gas. When there is no flow, a balanced bridge circuit is established to provide a zero output signal. As gas flows within the sensor, a temperature differential is created between the upstream and downstream sensors. This difference

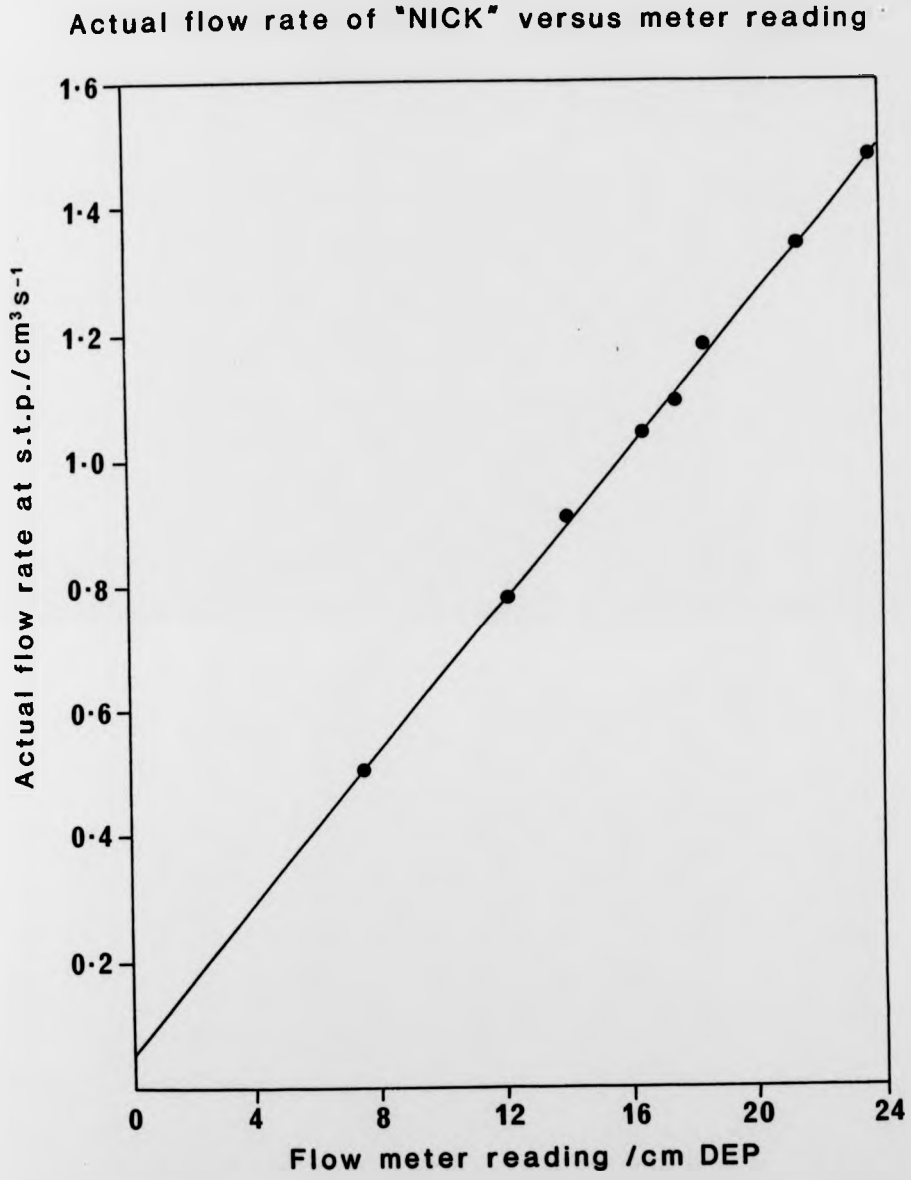

FIGURE 2.7 CALIBRATION FOR CAPILLARY FLOW METER "NICK"

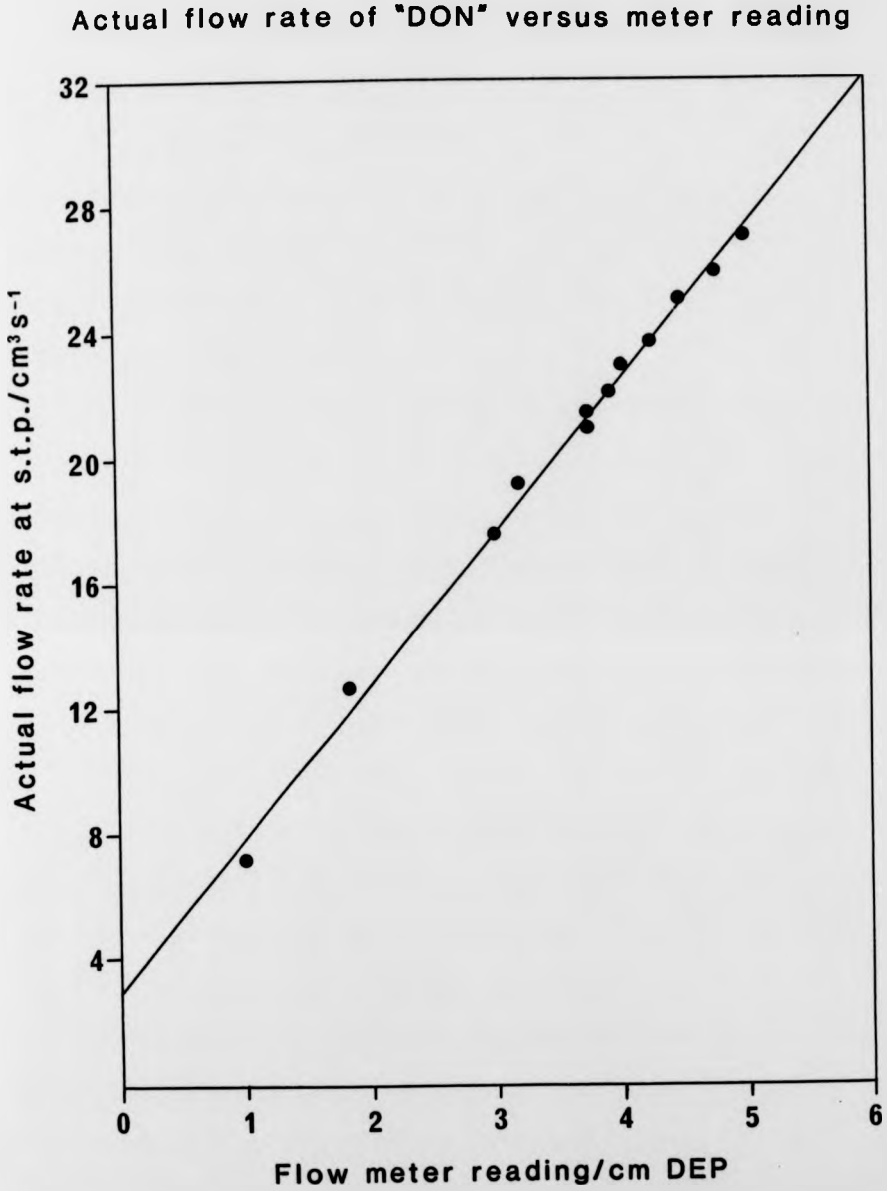

FIGURE 2.8 CALIBRATION OF CAPILLARY FLOW METER "DON"

generates a D.C. current which is directly proportional to the temperature difference and hence the mass flow rate. The mass flow rate is displayed on a meter in terms of ml per minute at s.t.p.

The precaution was taken of comparing the calibration of the mass flow meters with that of the capillary flow meters by installing a mass flow meter in series with a capillary flow meter. In this way their accuracies could be compared directly. Figure 2.9 shows the results of one of these tests.

After travelling through the flow sensor unit the gas is dried by passing through a column (60cm x 1.0cm i.d.) packed with type 4A molecular sieve. The columns are surrounded by a heating coil which facilitates the in situ regeneration of the molecular sieve. This is done by purging the system with nitrogen gas while the column is at a temperature of 453K. The exhaust gas exits before the needle valve which is closed to protect the remainder of the system from the wet gas.

The test gas then reaches the stainless steel fine control needle valve (Edwards Speedivac LB1B). This valve controls the flow of gas into the main tube. Steady flows from 0.10 $cm^3\ s^{-1}$ to 50.0 $cm^3\ s^{-1}$ are maintained with this arrangement.

Before entering the flow tube the gas passes through the final purification unit which is a trap, filled with type 4A molecular sieve , maintained at 77K by a Dewar of liquid nitrogen, which removes any volatile impurities that have avoided absorption by the molecular sieve in the room temperature column.

Table 2.1 lists the manufacturers and initial purity of the gases used.

Comparison of capillary and thermal mass flow meters

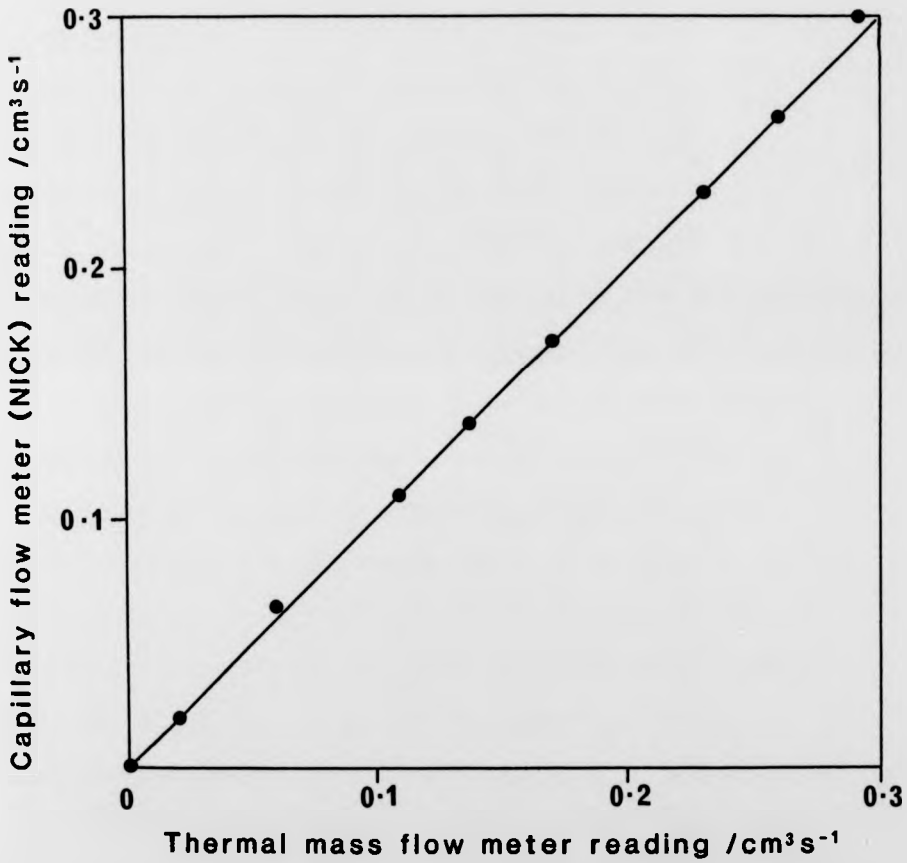

FIGURE 2.9 DIRECT CALIBRATION CHECK OF THERMAL MASS WITH CAPILLARY FLOW METERS

2.3 Measurement Techniques and Instrumentation

Emissions at 634nm and 762nm (Equations 1.14 and 1.15) were measured with two photomultipliers (EMI 9658B) fitted with interference filters (Baltzer). The photomultipliers are in housings which are electrically and magnetically shielded, and are operated at the manufacturers recommended voltage of 1.2 kV, using a Brandenburg 472 E.H.T. supply.

The geometry of the photomultiplier/filter/slit arrangement is considered in section 2.3.1 . The spectral response of the photomultipliers, taken from the manufacturer's data, is shown in Figure 2.6 . A Pye-Unicam spectrometer (SP8-100) was used to record the transmission characteristics of the filters (Figure 2.10 (a) and (b)).

The two photomultiplier units, comprising photomultiplier, adjustable slit mechanism and filter, are located 4.4 m from the diaphragm , perpendicular to the flow tube. One photomultiplier unit remains stationary at the observation station as a reference, while the other may be moved along a 2.5 m track parallel to the flow tube. By exchanging the filters one can measure the gradient of either emission with a reference of the same wavelength or monitor both emissions simultaneously.

The system for measurement and recording data is shown in Figure 2.1 and presented in more detail as a block diagram (Figure 2.11).

The output from each photomultiplier is copied by a voltage follower and fed to either a digital voltmeter (Solartron 7040) or to a transient recorder (Datalab 905) for rapid data collection during the post-shock period.

The transient recorders are triggered, by a signal from the laser light screens, upon the arrival of the shock front. The output

FIGURE 2.10 FILTER TRANSMISSION

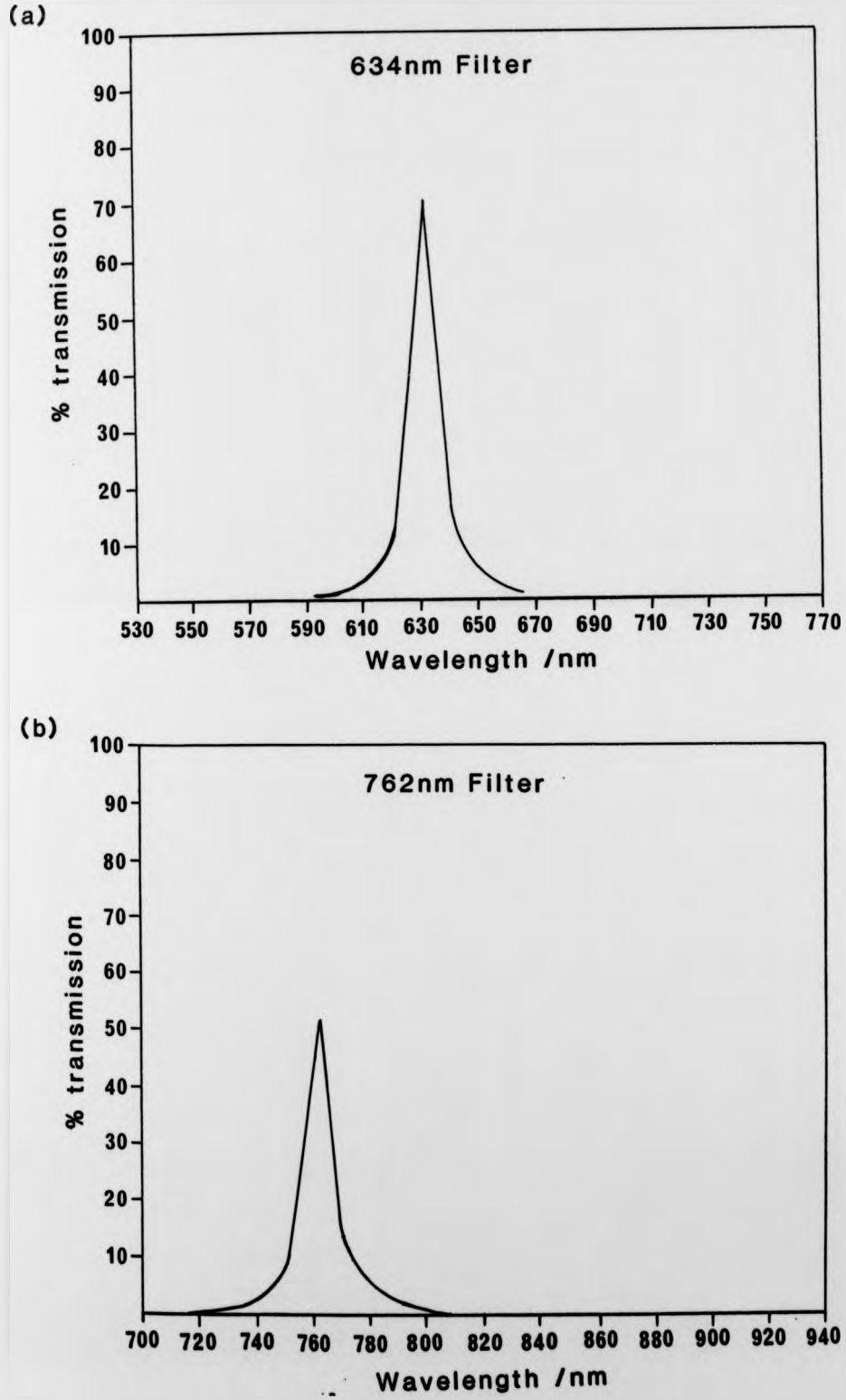

FIGURE 2.11 BLOCK DIAGRAM OF DETECTION AND RECORDING SYSTEM

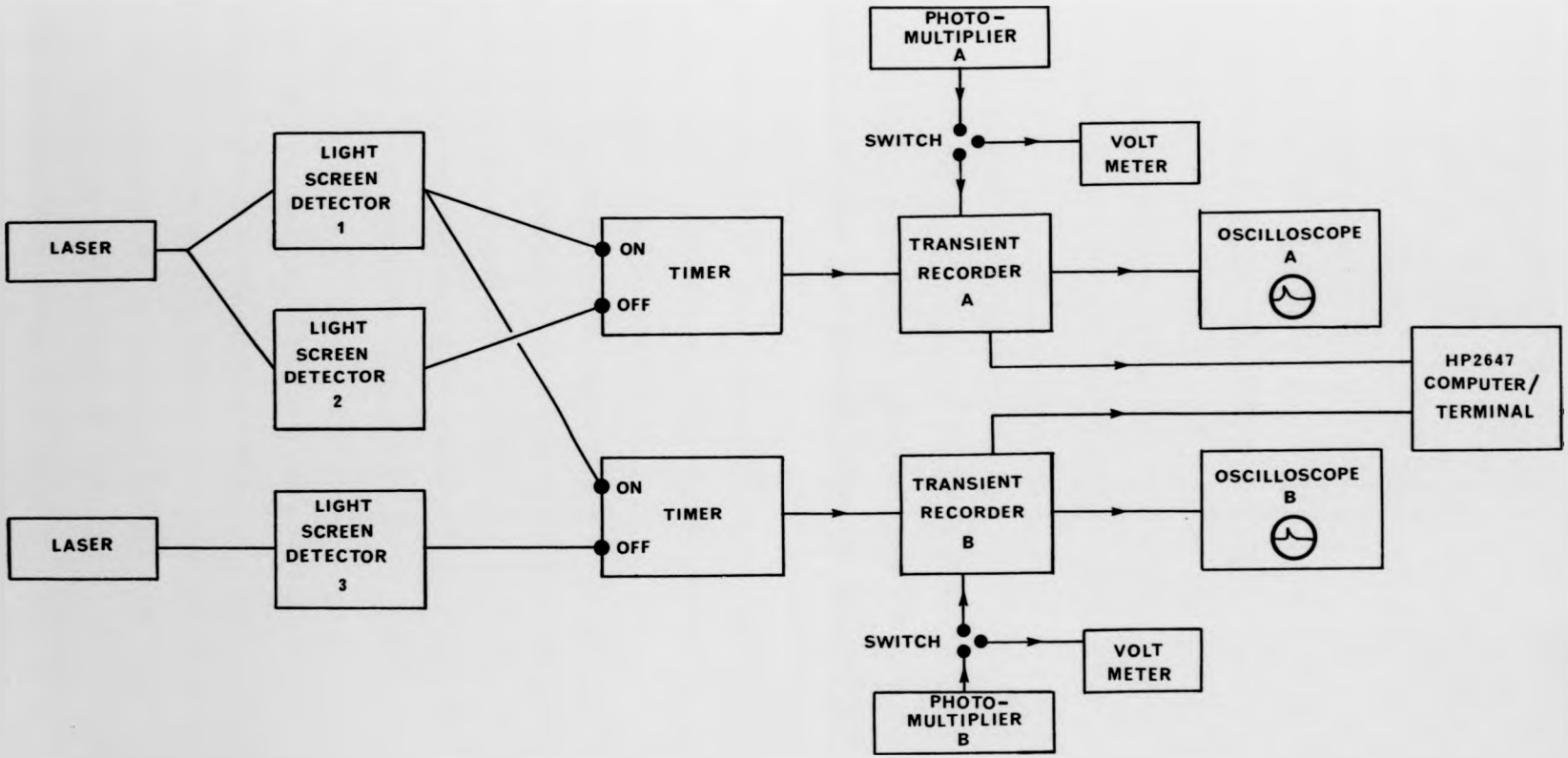

of the transient recorders is displayed on a pair of oscilloscopes (Hewlett Packard Series 140), which allows the trace to be photographed and retained for future reference.

Data from the transient recorder is transferred to the display memory of the graphics computer terminal (Hewlett Packard 2647A) and is then stored initially on magnetic tape. At a later stage the data are scaled and converted using the HP2647A in its computer mode, before the data are transferred to the University's main computer (GEC 4082).

The shock speed is determined by means of laser light screens which allow the passage of the shock front to be timed over a known distance. Two He/Ne lasers (Ferranti GP2, 1 mW and Rofin 7906, 1.5 mW) are used. The beam from the Rofin 7906 laser is split into two, using a half silvered mirror. The three laser beams cross the flow tube at an angle of 87^{o} and pass to three silicon photovoltaic detectors (RS 303-674) through a system of mirrors. Each light screen has a path length of approximately 5 m.

Screen 1 is located on the diaphragm side of the observation station and 2 and 3 are located 713 mm and 816 mm upstream of 1, on the opposite side of the observation station. The lasers, mirrors and detectors are mounted independently of the main apparatus so that vibration from the bursting of the diaphragm does not activate them prematurely.

The change in density at the shock front causes both reflection and refraction [46] of the incident laser beam which deflects it onto the detectors resulting in a sharp rise in output. The risetime of the photovoltaic detectors and their voltage followers, used in the light screens, is about 0.5 μs.

The pulse from light screen 1 starts the two timer-counters (Philips PM6671) and triggers the transient recorders. The timers are

stopped by pulses from light screens 2 and 3. Thus two independent determinations of the shock speed are made. The difference between these two measurements is always less than 0.5%.

The attenuation of the shock front has previously been checked by Pedley [46], and the deceleration was found to be less than 1% per metre. The observations made in this work are in agreement with this.

The risetime of the photomultiplier unit was determined experimentally and found to be mainly dependent upon slit width. This is discussed in detail in the next section.

The measurement of emission intensity (photomultiplier output voltage), pressure and time constitutes the fundemental experimental data on which this work is based. Therefore, checks were made on the devices concerned with these measurements to maintain their accuracy.

The output from the transient recorders, oscilloscopes and digital voltmeters were checked periodically against the output of a signal generator (Marconi TF210) to ensure that all gave the same outputs for the same input signal.

The time base of the oscilloscopes and the transient recorder was also checked using the crystal oscillator in the timer-counter.

2.3.1 Risetime of the Detection Equipment

The overall risetime may be considered as two components: the risetime of the electrical system and the risetime of the optical system. These two components are combined, to give the overall risetime, as the square root of the sum of their squares.

(a) Electrical Risetime

The risetime was measured by irradiating the photomultiplier unit with a light emitting diode supplied with a square wave signal. The risetime of the signal was in the 0.1 μs region. The response of

the photomultiplier and transient recorder was displayed on an oscilloscope. A plot of ln RISE versus time was made and the first order rate constant estimated. The risetime, τ, is the reciprocal of this rate constant.

$$\tau = 2.7 \pm 0.3 \ \mu s$$

(b) Optical Risetime

During this work the single slit arrangement used by previous workers was exchanged for a double slit mechanism, designed specifically for the flow tube and constructed by the University's main workshop. Risetimes for both mechanisms are discussed here.

The risetime for the optical system is the time taken for the shock front to pass through the volume viewed by the photomultiplier. From a knowledge of the geometry of the optical system this can be calculated for a variety of shock speeds. The optical paths were drawn out to actual scale (Figures 2.12 and 2.13) and the optical windows established for various slit widths.

A 2.0 mm slit was used during $O_2(b^1 \Sigma^+_g)$ emission monitoring (762nm) and a 5.0 mm slit was used for the less intense 'dimol' emission (634nm). The flow tube is made of borosilicate glass (QVF 7740) which has a refractive index of 1.474. The wall thickness is 3.85 mm, hence the angle of refraction may be calculated from the angle of incidence and the light path mapped. The effect of the tube wall is to slightly reduce the size of the optical window.

Plots of percentage area swept versus time were made for each slit mechanism for the appropriate slit widths and shock speeds. The time taken for the shock front to sweep 80% of the total area was considered to be the optical risetime. The first and last 10% of the area was neglected because of the sigmoidal nature of the curve. The

FIGURE 2.12 OPTICAL DETECTION SYSTEM - DOUBLE SLIT

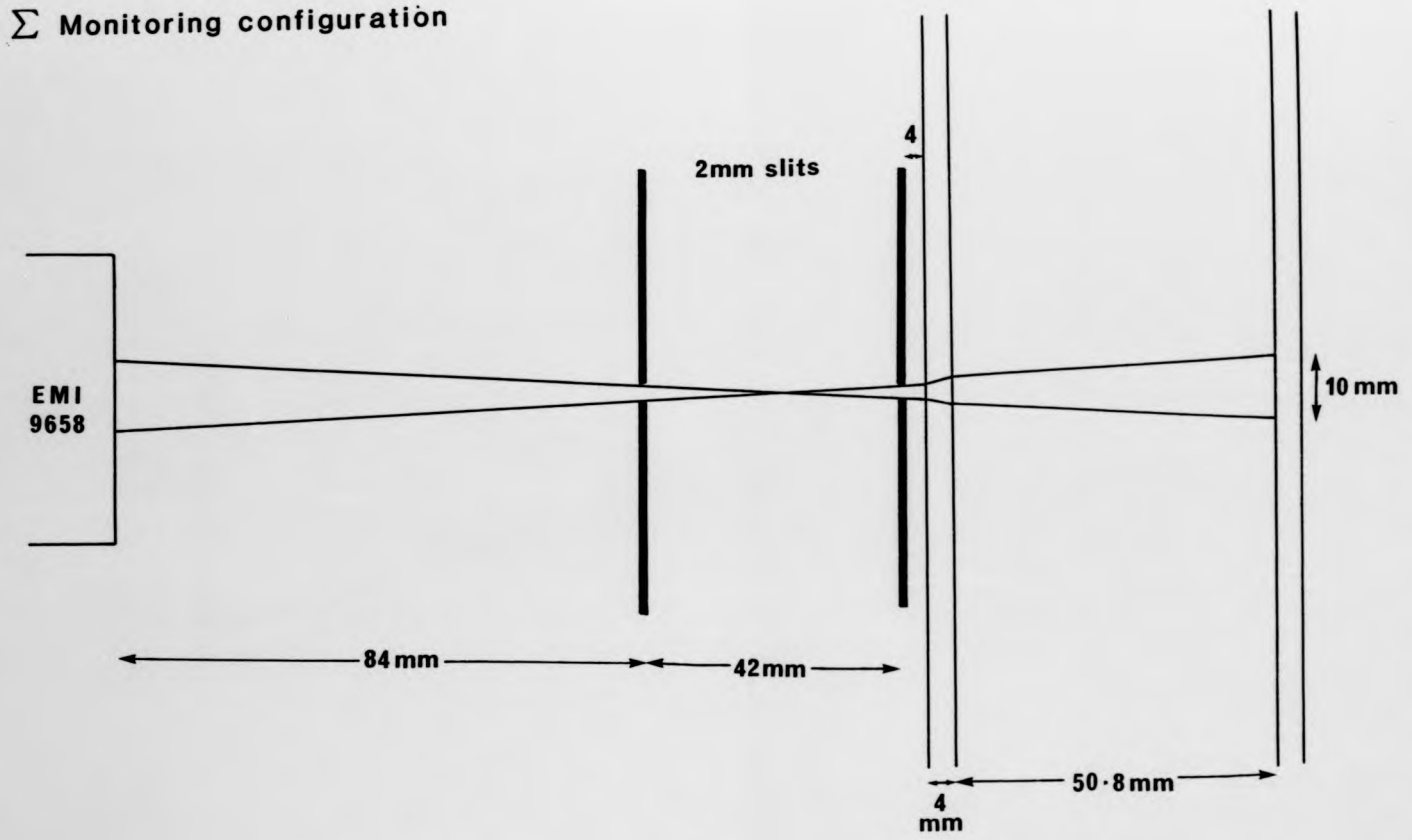

FIGURE 2.13 OPTICAL DETECTION SYSTEM - SINGLE SLIT

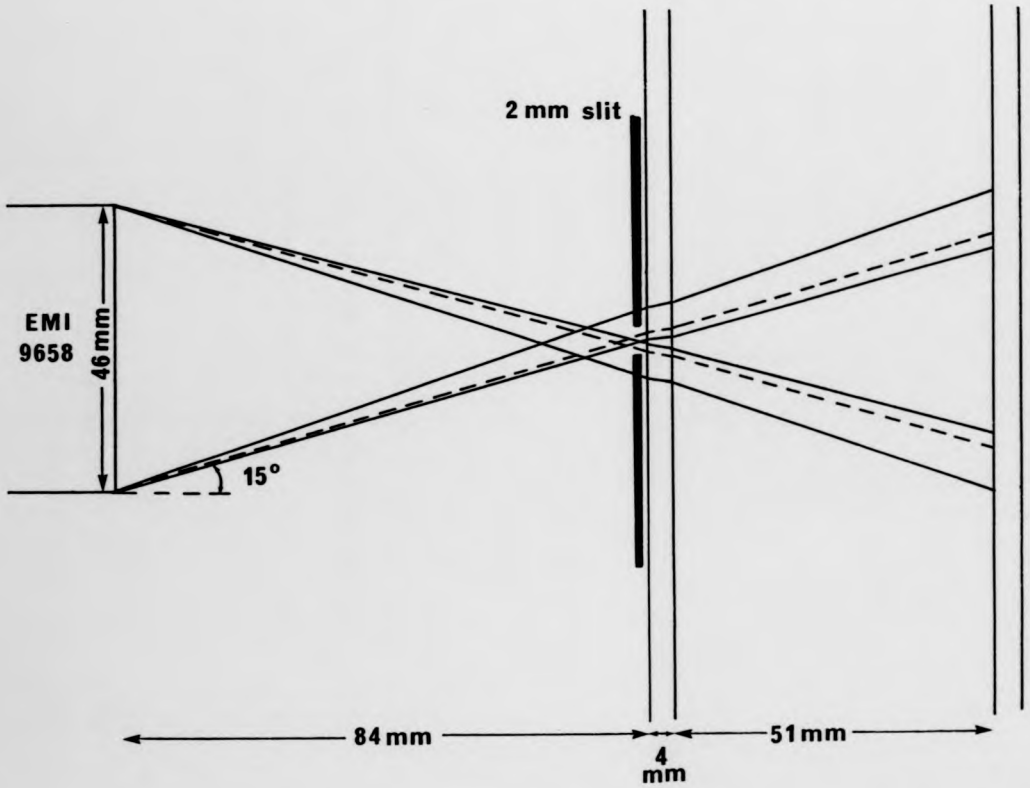

contribution from the off-axis plane was assumed to be insignificant.

Tables 2.2 and 2.3 compare the risetimes of the two optical systems.

These results show that the optical component of the system dominates the overall risetime, being responsible for over 90% of its value, in all cases. By using the double slit mechanism the risetime of the detection system is reduced by a factor of two.

These calculate risetimes may be used as integration times when the data is analysed reducing by one the number of parameters which are evaluated by iteration. A comparison of these calculated values with experimentally obtained values from 634nm data gave agreement within 1.0 μs.

2.3.2 Photomultiplier Calibration

A photomultiplier unit was calibrated to measure the concentration of $O_2(a^1\Delta_g)$, via the 634nm emission, under normal operating conditions.

The concentration of $O_2(a^1\Delta_g)$ was established using a titration reaction. The titrant chosen was 2,3-dimethylbut-2-ene (TME) which reacts with $O_2(a^1\Delta_g)$ to produce 2,3-dimethyl-3-hydroperoxybut-1-ene.

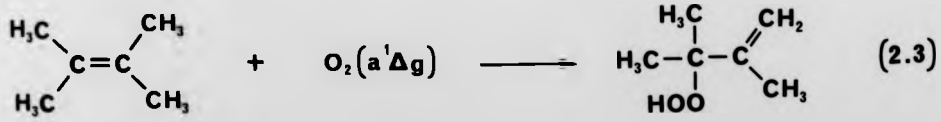

(2.3)

The stoichiometry of the of the reaction is 1:1 and it proceeds to give 100% conversion [50,51,52]. TME does not react with either $O_2(X^3\Sigma^-_g)$ or $O_2(b^1\Sigma^+_g)$, nor does it quench $O_2(a^1\Delta_g)$ [50,51].

TME is a liquid with an appreciable vapour pressure at ambient

Table 2.2. Risetimes for 762 nm Emission Monitoring

Shock Speed /km s^{-1}	Temperature /Kelvin	Single Slit Mechanism		Double Slit Mechanism	
		Optical Risetime/μs	Overall Risetime/μs	Optical Risetime/μs	Overall Risetime/μs
0.694	500	27.4	27.5	14.4	14.7
0.830	600	22.9	23.0	12.0	12.3
0.950	700	20.0	20.2	10.5	10.9
1.058	800	18.0	18.2	9.5	9.8
1.158	900	16.4	16.6	8.6	9.0
1.250	1000	15.2	15.4	8.0	8.4
1.336	1100	14.2	14.5	7.5	7.9
1.567	1400	12.1	12.5	6.4	6.9
1.709	1600	11.1	11.5	5.9	6.4

Table 2.3. Risetimes for 634 nm Emission Monitoring

Shock Speed /km s^{-1}	Temperature /Kelvin	Single Slit Mechanism		Double Slit Mechanism	
		Optical Risetime/μs	Overall Risetime/μs	Optical Risetime/μs	Overall Risetime/μs
0.694	500	43.9	44.0	30.3	30.4
0.830	600	36.7	36.8	25.3	25.4
0.950	700	32.1	32.2	22.1	22.3
1.058	800	28.8	28.9	19.8	20.0
1.158	900	26.3	26.5	18.1	18.3
1.250	1000	24.4	24.5	16.8	17.0
1.336	1100	22.8	23.0	15.7	15.7
1.567	1400	19.5	19.8	13.4	13.7
1.709	1600	17.8	18.1	12.3	12.6

temperatures. The vapour pressure was measured using the apparatus shown in Figure 2.14 . The liquid sample was frozen using a carbon dioxide/acetone bath and the apparatus evacuated. The system was then closed and the sample allowed to come to ambient temperature (18°C). The pressure of the system was then recorded. It was noted that there was always some liquid TME present.

This procedure was repeated several times, until a consistent pressure was obtained. The vapour pressure was measured as 89.5 mmHg at 18°C.

Thermal mass flow meters were used to measure the flow rate of TME. These flow meters need no calibration to operate at the reduced vapour pressure of TME. A scaling factor was necessary since these instruments rely on heat capacities and are calibrated to give readings corrected to s.t.p. for air. The scaling factor is given by:

$$SF = Cp(Air)/Cp(TME) = 0.228$$

The heat capacity of TME is 127.41 J/mol °C, and that for air is 29.05 J/mol °C [53].

Before carrying out the titration, an estimate was made of the reaction time under normal operating conditions. The titration kinetics are second order. At the end point the $O_2(a^1\Delta_g)$ and TME concentrations are identical, hence the half-life of the reaction is given by:

$$t_{1/2} = 1/k_{TME}[O_2(a^1\Delta_g)] \qquad (2.4)$$

The rate constant for the reaction is 7.7×10^5 mol^{-1} dm^3 s^{-1} [50,51,52] and the concentration of $O_2(a^1\Delta_g)$ was expected to be about

FIGURE 2.14 VAPOUR PRESSURE MEASUREMENT

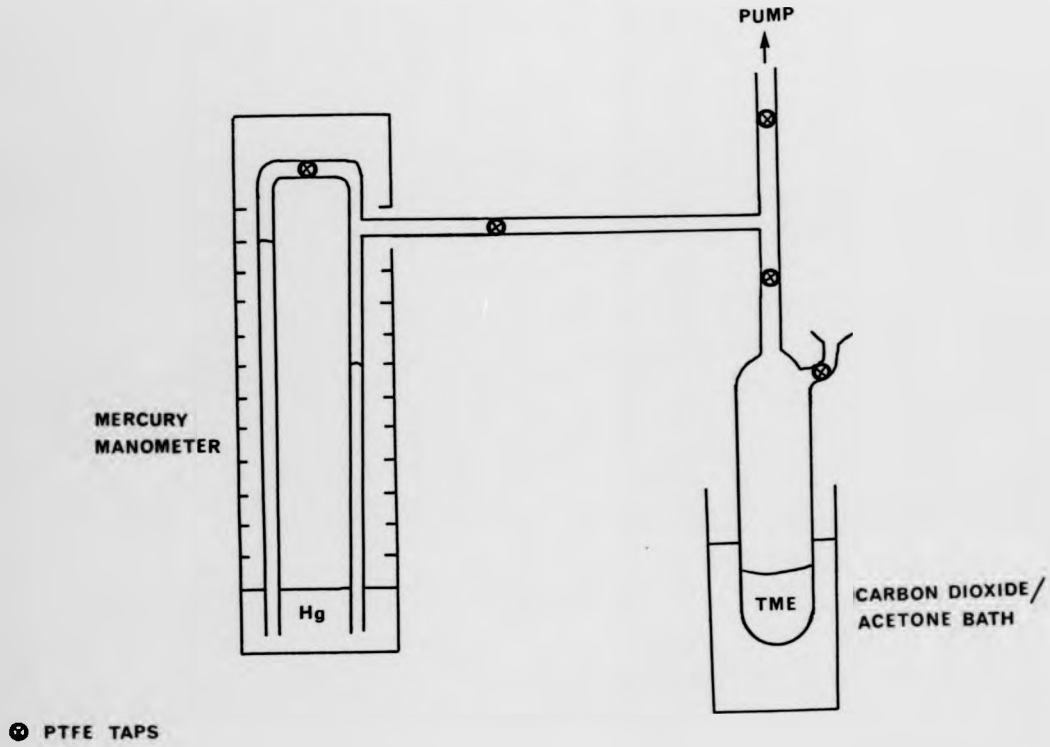

2×10^{-5} mol dm^{-3} (5% of the total O_2) under the normal operating conditions of 6 torr pressure and 100W discharge power. Thus a half-life of about 65 ms was expected. Therefore, at a linear flow velocity of 1.0 m s^{-1} , the reaction should reach completion (99%) within 0.5 m (0.5 s) of the mixing point. The titration is therefore sufficiently rapid to be monitored at the observation station which is 1.0 m downstream of the mixing point. There would be very little deactivation of $O_2(a^1\Delta_g)$ by $O_2(X^3\Sigma^-_g)$ under these conditions (half-life is approximately 3 s).

The end point of the titration was taken as the point where the 634nm emission is extinguished. Because the titration was carried out in a flowing gas it could be reversed, so there was little risk of over-shooting the end point.

The concentration of $O_2(a^1\Delta_g)$ was varied by altering the flow rate, pressure and discharge power. The flow rates of TME and O_2, pressure , temperature and photomultiplier output (prior to titration) were recorded for various $O_2(a^1\Delta_g)$ concentrations. The concentration of $O_2(a^1\Delta_g)$ may be calculated from the equation:

$$\text{Conc.} = 1000P \times (\text{Flow TME}) \,/\, 760RT \times (\text{Total Flow}) \quad \text{units: mol dm}^{-3} \qquad (2.5)$$

where the pressure, P, is in torr and the temperature, T, is in Kelvin. The units of the concentration are mol dm^{-3}.

Since the photomultiplier was set up to monitor the 'dimol' emission at 634nm, the relationship between photomultiplier output and the square of the $O_2(a^1\Delta_g)$ concentration should be linear. A plot of photomultiplier output versus $[O_2(a^1\Delta_g)]^2$ was made (Figure 2.15) and in fact found to be linear. This plot may be used to determine the $O_2(a^1\Delta_g)$ concentration from the photomultiplier output directly.

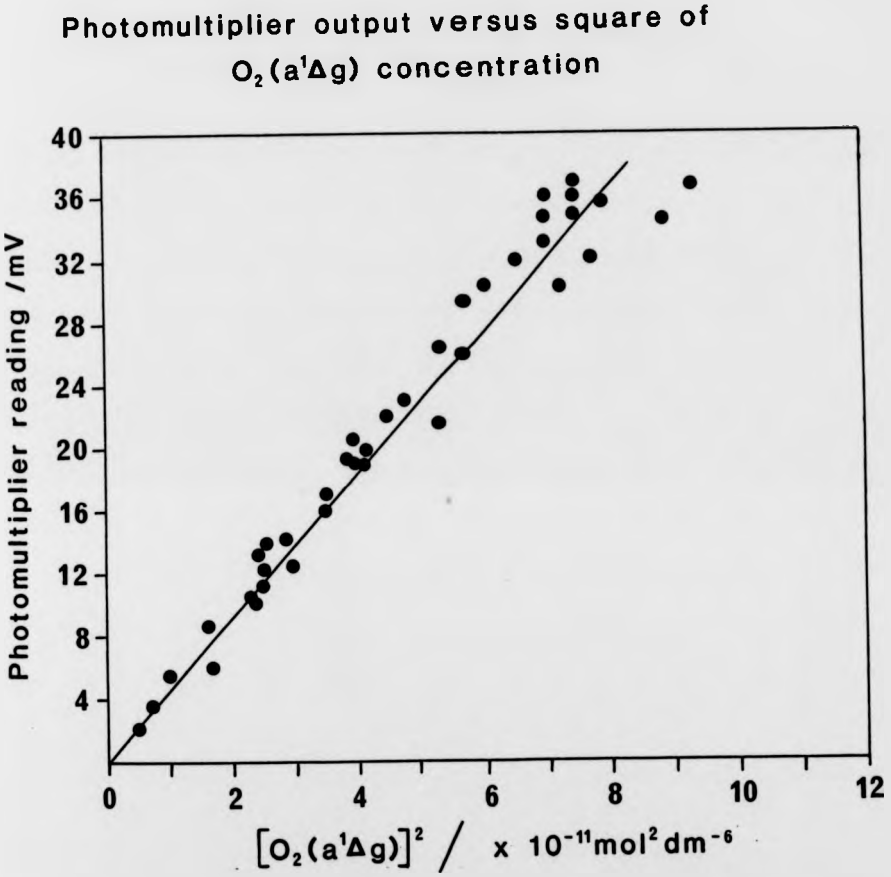

FIGURE 2.15 PHOTOMULTIPLIER CALIBRATION

The percentage error in the $O_2(a^1\Delta_g)$ concentration, determined in this manner, is 1.9% according to the least squares analysis.

A spin-off of this calibration was the investigation of the optimum flow rates, pressure and discharge power combinations for the production of $O_2(a^1\Delta_g)$ in this apparatus. It was found that the optimum conditions for a flow rate of 28 ml s^{-1} were, a pressure of 5-7 torr and a discharge power of 120W, which are very close to those already in use, and investigated by Pedley [46].

A back extrapolation, taking into account deactivation by $O_2(X^3\Sigma_g^-)$ and the wall, was made to calculate the percentage $O_2(a^1\Delta_g)$ in the oxygen flow immediately after the discharge cavity under optimum conditions. It was found to be 4%.

2.4 Routine Experimental Procedure

The following routine is carried out for a typical experiment, any deviations from this procedure being discussed in the appropriate chapter.

An aluminium diaphragm is positioned between the driver and flow tube sections. The liquid nitrogen traps protecting the main pump and in the purification system are filled. Both sections of the tube are evacuated, by continuous pumping, for 30 minutes.

The oxygen flow is switched on and adjusted to the required flow rate. The flow tube pressure is set to about 6 torr using the PTFE screw valve and measured accurately using a diethylphthalate manometer. The discharge is ignited using a Tesla coil and the compressed air cooling jet turned on. The output of the discharge is set to 100W and the reflected power checked. If necessary the cavity is tuned to reduce the reflected power to less than 2%. The photomultipliers' E.H.T. supply and the 10 volt light screen detector supply are switched on. The system is then left to stabilize for about 30 minutes, during which time the photomultiplier outputs are observed to ensure that they are stable before the next stage is begun.

The decay of the emission down the tube, at either wavelength , may be established manually using the travelling photomultiplier. The quenching gas is then added to the flow at a position about 0.2 m from the main flow tube. The flow of this gas is adjusted to the required rate and the pressure in the flow tube recorded again. Once the system has stabilized, the decay of the emission down the tube is measured again.

Having completed the room temperature measurements, the photomultipliers are placed opposite each other at the observation station. The lasers are switched on and the alignment of the light

screen detectors adjusted. The photomultiplier outputs (pre-shock glows) are recorded and their output destinations changed from the digital voltmeters to the transient recorders. The sweep speed, sensitivity and time delay of the recorders is set to cover the expected shock speed. The transient recorders and the time interval meters are primed and final checks are made on the flow rates and pressure are made before the manometer and flow sensors are isolated.

The vacuum pump connected to the driver section is isolated and the driver gas introduced at a steady rate. When the pressure of the driver section reaches the diaphragm bursting pressure a shock wave is propagated into the flowing gas. The driver gas inlet and the screw valve to the main pump are closed. The driver and the flow tube sections are then opened to the atmosphere and separated to replace the diaphragm. The system is immediately evacuated and the entire procedure repeated for the next run.

The times for the shock to pass between light screens 1 and 2 and also 1 and 3 are recorded as well as the dark current (base-line) reading of the photomultipliers. The data recorded by the transient recorders are transferred to the HP2647A computer and onto magnetic tape for storage and later analysis. These data are also displayed on an oscilloscope as an emission intensity vs time trace, which may be photographed for future reference.

The flow tube is cleaned at regular intervals using cotton wool, moistened with diethylether, followed by pumping for a full day. At such times the mercury reservoir is also changed to ensure a clean surface.

The flow tube and gas handling apparatus are checked daily for leaks by leaving them evacuated, but not pumping, overnight.

2.5 Safety Considerations

Potential hazards involved in operating the apparatus fall into five groups: chemical, low pressure, high pressure, electrical, and radiation.

(a) Chemical

The corrosive gases were handled in closed systems where possible and removed by liquid nitrogen traps before reaching the pumps. They were later disposed of by means of a water pump. The Teflon bag pressure regulator presented the greatest potential for leakage and was therefore located in a fumehood.

The possibility of explosion when hydrogen (or deuterium) and oxygen mixtures were shock heated in the presence of the microwave discharge was considered. There was little information available in the literature dealing with compositions in the range in which we were working. Experimentally, burning was observed, increasing as the mole fraction of hydrogen increased, and it was decided not to go above 4%. No trouble was experienced with mole fractions below this.

(b) Low Pressure

The risk of flying glass, should there be an implosion in the low pressure section, was reduced by wrapping the the glassware with tape. The manometers and capillary flow meters were provided with an overflow volume to prevent spillage should these units be subject to rapid pressurization. Care was taken to ensure that one section at a time experienced any pressure change so that an accident would not have a snowball effect.

(c) High Pressure

The presence of the diaphragm prevented the pressure in the

driver section from exceeding 6.5 atmospheres (660 KPa). Thus there was never any risk of structural damage to this section or the flow tube section. The bursting of the diaphragm was carried out at one end of the apparatus, where the operator was not adjacent to any glassware. The gas cylinder heads were checked for leaks to prevent accidental pressurization of the pre-regulator gas handling system , particularly when the teflon bag regulator was in use.

(d) Electrical

High voltage, low impedance, sources such as E.H.T. supplies were earthed for safety and also to reduce mains pick-up and stray interference.

(e) Radiation

Microwave leakage was minimized by surrounding the discharge cavity with a Faraday cage. The cavity was located away from the normal operating area to avoid continual contact on the part of the operator.

Viewing the laser beams (class 3A) directly was avoided. When close contact was necessary in setting up or adjusting the light screens only one beam was allowed to cross the room at any time. Crossing in front of the beams was unnecessary since there were on/off switches fitted to both sides of the apparatus.

SHOCK WAVE THEORY

3.1 Introduction

This chapter begins with a qualitative description of the formation of a shock wave and then goes on to discuss the nature of shock waves in gases and their associated phenomena. The basic relationships describing the conditions across the shock front are given and their derivation outlined. It is not intended to present a complete derivation in this thesis, as extensive treatments can be found in several texts [54,55,56]. The chapter concludes with the corrections necessary to allow for the occurrence of vibrational relaxation in the shocked gas and a comparison of particle and laboratory time under experimental conditions.

3.2 Formation of Shock Waves

A shock wave may be defined as a moving pressure disturbance in which the velocity and pressure amplitude are very much larger than that in an acoustic wave.

The concept of a shock wave is best understood by considering the accelerating piston model of Becker [54]. In this analogy, the driver gas is replaced by a piston accelerating to a constant velocity in the low pressure gas. The motion of the piston is divided into a large number of small successive movements. Each movement produces a pressure pulse which propagates into the test gas at the speed of sound and leaves the gas with a resultant motion in the same direction. The small increase in pressure will result in adiabatic heating of the gas. The second pulse, therefore, will travel at a velocity which is the result of the increased speed of sound in the heated gas and the velocity imparted to that gas by the previous pulse. Since each successive pulse will move with a velocity greater than the last, they will catch each other up. The pulses cannot actually pass one another and so they coalesce to form a single discontinuity moving at a velocity, relative to a stationary observer, above the speed of sound in the test gas.

In the shock tube, this discontinuity is known as the shock front. The depth of the shock front is of the order of a few mean free path lengths of the test gas. This supports the common theoretical approximation that the driver gas is accelerated, instantaneously, to a constant velocity and, as a consequence, so is the shock front.

3.3 Wave Structure in a Shock Tube

A simple shock tube assembly is shown in Figure 3.1(a). When the diaphragm is removed, by bursting or puncturing, a shock wave travels into the driven section and a rarefaction wave travels into the driver section. Behind the shock front is the leading edge of the expanding driver gas (contact surface), moving with a constant velocity away from the tail of the rarefaction wave. The distribution of pressure along the tube, before and after the diaphragm is removed, is shown in Figure 3.1(b) and (c).

When the shock wave reaches the end of the tube, it undergoes a reflection but maintains the characteristics of a shock wave. The rarefaction wave is also reflected, from the end of the driver section, and maintains the characteristics of a rarefaction wave but has an increased velocity, since it is then travelling through a moving gas in the same direction as the flow. These processes are summarized in Figure 3.2, which is a time versus distance plot of the progress of the waves in a shock tube.

The position of the shock front is represented by line OA and that of the contact surface by OB. At point B the reflected shock wave, AB, meets the contact surface where it undergoes a reflection once again and has the effect of slowing down the progress of the contact surface. The head of the rarefaction wave is represented by OC and its tail by OD. The rarefaction wave is also reflected, at a velocity described by CE and DF.

Observations must be made on the shock heated gas after the passage of the shock wave but before the arrival of either the contact surface or the reflected shock wave. The maximum observation time may be obtained from the height of the boundary of region 2 (OBA) above the lower limit (OA), at any point along the distance axis corresponding to the position of the observation station.

FIGURE 3.1 PROPAGATION OF WAVES IN A SHOCK TUBE

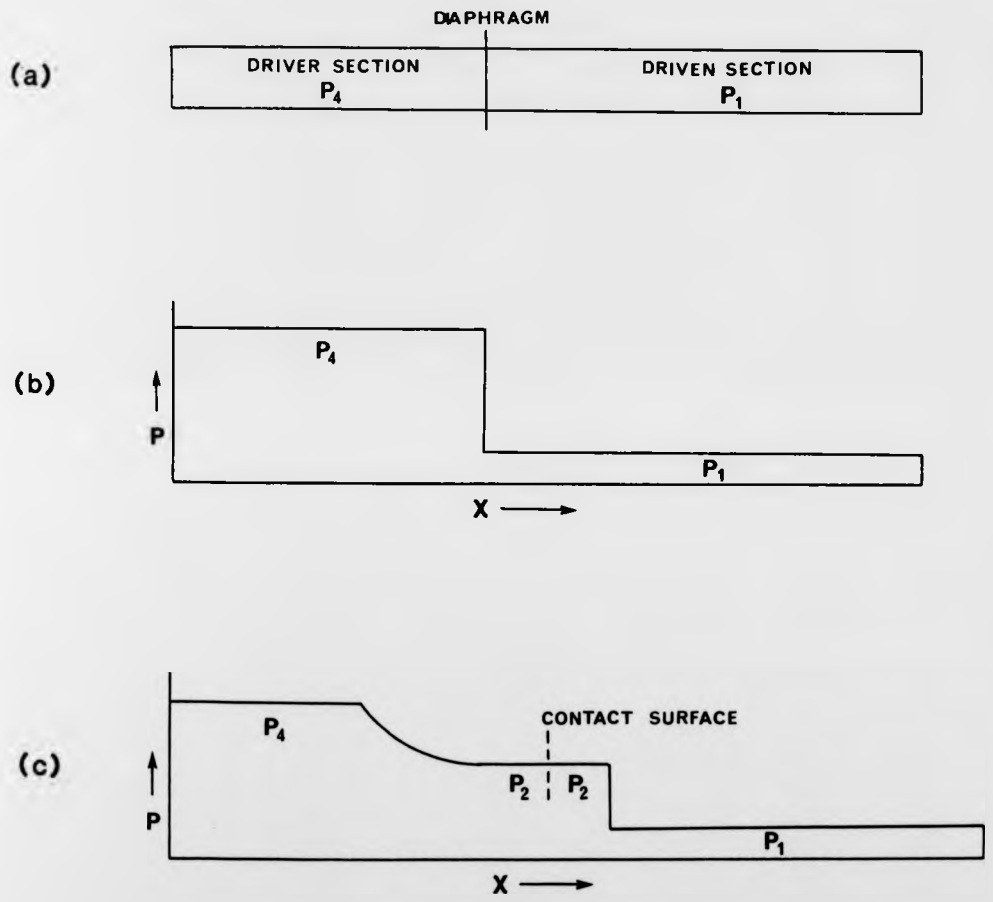

P denotes pressure and X denotes distance

FIGURE 3.2 TIME VERSUS DISTANCE PLOT OF EVENTS IN A SHOCK TUBE

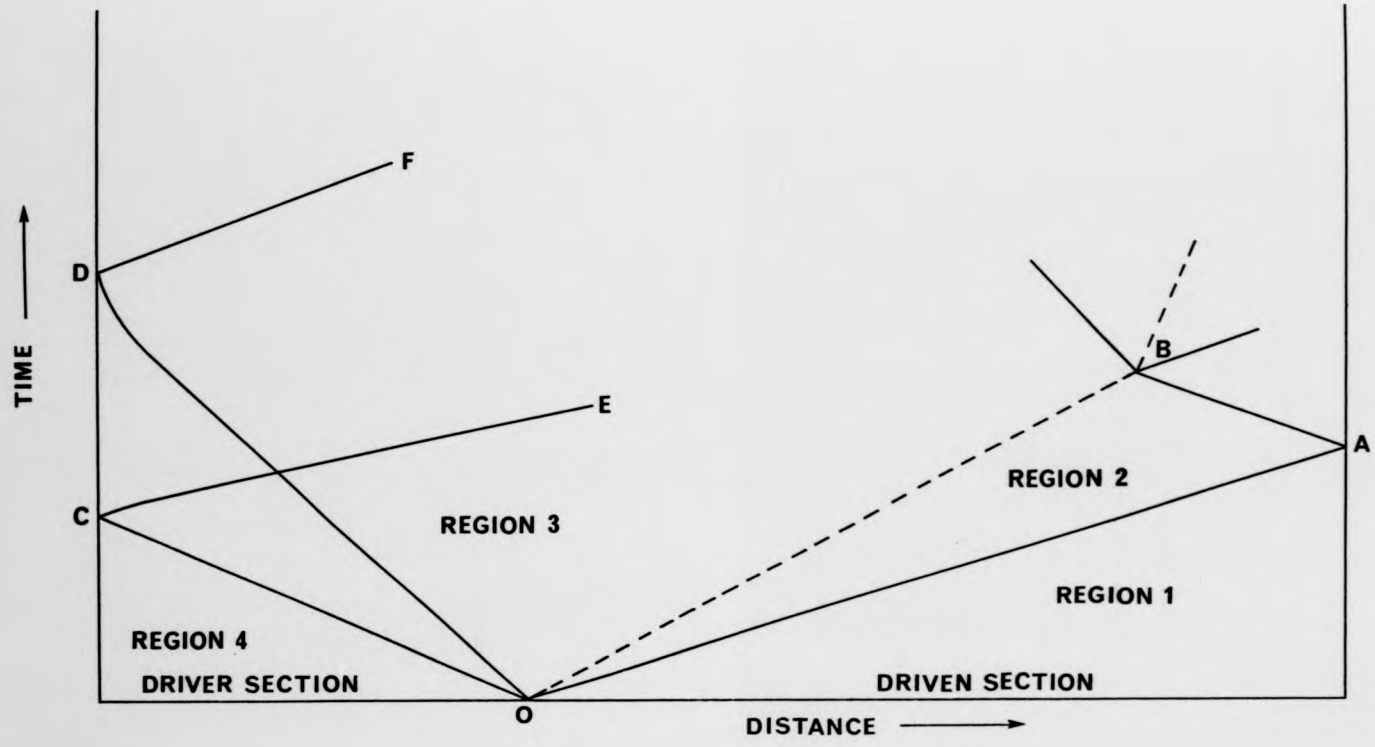

The length of the driver section may become a determining factor in the observation time because the reflected rarefaction wave travels at a velocity greater than that of the shock wave. It will, therefore, eventually catch up and destroy the shock wave. Extending the driver section increases the time period before the rarefaction wave is reflected and thus gives the shock wave a longer head start.

3.4 Shock Front Conditions

In order to derive the equations which define the conditions across the shock front, one must consider a control volume which encompasses the shock front (Figure 3.3). The upstream and downstream control planes, A and B, are set arbitrarily close to the shock front. The pressures, velocities and temperatures in the flowing gas change sufficiently slowly with distance, for heat conduction, viscous and all other internal irreversible processes to be neglected. These conditions are not isentropic, since there is an increase in entropy across the shock front associated with the randomization of the directed kinetic energy of the flow to thermal energy. However, the conservation laws of mass, momentum and energy still apply. Therefore the amount of these quantities entering the control volume at A is exactly balanced by the amount leaving at B. In the equations which follow, the quantities subscripted 1 refer to the pre-shock conditions and those subscripted 2 to post-shock conditions.

Assuming that the gas behind the shock front is in a state of thermodynamic equilibrium, the conditions on either side of this discontinuity are described by the equations of mass, momentum and energy conservation.

The conservation of mass states that the products of the flow velocity, μ, and density, ρ, of the gas entering and leaving the control volume are equal.

$$\rho_1 \mu_1 = \rho_2 \mu_2 \qquad \text{units: } kg\ m^{-2}\ s^{-1} \tag{3.1}$$

The sum of the pressure, P, and the flow momentum, $\rho\mu^2$, entering and leaving the control volume must also be equal, as

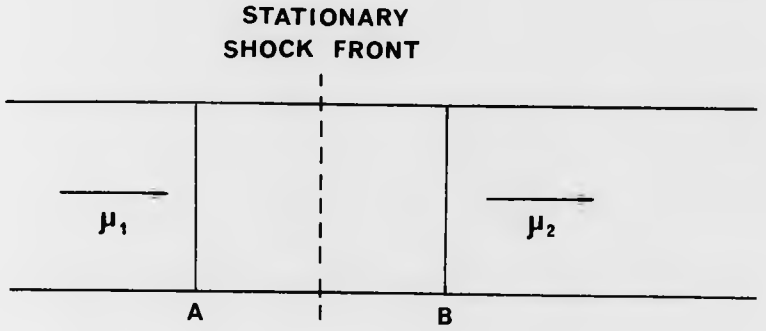

FIGURE 3.3 CONTROL VOLUME FOR DERIVATION OF SHOCK EQUATIONS

dictated by the law of conservation of momentum.

$$P_1 + \rho_1 u_1^2 = P_2 + \rho_2 u_2^2 \qquad \text{units: } N\ m^{-2} = kg\ m^{-1}\ s^{-2} \tag{3.2}$$

The energy of the system has a flow, $mu^2/2$, and a thermal component, mh, thus the conservation of energy law states that:

$$m_1 h_1 + m_1 u_1^2/2 = m_2 h_2 + m_2 u_2^2/2 \qquad \text{units: } J \tag{3.3}$$

where h is the specific enthalpy and m is the mass. Since mass is conserved, Equation (3.3) may be simplified to:

$$h_1 + u_1^2/2 = h_2 + u_2^2/2 \qquad \text{units: } J\ kg^{-1} \tag{3.4}$$

The solution of these equations will allow the conditions in the post-shock regime to be determined from those in the pre-shock regime. There are, however, three equations and four unknowns so a solution can only be found if another relationship between two or more of these quantities can be obtained. The specific enthalpy of an ideal gas is given by:

$$h = 10^3 Cp.T/M' = 10^3 RT[\gamma/\gamma-1]/M' \qquad \text{units: } J\ kg^{-1} \tag{3.5}$$

where $\gamma = Cp/Cv$, the ratio of the heat capacities at constant pressure and constant volume. The ideal gas equation may be written as:

$$P = 10^3 \rho RT/M' \qquad \text{units: N m}^{-2} \tag{3.6}$$

where M' is the average molar mass.

Manipulating Equations (3.1) to (3.6), in such a way that all variables but pressure and density are eliminated, results in an expression for the post-shock to pre-shock pressure ratio of:

$$P_2/P_1 = (\rho_2 - \mu^2\rho_1)/(\rho_1 - \mu^2\rho_2) \tag{3.7}$$

where $\mu^2=(\gamma-1)/(\gamma+1)$. The ratios ρ_2/ρ_1 and T_2/T_1 may be derived in a similar manner.

$$\rho_2/\rho_1 = [(P_2/\mu^2P_1)+1]/[(1/\mu^2)+(P_2/P_1)] \tag{3.8}$$

$$T_2/T_1 = (P_2/P_1)[(P_1+\mu^2P_2)/(P_2+\mu^2P_1)] \tag{3.9}$$

It is common practice to express these relationships in terms of the Mach Number of the shock, M_s.

$$M_s = V_s/a \tag{3.10}$$

where V_s is the shock wave velocity and a is the velocity of sound in the test gas, which is related to the heat capacity by:

$$a = (10^3 \gamma RT/M')^{1/2} \qquad \text{units: m s}^{-1}$$

(3.11)

Substituting M_s into the relationships for pressure, density and temperature ratios results in the final forms of these equations.

$$P_{21} = P_2/P_1 = [2\gamma M_s^2 - (\gamma-1)]/(\gamma+1)$$

(3.12)

$$\varrho_{21} = \rho_2/\rho_1 = M_s^2(\gamma-1)/[(\gamma-1)M_s^2+2]$$

(3.13)

$$T_{21} = T_2/T_1 = [2\gamma M_s^2 - [(\gamma-1)/(\gamma+1)]] \times [(\gamma-1)M_s^2+2]/[(\gamma+1)M_s^2]$$

(3.14)

Therefore, by measuring the pre-shock pressure in the flow tube, the laboratory temperature and determining experimentally the shock wave velocity, the conditions P_2, ρ_2 and T_2 behind the shock front may be calculated.

3.5 Experimental Control of High Temperatures

Control of the high temperature developed behind the shock front is achieved by controlling the velocity of the shock wave.

The velocity of the shock wave is controlled in the first instance by the pressure of the driver gas, P_4, and that of the driven gas, P_1. The heat capacity ratios of the driver gas, γ_4, and of the driven gas, γ_1, are also important, as is the ratio of the speed of sound in the two gases, a_1/a_4. A theoretical equation [56] describes the complex relationship between these factors, under perfect bursting conditions, where the diaphragm is removed cleanly and instantaneously.

$$P_4/P_1 = [2\gamma_1 M_s^2-(\gamma_1-1)]/(\gamma_1+1) \times [1-((M_s-(1/M_s))(\gamma_4-1)a_1/(\gamma_1+1)a_4)]^{-2\gamma_4/(\gamma_4-1)} \quad (3.15)$$

Knowing the constants γ_4, γ_1, a_4, and a_1 for the different gases used, a plot of log P_4/P_1 versus Mach Number may be produced. This has been done for helium, nitrogen and argon driver gases against an oxygen test gas. The results are shown on Figure 3.4, and may be used as a guide to the conditions required for particular shock strengths.

There are only two choices of diaphragm thickness (0.051 and 0.102 mm) which burst at pressure differences of approximately 2.5 and 6.5 atmospheres. The corresponding values of log P_4/P_1 for a flow tube pressure of 6 torr are also shown (Figure 3.4). If only pure gases are used, there are only three shock wave velocities attainable for each diaphragm. However, by mixing two gases, Mach Numbers which correspond to a gas with intermediate values of γ and a can be obtained. The relationship between Mach Number and gas composition is

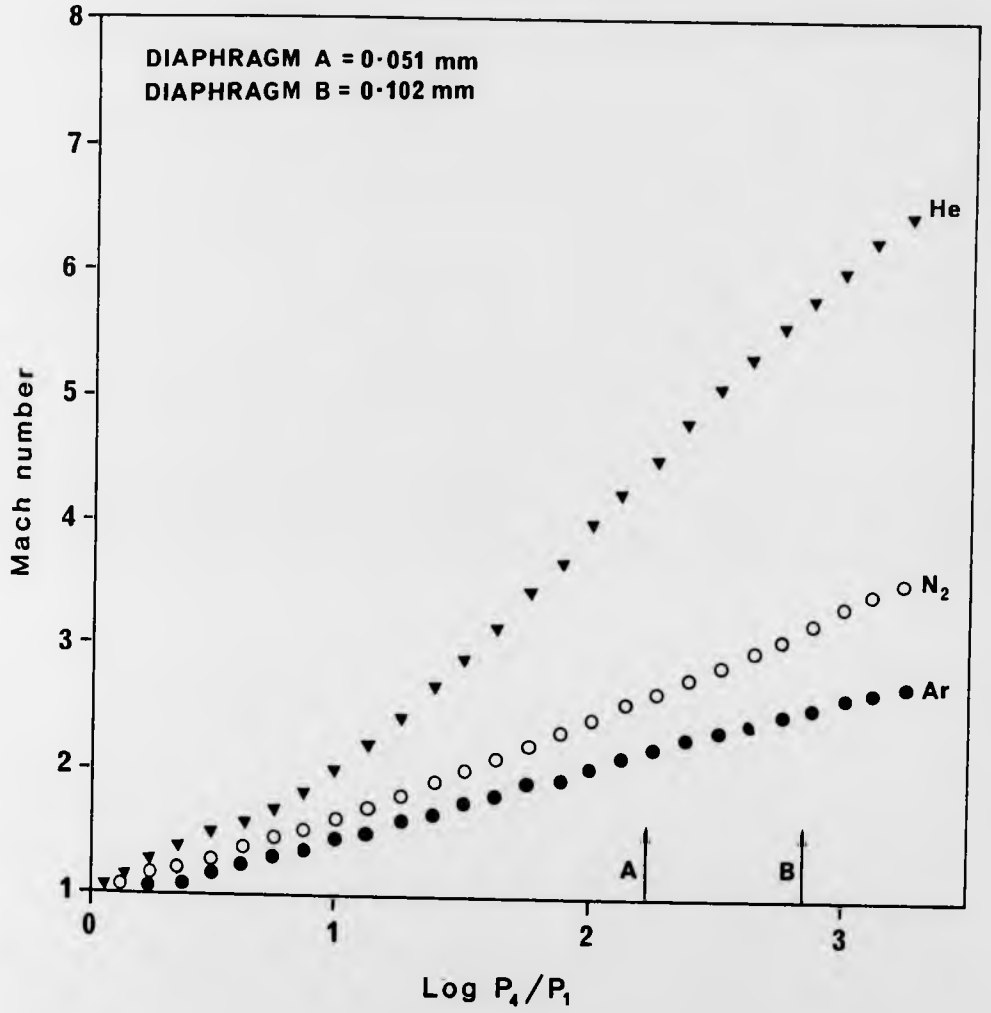

FIGURE 3.4 MACH NUMBER VERSUS LOG P_4/P_1 FOR VARIOUS DRIVER GASES

not linear. Consequently, there is a certain amount of trial and error involved in obtaining the required Mach Number. With a little experience, however, shock waves with velocities within Mach 0.1 of the required value can be obtained on a regular basis.

The high temperature, T_2, in the post-shock regime may be determined from the Mach Number of the shock wave (Equation 3.14). A plot has been made of T_2 versus Mach Number for an oxygen test gas shock heated from 295K (Figure 3.5). The full line represents the temperature of oxygen under frozen conditions (ideal gas) and the broken line the temperature when vibrational relaxation takes place rapidly after shock heating.

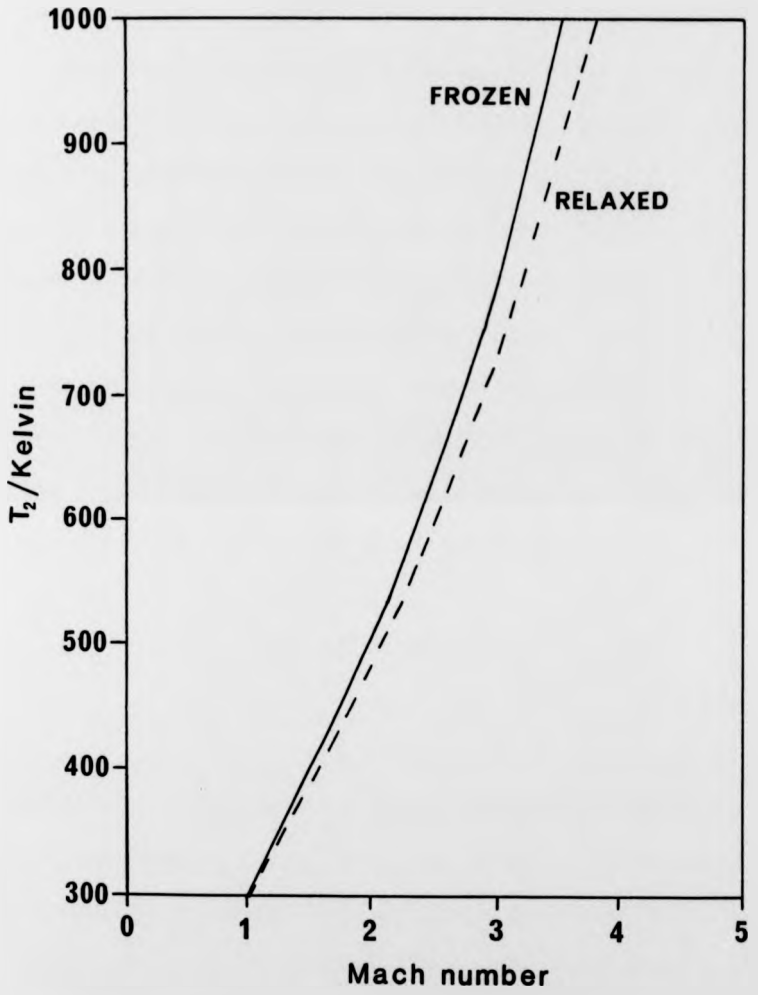

FIGURE 3.5 HIGH TEMPERATURE OF SHOCK HEATED OXYGEN GAS

3.6 Corrections for Vibrational Relaxation

The shock parameters, P_{21}, ρ_{21} and T_{21}, determined from Equations (3.12), (3.13) and (3.14) are valid only for gases with heat capacities independent of temperature. This is adequate to describe monatomic gases and polyatomic gases where there is no energy transfer between translational and vibrational or rotational modes. However, modifications are required to account for the reduction in translational energy, and therefore temperature, when vibrational relaxation takes place rapidly after shock heating.

If the temperature of a shocked gas is in a region where some of the translational energy may be transferred rapidly into vibrational energy, the heat capacity will no longer be independent of temperature. As a result, the molar enthalpy has a temperature dependence described by the polynomial expression:

$$H = A + BT + CT^2 + DT^3 + \ldots\ldots\ldots \qquad (3.16)$$

The coefficients in this equation are evaluated by polynomial curve fitting of the equation to values of the enthalpy of the gas at various temperatures, obtained from J.A.N.A.F. tables [58].

When vibrational relaxation occurs, the shock equations cannot be solved explicitly and an iterative procedure is carried out to determine the conditions behind the shock front. Starting values for the iteration are obtained from Equations (3.12), (3.13) and (3.14), assuming the gas to be frozen, and then used along with Equation (3.16) in the iterative process to obtain a new estimate for the enthalpy. This second estimate is used to make a second estimate of the values for pressure, density and temperature in the shock heated gas. The first iteration is now complete. The process is repeated,

using the second set of estimates to produce a third set of estimates and then a fourth set and so on. The iteration is completed when consistent values for these parameters are obtained.

The shock parameters for both frozen and relaxed test gases and test gas mixtures are determined by computer. The program was adapted from Millikan [59]. A table of these shock parameters over the expected range of shock wave velocities (Mach numbers) was compiled for each test gas or mixture of test gases, so that they were available for quick reference when analysing the kinetic data.

3.7 Comparison of Particle and Laboratory Time Scales

The shock heated gas is monitored using a photomultiplier unit mounted at a fixed position on the tube wall. Measurements made by the detector are carried out on a laboratory time scale, which is not identical to the particle time scale.

The difference may be understood by considering Figure 3.6 (a) and (b). When the shock front moving at a velocity V_s passes a particle at a distance d from the observation station, the particle is shock heated and will move in the same direction as the shock but at a lower velocity V_p. The shock front will pass in front of the detector after time d/V_s and the particle after time d/V_p has elapsed since shock heating. The difference in arrival time at the observation station is $d/V_p - d/V_s$, which is the time elapsed on the laboratory time scale. Therefore the particle time, t_p, is related to laboratory time, t_l, by:

$$t_p/t_l = (d/V_p)/[(d/V_p)-(d/V_s)] = V_s/(V_s-V_p) \qquad (3.17)$$

For 'shock fixed' coordinates as used in Section 3.4 (Figure 3.3) where the gas is treated as moving through a stationary shock front

$$\mu_1 = V_s \qquad (3.18)$$

and

$$\mu_2 = V_s - V_p \qquad (3.19)$$

Recalling that mass is conserved,

(Equation 3.1)

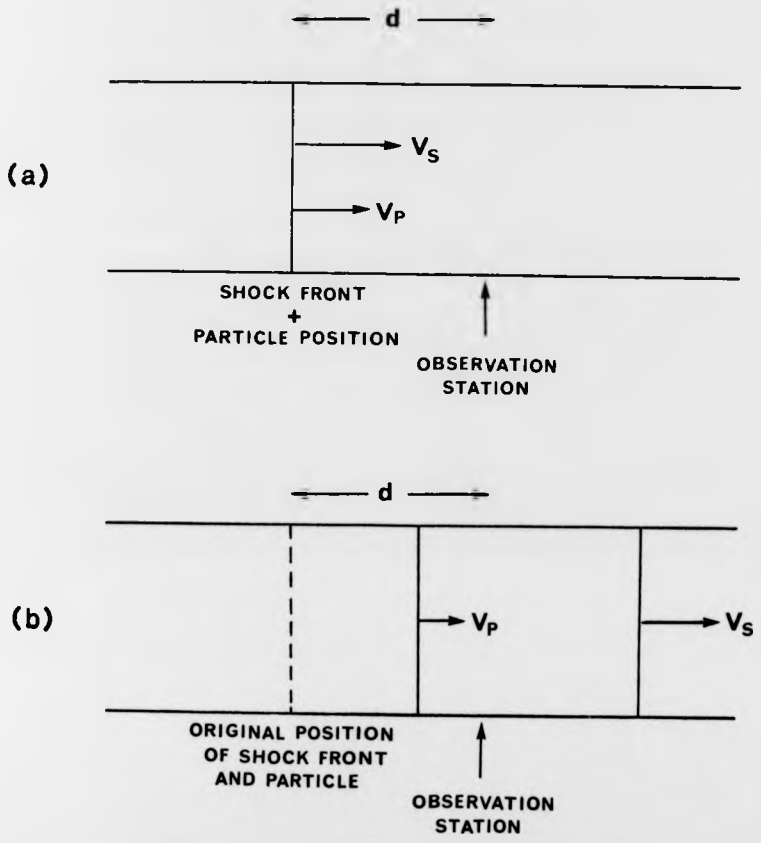

FIGURE 3.6 PARTICLE AND LABORATORY TIME SCALES

$$\mu_1/\mu_2 = \rho_2/\rho_1 = \rho_{21} \tag{3.20}$$

it follows that

$$t_p/t_1 = \rho_{21} \tag{3.21}$$

If the rate of a particular gaseous process behind the shock front is to be measured, it will be necessary to convert the data collected in laboratory time to particle time. This is done simply by multiplying the time coordinate by the density ratio.

The disadvantage of this 'time compression' effect is that the resolution time is reduced by the factor t_1/t_p, which increases the need for a rapid response detection system.

3.8 The Non-Ideality of a Real Shock Tube

The equations given in previous sections allow the conditions in an ideal shock tube to be determined. However, conditions in a real shock tube will deviate from the ideal conditions.

Non-uniform flow, caused by the formation of a boundary layer behind the shock front, may result in densities and temperatures in the shock heated gas which deviate from those calculated. The build up of the boundary layer in the apparatus used in this work was studied by Pedley [46]. His conclusion was that the effect is quite small and may be neglected. The effect of a boundary layer has, therefore, been ignored in this study.

The effect of drag at the walls will cause the shock front to decelerate. In long tubes with a small diameter this effect may be quite significant. However, the deceleration due to drag is quite small for tubes, such as the one used in this work which has a deceleration rate of less than 1% per metre, with diameters in excess of 5 cm [57].

Finally, the diaphragm tends to destroy the one-dimensional nature of the shock wave. Prior to bursting the diaphragm tends to bow, therefore, as it bursts the gas flow has a component towards the wall of the tube, rather than being directed purely along the axis. This effect results in a wave with some transverse character, which will lead to effectively higher shock velocities than those measured. The effect is minimized [55] and a good approximation to a one-dimensional shock wave achieved when the expansion chamber is at least 20 times the diameter of the tube. In the apparatus used in this work the length is 100 times the diameter of the tube.

KINETIC MODELS AND DATA ANALYSIS

4.1 Introduction

This chapter contains the derivation of the kinetic models for the deactivation of $O_2(a^1\Delta_g)$ and $O_2(b^1\Sigma^+_g)$ under pre-shock (room temperature) and post-shock (high temperature) conditions. Sensitivity analysis is considered in general and then applied to these models. The sensitivity of the models with respect to the variable parameters within the models is described and the implications discussed. Finally the application of the computer programs, developed from these models, to analyse the experimental data is outlined.

4.2 Room Temperature Deactivation of $O_2(a^1\Delta_g)$

$O_2(a^1\Delta_g)$ is generated by the microwave discharge in a pure oxygen matrix and removed by the following processes:

$$2O_2(a^1\Delta_g) \xrightarrow{k_1} 2O_2(X^3\Sigma^-_g) + h\nu \ (\lambda=634nm) \qquad (4.1)$$

$$2O_2(a^1\Delta_g) \xrightarrow{k_p} O_2(b^1\Sigma^+_g) + O_2(X^3\Sigma^-_g) \qquad (4.2)$$

$$O_2(a^1\Delta_g) + O_2(X^3\Sigma^-_g) \xrightarrow{k_d^o} 2O_2(X^3\Sigma^-_g) \qquad (4.3)$$

$$O_2(a^1\Delta_g) + \text{wall} \xrightarrow{k_w^\Delta} O_2(X^3\Sigma^-_g) \qquad (4.4)$$

$$O_2(a^1\Delta_g) \xrightarrow{k_5} O_2(X^3\Sigma^-_g) + h\nu \ (\lambda=1270nm) \qquad (4.5)$$

$$O_2(a^1\Delta_g) + M \xrightarrow{k_d^m} O_2(X^3\Sigma^-_g) + M \qquad (4.6)$$

The rate equation for the change in concentration of $O_2(a^1\Delta_g)$ is given by:

$$-d[O_2(a^1\Delta_g)]/dt = k_1[O_2(a^1\Delta_g)]^2 + k_p[O_2(a^1\Delta_g)]^2 + k_5[O_2(a^1\Delta_g)] + k_w^{\Delta}[O_2(a^1\Delta_g)] + k_d^{o}[O_2(a^1\Delta_g)][O_2(X^3\Sigma^-_g)] + k_d^{m}[M][O_2(a^1\Delta_g)] \quad (4.7)$$

Reaction (4.5) is a forbidden radiative process and, as a result, is very slow in comparison to the other loss processes. The simultaneous transition described by equation (4.1) is not forbidden but relies on the square of the $O_2(a^1\Delta_g)$ concentration and thus becomes less significant when the concentration of $O_2(a^1\Delta_g)$ is low. According to Borrell, Borrell and Pedley [19], reaction (4.2) is only significant for high concentrations of $O_2(a^1\Delta_g)$. In the apparatus used, the concentration of $O_2(a^1\Delta_g)$ is low (less than 1×10^{-6} mol dm^{-3}) and, therefore, reaction (4.2) is an insignificant removal process compared with the main loss processes (equations 4.3, 4.4, and 4.6).

Neglecting the slow reactions (equations 4.1, 4.2, and 4.5), the rate equation becomes:

$$-d[O_2(a^1\Delta_g)]/dt = k_d^{o}[O_2(X^3\Sigma^-_g)][O_2(a^1\Delta_g)] + k_d^{m}[M][O_2(a^1\Delta_g)] + k_w^{\Delta}[O_2(a^1\Delta_g)] \quad (4.8)$$

which may be simplified to:

$$-d[O_2(a^1\Delta_g)]/dt = (k_d^{o}[O_2(X^3\Sigma^-_g)] + k_d^{m}[M] + k_w^{\Delta})[O_2(a^1\Delta_g)] = k'[O_2(a^1\Delta_g)] \quad (4.9)$$

where k' is the overall pseudo-first order rate constant for the removal or deactivation of $O_2(a^1\Delta_g)$ in the system. Integrating equation (4.9), between t=0 and t=t, one obtains the expression:

$$\ln ([O_2(a^1\Delta_g)]/[O_2(a^1\Delta_g)]_o) = -k't \qquad (4.10)$$

From equation (4.1), $^{634}I \propto [O_2(a^1\Delta_g)]^2$, therefore

$$1/2\ln(^{634}I/^{634}I_o) = \ln([O_2(a^1\Delta_g)]/[O_2(a^1\Delta_g)]_o) \qquad (4.11)$$

A plot of $1/2\ln(^{634}I/^{634}I_o)$ versus time will yield the pseudo-first order rate constant, k', as its gradient. The validity of this procedure has been verified by Borrell [60] who compared the emissions at 634nm and 1270nm over a range of pressures in the same discharge flow apparatus.

It is also possible to obtain k' by monitoring the $O_2(b^1\Sigma^+_g)$ emission at 762nm. $O_2(b^1\Sigma^+_g)$ is produced through the 'energy pooling' reaction (equation 4.2) and is removed by the following processes:

$$O_2(b^1\Sigma^+_g) \xrightarrow{k_{12}} O_2(X^3\Sigma^-_g) + h\nu(\lambda=762nm) \qquad (4.12)$$

$$O_2(b^1\Sigma^+_g) + \text{wall} \xrightarrow{k_w^{\Sigma}} O_2(X^3\Sigma^-_g) \qquad (4.13)$$

$$O_2(b^1\Sigma^+_g) + O_2(X^3\Sigma^-_g) \xrightarrow{k_q^{o}} O_2(a^1\Delta_g) + O_2(X^3\Sigma^-_g) \qquad (4.14)$$

$$O_2(b^1\Sigma^+_g) + M \xrightarrow{k_q^m} O_2(a^1\Delta_g) + M \qquad (4.15)$$

The rate equation for the change in $[O_2(b^1\Sigma^+_g)]$ with time may be written as:

$$d[O_2(b^1\Sigma^+_g)]/dt = k_p[O_2(a^1\Delta_g)]^2 - k_q^o[O_2(X^3\Sigma^-_g)][O_2(b^1\Sigma^+_g)] - k_w^{\Sigma}[O_2(b^1\Sigma^+_g)] - k_{12}[O_2(b^1\Sigma^+_g)] - k_q^m[M][O_2(b^1\Sigma^+_g)] \qquad (4.16)$$

The concentration of $O_2(b^1\Sigma^+_g)$ is at steady state at any point in the flow [44], therefore $d[O_2(b^1\Sigma^+_g)]/dt = 0$, and equation (4.16) may be rearranged to give:

$$[O_2(b^1\Sigma^+_g)] = k_p[O_2(a^1\Delta_g)]^2/(k_q^o[O_2(X^3\Sigma^-_g)] + k_q^m[M] + k_{12} + k_w^{\Sigma}) \qquad (4.17)$$

From equation (4.12), it is clear that $^{762}I \alpha [O_2(b^1\Sigma^+_g)]$, and from equation (4.17) it may be deduced that $[O_2(b^1\Sigma^+_g)] \alpha [O_2(a^1\Delta_g)]^2$, therefore $^{762}I^{1/2} \alpha [O_2(a^1\Delta_g)]$. A plot of $1/2\ln(^{762}I/^{762}I_o)$ versus time will also have a gradient which is equal to k'.

If a value of k' is obtained for the deactivation of $O_2(a^1\Delta_g)$ both in the presence and the absence of a test gas, M, then a value for k_d^m may be obtained by difference, provided that the concentration of $O_2(X^3\Sigma^-_g)$ and the wall deactivation remain constant. From equations (4.8 and 4.9)

$$k' = k_d^{o}[O_2(X^3\bar{\Sigma}_g)] + k_d^{m}[M] + k_w^{\Delta} \qquad (4.18)$$

in the presence of a quencher, and

$$k' = k_d^{o}[O_2(X^3\bar{\Sigma}_g)] + k_w^{\Delta} \qquad (4.19)$$

when only oxygen is present.

The difference in k' is determined for several concentrations of M by varying both the percentage of M added and the total pressure of the test gas mixture. A plot of the difference in k' versus the concentration of M is constructed and the value of k_d^{m} extracted as the gradient.

It is possible that a given additive may be adsorbed onto the tube wall, thereby changing the rate constant for the wall deactivation. If this occurs, there are three possible effects.

(a) The change in the wall deactivation rate constant is independent of the concentration of M, producing a difference plot which does not pass through the origin. In this case, the value of k_d^{m} will remain the true value and the procedure will remain valid.

(b) The change in the wall deactivation rate constant is dependent upon the concentration of M but has a different functionality from the linear one of the deactivation rate due to M, upon the concentration of M. In this case, the difference plot will be curved and, therefore, the value of k_d^{m} will be incorrect. However, the curvature of the plot will alert the experimenter to this situation.

(c) The dependence of both the rate of deactivation at the wall and by M, upon the concentration of M may both be linear. In this case, errors will not become apparent under normal conditions. It is possible to check for the presence of such an effect with particular additives, by coating the tube walls with another material to deliberately change the wall characteristics. The experiment is repeated and a comparison made between the two values of k_d^m. A difference between the two values would indicate a concentration-dependent change in the wall constant for one of these surfaces. However, it would not be possible say whether one wall deactivation rate constant is reduced or the other increased by the presence of the test gas, M.

In practice the decay of the 634nm and 762nm emissions in the flow tube are not measured as a function of time but as a function of distance. The decay rate with time given in equation (4.9) is related to that with distance by:

$$d[O_2(a^1\Delta_g)]/dt = d[O_2(a^1\Delta_g)]/dl \times dl/dt \qquad (4.20)$$

where dl/dt is the linear flow velocity, which remains constant during an individual experiment. The experimental rate constant k' is described, initially, as a function of distance and then converted to time by dividing by the linear flow velocity.

$$LFV = 760(VFR)/P_1 \pi r^2 \qquad (4.21)$$

where VFR is the total volume flow rate, r is the radius of the flow tube and P_1 is the pressure in the flow tube. Therefore, the manipulation of the kinetic equations can be carried out entirely as a function of time.

4.3 High Temperature Deactivation of $O_2(a^1\Delta_g)$

Analogously with equation (4.9) the rate of change of $O_2(a^1\Delta_g)$ concentration at high temperatures expressed in particle time (see section 3.7) is:

$$d[O_2(a^1\Delta_g)]/dt_p = -(k_d^m[M] + k^o_d[O_2(X^3\Sigma^-_g)] + k_w^{\Delta})[O_2(a^1\Delta_g)] \quad (4.22)$$

At the high temperatures generated by the shock wave the deactivation at the wall is very much slower than the collisional deactivation, since the wall remains at room temperature. Borrell [60] has shown that the deactivation rate due to pure oxygen is below the detection limit in our system at high temperatures. Equation (4.22) may therefore be simplified to:

$$d[O_2(a^1\Delta_g)]/dt_p = -k_d^m[M][O_2(a^1\Delta_g)] \quad (4.23)$$

Integrating equation (4.23) between the limits $t_p = t_o$ and $t_p = t_p$, one arrives at the expression:

$$[O_2(a^1\Delta_g)]_{t_p}/[O_2(a^1\Delta_g)]_o = \exp(-k_d^m[M]t_p) \quad (4.24)$$

since the decay of $O_2(a^1\Delta_g)$ due to M at high temperatures is zero at time $t_p = 0$. $[O_2(a^1\Delta_g)]_{t_p}$ is the concentration of $O_2(a^1\Delta_g)$ at time t_p after the arrival of the shock front, at any point in the tube, and $[O_2(a^1\Delta_g)]_o$ decays along the tube due to the concentration gradient in the pre-shock flow and is related to the immediate post-shock concentration by:

$$[O_2(a^1\Delta_g)]_o = [O_2(a^1\Delta_g)]_o^{obs} \exp(-\alpha_t t_p/2) \quad (4.25)$$

where $\alpha_t/2$ is the room temperature decay of $O_2(a^1\Delta_g)$ expressed in particle time. Combining equations (4.24 and 4.25),

$$[O_2(a^1\Delta_g)]_{t_p}/[O_2(a^1\Delta_g)]_o^{obs} = \exp(-t_p((\alpha_t/2) + k_d^m[M])) \quad (4.26)$$

Replacing the concentration ratio with the emission intensity ratio and noting that $^{634}I \propto [O_2(a^1\Delta_g)]^2$,

$$^{634}I_{t_p}/^{634}I_o^{obs} = \exp(-t_p(\alpha_t + 2k_d^m[M])) \quad (4.27)$$

If the 'dimol' emission at 634nm is a simple collisional process then the immediate post-shock emission intensity, $^{634}I_o^{obs}$ can be related to the pre-shock glow, $^{634}I_{psg}$ at room temperature by:

$$^{634}I_o^{obs}/^{634}I_{psg} = (\rho_{21})^2(T_{21})^{1/2}.^{634}K \quad (4.28)$$

where ^{634}K is a constant for any enhancement above that predicted by the simple collisional process, for which $^{634}K = 1$. Substitution of the expression for $^{634}I_o^{obs}$ from equation (4.28) into equation (4.27) results in the following equation for the high temperature deactivation of $O_2(a^1\Delta_g)$, monitored through the 634nm emission.

$$^{634}I_{t_p} / {}^{634}I_{psg} = (\rho_{21})^2 (T_{21})^{1/2} \cdot {}^{634}K \exp(-t_p(2k_d^m[M]+\alpha_t))$$

(4.29)

Therefore, the rate constant for the increased deactivation of $O_2(a^1\Delta_g)$ at the high temperature can be determined by plotting the measured intensity against particle time and establishing the increase in gradient over that of the pre-shock decay. The pre-shock decay $\alpha_1/2$, measured as a function of distance,

$$-d[O_2(a^1\Delta_g)]/dl = k'[O_2(a^1\Delta_g)]$$

(4.30)

must be converted to particle time.

$$-d[O_2(a^1\Delta_g)]/dt_p = -d[O_2(a^1\Delta_g)]/dl \times dl/dt_p$$

(4.31)

By definition, $dl/dt_p = V_p$, the velocity of the shocked gas in particle time, so:

$$\alpha_t/2 = \alpha_1/2 \times V_p$$

(4.32)

From equations (3.17 and 3.21),

$$V_p = V_s[1-(1/\rho_{21})]$$

(4.33)

hence,

$$\alpha_t/2 = V_s \alpha_1 [1-(1/\rho_{21})]/2 \qquad (4.34)$$

Equation (4.29) predicts an instantaneous rise in emission intensity at the shock front followed by a decay. This ideal pattern for the observed emission is shown on figure 4.1(a). The actual emission-time trace is represented in figure 4.1(b). Four distinct regions may be distinguished in the observed trace:

(A) The pre-shock glow, $^{634}I_{psg}$, before the arrival of the shock front.

(B) A rapid, but not instantaneous, increase in emission, due to the increase in density and temperature upon the arrival of the shock front.

(C) A fall off in emission intensity, as a result of the $O_2(a^1\Delta_g)$ concentration gradient at room temperature.

(D) The total loss of emission, due to the arrival of the contact surface.

Regions A and C are exactly as predicted by the kinetic model. The risetime, which characterizes region B is due to the finite slit width of the photomultiplier unit. In order to allow for this, equation (4.29) is integrated over the risetime, t_s.

$$^{634}I_{t_p} = {}^{634}K\,{}^{634}I_{psg}(\rho_{21})^2(T_{21})^{1/2} \int_{t_p-t_s}^{t_p} \exp(-t_p(2k_d{}^m[M]+\alpha_t))\, dt_p/t_s \qquad (4.35)$$

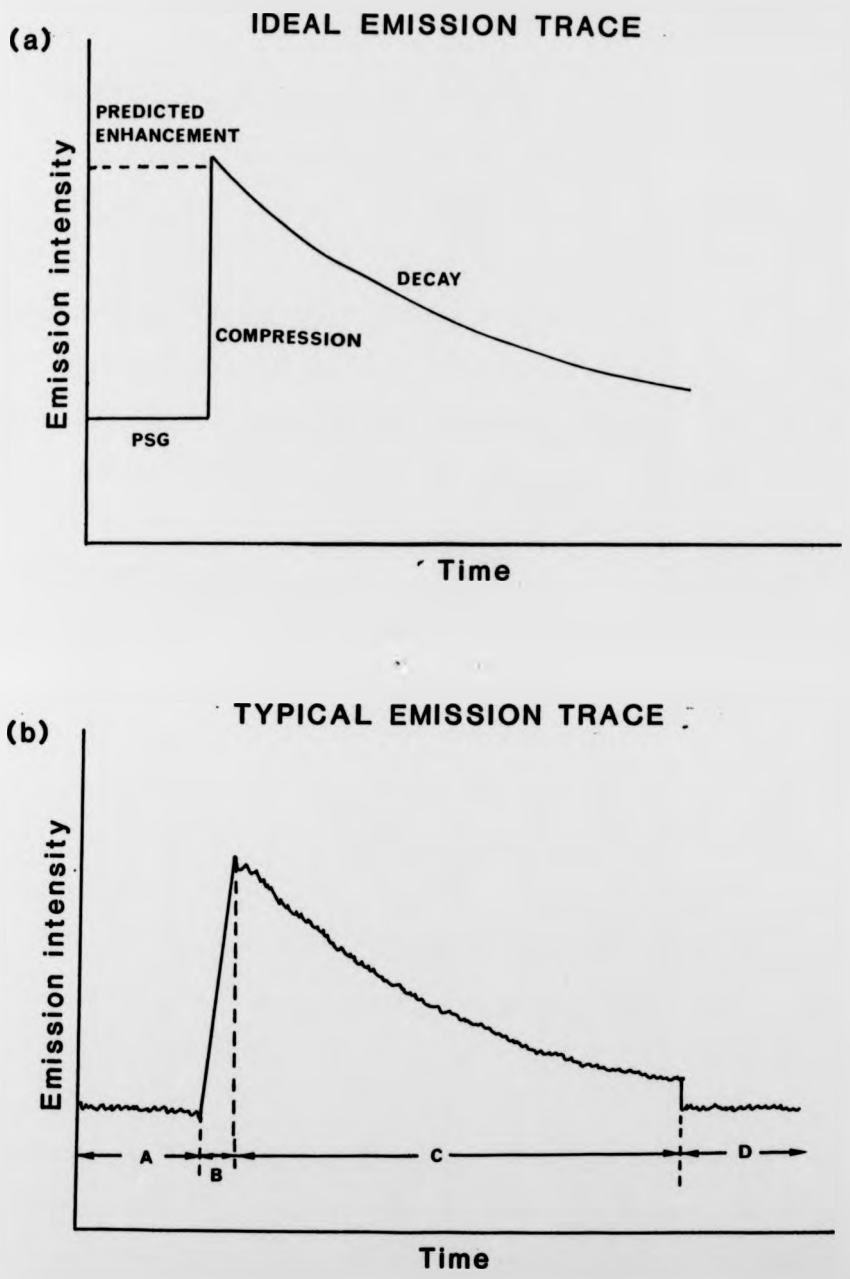

FIGURE 4.1 634nm EMISSION

The integrated form being:

$$^{634}I_{t_p} = {}^{634}K\,{}^{634}I_{psg}(\rho_{21})^2(T_{21})^{1/2}\ \exp(-t_p(2k_d^m[M]+\alpha_t))] \times (\exp(t_s(2k_d^m[M]+\alpha_t))-1)/(t_s(2k_d^m[M]+\alpha_t)) \quad (4.36)$$

When $t_p<t_s$, part of the integration area falls in the pre-shock glow. Therefore the integration of equation (4.29) is performed between t_p and zero with a component for the pre-shock glow added to the area defined.

$$^{634}I_{t_p} = {}^{634}I_{psg}\,{}^{634}K(\rho_{21})^2(T_{21})^{1/2} \times \int_0^{t_p} \exp(-t_p(2k_d^m[M]+\alpha_t))\ dt_p/t_s + {}^{634}I_{psg}(t_s-t_p)/t_s \quad (4.37)$$

Therefore,

$$^{634}I_{t_p} = {}^{634}I_{psg}\,{}^{634}K(\rho_{21})^2(T_{21})^{1/2}((-1/t_s(2k_d^m[M]+\alpha_t)) \times (\exp(-t_p(2k_d^m[M]+\alpha_t))-1) + {}^{634}I_{psg}(t_s-t_p)/t_s \quad (4.38)$$

While equation (4.35) can be integrated explicitly over the whole trace (equation 4.38), it is, in fact, integrated numerically from the point where the shock front arrives (common boundary of regions A and B, figure 4.1) using Simpson's Rule. This method of integration allows corrections, if necessary, for the variation in density, pressure and temperature due to vibrational relaxation to be made.

The fitting of equation (4.35) to the experimental data is done using an interactive computer graphics technique, which involves

the iteration of the parameters in the equation until the best non-linear least squares fit is obtained. This procedure is described in section 4.3.3.

4.3.1 Sensitivity Analysis of the $O_2(a^1\Delta_g)$ Kinetic Model

In the kinetic model used to evaluate the high temperature rate constant for the deactivation of $O_2(a^1\Delta_g)$, the parameters ^{634}K, t_s and $(2k_d^m[M]\alpha_t)$ are obtained by fitting the model to the experimental data rather than by independent measurement. As a result, the parameters are inter-related and may not be determined to a high degree of precision. Therefore, the values obtained by the fitting are subject to uncertainty. Sensitivity analysis is used to determine the sensitivity of the model to small changes in each of these parameters. By comparing the regions of the maximum sensitivity of the model to individual parameters, one can gain an insight into the influence of errors in one parameter upon the precision of another. It may also be used to determine which parameters dominate the fit of the model to the data.

Sensitivity analysis may be carried out to determine the absolute sensitivity, S, of one parameter in an equation with respect to another. A simple function,

$$C = C_o\exp(-kt) \qquad (4.39)$$

is chosen here to illustrate the definition of sensitivity and indicate the type of information which it can provide.

The absolute sensitivity of C with respect to k (equation 4.39) is given by the rate of change of C with respect to a small change in k.

$$S = dC/dk \tag{4.40}$$

therefore,

$$S = -tC_o\exp(-kt) \tag{4.41}$$

The absolute error in C increases linearly with time (independent variable) until such time as exp(-kt) becomes significant, then the error ceases to increase and begins to reduce. In other words, the error in the calculated concentration of a substance, which is decaying according to first order kinetics, as a result of the error in the rate constant, becomes less significant as the decay proceeds than in the initial stages. The sensitivity of C with respect to k is greatest when the rate of change of the sensitivity function with time is zero, $dS/dt = 0$.

$$dS/dt = C_o(kt-1)\exp(-kt) = 0 \tag{4.42}$$

hence, when $dS/dt = 0$,

$$1/k = t \tag{4.43}$$

Therefore, the value of C, derived from equation (4.39) will be most sensitive to an error in k after one lifetime of the decay process. Conversely, if k is obtained from fitting equation (4.39) to a set of experimental data, which involves the measurement of C, the quality

of the data after one lifetime will have more influence upon the accuracy and precision with which k is determined, than at any other time during the decay. Since small changes in k at this point produce large changes in C, the errors produced in k due to errors in the experimental data will be small. Therefore, it is important to include the first lifetime when extracting first order rate constants from experimental data.

If an error in C with respect to C_o is considered,

$$S = dC/dC_o = \exp(-kt) \tag{4.44}$$

The above expression indicates that the error in C caused by an error in C_o becomes less significant as time increases, according to the function exp(-kt). However, if C is measured and C_o is determined by extrapolation from a fitting of equation (4.39) to experimental data, then the data at the beginning of the decay will have most influence upon the determined value of C_o.

By comparing the sensitivity of C with respect to k, and C with respect to C_o, it can be deduced that k will dominate the fitting of equation (4.39) to a set of experimental data. These conclusions are not unexpected from the simple function which describes first order decay; however, the situation is likely to be less clear when more complex functions are involved. In such cases, sensitivity analysis would be a powerful tool in deciding which factors carry greater influence and which parameters are subject to large errors from small errors in other parameters.

A computer program was written to deal with the sensitivity analysis of equation (4.35) with respect to each of the fitted

parameters. The program is called SENDEL and is presented in Appendix 1.

Equation (4.35) is evaluated over a chosen integration period, using the Trapezium Rule. The integration period is divided into five sections, each of which is geometrically approximated to a trapezium. The area of each trapezium is calculated, all five areas are summed, and the mean average area for a 1 μs time interval calculated by dividing the total area by t_s. The overall time, t_p, is increased by $t_s/5$ and the procedure repeated. When a division of the integration period falls in the pre shock glow ($t_p<0$), then the value of the pre-shock glow is selected instead of the value obtained from equation (4.35).

The emission intensity - time data obtained from the numerical integration of equation (4.35) is differentiated with respect to the paramaters: ^{634}K (AK in the program); the overall decay constant $2k_d^m[M]\alpha_t$, (DK in the program); and the integration time, t_s, (TS in the program). Differentiation is carried out by first evaluating equation (4.35) and then increasing the value of the appropriate parameter by a factor of 1.0001. The differential of equation (4.35) with respect to the selected parameter is given by the difference in emission intensity divided by the increase in the value of the selected parameter.

The original emission intensity - time coordinates, generated from equation (4.29), the unintegrated form of equation (4.35) are stored in file RSEND and the results of the differentiation of the kinetic model (equation 4.35) with respect to the selected parameter are stored in file RES. The results of the differentiation constitute the sensitivity analysis of the kinetic model with respect to the selected parameter.

The data stored in files RES and RSEND may be plotted using

the standard plotting routines available in the Chemistry Department at Keele.

Figures 4.2 to 4.4 show the sensitivity of the emission intensity generated from equation (4.35), the kinetic model, with respect to each of the three variable parameters, as a function of the independent variable, t_p. Whether the sensitivity is positive or negative is unimportant at this stage. The magnitude of the sensitivity of the emission with respect to the appropriate parameter as a function of time is the important result of the analysis.

Figure 4.2, shows the sensitivity of the kinetic model with respect to the enhancement factor, ^{634}K. As expected, the model is more sensitive to errors in ^{634}K immediately after the shock, when the physical processes involving the enhancement take place. Errors in ^{634}K become less significant as the experiment proceeds.

Figure 4.3 shows the sensitivity of the model with respect to the overall decay constant. As one might expect from the discussion of the simple first order decay (equation 4.39) at the beginning of this section, the model is most sensitive to the deactivation rate constant $2k_d^m[M]\alpha_t$ after one half-life, and is less sensitive during the final stage, where the decay curve may more easily be approximated to a straight line.

Figure 4.4 shows the sensitivity of the model with respect to the integration time, t_s. The model is most sensitive at the beginning of the emission intensity profile, when the most dramatic changes in emission intensity are taking place. Compared to this region, the rest of the profile shows a negligible degree of sensitivity to t_s. This is not unexpected since the integration time has the effect of averaging the emission signal and will create the greatest error in the emission intensity during the period when the change in concentration of $O_2(a^1\Delta_g)$, and therefore emission

FIGURE 4.2 SENSITIVITY OF 634nm KINETIC MODEL WITH RESPECT TO ^{634}K

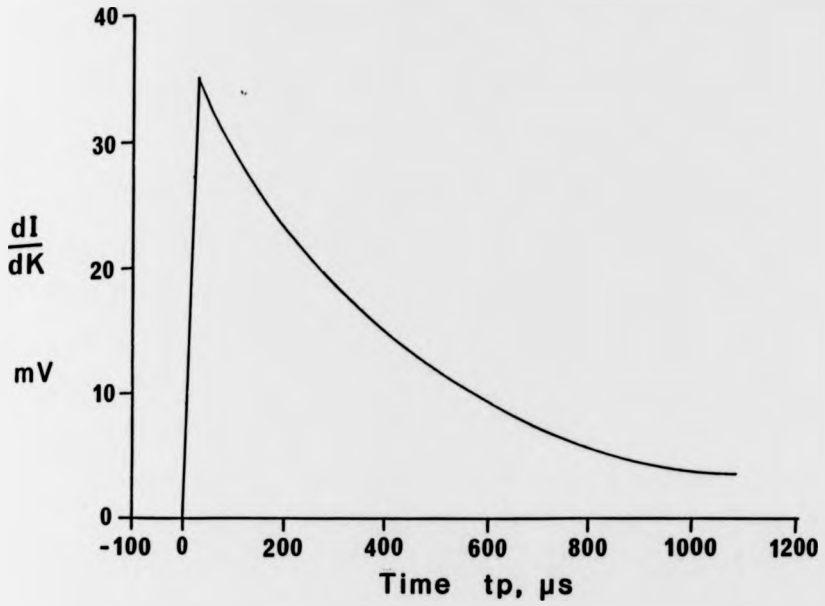

FIGURE 4.3 SENSITIVITY OF 634nm KINETIC MODEL WITH RESPECT TO OVERALL DECAY CONSTANT

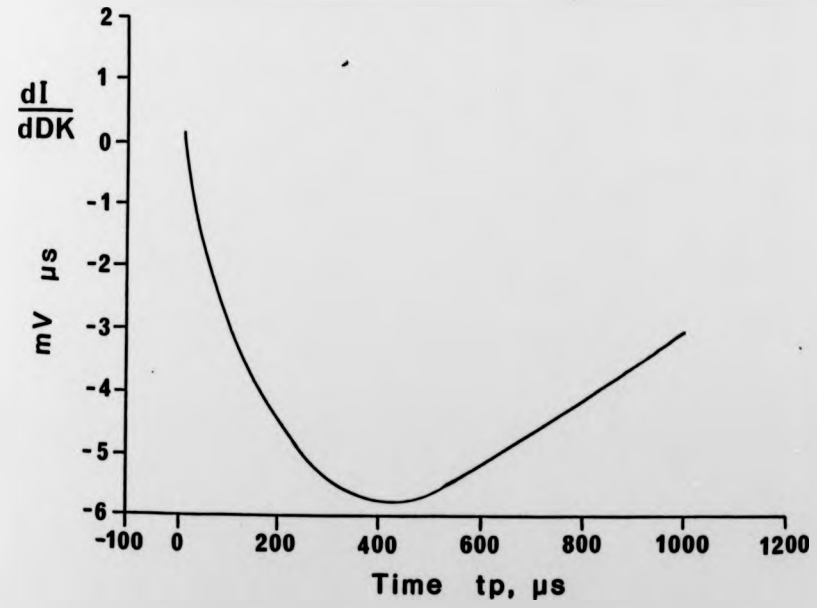

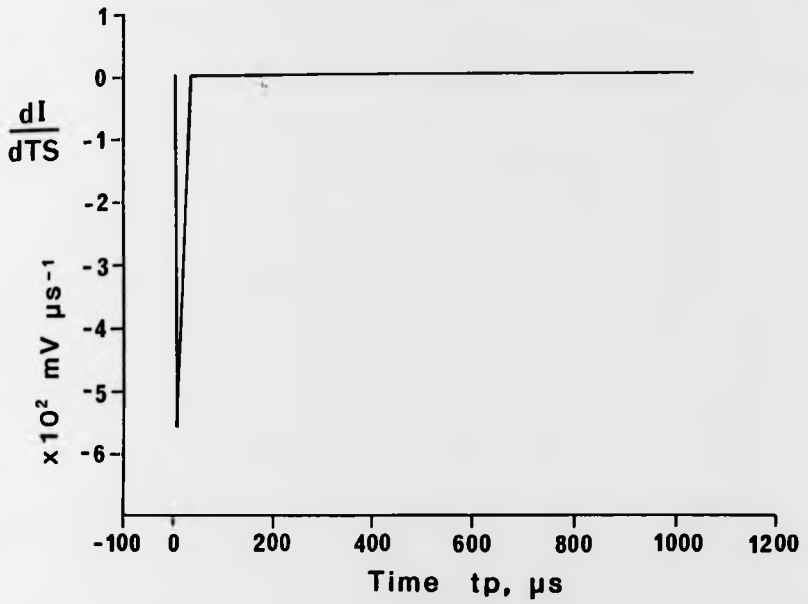

FIGURE 4.4 SENSITIVITY OF 634nm KINETIC MODEL WITH RESPECT TO INTEGRATION TIME

intensity, is greatest.

Considering the sensitivity - time plots (figures 4.2 to 4.4), one can see that the sensitivity of the model with respect to the integration time and the overall decay constant is well separated in time. Therefore, the regions of the experimental data which best define these quantities are also well separated. As a result, the determinations of t_s and $2k_d^m[M]+\alpha_t$ are essentially independent of each other. That is to say, errors in one exert very little influence upon the value of the other.

The sensitivity of the model with respect to the enhancement factor is significant over the whole time axis and coincides with the regions of sensitivity with respect to both the integration time and the overall decay constant. The overlap with the sensitivity of the model to the integration time is very small and the overlap with the sensitivity of the model to the overall decay constant occurs when the sensitivity of with respect to ^{634}K is reducing. Thus the evaluation of ^{634}K by fitting the model to the experimental data will be essentially independent of t_s and $k_d^m[M]+\alpha_t$ over the region where ^{634}K is least sensitive to the experimental data and therefore better defined.

The conclusion may be drawn that the values of t_s, ^{634}K and $k_d^m[M]+\alpha_t$ obtained from the fitting of the model to the experimental data are well defined and that errors in these values are more likely to arise from the quality of the data rather than the inter-relation of the parameters.

4.3.2 Corrections for $O_2(b^1\Sigma^+_g)$ as a Source or Sink for $O_2(a^1\Delta_g)$

From equations (4.14 and 4.15) it is evident that the deactivation of $O_2(b^1\Sigma^+_g)$ is a source of $O_2(a^1\Delta_g)$. Since the concentration of $O_2(b^1\Sigma^+_g)$ at any time is approximately 0.1% that of

$O_2(a^1\Delta_g)$, the contribution from this source to the total concentration of $O_2(a^1\Delta_g)$ is insignificant and may be neglected. The reversal of the processes described by equations (4.14 and 4.15),

$$O_2(a^1\Delta_g) + M \text{ ----> } O_2(b^1\Sigma^+_g) + M \qquad (4.45)$$

where M includes $O_2(X^3\Sigma^-_g)$ as a test gas, introduces the possibility of an alternative deactivation of $O_2(a^1\Delta_g)$ producing the higher energy species $O_2(b^1\Sigma^+_g)$. Clearly, this reaction will be very slow compared to the forward reaction, particularly at lower shock temperatures. Over the temperature range of the experiments carried out in this work (500 to 1200K), it is insignificant as a process for the removal of $O_2(a^1\Delta_g)$. Therefore no corrections are necessary to account for the participation of $O_2(b^1\Sigma^+_g)$ in the $O_2(a^1\Delta_g)$ rate equation.

It is thought, however, that this reaction may be a significant source of $O_2(b^1\Sigma^+_g)$ at temperatures above 1200K. Corrections for such a situation are discussed in section 4.5.2.

4.3.3 Computer Analysis of $O_2(a^1\Delta_g)$ Data

The kinetic model (equation 4.35) for $O_2(a^1\Delta_g)$ has been developed into an interactive computer graphics program by Borrell [61] for use with the GEC 4082 computer using the HP2647A graphics terminal.

The analysis proceeds by displaying the experimentally obtained emission intensity - time data as a plot. The point where the arrival of the shock front causes a rapid rise in emission intensity is set by eye as the starting point $t_p = 0$. The end point is set just before the arrival of the contact surface causes complete

loss of the emission.

Reasonable values of t_s, ^{634}K and $2k_d^m[M]+\alpha_t$ for the start of the numerical fitting of the kinetic model are chosen. This is done interactively, using graphics to obtain an approximate fit to the plot by eye. The value of t_s may also be obtained from tables 2.2 and 2.3.

The analysis then continues by fitting equation (4.35), with rough values of the three variable parameters, to the experimental data by a non-linear least squares method. An iterative process is carried out to achieve the best fit values of t_s, ^{634}K and $2k_d^m[M]+\alpha_t$. The value for $2k_d^m[M]+\alpha_t$ is compared with the calculated value for α_t, derived from the measured pre-shock decay, α_1, to obtain a value for $2k_d^m[M]$.

Figure 4.5 shows the fit obtained for an actual set of data (run DSR212A) recorded during the study of the deactivation of $O_2(a^1\Delta_g)$ by nitrogen. The line through the points is the fit obtained using equation (4.35). There is no additional deactivation at the high temperature in this case.

Figure 4.6 (run DSR405A) shows a fit for experimental data recorded during the study of the deactivation of $O_2(a^1\Delta_g)$ by hydrogen. In this case, there is additional deactivation at the high temperature. The dotted line shows the curve predicted from the room temperature measurements, assuming $k_d^m = 0$.

A comparison of figures 4.5 and 4.6 with figure 4.1 shows that the shape of the shock trace is in agreement with the predicted profile and confirms that the kinetic model is a good representation of the physical processes involved.

The use of interactive computer graphics, to fit the model to the experimental data, allows the operator to check the quality of the fit by superimposing the predicted profile onto the experimental

FIGURE 4.5

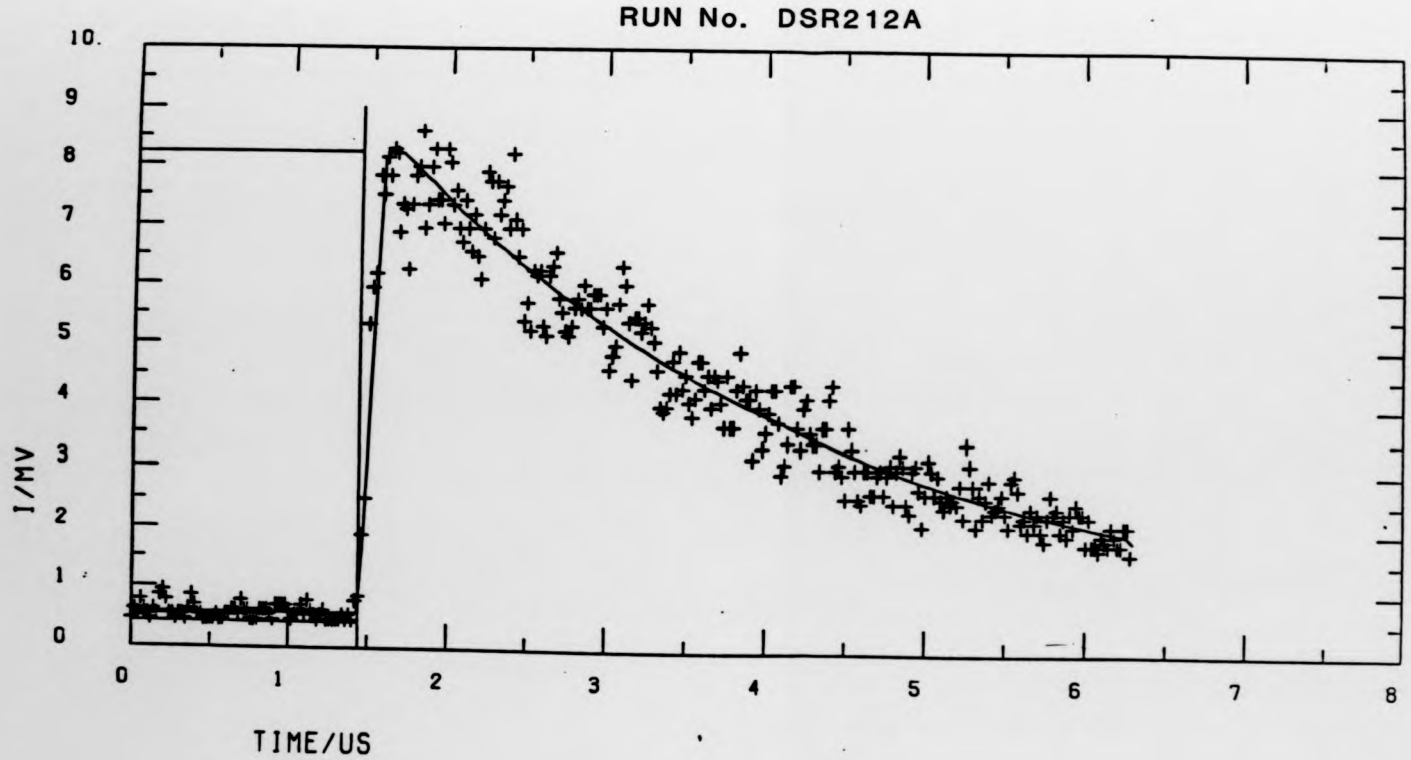

FIGURE 4.6

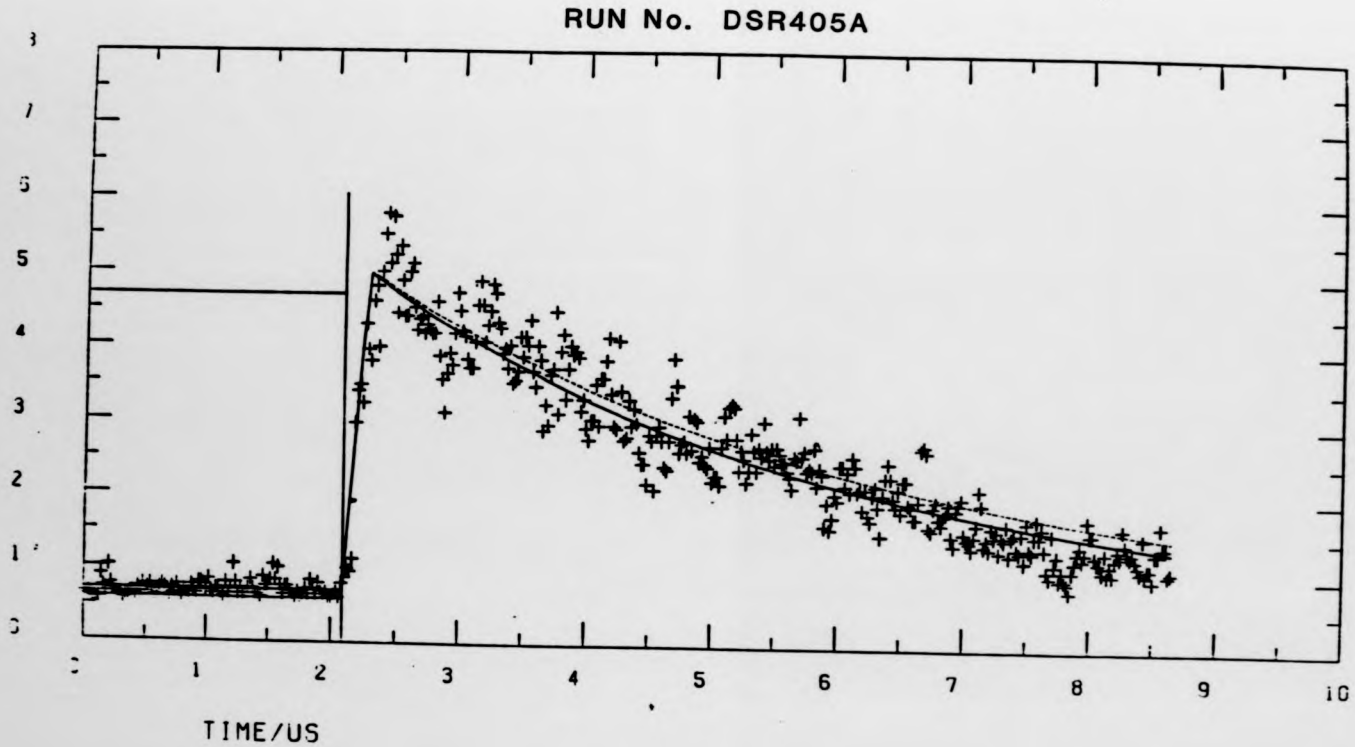
RUN No. DSR405A
0
1
2
3
4
5
6
7
8
9
10
TIME/US
XAXIS SCALE = X * (10 **-2)
YAXIS SCALE = Y * (10 **-2)

points.

It is also possible to fix one of the parameters and fit the others so that the effect of variations in the value of a parameter can be explored. Such an exercise is useful, since it allows the experimenter to develop both a feel for the kinetic model and to explore the effect of errors in the measured quantities directly. This facility permitted the discovery of the fact that fixing the value of the integration time to that obtained from tables 2.2 and 2.3 gives a more precise value for $2k_d^m[M]+\alpha_t$. This observation was later supported by the sensitivity analysis discussed in section 4.3.1. Another benefit of fixing the integration time was the reduced time required to complete the iteration process.

The program itself is quite complex and consists of numerous sub-routines. A comprehensive and detailed description of the program has been written by Pedley [46]. Since it has remained essentially unchanged, a description of the workings of the program will not be given here.

4.4 Room Temperature Deactivation of $O_2(b^1\Sigma^+_g)$

$O_2(b^1\Sigma^+_g)$ is generated via the energy pooling reaction (equation 4.2) and removed by the following processes:

$$O_2(b^1\Sigma^+_g) \xrightarrow{k_{12}} O_2(X^3\Sigma^-_g) + h\nu(\lambda=762nm) \qquad (4.12)$$

$$O_2(b^1\Sigma^+_g) + \text{wall} \xrightarrow{k_w^{\Sigma}} O_2(X^3\Sigma^-_g) \qquad (4.13)$$

$$O_2(b^1\Sigma^+_g) + O_2(X^3\Sigma^-_g) \xrightarrow{k_q^{o}} O_2(a^1\Delta_g) + O_2(X^3\Sigma^-_g) \qquad (4.14)$$

$$O_2(b^1\Sigma^+_g) + M \xrightarrow{k_q^{m}} O_2(a^1\Delta_g) + M \qquad (4.15)$$

Compared with the main loss processes (equations 4.13, 4.14, and 4.15), the radiative decay of $O_2(b^1\Sigma^+_g)$ is insignificant [28] and may be neglected. The rate equation for the removal of $O_2(b^1\Sigma^+_g)$ may be written as:

$$d[O_2(b^1\Sigma^+_g)]/dt = k_p[O_2(a^1\Delta_g)]^2 - k_q^{o}[O_2(X^3\Sigma^-_g)][O_2(b^1\Sigma^+_g)] - k_q^{m}[M][O_2(b^1\Sigma^+_g)] - k_w^{\Sigma}[O_2(b^1\Sigma^+_g)] \qquad (4.46)$$

Since the concentration of $O_2(b^1\Sigma^+_g)$ is at steady state at any point in the flow, $d[O_2(b^1\Sigma^+_g)]/dt = 0$, equation (4.46) may be rearranged to:

$$[O_2(b^1\Sigma^+_g)]/[O_2(a^1\Delta_g)]^2 = k_p/(k_q^o[O_2(X^3\Sigma^-_g)]+k_q^m[M]+k_w^{\Sigma})$$

(4.47)

From section 4.2,

$$[O_2(b^1\Sigma^+_g)]/[O_2(a^1\Delta_g)]^2 \propto {}^{762}I/{}^{634}I$$

Therefore,

$$\Phi_m = {}^{762}I/{}^{634}I = Qk_p/(k_q^o[O_2(X^3\Sigma^-_g)]+k_q^m[M]+k_w^{\Sigma 1})$$

(4.48)

where Q is a constant of proportionality. In the absence of a test gas, M, equation (4.48) becomes:

$$\Phi_o = {}^{762}I/{}^{634}I = Qk_p/(k_q^o[O_2(X^3\Sigma^-_g)]+k_w^{\Sigma 2}$$

(4.49)

In equations (4.48 and 4.49), $k_w^{\Sigma 1}$ and $k_w^{\Sigma 2}$ are different wall constants, as a result of the increase in pressure when M is added. These constants may be determined from equation (4.50) taken from Derwent and Thrush [67].

$$k_w^{\Sigma} = 1/(r^2(P_1/P_o)/(8D_o)+(2r/\gamma C'))$$

(4.50)

where r is the radius of the flow tube; D_o is the diffusion coefficient for $O_2(b^1\Sigma^+_g)$ at atmospheric pressure, P_o; P_1 is the flow tube pressure; γ is the wall efficiency; and C' is the mean velocity of $O_2(b^1\Sigma^+_g)$, which is assumed to be the same as that for $O_2(X^3\Sigma^-_g)$.

Combining equations (4.48 and 4.49) as $(\Phi_m-\Phi_o)/\Phi_o$ one obtains:

$$(\Phi_m-\Phi_o)/\Phi_o = (k_q^m[M]+k_w^{\Sigma 2}-k_w^{S1})/(k_q^o[O_2(X^3\Sigma^-_g)]+k_w^{\Sigma 1}) \qquad (4.51)$$

Rearrangement gives:

$$k_q^m[M] = ((k_q^o[O_2(X^3\Sigma^-_g)]+k_w^{\Sigma 1})(\Phi_m-\Phi_o/\Phi_o)-(k_w^{\Sigma 2}-k_w^{\Sigma 1}) \qquad (4.52)$$

For brevity,

$$k_q^m[M] = f(\Phi_m, \Phi_o) \qquad (4.53)$$

Therefore a plot of $f(\Phi_m, \Phi_o)$ versus [M] will yield k_q^m as the gradient. Such a plot should pass through the origin, assuming that there is no modification of the wall efficiency due to the adsorption of the test gas. There have been no indications of wall modification either in this work or in the work of Pedley [46], Grant [13], Borrell [60] or Boodaghians [44] during measurements of $O_2(b^1\Sigma^+_g)$ deactivation at room temperature in the apparatus used here.

4.5 High Temperature Deactivation of $O_2(b^1\Sigma^+_g)$

The derivation which follows first assumes that there is no deactivation of $O_2(a^1\Delta_g)$ at high temperatures, and therefore that the decay of the emission intensity is entirely a result of the pre-shock decay. The rate equations derived in this way are then modified to allow for the deactivation of $O_2(a^1\Delta_g)$ at high temperatures.

(a) With no additional deactivation of $O_2(a^1\Delta_g)$ at high temperatures

Analogously with equation (4.46), the equation for the rate of change of $O_2(b^1\Sigma^+_g)$ concentration at high temperatures, expressed in particle time, is:

$$d[O_2(b^1\Sigma^+_g)]/dt_p = k_p[O_2(a^1\Delta_g)]^2-(k_q^m[M]+k_q^o[O_2(X^3\Sigma^-_g)]+k_w^{\Sigma}) \times [O_2(b^1\Sigma^+_g)] \qquad (4.54)$$

The wall deactivation of $O_2(b^1\Sigma^+_g)$ is considerably reduced under shock conditions because of the short duration of the observation time. The collisional deactivation increases at high temperatures, while the wall deactivation remains the same. Hence, the wall deactivation may be neglected in the high temperature experiments. However, the deactivation of $O_2(b^1\Sigma^+_g)$ due to $O_2(X^3\Sigma^-_g)$ is significant at high temperatures. If the collisional deactivation rate constants are combined,

$$k_q^m[M]+k_q^o[O_2(X^3\Sigma^-_g)] = (k_q^m x_m+k_q^o x_o)[M'] = k_q^{m'}[M'] \qquad (4.55)$$

where x_m and x_o are the mole fractions of M and $O_2(X^3\Sigma^-_g)$ respectively; [M'] is the concentration of the mixture; and $k_q^{m'}$ is

the effective rate constant of the mixture. Equation (4.54) may now be simplified to:

$$d[O_2(b^1\Sigma^+_g)]/dt_p = k_p[O_2(a^1\Delta_g)]^2 - k_q^{m'}[M'][O_2(b^1\Sigma^+_g)] \quad (4.56)$$

Assuming that $[O_2(b^1\Sigma^+_g)] << [O_2(a^1\Delta_g)]$, in other words $[O_2(a^1\Delta_g)]$ is essentially constant, equation (4.56) may be integrated between t=0 and $t=t_p$

$$\int_{[\Sigma]_0}^{[\Sigma]_{t_p}} d[O_2(b^1\Sigma^+_g)]/(k_p[O_2(a^1\Delta_g)]^2 - k_q^{m'}[M'][O_2(b^1\Sigma^+_g)] = \int_0^{t_p} dt_p \quad (4.57)$$

Therefore,

$$\ln((k_p[O_2(a^1\Delta_g)]^2 - k_q^{m'}[M'][O_2(b^1\Sigma^+_g)]_{t_p}/ (k_p[O_2(a^1\Delta_g)]^2 - k_q^{m'}[M'][O_2(b^1\Sigma^+_g)]_o)) = -k_q^{m'}[M']t_p \quad (4.58)$$

Rearrangement gives:

$$[O_2(b^1\Sigma^+_g)]_t /[O_2(b^1\Sigma^+_g)]_o = (1-(k_p[O_2(a^1\Delta_g)]^2/k_q^{m'}[M'][O_2(b^1\Sigma^+_g)]_o \exp(-k_q^{m'}[M']t_p) + (k_p[O_2(a^1\Delta_g)]^2/k_q^{m'}[M'][O_2(b^1\Sigma^+_g)]_o) \quad (4.59)$$

where $[O_2(b^1\Sigma^+_g)]_o$ is the concentration at any point in the tube immediately after the shock and $[O_2(b^1\Sigma^+_g)]_{t_p}$ is that after time, t_p. As t_p approaches infinity, a steady state will be reached. Under such conditions, equation (4.59) reduces to:

$$[O_2(b^1\Sigma^+_g)]_{t_p} = k_p[O_2(a^1\Delta_g)]^2/k_q{}^{m'}[M'] \tag{4.60}$$

Equations (4.47 and 4.60) may be written as:

$$([O_2(a^1\Delta_g)]^2/[O_2(b^1\Sigma^+_g)][M'])_{T_1} = ((k_q{}^{m'}+(k_w{}^{\Sigma}/[M']))/k_p)_{T_1} \tag{4.61}$$

$$([O_2(a^1\Delta_g)]^2/[O_2(b^1\Sigma^+_g)][M'])_{T_2} = (k_q{}^{m'}/k_p)_{T_2} \tag{4.62}$$

The concentrations at t_p=0 (immediately after the shock) are those in the pre-shock multiplied by the density ratio, ρ_{21}.

$$([O_2(a^1\Delta_g)]^2/[O_2(b^1\Sigma^+_g)][M'])_{T_1} \times (\rho_{21})^2/(\rho_{21})^2 = ([O_2(a^1\Delta_g)]^2/[O_2(b^1\Sigma^+_g)][M'])_{T_2} \tag{4.63}$$

The enhancement factor, ^{762}K is defined as the ratio of the observed post-shock emission, $^{762}I_{ips}$, immediately after the shock, to the predicted post-shock emission, $^{762}I_{pps}$.

$$^{762}K = {}^{762}I_{ips}/{}^{762}I_{pps} = (\rho_{21})[O_2(b^1\Sigma^+_g)]_{T_1}/[O_2(b^1\Sigma^+_g)]_{T_2} \tag{4.64}$$

Substituting for $(\rho_{21})[O_2(b^1\Sigma^+_g)]_{T_1}/[O_2(b^1\Sigma^+_g)]_{T_2}$ from equation (4.63),

$$^{762}K = ([O_2(a^1\Delta_g)]^2/[M'])_{T_2}([M']/[O_2(a^1\Delta_g)]^2)_{T_1}(1/\rho_{21}) \quad (4.65)$$

Substituting expressions for $([O_2(a^1\Delta_g)]^2/[M'])_{T_2}$ and $([M']/[O_2(a^1\Delta_g)]^2)_{T_1}$ from equations (4.61 and 4.62),

$$^{762}K = ([O_2(b^1\Sigma^+_g)]k_q^{m'}/k_p)_{T_2}/(k_p[O_2(b^1\Sigma^+_g)]/(k_q^{m'}+(k_w^{\Sigma}/[M'])))_{T_1} \times (\rho_{21}) \quad (4.66)$$

But $[O_2(b^1\Sigma^+_g)]_{T_1}(\rho_{21}) = [O_2(b^1\Sigma^+_g)]_{T_2}$, therefore

$$^{762}K = (k_q^{m'}/k_p)_{T_2}/(k_p/(k_q^{m'}+(k_w^{\Sigma}/[M'])))_{T_1} \quad (4.67)$$

^{762}K may be expressed as:

$$^{762}K = (k_p/k_q^{m'})/([O_2(a^1\Delta_g)]^2/[M'][O_2(b^1\Sigma^+_g)]_o) \quad (4.68)$$

where concentrations and rate constants refer to the post-shock (high temperature) conditions and $[O_2(b^1\Sigma^+_g)]_o$ is the concentration of $O_2(b^1\Sigma^+_g)$ immediately after the shock. Therefore, equation (4.59) becomes:

$$[O_2(b^1\Sigma^+_g)]_{t_p}/[O_2(b^1\Sigma^+_g)]_o = (1-^{762}K)\exp(-k_q^{m'}[M']t_p) + ^{762}K \quad (4.69)$$

As in the $O_2(a^1\Delta_g)$ kinetic model, the fall off in concentration under the post-shock conditions is a result of the pre-shock decay of

$$^{762}K = ([O_2(a^1\Delta_g)]^2/[M'])_{T_2}([M']/[O_2(a^1\Delta_g)]^2)_{T_1}(1/\rho_{21}) \quad (4.65)$$

Substituting expressions for $([O_2(a^1\Delta_g)]^2/[M'])_{T_2}$ and $([M']/[O_2(a^1\Delta_g)]^2)_{T_1}$ from equations (4.61 and 4.62),

$$^{762}K = ([O_2(b^1\Sigma^+_g)]k_q^{m'}/k_p)_{T_2}/(k_p[O_2(b^1\Sigma^+_g)]/(k_q^{m'}+(k_w^{\Sigma}/[M'])))_{T_1} \times (\rho_{21}) \quad (4.66)$$

But $[O_2(b^1\Sigma^+_g)]_{T_1}(\rho_{21}) = [O_2(b^1\Sigma^+_g)]_{T_2}$, therefore

$$^{762}K = (k_q^{m'}/k_p)_{T_2}/(k_p/(k_q^{m'}+(k_w^{\Sigma}/[M'])))_{T_1} \quad (4.67)$$

^{762}K may be expressed as:

$$^{762}K = (k_p/k_q^{m'})/([O_2(a^1\Delta_g)]^2/[M'][O_2(b^1\Sigma^+_g)]_o) \quad (4.68)$$

where concentrations and rate constants refer to the post-shock (high temperature) conditions and $[O_2(b^1\Sigma^+_g)]_o$ is the concentration of $O_2(b^1\Sigma^+_g)$ immediately after the shock. Therefore, equation (4.59) becomes:

$$[O_2(b^1\Sigma^+_g)]_{t_p}/[O_2(b^1\Sigma^+_g)]_o = (1-^{762}K)\exp(-k_q^{m'}[M']t_p) + ^{762}K \quad (4.69)$$

As in the $O_2(a^1\Delta_g)$ kinetic model, the fall off in concentration under the post-shock conditions is a result of the pre-shock decay of

$O_2(a^1\Delta_g)$ along the flow tube hence,

$$[O_2(b^1\Sigma^+_g)]_o = [O_2(b^1\Sigma^+_g)]_o^{obs} \exp(-\alpha_t t_p) \tag{4.70}$$

where, $[O_2(b^1\Sigma^+_g)]_o^{obs}$ is the initial post-shock concentration at the observation station. The combination of equations (4.69 and 4.70) gives:

$$[O_2(b^1\Sigma^+_g)]_{t_p}/[O_2(b^1\Sigma^+_g)]_o^{obs} = ({}^{762}K + (1 - {}^{762}K)\exp(-k_q^{m'}[M']t_p))\exp(-\alpha_t t_p) \tag{4.71}$$

Since

$${}^{762}I_{t_p}/{}^{762}I_o^{obs} = [O_2(b^1\Sigma^+_g)]_t /[O_2(b^1\Sigma^+_g)]_o^{obs} \tag{4.72}$$

and at the observation station the pre-shock glow is related to the immediate post-shock glow by:

$${}^{762}I_o^{obs} = {}^{762}I_{psg}(\rho_{21}); \tag{4.73}$$

then,

$${}^{762}I_{t_p} = {}^{762}I_{psg}(\rho_{21})({}^{762}K+(1-{}^{762}K)\exp(-k_q^{m'}[M']t_p))\exp(-\alpha_t t_p) \tag{4.74}$$

Figure 4.7(a) shows the emission intensity - time profile predicted by equation (4.74). An instantaneous increase in the

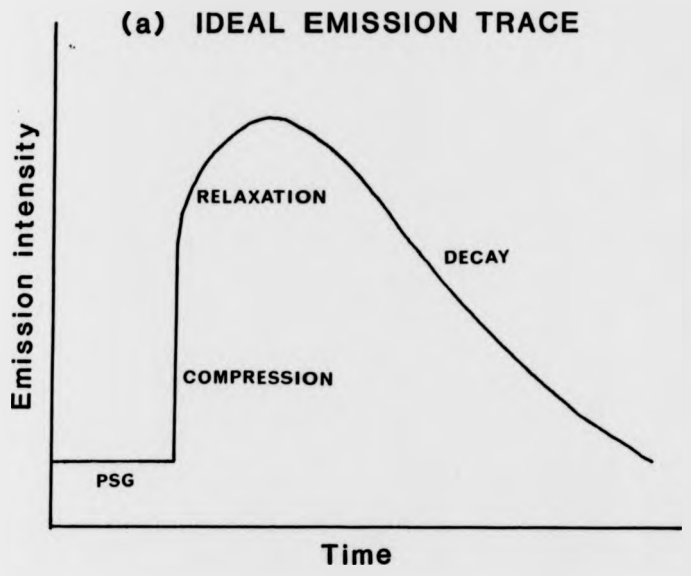

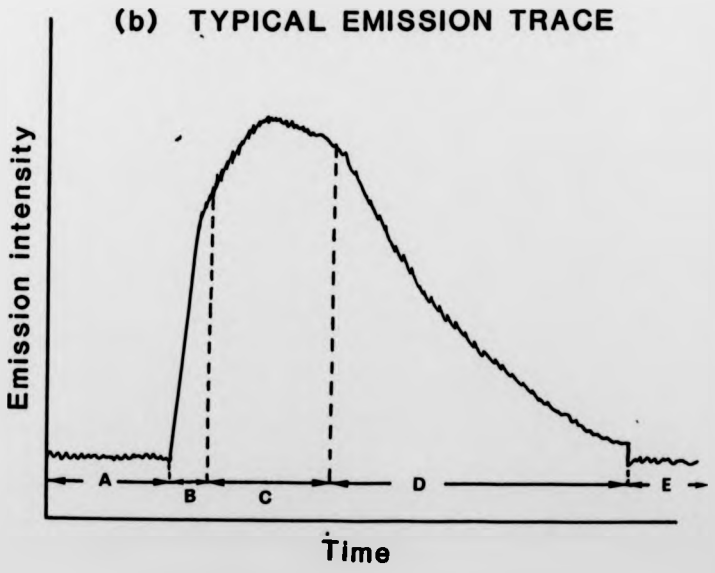

FIGURE 4.7 762nm EMISSION

emission intensity at the shock front, followed by a relaxation period and then a decay is predicted. The form of a typical emission intensity - time trace is represented in figure 4.7(b). Five distinct regions may be distinguished in the observed trace:

(A) The pre-shock glow, $^{762}I_{psg}$, before the arrival of the shock front.

(B) A rapid, but not instantaneous, increase in emission due to the increase in density after the arrival of the shock front.

(C) A period of relaxation to the new, high temperature, steady state.

(D) The decay of the emission, which reflects the fall-off in concentration of $O_2(a^1\Delta_g)$ in the pre-shock glow.

(E) The complete loss of the signal upon the arrival of the contact surface.

Regions A, C and D are as predicted by equation (4.74), but region B shows a risetime which is a result of the finite slit width of the photomultiplier unit. As with the $O_2(a^1\Delta_g)$ kinetic model, the analysis equation must be integrated over the risetime, t_s.

$$^{762}I_{t_p} = {}^{762}I_{psg}(\rho_{21}) \int_{t_p - t_s}^{t_p} ({}^{762}K + (1 - {}^{762}K)\exp(-k_q{}^{m'}[M']t_p)) \times \exp(-\alpha_t t_p)dt_p/t_s \qquad (4.75)$$

While equation (4.75) can be integrated explicitly over the whole trace, it is in fact integrated numerically using Simpson's Rule, in the same manner as equation (4.35), the kinetic model for $O_2(a^1\Delta_g)$.

Equation (4.75) was originally used as the kinetic model for the analysis of the high temperature data; however, as the types of deactivating species studied expanded, modifications became necessary to account for the simultaneous deactivation of $O_2(a^1\Delta_g)$.

(b) With deactivation of $O_2(a^1\Delta_g)$ at high temperature

To allow for the deactivation of $O_2(a^1\Delta_g)$ by M at the high temperature, it is necessary to modify the rate equations. From the derivation of the $O_2(a^1\Delta_g)$ kinetic model, the deactivation of $O_2(a^1\Delta_g)$ can be represented as a function of time at any point in the post-shock regime by:

$$[O_2(a^1\Delta_g)]_{t_p}/[O_2(a^1\Delta_g)]_o{}^{obs} = \exp(-t_p((\alpha_t/2)+k_d{}^{m'}[M'])) \qquad (4.26)$$

Combining equation (4.26) with the rate equation for $O_2(b^1\Sigma^+_g)$, equation (4.56),

$$d[O_2(b^1\Sigma^+_g)]/dt_p = k_p([O_2(a^1\Delta_g)]_o^{obs})^2 \exp(-t_p(2k_d^{m'}[M']+\alpha_t)) - k_q^{m'}[M'][O_2(b^1\Sigma^+_g)] \quad (4.76)$$

Integrating equation (4.76) with between $t_p=t_p$ and $t_p=0$ and carrying out the substitution process for ^{762}K, results in the following expression:

$$[O_2(b^1\Sigma^+_g)]_{t_p}/[O_2(b^1\Sigma^+_g)]_o^{obs} = (^{762}K\exp(-2k_d^{m'}[M']t_p)+(1-^{762}K) \times \exp(-k_q^{m'}[M']t_p))\exp(-\alpha_t t_p) \quad (4.77)$$

provided that ^{762}K is redefined as:

$$^{762}K = (k_p/(k_q^{m'}-k_d^{m'}))_{T_2}/(k_p/(k_q^{m'}-k_d^{m'}-(k_w^{\Sigma}/[M'])))_{T_1} \quad (4.78)$$

Considering equations (4.72 and 4.73),

$$^{762}I_{t_p} = {}^{762}I_{psg}(\rho_{21})(^{762}\exp(-2k_d^{m'}[M']t_p)+(1-^{762}K) \times \exp(-k_q^{m'}[M']t_p)) \times \exp(-\alpha_t) \quad (4.79)$$

Integration over the risetime, t_s, gives:

$$^{762}I_{t_p} = {}^{762}I_{psg}(\rho_{21})\int_{t_p-t_s}^{t_p} ({}^{762}K\exp(-2k_d^{m'}[M']t_p) + (1-{}^{762}K)\exp(-k_q^{m'}[M']t_p)) \times \exp(-\alpha_t t_p)\, dt_p/t_s \qquad (4.80)$$

This equation is the kinetic model for the deactivation $O_2(b^1\Sigma^+_g)$ allowing for simultaneous deactivation of $O_2(a^1\Delta_g)$. Equation (4.80) is integrated numerically using Simpson's Rule. The fitting of the kinetic model (equation 4.80) to the experimental data is done using an interactive computer graphics technique, which involves the iteration of the parameters in the equation until the best non-linear least squares fit is obtained. This procedure is described in section 4.5.3.

This kinetic model (equation 4.80) is used throughout this work to analyse the high temperature data recorded in the study of the deactivation of $O_2(b^1\Sigma^+_g)$.

4.5.1 Sensitivity Analysis of the $O_2(b^1\Sigma^+_g)$ Kinetic Model

As with the sensitivity analysis of the $O_2(a^1\Delta_g)$ kinetic model, a computer program was written to carry out the evaluation, integration and differentiation of the analysis equation, with respect to selected parameters. The program is called SENSIG, and may be found in Appendix 2. It is an adaptation of the SENDEL program and operates in the same manner. However, the number of variable parameters is increased. The dependent variables are: the enhancement factor ^{762}K, (called AK in the program); the $O_2(a^1\Delta_g)$ decay increment, $2k_d^{m'}[M']$, (DDK in the program); the pseudo-first order $O_2(b^1\Sigma^+_g)$ decay constant, $k_q^{m'}[M']$, (SDK in the program); the room temperature decay of $O_2(a^1\Delta_g)$, α_t, (RDK in the program); and the

integration time, t_s, (TS in the program).

The data from the evaluation of equation (4.79) over time, t_p, are stored in file RSIG, while the data from the sensitivity analysis of the model with respect to the selected parameter are stored in file RESULT. Both files may be plotted out using the standard plotting routines available for general use in the Chemistry Department at Keele.

Figures 4.8 to 4.12 show the sensitivity of the emission intensity generated from equation (4.80), the kinetic model, with respect to each of the five dependent variables, as a function of the independent variable t_p. Again it is the magnitude of the sensitivity with respect to the selected parameter which is the important result, rather than the sign.

Figure 4.8 shows the sensitivity of the kinetic model with respect to the enhancement factor, ^{762}K. As expected, the sensitivity is greatest immediately after the shock heating when the physical processes involved in the enhancement take place. Errors in ^{762}K become less significant as the experiment proceeds.

Figure 4.9 shows the sensitivity of the model with respect to the pseudo-first order $O_2(b^1\Sigma^+_g)$ decay constant, $k_q^{m'}[M']$. The model is most sensitive to errors in this constant over the relaxation period and shows no sensitivity when the relaxation is complete.

Figure 4.10 shows the sensitivity of the model with respect to the increment in the $O_2(a^1\Delta_g)$ decay at the high temperature, $k_d^{m'}[M']$. As one might expect, the sensitivity follows the same pattern as the sensitivity of the $O_2(a^1\Delta_g)$ kinetic model to the overall $O_2(a^1\Delta_g)$ decay constant. The model is most sensitive after one lifetime (in this case 230 μs). It is less sensitive immediately after shock heating and towards the end of the decay, when the decay curve may be approximated to a straight line.

FIGURE 4.8 SENSITIVITY OF 762nm KINETIC MODEL WITH RESPECT TO ^{762}K

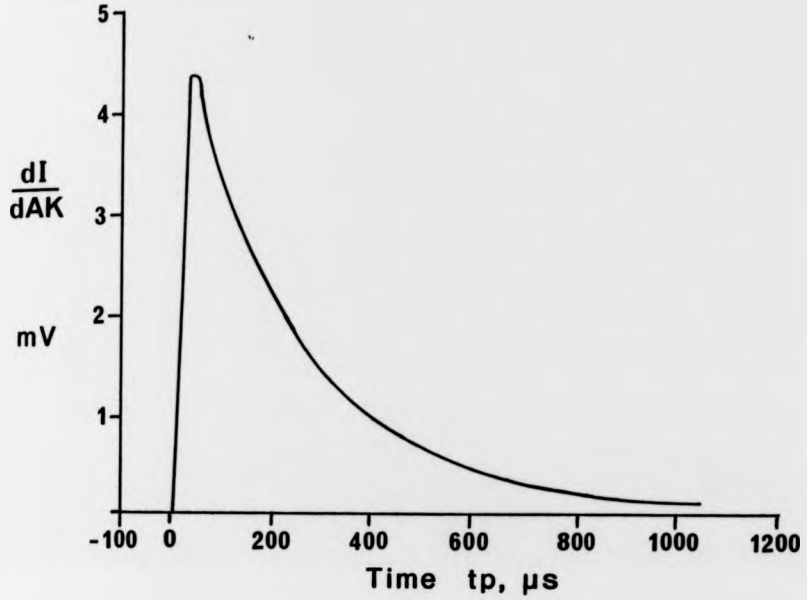

FIGURE 4.9 SENSITIVITY OF 762nm KINETIC MODEL WITH RESPECT TO SIGMA DECAY CONSTANT

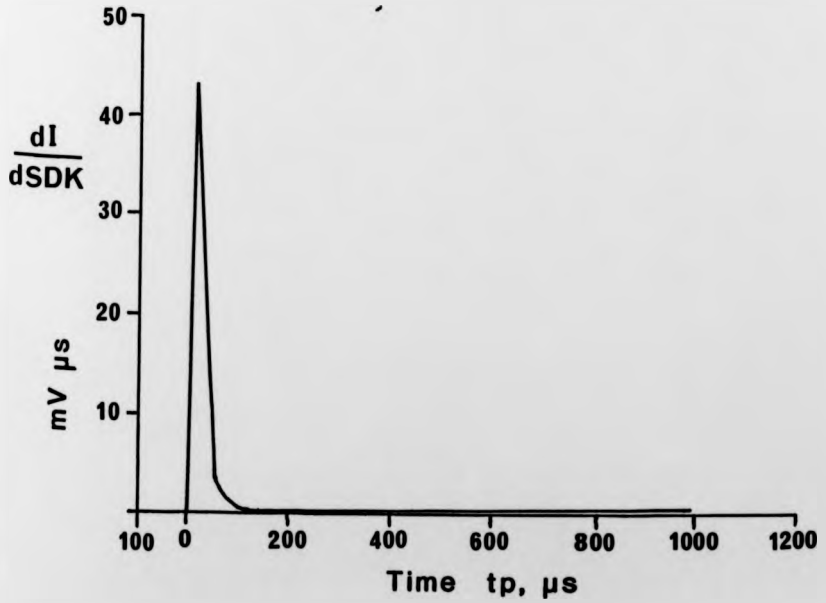

FIGURE 4.10 SENSITIVITY OF 762nm KINETIC MODEL WITH RESPECT TO DELTA DECAY INCREMENT

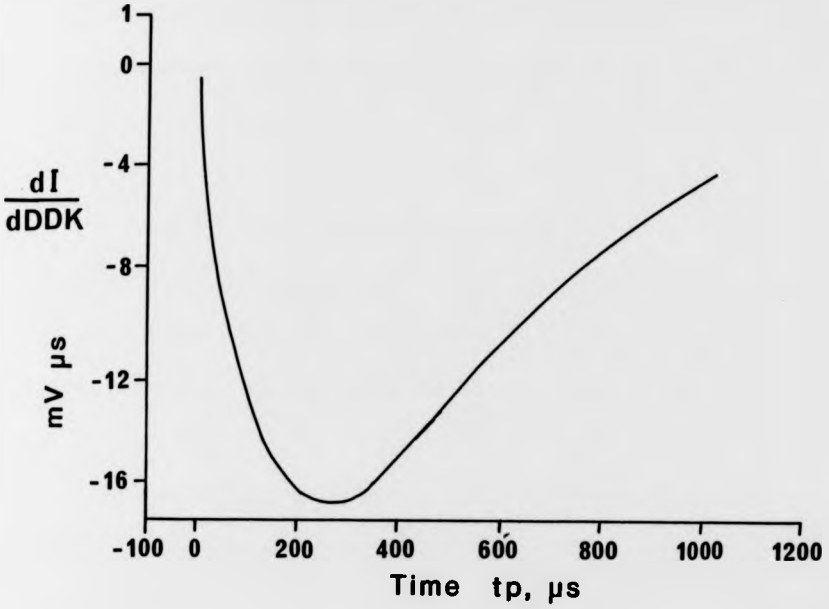

FIGURE 4.11 SENSITIVITY OF 762nm KINETIC MODEL WITH RESPECT TO ROOM TEMPERATURE DECAY

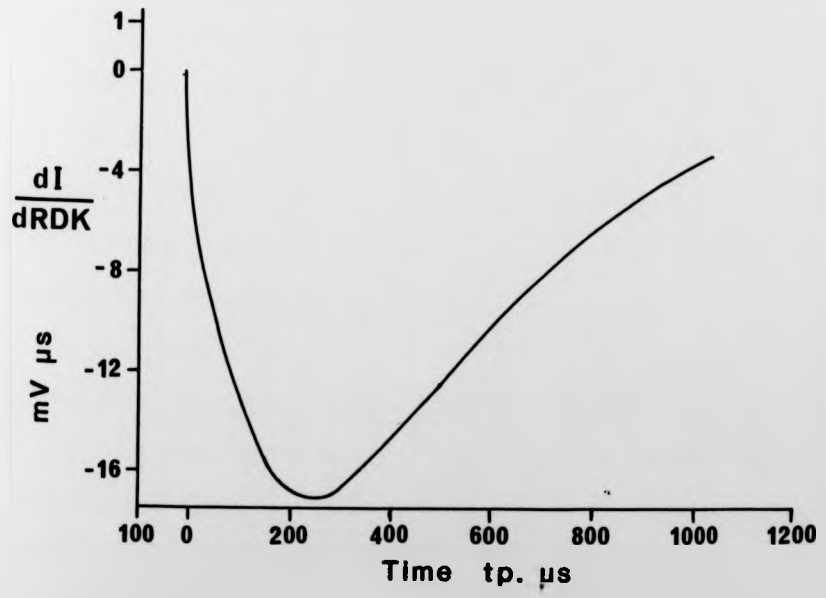

Figure 4.11 shows the sensitivity of the model with respect to the room temperature decay constant. The pattern is the same as that for the sensitivity with respect to the increment in the $O_2(a^1\Delta_g)$ decay constant at high temperature, for exactly the same reasons.

Figure 4.12 shows the sensitivity of the model with respect to the integration time, t_s. As with the $O_2(a^1\Delta_g)$ kinetic model, the sensitivity maximum lies immediately after the arrival of the shock front, when the most dramatic changes in the emission intensity take place.

From these figures it may be deduced that the sensitivity of the $O_2(b^1\Sigma^+_g)$ kinetic model with respect to the decay constants for $O_2(b^1\Sigma^+_g)$ and $O_2(a^1\Delta_g)$ is well separated in time; errors in one constant should therefore, have very little influence upon the evaluation of the other. The sensitivity of the model with respect to the room temperature and high temperature decay of $O_2(a^1\Delta_g)$ may be superimposed; one will therefore, have great influence upon the other. This is not suprising since $2k_d^{m'}[M']$ is obtained by subtracting a_t from the observed high temperature decay. It does, however, reinforce the fact that a_1 must be an accurately measured experimental quantity.

The region which best defines the rate constants for the deactivation of $O_2(a^1\Delta_g)$ is also well separated from the region in which the model is most sensitive to the integration time; hence errors in t_s will have very little effect upon $k_d^{m'}$.

The regions of the model's sensitivity to the integration time and the $O_2(b^1\Sigma^+_g)$ decay constant coincide, particularly when the relaxation time is short. Thus, these two parameters will have great influence upon each other. This has been observed experimentally as well as deduced from the sensitivity analysis. Clearly, it would

FIGURE 4.12 SENSITIVITY OF 762nm KINETIC MODEL WITH RESPECT TO INTEGRATION TIME

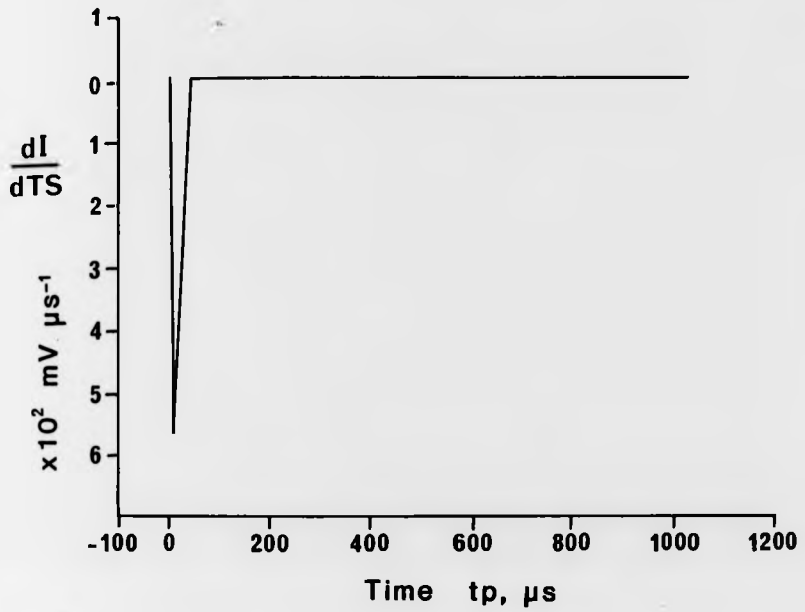

be useful to have an accurate and independently measured value for t_s.

It was for this reason that the calculation of integration times, described in Chapter 2, was carried out. These values (table 2.2) have been used as fixed parameters in the analysis of the high temperature data throughout this work.

The model is sensitive to ^{762}K over the whole time axis and overlaps with the regions of greatest sensitivity to t_s, $k_q^{m'}[M']$, $2k_d^{m'}[M']$, and q_t. Since, t_s and q_t are independently calculated and measured quantities respectively, then provided their values are determined accurately, the errors produced from the imprecision of the fitting will involve only $2k_d^{m'}[M']$, $k_q^{m'}[M']$ and ^{762}K. The sensitivity of ^{762}K to the experimental data is smallest (dI/dAK is largest) early in the experiment; therefore, ^{762}K will be better defined when the relaxation time is short. Conversely, the $O_2(b^1\Sigma_g^+)$ decay constant is better defined when the relaxation time is long.

4.5.2 Corrections For $O_2(a^1\Delta_g)$ as a Source of $O_2(b^1\Sigma_g^+)$

In previous studies carried out in this laboratory [72], it was noticed that the deactivation of $O_2(b^1\Sigma_g^+)$ tended to 'fall off' at higher temperatures. After examining the possibility of systematic errors, the possibility of $O_2(a^1\Delta_g)$ becoming a source of $O_2(b^1\Sigma_g^+)$ at high temperatures was examined. This section describes the corrections which would apply if this were the case.

The primary source of $O_2(b^1\Sigma_g^+)$ is the energy pooling reaction (equation 4.2), which is one of the fundamental processes involved in the rate equation for $O_2(b^1\Sigma_g^+)$ and has therefore been accounted for in the derivation of the kinetic models. However, the process described by equation (4.45),

$$O_2(a^1\Delta_g) + M \xrightarrow{k_q^r} O_2(b^1\Sigma^+_g) + M \qquad (4.45)$$

is thought to become significant at high temperatures. Dr P. Borrell has derived the following equations to account for the presence of this reaction in the kinetic scheme. $k_q^{m'}$ as determined from the kinetic model is actually:

$$k_q^{m'} = k_q^f + k_q^r \qquad (4.81)$$

where k_q^f and k_q^r are the forward and reverse rate constants for the collisional deactivation of $O_2(b^1\Sigma^+_g)$ to $O_2(a^1\Delta_g)$. By the principle of microscopic reversibility,

$$k_q^f = k_q^{m'}/(1+0.5\exp(-\Theta/T)) \qquad (4.82)$$

where $\Theta = 7555$ Kelvin.

The factors for the correction of $k_q^{m'}$ to the rate constant for the deactivation of $O_2(b^1\Sigma^+_g)$, k_q^f, are given in table 4.1. Clearly, reaction (4.45) has an insignificant effect upon the value of $k_q^{m'}$ ($k_q^{m'} = k_q^f$) over the temperature range studied in this work (295 to 1200K).

The values obtained for the energy pooling rate constant must also be corrected for the presence of reaction (4.45) in the kinetic scheme. The equation for the correction is:

Table 4.1 Correction Factors for $O_2(b^1\Sigma_g^+)$ Deactivation

Temperature/Kelvin	Correction Factor
295	1.0000
1200	0.9991
2000	0.9887
5000	0.9006

$$k_p' = k_p - (k_q^{m'}[M']/((1+2\exp(\theta/T))[O_2(a^1\Delta_g)])) \quad (4.83)$$

where k_p' is the corrected value of the experimentally obtained energy pooling constant, k_p. The correction of k_p relies on the magnitude of the deactivation rate constant for $O_2(b^1\Sigma_g^+)$, and upon the mole fraction of $O_2(a^1\Delta_g)$ present ($[O_2(a^1\Delta_g)]/[M']$). Assuming a typical mole fraction of $O_2(a^1\Delta_g)$ to be 0.04, then the correction equation may be evaluated at various temperatures.

(T=295K) $$k_p' = k_p - (9 \times 10^{-11} k_q^{m'}) \quad (4.84)$$

(T=1000K) $$k_p' = k_p - (6 \times 10^{-3} k_q^{m'}) \quad (4.85)$$

(T=1200K) $$k_p' = k_p - (2 \times 10^{-2} k_q^{m'}) \quad (4.86)$$

Typical values of the effective deactivation rate constant for the test gas mixture range from 1×10^5 to 1×10^6 mol^{-1} dm^3 s^{-1}. The error in k_p, even for the most efficient test gas mixtures studied is negligible at room temperature but begins to become significant at 1000K where the error is approximately 6% in the worst cases. At 1200K, which is the high temperature limit of this work, the error may be as much as 20%. Errors of this magnitude are clearly important; therefore a routine has been added to the computer program for the analysis of $O_2(b^1\Sigma_g^+)$ to allow these errors to be calculated and corrections made.

Since the vast majority of the determinations carried out in this work (over 90%) were at temperatures below 900K where errors in k_p are small, a rigorous test of these corrections has yet to be

carried out with experimental data.

4.5.3 Computer Analysis of $O_2(b^1\Sigma^+_g)$ Kinetic Data

The kinetic model (equation 4.80) has been developed into an interactive computer graphics program by Borrell [61], for use with the GEC 4082 computer using the HP2647A graphics terminal.

The analysis proceeds in the same manner as that for the $O_2(a^1\Delta_g)$ kinetic data, with the exception that there is one more variable parameter, $k_q^{m'}[M']$, involved. The final result yields $k_q^{m'}$, $k_d^{m'}$, t_s and ^{762}K directly from the fitting of the kinetic model to the experimental data. The variable k_p is determined from these rate constants using equation (4.78). The corrections described in section 4.5.2 are then made to the rate constants k_p and $k_q m'$. The rate constant for the deactivation of $O_2(b^1\Sigma^+_g)$ due to the additive, M, alone may be calculated from equation (4.55) by hand.

Figure 4.13 shows the fit obtained with a set of experimental data (Run DSR211B) obtained during the study of the deactivation of $O_2(b^1\Sigma^+_g)$ by nitrogen. The line through the points is the fit obtained using equation (4.80). There is no increase in the deactivation of $O_2(a^1\Delta_g)$, at the high temperature, in this case.

A comparison with figure 4.7 shows that the predicted profile is in agreement with the the experimental data and confirms that the $O_2(b^1\Sigma^+_g)$ kinetic model is a good representation of the physical processes involved.

A detailed description of this program was also given by Pedley [46] and has remained essentially unchanged, except for the addition of the correction routine. Therefore, a description of the workings of the program will not be given here.

FIGURE 4.13

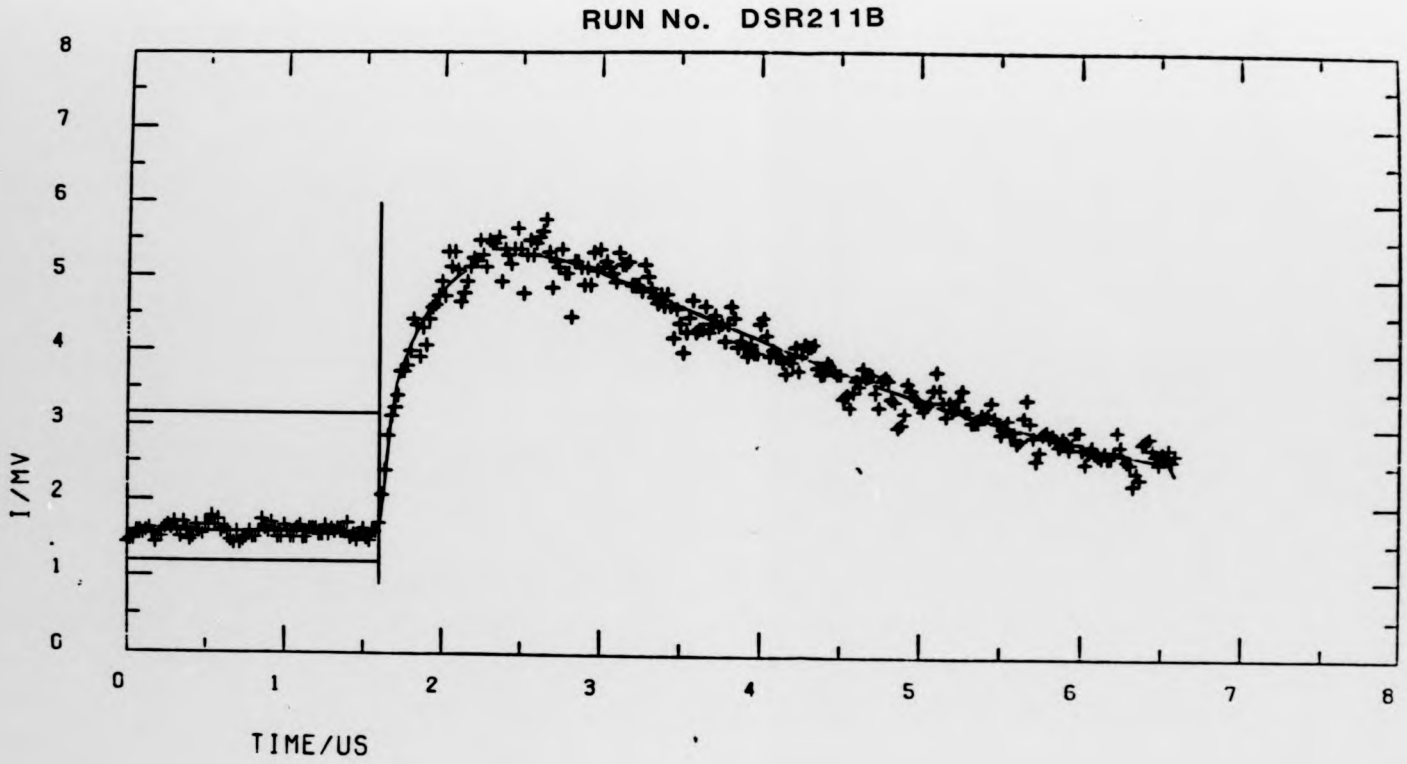
RUN No. DSR211B
I/MV
TIME/US
0
1
2
3
4
5
6
7
8
XAXIS·SCALE = X * (10 **-2)
YAXIS·SCALE = Y * (10 **-3)

THE COLLISIONAL DEACTIVATION OF $O_2(a^1\Delta_g)$

5.1 Introduction

The results of the determination of the temperature dependence of the collisional deactivation of $O_2(a^1\Delta_g)$ by HCl, HBr, H_2 and D_2 are presented here. The chapter begins with the room temperature deactivation of $O_2(a^1\Delta_g)$ by these species and then discusses the high temperature results obtained through shock heating. Arrhenius expressions are obtained for the temperature dependence of the deactivation rate constant$.

During the course of these studies several unexpected emissions were observed. The nature and origin of these emissions is discussed in the final section.

This chapter serves only to present the results and comment upon their validity. A detailed discussion of these results is given in chapter 7.

5.2 Studies of the Collisional Deactivation of $O_2(a^1\Delta_g)$ at 295K

The determination of the room temperature rate constants for the deactivation of $O_2(a^1\Delta_g)$ by HCl, HBr, H_2 and D_2 was carried out by the method described in section 4.2. The decay of $O_2(a^1\Delta_g)$ in pure O_2, along the flow tube, was measured using a movable photomultiplier equipped with either a 634nm or a 762nm filter. A test gas was then introduced into the flow, giving a 1-7% mixture by volume of the additive in pure O_2, and the decay of $O_2(a^1\Delta_g)$ along the flow tube was measured again. A series of such measurements was performed in the pressure range 4-8 torr with linear flow velocities between 1.0 and 2.5 m s^{-1}. The difference in the observed rate constants, $\Delta k'$, gives the pseudo-first order rate constant for the deactivation of $O_2(a^1\Delta_g)$ by M.

$$\Delta k' = k_d^m[M]$$

which, when plotted against the concentration of the additive [M], allows the second order rate constant for the deactivation of $O_2(a^1\Delta_g)$ by M to be evaluated from the gradient.

$$k_d^{HCl} = (8.00 \pm 0.34) \times 10^4 \quad mol^{-1}\ dm^3\ s^{-1}$$

$$k_d^{HBr} = (4.2 \pm 2.8) \times 10^4 \quad mol^{-1}\ dm^3\ s^{-1}$$

$$k_d^{H_2} = (2.22 \pm 0.26) \times 10^4 \quad mol^{-1}\ dm^3\ s^{-1}$$

$$k_d^{D_2} = (2.56 \pm 1.30) \times 10^3 \quad mol^{-1}\ dm^3\ s^{-1}$$

Error limits are 2σ (95% confidence limits).

5.2.1 Deactivation of $O_2(a^1\Delta_g)$ by HCl at 295K

The determination of the room temperature deactivation of $O_2(a^1\Delta_g)$ by HCl was carried out by Boodaghians [44,68]. The result is described here because it is an important part of the temperature dependence study, which was carried out jointly.

Figure 5.1 shows an example (Run R9) of a plot of $0.5\ln(^{634}I/^{634}I_o)$ versus distance along the flow tube, both with and without 5% HCl added. The gradients of the two lines are taken and multiplied by the respective linear flow velocities to give pseudo-first order rate constants for the deactivation of $O_2(a^1\Delta_g)$, both in the presence and absence of 5% HCl. In this case the change in the observed rate constants is quite large (approximately a factor of 2), therefore little scatter is expected in the plot of $\Delta k'$ versus [HCl].

Table 5.1 lists the experimental results and figure 5.2 shows a plot of $\Delta k'$ against [HCl]. The gradient gives the second order rate constant, k_d^{HCl}, for the deactivation of $O_2(a^1\Delta_g)$ by HCl.

$$k_d^{HCl} = (8.00 \pm 0.34) \times 10^4 \text{ mol}^{-1} \text{ dm}^3 \text{ s}^{-1}$$

The error limits are 2σ (95% confidence limits).

The only other result available is shortly to be published by Singh, Bachar and Setser [69], who found:

$$k_d^{HCl} = (2.4 \pm 1.8) \times 10^3 \quad \text{mol}^{-1} \text{ dm}^3 \text{ s}^{-1}$$

They observed non-linear behaviour in the deactivation of $O_2(a^1\Delta_g)$ with HCl concentrations below 1×10^{-5} mol dm^{-3} in an uncoated pyrex reactor but not when the reactor was coated with halocarbon wax.

The determinations carried out here were above

Figure 5.1 Run R7 An example of observed decay gradients of $O_2(a\,^1\Delta g)$

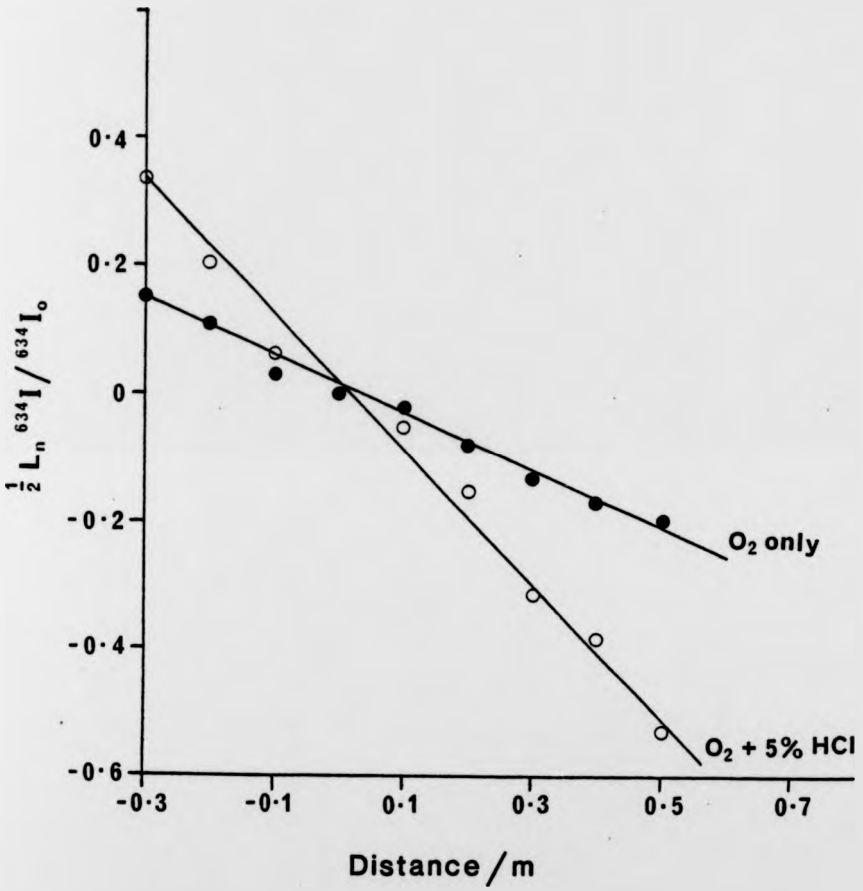

	P_1 /torr	LFV/ms^{-1}	Gradient/m^{-1}	Gradient/s^{-1}	Δk/s^{-1}
O_2 only	5·79	1·72	-0·403	0·694	1·243
O_2 + 5% HCl	5·96	1·76	-0·101	1·937	

Table 5.1 Deactivation of $O_2(a^1\Delta_g)$ by HCl at 295 K

Run No	P_1/torr	$\Delta k'/s^{-1}$	[HCl]/mol dm^{-3}	LFV/ms^{-1}	k_d^{HCl}/mol^{-1} dm^3 s^{-1}
R9	5.79			1.72	
RA9	5.96	1.25	1.63×10^{-5}	1.76	7.67×10^4
R10	5.09			1.96	
RA10	5.22	1.11	1.43×10^{-5}	2.01	7.76×10^4
R11	6.45			1.54	
RA11	6.62	1.52	1.81×10^{-5}	1.58	8.40×10^4
R12	4.05			2.46	
RA12	4.14	0.92	1.13×10^{-5}	2.54	8.85×10^4

Figure 5.2 Deactivation of $O_2(a\,^1\Delta g)$ by HCl at room temperature

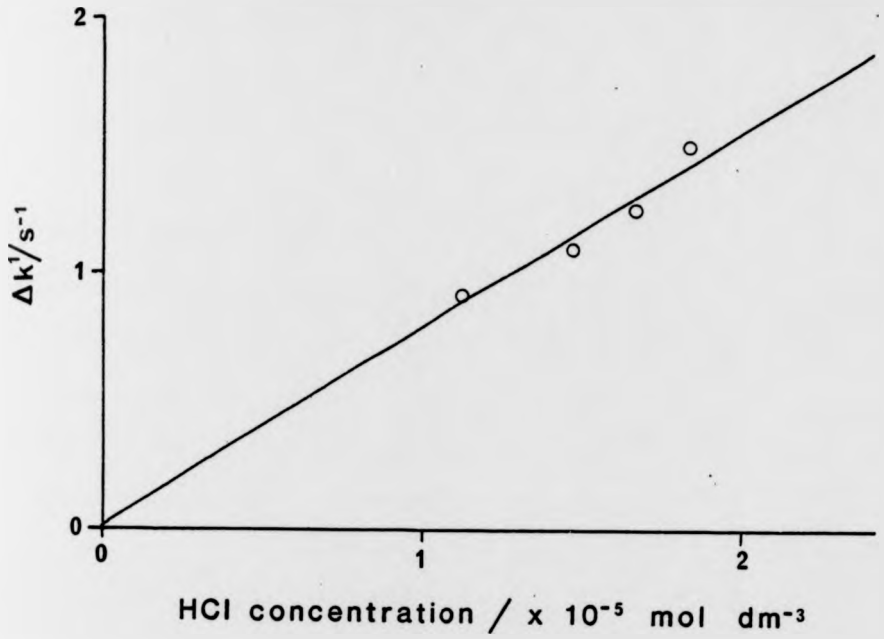

Figure 5.3 Deactivation of $O_2(a\,^1\Delta g)$ by HBr at room temperature

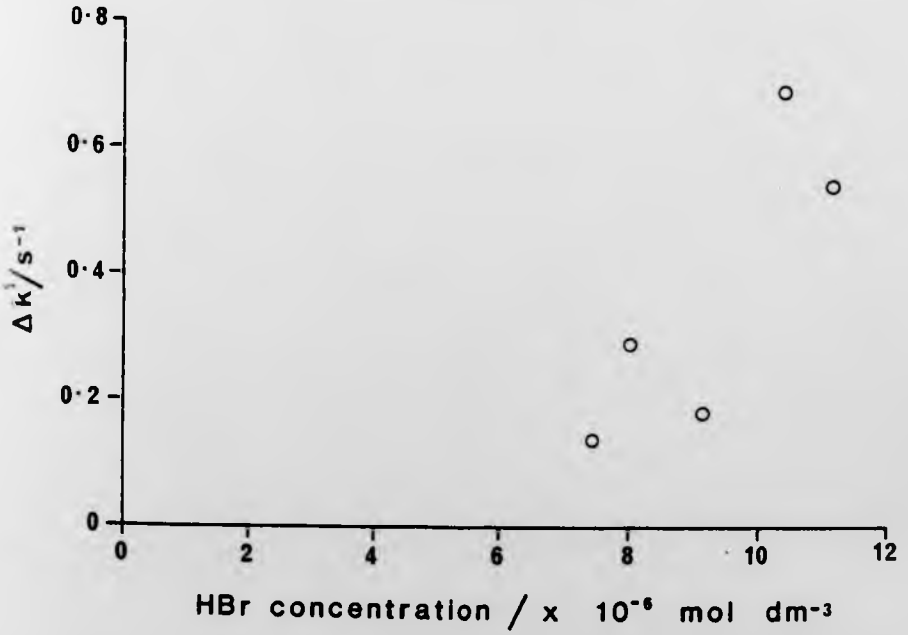

1×10^{-5} mol dm^{-3}. The plot is linear and has an intercept at the origin (0,0), which indicates that there is no wall modification in this case. During the course of the high temperature experiments the room temperature decay along the tube was measured with HCl present many times. There was no observable difference between the decay gradients measured immediately after cleaning the flow tube and those measured after several days of experiments, which suggests that there was no additional deactivation due to a build up of HCl on the walls of our apparatus. In the light of these observations, the rate constant for the collisional deactivation of $O_2(a^1\Delta_g)$ by HCl determined in this work is preferred.

5.2.2 Deactivation of $O_2(a^1\Delta_g)$ by HBr at 295K

The results of the determination of the room temperature deactivation of $O_2(a^1\Delta_g)$ by HBr failed to give either a straight line or a recognisable curve when $\Delta k'$ was plotted against [HBr]. This was attributed to a change in the wall reaction. This change, however, failed to stabilize itself sufficiently to reduce the scatter in the plot, as long as 60 minutes after the addition of HBr to the flow.

When the system was not allowed to settle and the decay gradient was recorded immediately after the addition of HBr, in order to minimize the change in the wall reaction, the scatter was improved but not sufficiently to give a straight line (figure 5.3). Assuming that the change in the wall reaction under these conditions is zero, k_d^{HBr} was estimated from single point determinations, (table 5.2). The average value of these individual determinations was

Table 5.2 Deactivation of $O_2(a^1\Delta_g)$ by HBr at 295 K

Run No	P_1/torr	$\Delta k'/s^{-1}$	[HBr]/mol dm^{-3}	LFV/ms^{-1}	k_d^{HBr}/mol^{-1} dm^3 s^{-1}
D1	3.96			2.60	
DA1	4.04	0.54	1.11×10^{-5}	2.68	4.9×10^4
D2	4.37			2.40	
DA2	4.50	0.14	7.40×10^{-6}	2.41	1.9×10^4
D3	4.70			2.23	
DA3	4.87	0.29	8.00×10^{-6}	2.24	3.6×10^4
D4	5.36			1.96	
DA4	5.53	0.18	9.10×10^{-6}	1.96	2.0×10^4
D5	3.67			2.81	
DA5	3.80	0.69	1.04×10^{-5}	2.86	6.6×10^4

$$k_d^{HBr} = (4.2 \pm 2.8) \times 10^4 \quad mol^{-1}\ dm^3\ s^{-1}$$

When cleaning the flow tube an acidic vapour was observed, presumably released from the walls of the flow tube, which is further evidence for adsorption of HBr onto the tube walls.

Again the only other value available is shortly to be published by Singh, Bachar, and Setser [69].

$$k_d^{HBr} = (4.8 \pm 2.4) \times 10^3 \quad mol^{-1}\ dm^3\ s^{-1}$$

As with HCl, they observed that the experimental pseudo-first order rate constant, obtained using an uncoated pyrex tube, was far from linear at HBr concentrations below 1×10^{-5} mol dm^{-3}, which includes the range studied in this experiment. They solved the problem by coating their reactor with a halocarbon wax which should not permit any wall modification. The walls of the apparatus used in this work were not coated because of the practical difficulties involved in producing and maintaining a homogeneous coating on a 5 m long, 50.8 mm diameter tube which must remain horizontal and is used as the driven section of a shock tube.

In view of the difficulty experienced in obtaining the rate constant, k_d^{HBr}, in this work, the result of Singh, Bachar and Setser is preferred. Since there is a large difference in the values for k_d^{HBr} obtained in the two laboratories, it is thought worthwhile to record here the value obtained for k_d^{HBr} in this laboratory.

5.2.3 Deactivation of $O_2(a^1\Delta_g)$ by H_2 at 295K

The results (table 5.3) of the determination of the room temperature deactivation of $O_2(a^1\Delta_g)$ by H_2 gave a good straight line

Table 5.3 Deactivation of $O_2(a^1\Delta_g)$ by H_2 at 295 K

Run No	P_1/torr	$\Delta k'/s^{-1}$	$[H_2]$/mol dm^{-3}	LFV/ms^{-1}	$k_d^{H_2}$/mol^{-1} dm^3 s^{-1}
D6	5.65			1.83	
DA6	5.69	0.095	4.63×10^{-6}	1.84	2.06×10^4
D7	4.74			2.22	
DA7	4.79	0.089	3.83×10^{-6}	2.22	2.32×10^4
D8	4.29			2.45	
DA8	4.33	0.072	3.49×10^{-6}	2.46	2.06×10^4
D9	4.21			2.49	
DA9	4.25	0.129	5.46×10^{-6}	2.53	2.35×10^4
D10	4.21			2.49	
DA10	4.25	0.162	6.73×10^{-6}	2.54	2.41×10^4
D11	4.74			2.22	
DA11	4.79	0.136	6.12×10^{-6}	2.24	2.23×10^4
D12	4.74			2.22	
DA12	4.79	0.167	7.56×10^{-6}	2.25	2.21×10^4
D13	5.16			2.03	
DA13	5.24	0.155	6.69×10^{-6}	2.05	2.32×10^4
D14	5.16			2.03	
DA14	5.24	0.165	8.27×10^{-6}	2.06	2.00×10^4

(figure 5.4) with an intercept at 0.01 s^{-1}, indicating that there is no significant change in the wall reaction. The gradient of the line gives the second order rate constant:

$$k_d^{H_2} = (2.22 \pm 0.26) \times 10^4 \text{ mol}^{-1} \text{ dm}^3 \text{ s}^{-1}$$

The error limits are 2σ (95% confidence limits).

The result is approximately a factor of 10 higher than those of Findlay and Snelling [70] and Becker and co-workers [71]. Findlay and Snelling used a flash photolysis technique which involved subtracting values for the deactivation of $O_2(a^1\Delta_g)$ by O_2 alone. Their value for $k_d^{O_2}$ was 50% higher than the currently preferred value. This would, therefore, clearly lead to a lower value of $k_d^{H_2}$.

Becker and co-workers experienced some difficulty in obtaining values of k_d^m for a variety of deactivators [84]. In some cases, the deactivation of $O_2(a^1\Delta_g)$ actually reduced upon the addition of the test gas. They attributed this phenomenon to wall effects and the slowing down of diffusion.

The experiments were repeated but gave the same result, within experimental error. Billington [83] working with a 2.5cm diameter discharge flow tube obtained:

$$k_d^{H_2} = 2.5 \times 10^4 \text{ mol}^{-1} \text{ dm}^3 \text{ s}^{-1}$$

with no indication of a change in the wall deactivation rate constant. This agrees well with the value reported in this work, which is preferred to that of other workers.

(figure 5.4) with an intercept at 0.01 s^{-1}, indicating that there is no significant change in the wall reaction. The gradient of the line gives the second order rate constant:

$$k_d^{H_2} = (2.22 \pm 0.26) \times 10^4 \text{ mol}^{-1} \text{ dm}^3 \text{ s}^{-1}$$

The error limits are 2σ (95% confidence limits).

The result is approximately a factor of 10 higher than those of Findlay and Snelling [70] and Becker and co-workers [71]. Findlay and Snelling used a flash photolysis technique which involved subtracting values for the deactivation of $O_2(a^1\Delta_g)$ by O_2 alone. Their value for $k_d^{O_2}$ was 50% higher than the currently preferred value. This would, therefore, clearly lead to a lower value of $k_d^{H_2}$.

Becker and co-workers experienced some difficulty in obtaining values of k_d^m for a variety of deactivators [84]. In some cases, the deactivation of $O_2(a^1\Delta_g)$ actually reduced upon the addition of the test gas. They attributed this phenomenon to wall effects and the slowing down of diffusion.

The experiments were repeated but gave the same result, within experimental error. Billington [83] working with a 2.5cm diameter discharge flow tube obtained:

$$k_d^{H_2} = 2.5 \times 10^4 \text{ mol}^{-1} \text{ dm}^3 \text{ s}^{-1}$$

with no indication of a change in the wall deactivation rate constant. This agrees well with the value reported in this work, which is preferred to that of other workers.

Figure 5.4 Deactivation of $O_2(a\ ^1\Delta g)$ by H_2 at room temperature

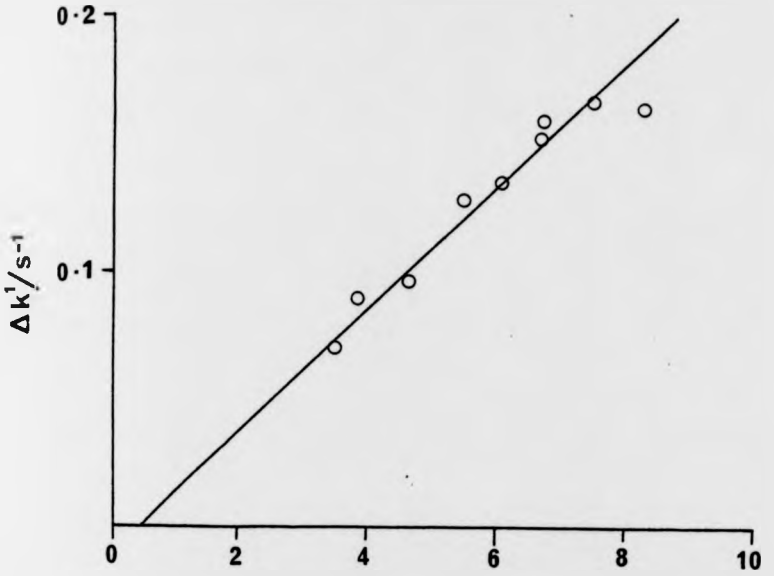

Figure 5.5 Deactivation of $O_2(a\ ^1\Delta g)$ by D_2 at room temperature

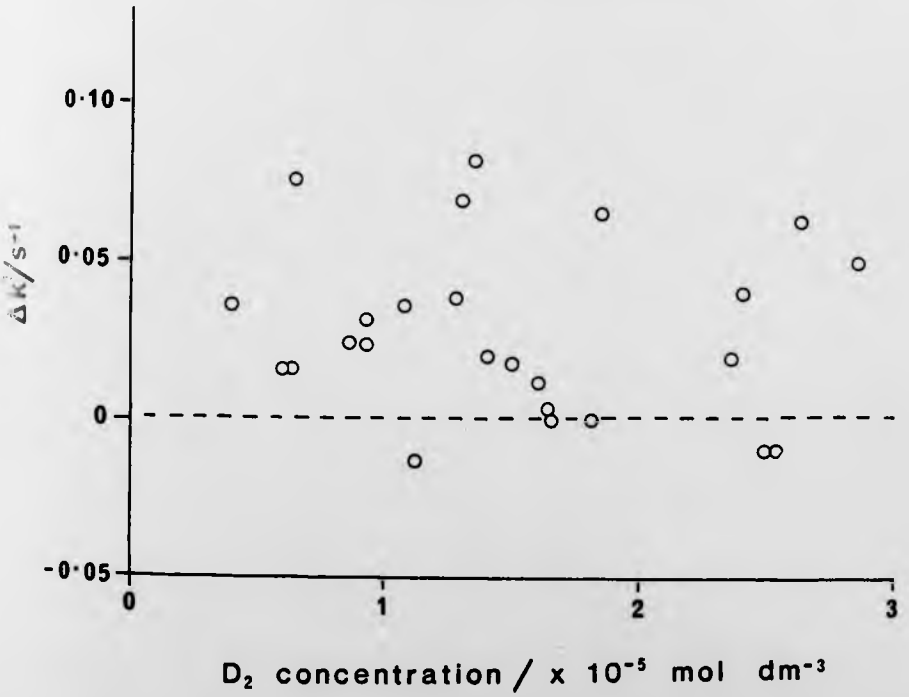

5.2.4 Deactivation of $O_2(a^1\Delta_g)$ by D_2 at 295K

The results of the room temperature deactivation of $O_2(a^1\Delta_g)$ by D_2 (table 5.4) are very scattered and did not give a straight line plot, (figure 5.5). It is thought unlikely that this is due to wall modification by D_2, which is a non-polar species, particularly since no wall deactivation changes were observed during the study of the deactivation of $O_2(a^1\Delta_g)$ by H_2. The reason for the scatter is more likely to be that the small difference (less than 5%) in the measured gradients, as shown in figure 5.6, produces quite large errors in an individual $\Delta k'$ value.

For this reason, a large number of determinations were carried out. The value of $k_d^{D_2}$ from each experiment was evaluated and the mean value of 28 separate experiments calculated. The standard error of the mean was calculated according to the formula:

$$\sigma = \pm(\Sigma(\nu)/(n^2-n))^{1/2} \qquad (5.1)$$

where ν is the deviation from the average value ($\nu_i = k_i - k_{av}$) and n is the number of points.

The value for the room temperature deactivation of $O_2(a^1\Delta_g)$ by D_2 is thus:

$$k_d^{D_2} = (2.56 \pm 1.30) \times 10^3 \quad mol^{-1}\ dm^3\ s^{-1}$$

No values for this constant were found in the literature, although it does compare well with the recent work of Billington [83] who obtained:

$$k_d^{D_2} = 2.5 \times 10^3 \text{ mol}^{-1} \text{ dm}^3 \text{ s}^{-1}$$

Figure 5.6 Run D17 An example of observed decay gradients of $O_2(a\ ^1\Delta g)$

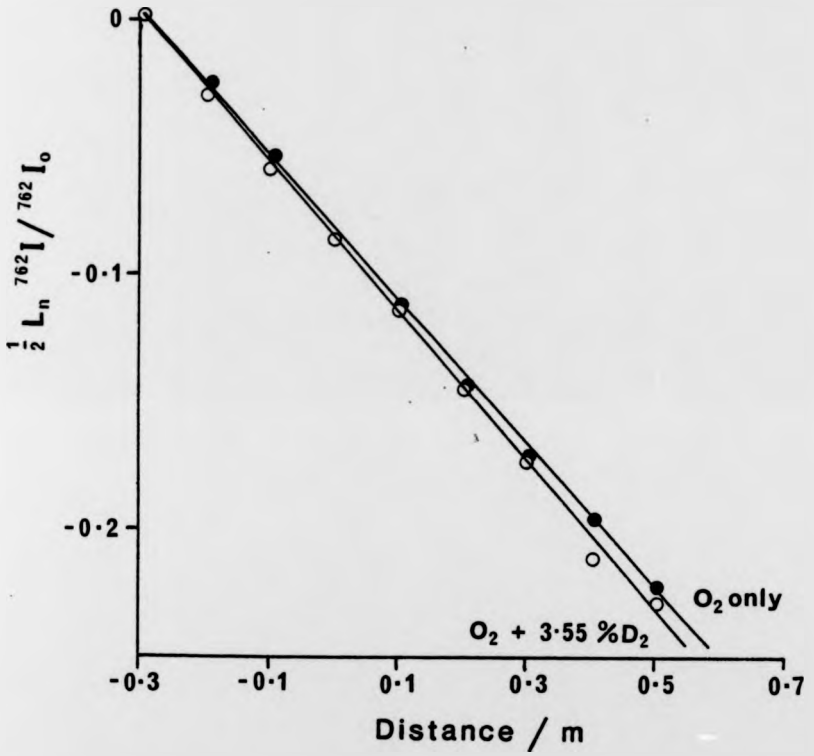

	P_1/torr	LFV/ms^{-1}	Gradient/m^{-1}	Gradient/s^{-1}	Δk^1/s^{-1}
O_2 only	4·87	2·16	-0·283	-0·610	0·034
O_2 + 3·55%D_2	4·95	2·20	-0·293	-0·644	

Table 5.4 Deactivation of $O_2(a^1\Delta_g)$ by D_2 at 295 K

Run No	P_1/torr	$\Delta k'/s^{-1}$	$[D_2]$/mol dm^{-3}	LFV/ms^{-1}	$k_d^{D_2}$/mol^{-1} dm^3 s^{-1}
D15	4.62			2.27	
DA15	4.66	0.035	3.76×10^{-6}	2.29	9.33×10^3
D16	4.87			2.16	
DA16	4.91	0.015	6.29×10^{-6}	2.19	2.40×10^3
D17	4.87			2.16	
DA17	4.95	0.034	9.60×10^{-6}	2.20	3.50×10^3
D18	5.36			1.96	
DA18	5.49	0.026	8.63×10^{-6}	1.97	2.99×10^3
D19	5.36			1.96	
DA19	5.53	0.037	1.29×10^{-5}	1.98	2.89×10^3
D20	5.82			1.80	
DA20	5.90	0.025	9.28×10^{-6}	1.83	2.74×10^3
D21	5.82			1.80	
DA21	5.94	0.021	1.39×10^{-5}	1.85	2.54
D22	6.93			1.52	
DA22	7.10	0.068	1.34×10^{-5}	1.53	5.10×10^3
D23	7.80			1.35	
DA23	8.00	0.018	1.51×10^{-5}	1.36	1.17×10^3
D24	7.76			1.35	
DA24	8.09	-0.010	2.49×10^{-5}	1.38	-3.82×10^2

Table 5.4 continued

Run No	P_1/torr	$\Delta k'/s^{-1}$	$[D_2]$/mol dm^{-3}	LFV/ms^{-1}	$k_d^{D_2}$/mol^{-1} dm^3 s^{-1}
D25	5.36			1.96	
DA25	5.57	-0.007	1.87×10^{-5}	2.01	-3.58×10^{2}
D26	6.02			1.74	
DA26	6.19	0.083	1.36×10^{-5}	1.77	6.12×10^{3}
D27	6.02			1.74	
DA27	6.29	0.066	1.93×10^{-5}	1.77	3.40×10^{3}
D28	6.02			1.74	
DA28	6.31	0.039	2.40×10^{-5}	1.79	1.63×10^{3}
D29	6.35			1.65	
DA29	6.44	0.079	5.59×10^{-6}	1.66	1.40×10^{4}
D30	6.35			1.65	
DA30	6.52	0.039	1.08×10^{-5}	1.66	3.62×10^{3}
D31	6.02			1.74	
DA31	6.35	0.046	2.85×10^{-5}	1.80	1.93×10^{3}
D32	6.35			1.65	
DA32	6.56	0.010	1.60×10^{-5}	1.68	6.44×10^{2}
D33	6.35			1.65	
DA33	6.64	0.061	2.62×10^{-5}	1.70	2.32×10^{3}
D34	6.85			1.53	
DA34	6.93	0.016	6.02×10^{-6}	1.54	2.72×10^{3}
D35	6.85			1.53	
DA35	7.01	-0.011	1.16×10^{-5}	1.54	-9.60×10^{2}

Table 5.4 continued

Run No	P_1/torr	$\Delta k'/s^{-1}$	$[D_2]$/mol dm^{-3}	LFV/ms^{-1}	$k_d^{D_2}$/mol^{-1} dm^3 s^{-1}
D36	6.85			1.53	
DA36	7.05	0.004	1.68×10^{-5}	1.56	2.44×10^{2}
D37	6.85			1.53	
DA37	7.14	0.019	2.35×10^{-5}	1.56	8.21×10^{2}
D38	5.90			1.78	
DA38	6.11	0.001	1.71×10^{-5}	1.83	$7.6 \times 10'$
D39	5.90			1.78	
DA39	6.19	-0.013	2.43×10^{-5}	1.83	-5.31×10^{2}
D40	5.90			1.78	
DA40	6.27	-0.026	3.34×10^{-5}	1.85	-7.81×10^{2}
D41	5.90			1.78	
DA41	6.31	-0.020	3.52×10^{-5}	1.85	-5.80×10^{2}

5.3 High Temperature Studies of the Collisional Deactivation of $O_2(a^1\Delta_g)$

The determination of the rate constants for the deactivation of $O_2(a^1\Delta_g)$ at high temperature by each additive was carried out by the method described in section 4.3. The rate constants for the deactivation of $O_2(a^1\Delta_g)$ by HCl, H_2 and D_2 were measured between 500 and 1200 Kelvin. It was not possible to carry out high temperature studies of the deactivation of $O_2(a^1\Delta_g)$ by HBr, since no post-shock signal was obtained.

In the studies with the other three additives, experiments were performed with mixtures containing between 0.5 and 7.0 percent of the additive. The overall volume flow rate at s.t.p. was 28.0 $cm^3\ s^{-1}$, at a total pressure of approximately 6 torr, giving a linear flow velocity of approximately 1.6 $m\ s^{-1}$. Before shock heating, the pre-shock decay of $O_2(a^1\Delta_g)$ along the flow tube was measured using a movable photomultiplier unit.

The following Arrhenius expressions were obtained for the temperature dependence of the deactivation of $O_2(a^1\Delta_g)$.

$$k_d^{HCl} = (2.75\pm1.70) \times 10^7 \exp[-(1750\pm190)/T]\ mol^{-1}\ dm^3\ s^{-1}$$

$$k_d^{H_2} = (1.32\pm1.08) \times 10^8 \exp[-(2600\pm180)/T]\ mol^{-1}\ dm^3\ s^{-1}$$

$$k_d^{D_2} = (2.75\pm0.75) \times 10^7 \exp[-(2740\pm90\ )/T]\ mol^{-1}\ dm^3\ s^{-1}$$

5.3.1 Deactivation of $O_2(a^1\Delta_g)$ by HBr at High Temperatures

The attempt to study the deactivation of $O_2(a^1\Delta_g)$ by HBr at high temperatures was unsuccessful. No recognisable post-shock signal could be seen in the very noisy traces which were recorded. The

monitoring system was checked by shock heating pure oxygen to approximately the same temperature as the HBr/O_2 mixtures. This produced traces which showed that the monitoring apparatus was working correctly. The lack of signal was, therefore, not due to instrument failure and must have a chemical or physical explanation.

After several attempts to record high temperature HBr/O_2 data, the flow tube became coated with a brown deposit thought to be bromine. Such evidence of a chemical reaction suggests that the explanation for the lack of signal might involve an extremely rapid chemical reaction which removes $O_2(a^1\Delta_g)$.

5.3.2 Deactivation of $O_2(a^1\Delta_g)$ by HCl at High Temperatures

This experimental work was carried out in collaboration with Boodaghians [44]. However, the data have been reanalysed here, using calculated integration times from table 2.3.

The results of the analysis are given in table 5.5, and the input parameters for each run are listed in Appendix 3. Figure 5.7 shows the temperature dependence of k_d^{HCl}. Since the temperature dependence is positive, an Arrhenius plot was made (figure 5.8). The high temperature values are extrapolated to the room temperature value, determined in section 5.2.1. The Arrhenius equation obtained between 295 and 1180K, by least squares analysis is:

$$k_d^{HCl} = (2.75 \pm 1.70) \times 10^7 \exp[-(1750 \pm 190)/T] \text{ mol}^{-1} \text{ dm}^3 \text{ s}^{-1}$$

The equation predicts an activation energy of (14.5 ± 1.7) kJ mol^{-1}.

This analysis agrees well with the previous analysis by Boodaghians, in which the integration time remained a dependent variable in the fitting of the 634nm Kinetic Model (equation 4.35).

Table 5.5 High Temperature Deactivation of $O_2(a^1\Delta_g)$ by HCl

HCl %	Run No	T_2 Kelvin	^{634}K	k_d^{HCl} x 10^6 mol^{-1} dm^3 s^{-1}	log k_d^{HCl}
3.0	R347	599	0.92	1.95	6.29
3.0	R348	630	0.86	1.87	6.27
3.0	R346	705	0.98	2.78	7.01
3.0	R345	707	0.91	3.22	6.45
3.0	R344	725	0.91	1.98	6.51
3.0	R343	789	1.05	4.05	6.61
3.0	R341	838	1.09	3.03	6.48
3.0	R340	893	0.84	2.08	6.32
3.0	R339	964	1.22	9.09	7.00
3.0	R342	1038	1.28	3.65	6.56
5.0	R334	725	1.26	2.86	6.46
5.0	R350	735	0.95	1.13	6.50
5.0	R332	825	1.08	5.41	6.73
5.0	R330	891	0.99	3.88	6.59
5.0	R331	944	1.18	3.49	6.54
5.0	R355	1021	1.34	5.32	6.73
5.0	R353	1032	1.29	2.88	6.46
5.0	R352	1046	1.27	4.36	6.40
5.0	R356	1112	1.36	5.40	6.73
5.0	R354	1172	1.31	5.90	6.77
7.0	R364	605	1.03	2.52	6.40
7.0	R363	683	1.03	1.88	6.27
7.0	R362	701	1.00	2.56	6.40

Figure 5.7 Rate constants for the deactivation of $O_2(a\ ^1\Delta g)$ by HCl

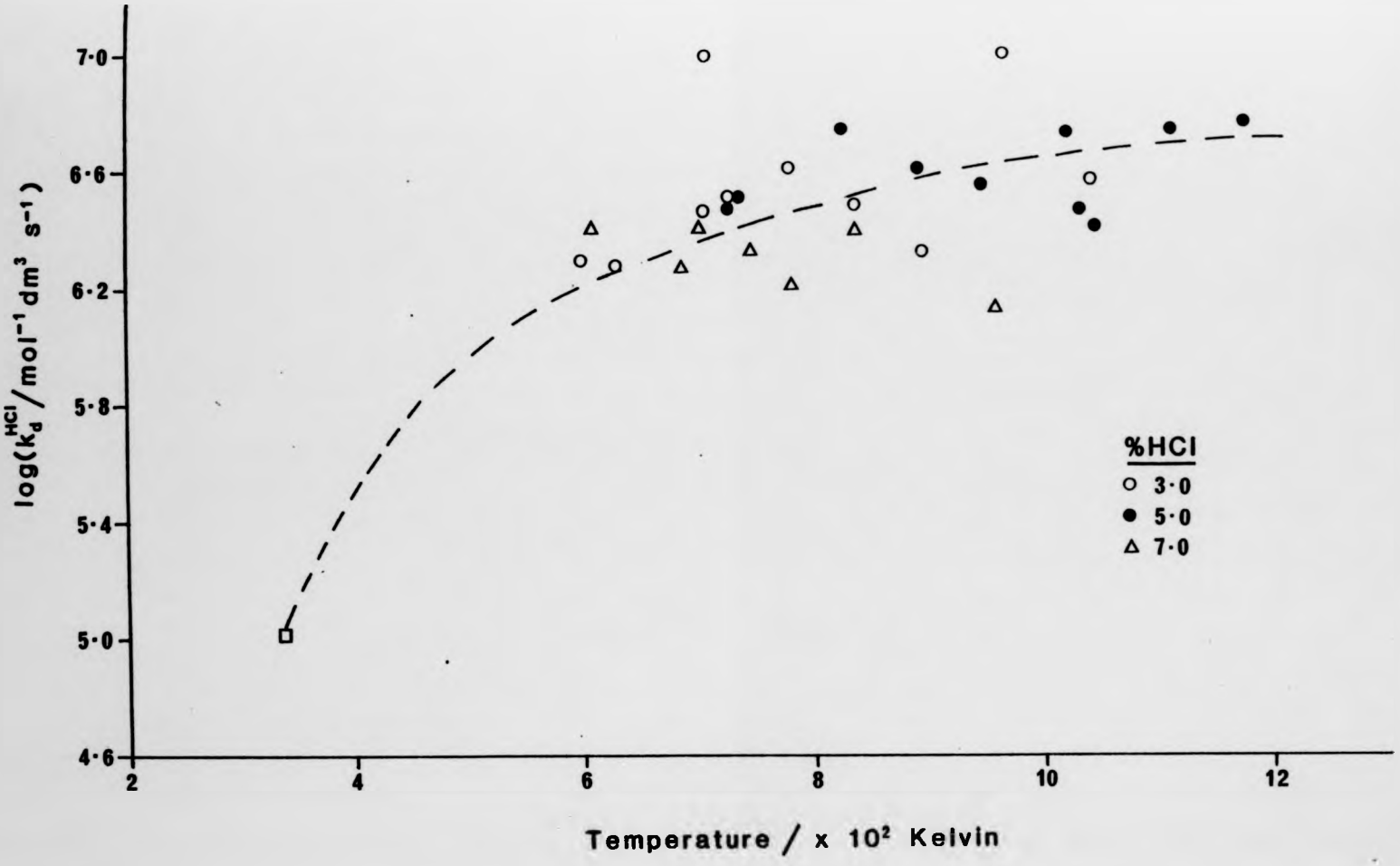

Figure 5.8 Arrhenius plot of the rate constants for the deactivation of $O_2(a\ ^1\Delta g)$ by HCl

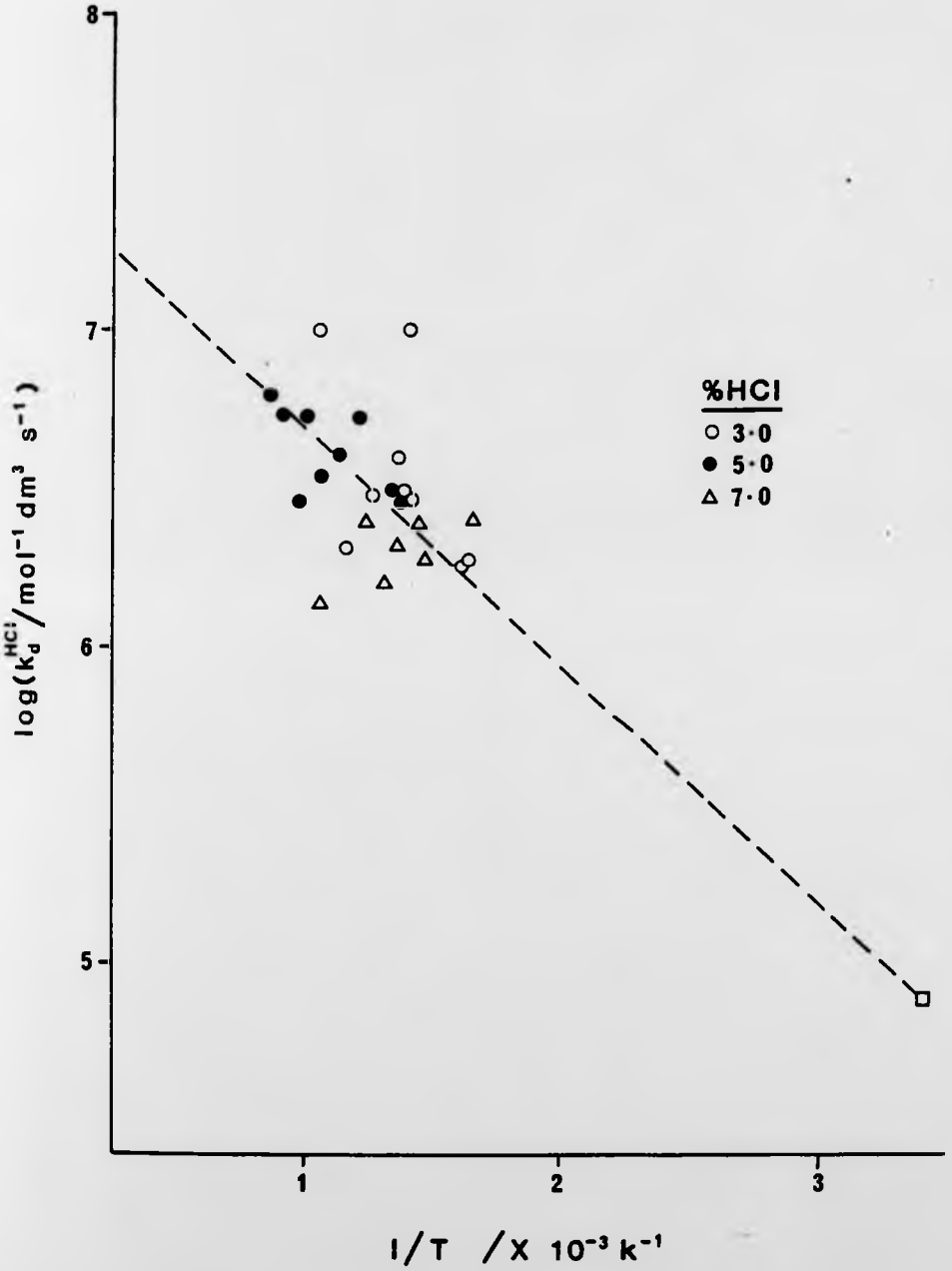

Boodaghians obtained:

$$k_d^{HCl} = (2.34 \pm 1.0) \times 10^7 \exp[-(1660 \pm 180)/T] \text{ mol}^{-1} \text{ dm}^3 \text{ s}^{-1}$$

It was hoped that the scatter would be reduced by reanalysis with a fixed t_s, but in fact, no improvement was observed. Subsequently, sensitivity analysis (section 4.3.1) showed that little change in the results could be expected through fixing t_s.

The scatter is typical of shock tube measurements, in which the errors are associated with the bursting of the diaphragm and the establishment of the shock front. Since HCl is an efficient deactivator of $O_2(a^1\Delta_g)$, a low signal to noise ratio is observed under the pre-shock conditions. Small absolute errors in the measurement of the pre-shock glow will lead to large relative errors, particularly when it is used to predict the enhanced signal under post-shock conditions. This will clearly increase the degree of scatter in this case.

5.3.3 Deactivation of $O_2(a^1\Delta_g)$ by H_2 at High Temperature

A series of determinations was carried out on mixtures containing 0.5 and 1.0 percent H_2 in pure oxygen. The results of the analysis are given in table 5.6. The input parameters for each run are given in Appendix 4. Figure 5.9 shows an increase in $k_d^{H_2}$ with temperature.

At approximately 850K, an additional emission is seen at 634nm, in the later part of the trace (figure 5.16), which allows the analysis of only the first part of the data recorded. The time to the beginning of the additional emission shortened with temperature so that above 1000K, it was not possible to analyse the data at all, as

Figure 5.9 Rate constants for the deactivation of $O_2(a\ ^1\Delta g)$ by H_2

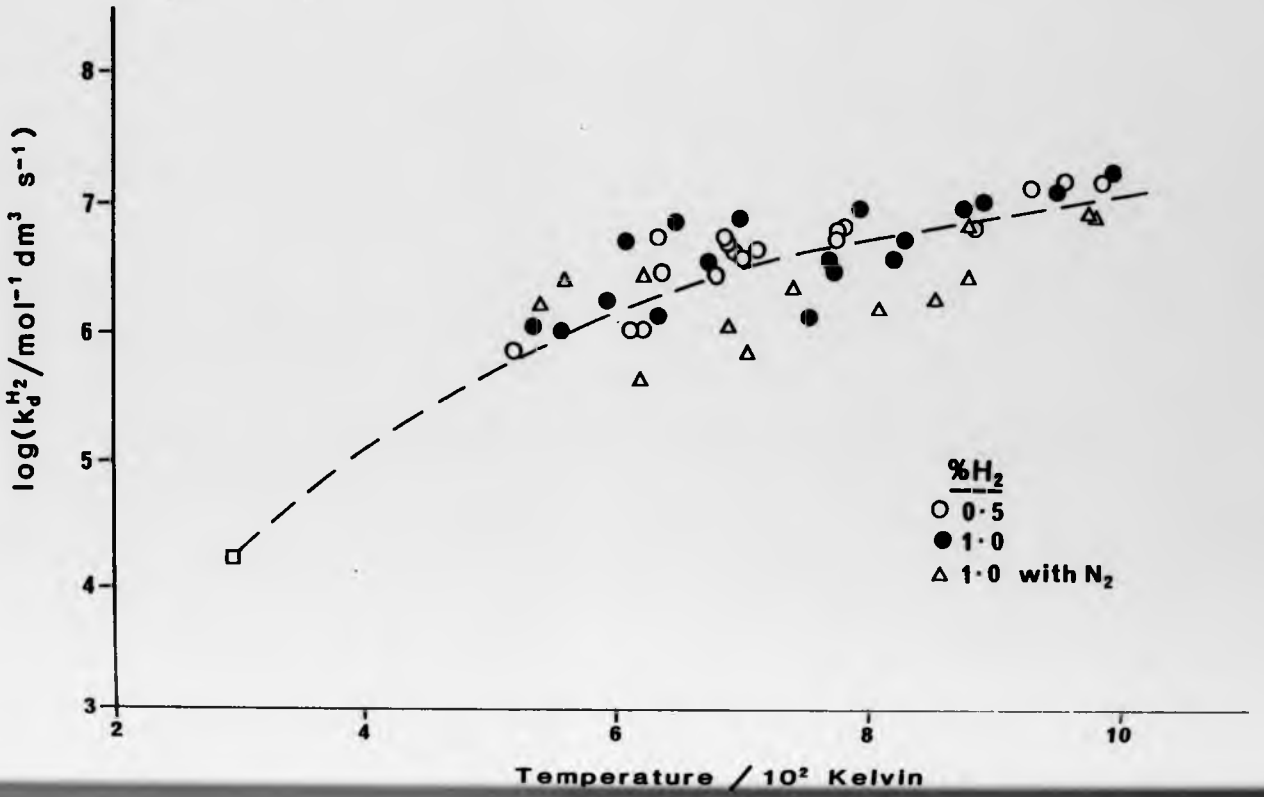

Table 5.6 High Temperature Deactivation of $O_2(a^1\Delta_g)$ by H_2

H_2 %	Run No	T_2 Kelvin	^{634}K	$k_d^{H_2}$ x 10^6 mol^{-1} dm^3 s^{-1}	log $k_d^{H_2}$
0.5	DSR61A	516	0.95	0.64	5.81
0.5	DSR30A	609	0.91	0.93	5.97
0.5	DSR27A	617	0.92	1.01	6.00
0.5	DSR21A	628	1.01	5.10	6.71
0.5	DSR33A	633	1.02	2.94	6.47
0.5	DSR36A	676	0.99	2.70	6.43
0.5	DSR38A	684	1.08	3.73	6.57
0.5	DSR34A	685	0.97	3.36	6.53
0.5	DSR39A	689	1.14	3.34	6.52
0.5	DSR40A	691	1.08	3.10	6.49
0.5	DSR37A	706	1.08	6.45	6.65
0.5	DSR43A	769	1.01	4.89	6.69
0.5	DSR44A	769	1.16	5.65	6.75
0.5	DSR41A	775	1.10	7.85	6.89
0.5	DSR46A	887	1.15	8.00	6.90
0.5	DSR47A	923	1.15	13.3	7.12
0.5	DSR49A	950	1.23	17.6	7.25
0.5	DSR48A	979	1.20	18.7	7.27
1.0	DSR59A	532	0.99	1.28	6.11
1.0	DSR52A	555	0.91	0.85	5.93
1.0	DSR54A	591	1.02	1.74	6.24
1.0	DSR55A	603	1.01	4.87	6.68
1.0	DSR50A	633	0.92	1.21	6.08

Table 5.6 continued

H_2 %	Run No	T_2 Kelvin	^{634}K	$k_d^{H_2}$ x 10^6 mol^{-1} dm^3 s^{-1}	log $k_d^{H_2}$
1.0	DSR9A	644	1.01	6.90	6.84
1.0	DSR10A	668	1.04	3.20	6.51
1.0	DSR18A	701	0.99	4.95	6.69
1.0	DSR11A	750	1.00	1.16	6.06
1.0	DSR15A	765	0.98	3.40	6.53
1.0	DSR12A	767	0.99	2.89	6.46
1.0	DSR24A	789	1.00	9.30	6.97
1.0	DSR17A	814	0.95	3.64	6.56
1.0	DSR19A	818	1.11	5.00	6.70
1.0	DSR23A	870	1.22	8.50	6.93
1.0	DSR20A	879	1.23	10.1	7.00
1.0	DSR25A	946	1.19	12.0	7.08
1.0	DSR22A	987	1.30	15.8	7.20

Figure 5.10 Arrhenius plot of the rate constants for the deactivation of $O_2(a\ ^1\Delta g)$ by H_2

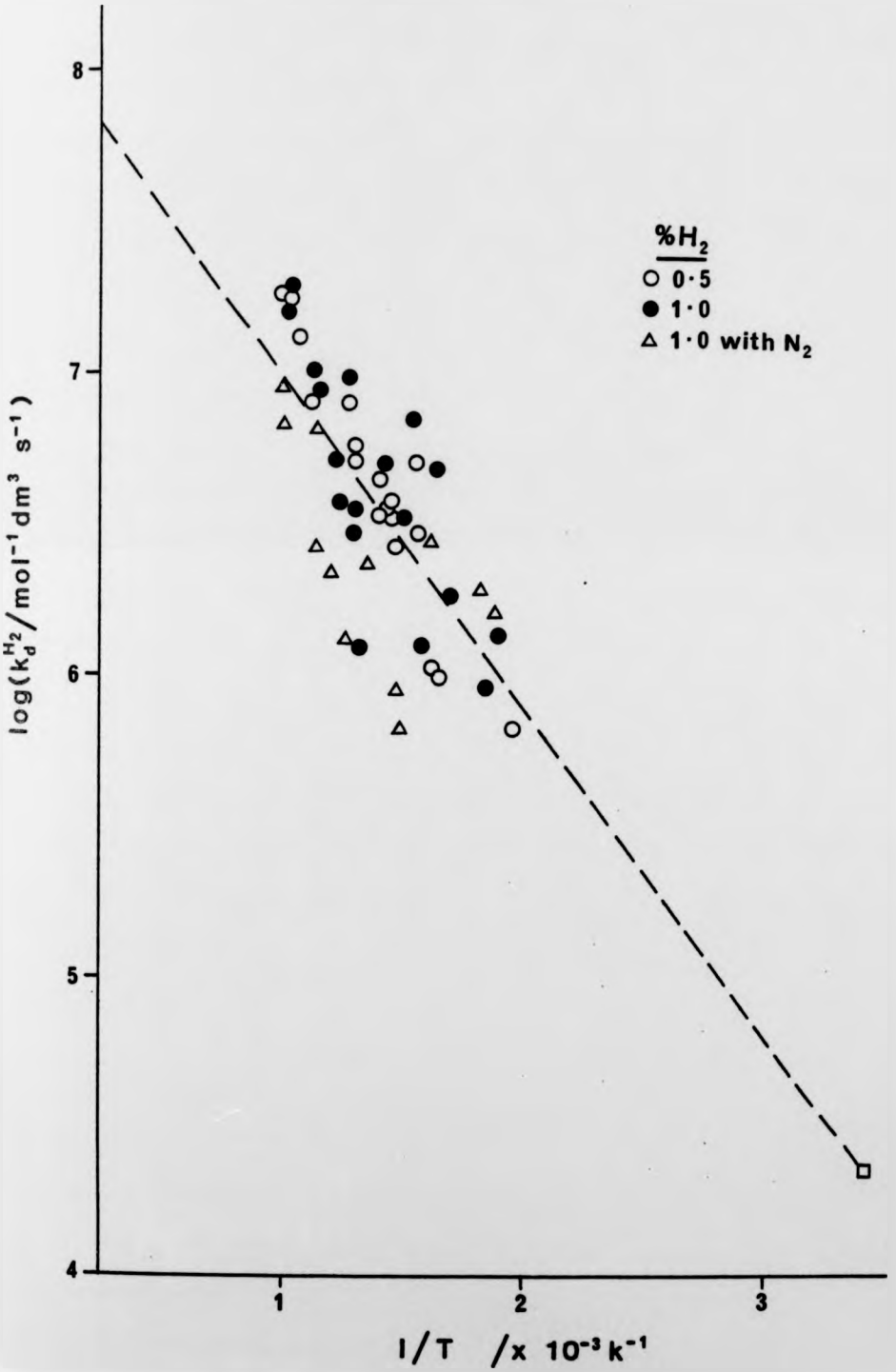

the additional emission became dominant. The nature and origin of this emission is discussed in section 5.4.

In an attempt to remove the additional emission, and hence extend the temperature range above 1000K, nitrogen was added to the test mixture. In order to establish the effect of N_2 upon the deactivation of $O_2(a^1\Delta_g)$, mixtures of 10, 25 and 50 percent N_2 and O_2 were tested in the same manner as the H_2/O_2 mixtures. No additional deactivation of $O_2(a^1\Delta_g)$ was observed at the high temperatures (500-1400K). Results for these mixtures are given in table 5.7. Run parameters may be found in Appendix 5.

The determination of the deactivation of $O_2(a^1\Delta_g)$ by H_2 at high temperatures was repeated using 1.0% H_2, 24.0% N_2 and 75.0% O_2 mixtures (table 5.8). The run parameters are also given in Appendix 4. Unfortunately the addition of N_2 only shifted the appearance temperature of the additional emission to approximately 900K, preventing the extension of the temperature range. The results are included in figures 5.9 and 5.10.

The positive temperature dependence gave the Arrhenius plot shown in figure 5.10. The high temperature values are extrapolated to the room temperature value determined in section 5.2.3.

The Arrhenius equation obtained between 295 and 1000K by least squares analysis is:

$$k_d^{H_2} = (1.32 \pm 1.08) \times 10^8 \exp[-(2600 \pm 180)/T] \text{ mol}^{-1} \text{ dm}^3 \text{ s}^{-1}$$

The equation predicts an activation energy of (21.6 ± 1.5) kJ mol^{-1}.

Again the scatter is typical of shock-tube measurements and is influenced by the low signal to noise ratio observed when an efficient deactivator is studied.

Table 5.7 High Temperature Deactivation of $O_2(a^1\Delta_g)$ by N_2/O_2 Mixtures

N_2 %	Run No	T_2 Kelvin	^{634}K	k_d^m x 10^4 mol^{-1} dm^3 s^{-1}
10	DSR234A	519	0.71	-1.09
10	DSR235A	519	1.34	+1.09
10	DSR236A	536	0.63	-1.07
10	DSR229A	605	0.74	+2.03
10	DSR230A	611	0.70	-0.43
10	DSR228A	679	0.78	-2.65
10	DSR227A	741	0.73	+2.24
10	DSR225A	829	0.78	-2.70
10	DSR232A	1039	0.87	+2.45
10	DSR224A	1110	0.79	-2.83
10	DSR223A	1127	0.89	-5.02
10	DSR233A	1263	0.95	+3.43
10	DSR231A	1492	1.15	+5.60
25	DSR238A	525	0.81	+1.06
25	DSR239A	528	0.75	-3.10
25	DSR216A	609	0.74	-0.79
25	DSR222A	611	0.80	-1.39
25	DSR221A	656	0.83	-0.78
25	DSR218A	742	0.86	+0.73
25	DSR217A	781	0.81	+0.77
25	DSR220A	814	0.88	-0.80
25	DSR219A	874	0.85	+0.85

Table 5.7 continued

N_2 %	Run No	T_2 Kelvin	^{634}K	k_d^m x 10^4 mol^{-1} dm^3 s^{-1}
25	DSR211A	1003	1.01	+3.20
25	DSR212A	1087	1.05	+2.23
25	DSR215A	1135	1.09	+0.57
25	DSR214A	1375	1.67	-2.15
25	DSR213A	1424	1.93	+0.64
50	DSR208A	523	0.84	-1.58
50	DSR209A	526	0.86	+2.15
50	DSR210A	561	0.93	+0.97
50	DSR207A	607	0.89	-0.97
50	DSR206A	615	0.89	-0.99
50	DSR205A	717	0.85	+1.21
50	DSR203A	769	0.82	+2.00
50	DSR204A	844	0.96	-1.71
50	DSR201A	858	0.98	+1.87
50	DSR202A	1149	1.32	+0.61

Table 5.8 High Temperature Deactivation of $O_2(a^1\Delta_g)$ by H_2 in an $H_2/N_2/O_2$ Mixture

H_2 %	N_2 %	Run No	T_2 Kelvin	634_K	$k_d^{H_2}$ x 10^6 mol^{-1} dm^3 s^{-1}	log $k_d^{H_2}$
1.0	24.0	DSR420A	514	0.90	-1.50	-
1.0	24.0	DSR422A	525	0.87	-2.12	-
1.0	24.0	DSR421A	535	1.02	1.61	6.21
1.0	24.0	DSR423A	557	1.02	1.92	6.28
1.0	24.0	DSR417A	618	1.02	2.78	6.44
1.0	24.0	DSR419A	620	1.01	0.38	5.58
1.0	24.0	DSR412A	682	1.08	-0.06	-
1.0	24.0	DSR410A	691	1.06	0.82	5.92
1.0	24.0	DSR414A	704	1.05	0.61	5.79
1.0	24.0	DSR411A	738	1.08	2.31	6.36
1.0	24.0	DSR404A	807	1.07	1.22	6.09
1.0	24.0	DSR405A	849	1.10	2.07	6.32
1.0	24.0	DSR401A	877	1.10	2.58	6.41
1.0	24.0	DSR409A	877	1.15	6.50	6.81
1.0	24.0	DSR407A	968	1.16	8.45	6.93
1.0	24.0	DSR406A	978	1.24	6.45	6.81

5.3.4 Deactivation of $O_2(a^1\Delta_g)$ by D_2 at High Temperatures

A series of determinations was carried out on mixtures containing 1.5 and 3.0 percent D_2 in pure oxygen. The results of the analysis are given in table 5.9. The input parameters for each run are given in Appendix 6.

An additional emission was observed at temperatures above 900K. This emission was similar to that observed in the previous section and prevented the analysis of the full trace above 900K. It was not possible to analyse data obtained at temperatures above 1200K at all. This additional emission is included in the discussion in section 5.4.

Figure 5.11 shows an increase in $k_d^{D_2}$ with temperature, therefore an Arrhenius plot was made (figure 5.12) which gave the following equation for the temperature dependence of the deactivation of $O_2(a^1\Delta_g)$ by D_2.

$$k_d^{D_2} = (2.88 \pm 1.24) \times 10^8 \exp[-(3430 \pm 170)/T] \text{ mol}^{-1} \text{ dm}^3 \text{ s}^{-1}$$

The equation predicts an activation energy of (28.5 ± 1.4) kJ mol^{-1}.

A series of determinations was also carried out on $D_2/N_2/O_2$ mixtures in an attempt to remove the additional emission. The results of these determinations are given in table 5.10, and are shown on figure 5.13. As in the determination of $O_2(a^1\Delta_g)$ by H_2, the addition of N_2 did not dilute the $O_2(X^3\Sigma^-_g)$ sufficiently to remove the additional emission.

The rate constants determined in the presence of N_2 are consistently lower than those determined in pure O_2. The Arrhenius plot (figure 5.14) gives the expression:

Figure 5.11 Rate constants for the deactivation of $O_2(a\ ^1\Delta g)$ by D_2 in pure O_2

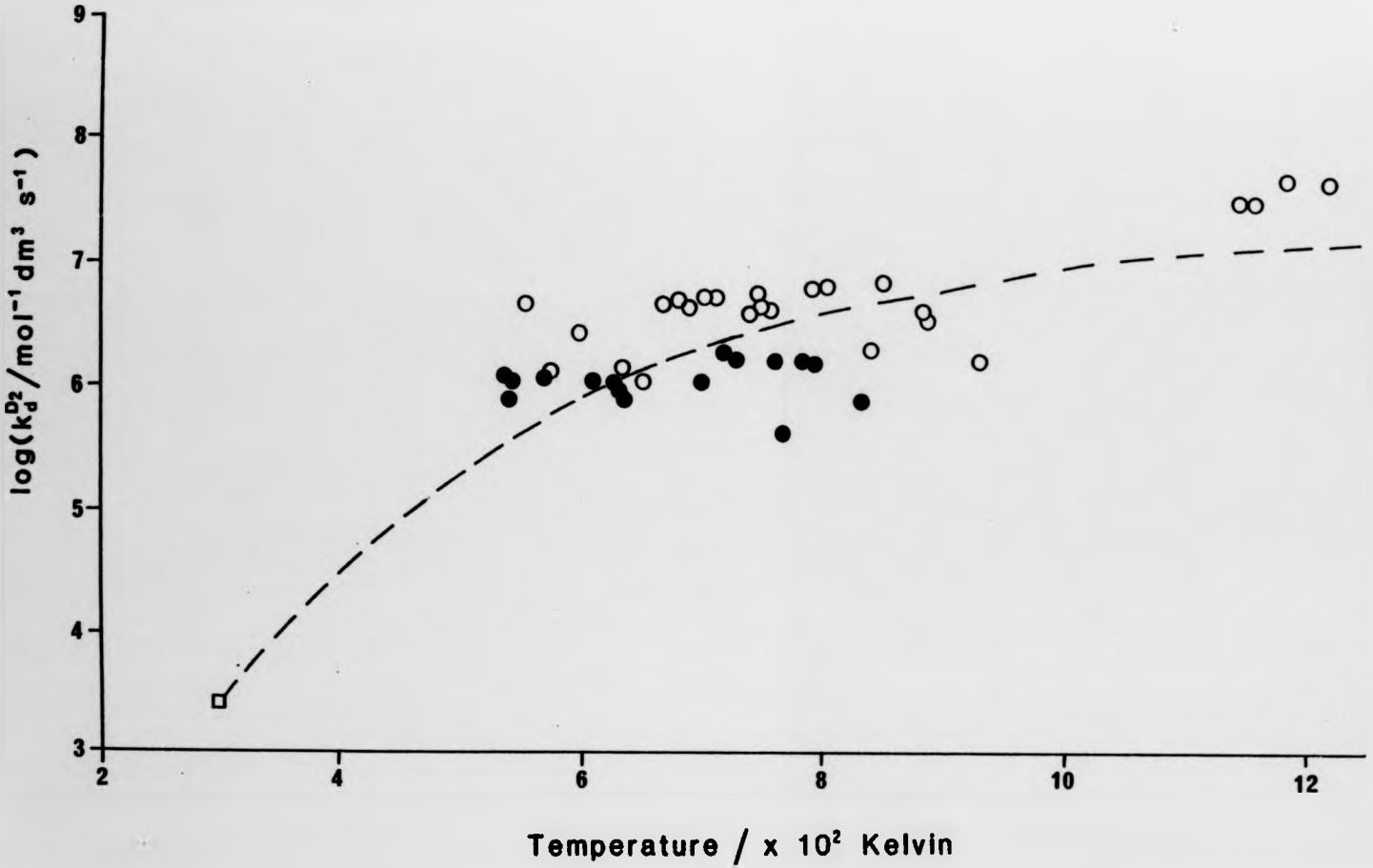

Figure 5.12 Arrhenius plot of the rate constants for the deactivation of $O_2(a\ ^1\Delta g)$ by D_2 in pure O_2

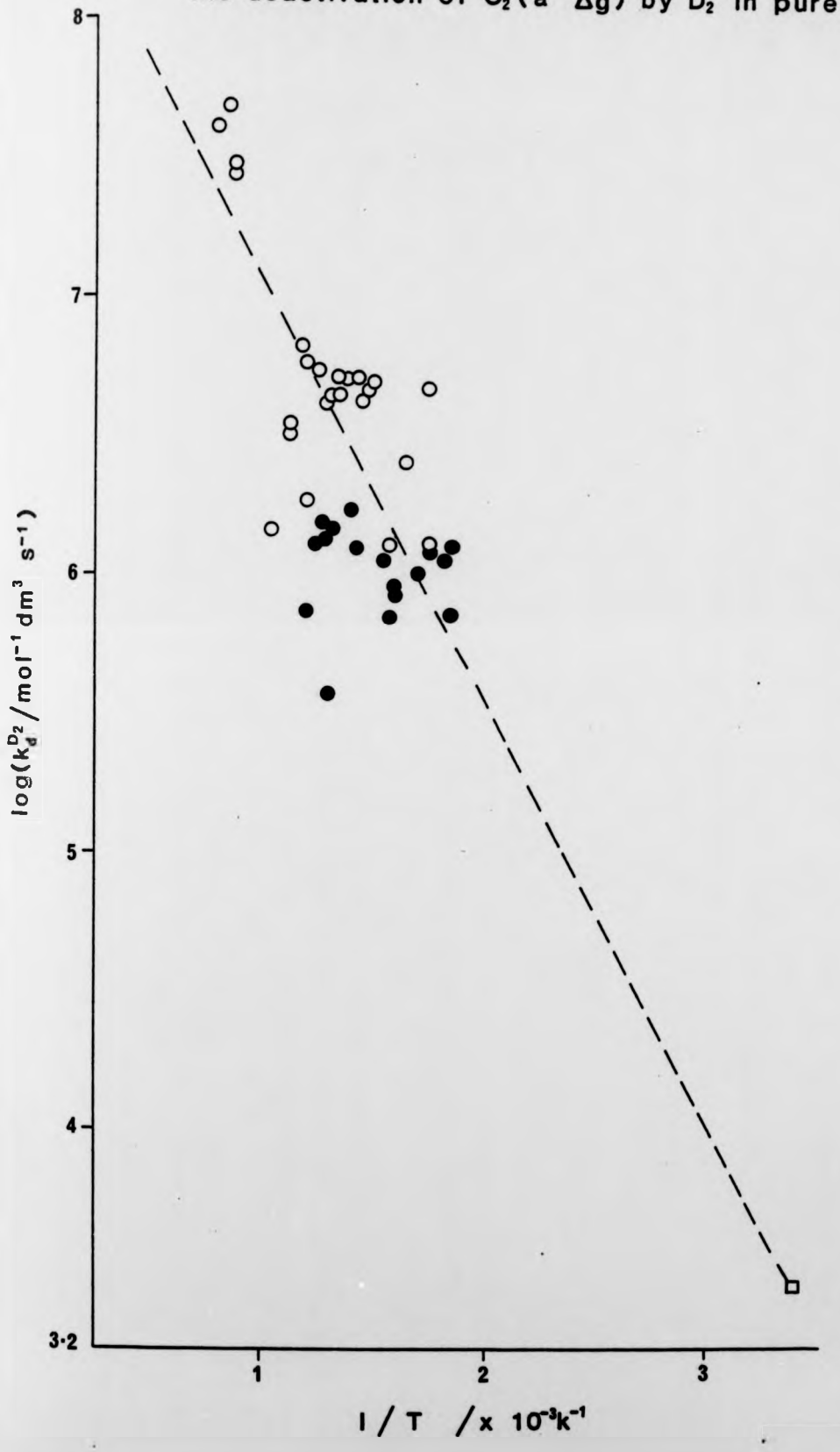

Figure 5.13 Rate constants for the deactivation of $O_2(a\ ^1\Delta g)$ by D_2 in N_2/O_2

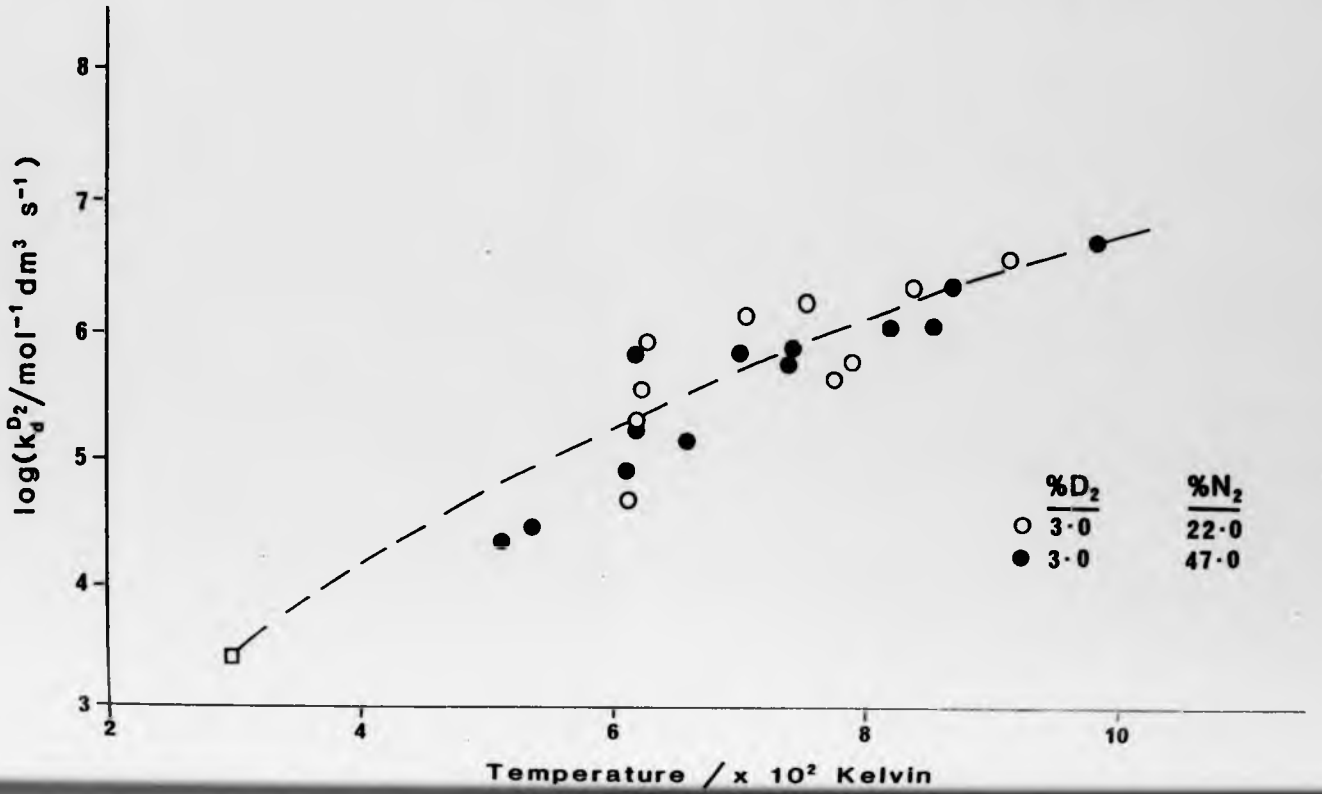

Figure 5.14 Arrhenius plot of the rate constants for the deactivation of $O_2(a\ ^1\Delta g)$ by D_2 in O_2/N_2

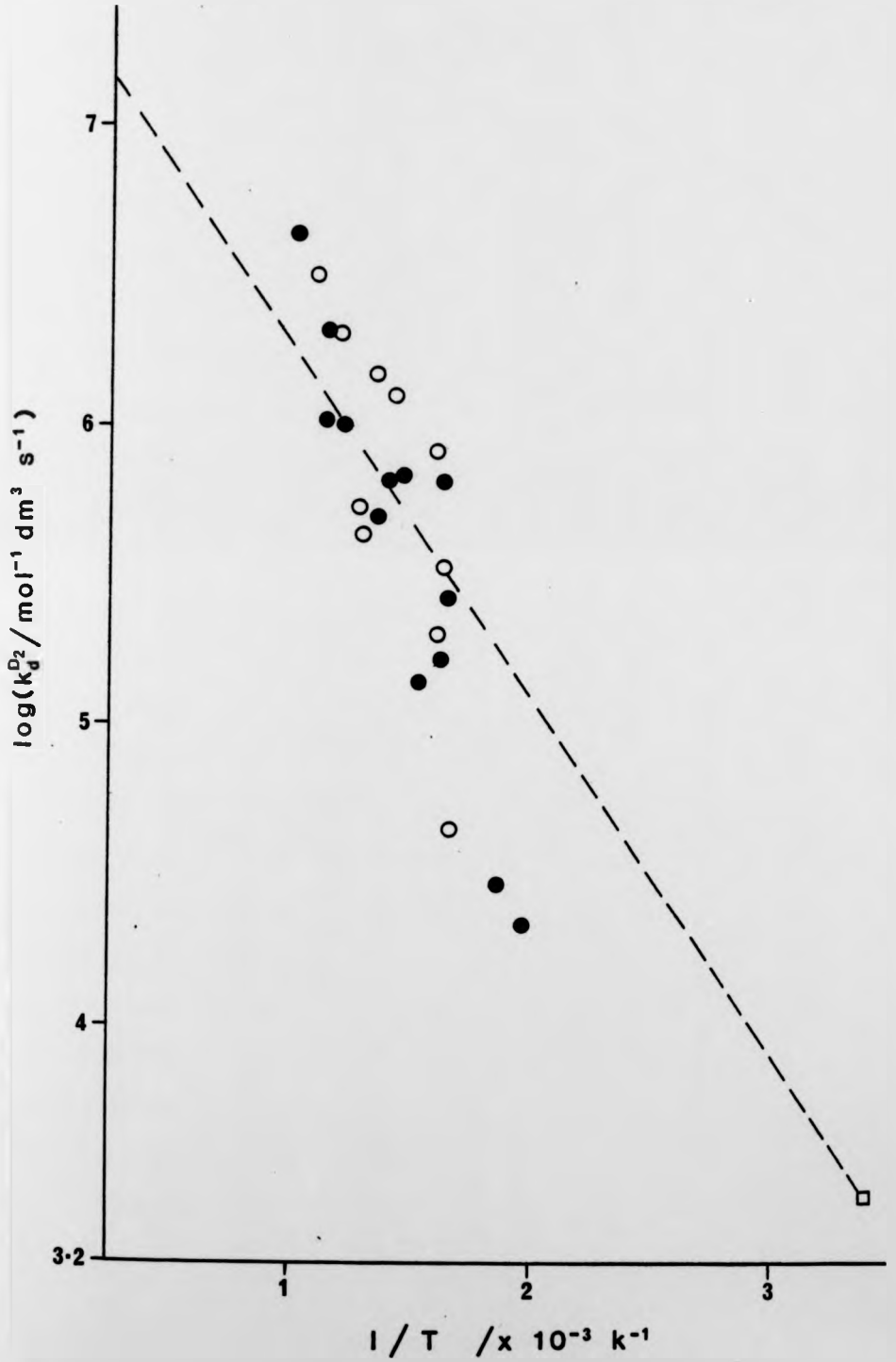

Table 5.9 High Temperature Deactivation of $O_2(a^1\Delta_g)$ by D_2

D_2 %	Run No	T_2 Kelvin	^{634}K	$k_d^{D_2}$ x 10^6 mol^{-1} dm^3 s^{-1}	log $k_d^{D_2}$
1.5	DSR121A	533	0.77	-0.49	-
1.5	DSR119A	537	0.80	-0.07	-
1.5	DSR120A	545	0.78	-0.10	-
1.5	DSR118A	554	0.70	4.67	6.67
1.5	DSR122A	575	0.83	1.28	6.11
1.5	DSR124A	602	0.74	2.45	6.39
1.5	DSR123A	634	0.84	1.24	6.09
1.5	DSR107A	669	0.77	4.87	6.69
1.5	DSR106A	681	0.76	4.53	6.66
1.5	DSR122A	689	0.82	4.07	6.61
1.5	DSR103A	706	0.81	4.93	6.69
1.5	DSR104A	708	0.90	5.00	6.70
1.5	DSR114A	745	0.84	4.40	6.64
1.5	DSR117X	748	0.91	5.10	6.71
1.5	DSR117B	748	0.91	4.33	6.64
1.5	DSR113A	756	0.83	4.13	6.62
1.5	DSR109A	795	0.82	5.80	6.76
1.5	DSR115A	799	0.86	5.40	6.73
1.5	DSR125A	842	0.89	1.82	6.26
1.5	DSR105A	848	0.79	6.73	6.83
1.5	DSR116A	885	0.61	3.47	6.54
1.5	DSR116B	885	0.68	3.23	6.51

Table 5.9 continued

D_2 %	Run No	T_2 Kelvin	^{634}K	$k_d^{D_2}$ x 10^6 mol^{-1} dm^3 s^{-1}	log $k_d^{D_2}$
1.5	DSR126A	954	0.93	1.45	6.16
1.5	DSR102A	1146	1.18	30.6	7.48
1.5	DSR110A	1155	1.07	28.4	7.45
1.5	DSR111A	1178	1.39	48.3	7.68
1.5	DSR101A	1216	1.42	39.6	7.60
3.0	DSR129A	537	0.89	1.13	6.05
3.0	DSR127A	541	0.87	0.71	5.85
3.0	DSR128A	546	0.81	1.10	6.04
3.0	DSR130A	572	0.91	1.17	6.07
3.0	DSR131A	611	0.88	0.95	5.98
3.0	DSR132A	627	0.87	0.90	5.96
3.0	DSR136A	628	0.74	-0.43	-
3.0	DSR141A	630	0.88	0.81	5.91
3.0	DSR135A	636	0.87	0.71	5.85
3.0	DSR142A	649	0.88	1.10	6.04
3.0	DSR140A	698	0.86	1.19	6.07
3.0	DSR138A	719	0.98	1.63	6.21
3.0	DSR143A	728	0.93	1.46	6.16
3.0	DSR139A	763	0.91	1.33	6.12
3.0	DSR146A	768	0.82	0.36	5.55
3.0	DSR145AX	782	0.87	1.46	6.16
3.0	DSR144A	791	0.90	1.32	6.12
3.0	DSR137A	837	0.90	0.69	5.84

Table 5.10 High Temperature Deactivation of $O_2(a^1\Delta_g)$ by D_2 in $D_2/N_2/O_2$ mixtures

D_2 %	N_2 %	Run No	T_2 Kelvin	^{634}K	$k_d^{D_2}$ x 10^5 mol^{-1} dm^3 s^{-1}	log $k_d^{D_2}$
3.0	22.0	DSR316A	513	0.83	-2.25	-
3.0	22.0	DSR317A	514	0.81	-7.43	-
3.0	22.0	DSR314A	547	0.76	-1.04	-
3.0	22.0	DSR310A	596	0.83	-4.53	-
3.0	22.0	DSR315A	610	0.82	0.42	4.63
3.0	22.0	DSR311A	617	0.79	-0.11	-
3.0	22.0	DSR312A	618	0.82	3.37	5.53
3.0	22.0	DSR313A	626	0.84	1.98	5.30
3.0	22.0	DSR309A	627	0.83	8.37	5.92
3.0	22.0	DSR308A	703	0.93	12.6	6.10
3.0	22.0	DSR307A	749	0.84	15.1	6.18
3.0	22.0	DSR305A	767	0.81	4.30	5.63
3.0	22.0	DSR306A	786	0.87	5.40	5.73
3.0	22.0	DSR302A	833	0.85	19.5	6.29
3.0	22.0	DSR304A	912	0.97	31.4	6.50
3.0	47.0	DSR330A	511	0.89	-4.57	-
3.0	47.0	DSR331A	511	0.99	0.21	4.32
3.0	47.0	DSR332A	537	0.88	0.29	4.47
3.0	47.0	DSR333A	610	0.97	2.60	5.42
3.0	47.0	DSR327A	614	0.83	6.53	5.81
3.0	47.0	DSR320A	617	0.81	1.65	5.22

Table 5.10 continued

D_2 %	N_2 %	Run No	T_2 Kelvin	^{634}K	$k_d^{D_2}$ x 10^5 mol^{-1} dm^3 s^{-1}	log $k_d^{D_2}$
3.0	47.0	DSR326A	657	0.91	1.35	5.13
3.0	47.0	DSR324A	692	0.93	6.80	5.84
3.0	47.0	DSR325A	717	0.91	6.60	5.82
3.0	47.0	DSR323A	734	0.90	4.93	5.69
3.0	47.0	DSR328A	817	0.90	9.73	5.99
3.0	47.0	DSR329A	852	0.97	10.4	6.02
3.0	47.0	DSR319A	864	0.99	20.2	6.31
3.0	47.0	DSR318A	978	1.16	44.3	6.65

$$k_d^{D_2} = (2.75 \pm 0.75) \times 10^7 \exp[-(2740 \pm 90)/T] \text{ mol}^{-1} \text{ dm}^3 \text{ s}^{-1}$$

for the temperature dependence. An activation energy of (22.8 ±0.7) kJ mol^{-1} is predicted.

Again the scatter is typical of shock tube results, but in this case the signal to noise ratio is higher than was observed for the two previous deactivators because D_2 is a relatively inefficient deactivator at room temperature. This is reflected in the smaller errors which occur in the Arrhenius expression.

The first determination of the high temperature deactivation of $O_2(a^1\Delta_g)$ by D_2 was carried out, on the same apparatus, after the determination of the deactivation of $O_2(a^1\Delta_g)$ by H_2; it is therefore possible that some H_2 remained in the system during the early runs (1.5% D_2). Since H_2 is a more efficient deactivator of $O_2(a^1\Delta_g)$ (approximately a factor of 10 at room temperature), even a small amount of this additive mixed with the D_2 would increase the value of $k_d^{D_2}$. The apparatus was then checked and the earthing of the monitoring instruments improved. The studies on O_2/N_2 mixtures described in section 5.3.2 were then carried out before the second determination of k_d^m (in $D_2/O_2/N_2$ mixtures) was made. On completion of this second determination, the $H_2/O_2/N_2$ experiments were carried out to check on the H_2/O_2 determination of $k_d^{H_2}$. As shown by figures 5.9 and 5.10, the two sets of H_2 results agreed well.

Therefore the expression for the temperature dependence of the deactivation of $O_2(a^1\Delta_g)$ by D_2 carried out in the presence of N_2 is preferred.

5.3.5 The Enhancement Factor, ^{634}K

Figure 5.15 shows a plot of the enhancement factor, ^{634}K,

Figure 5.15 Variation of ^{634}K with temperature

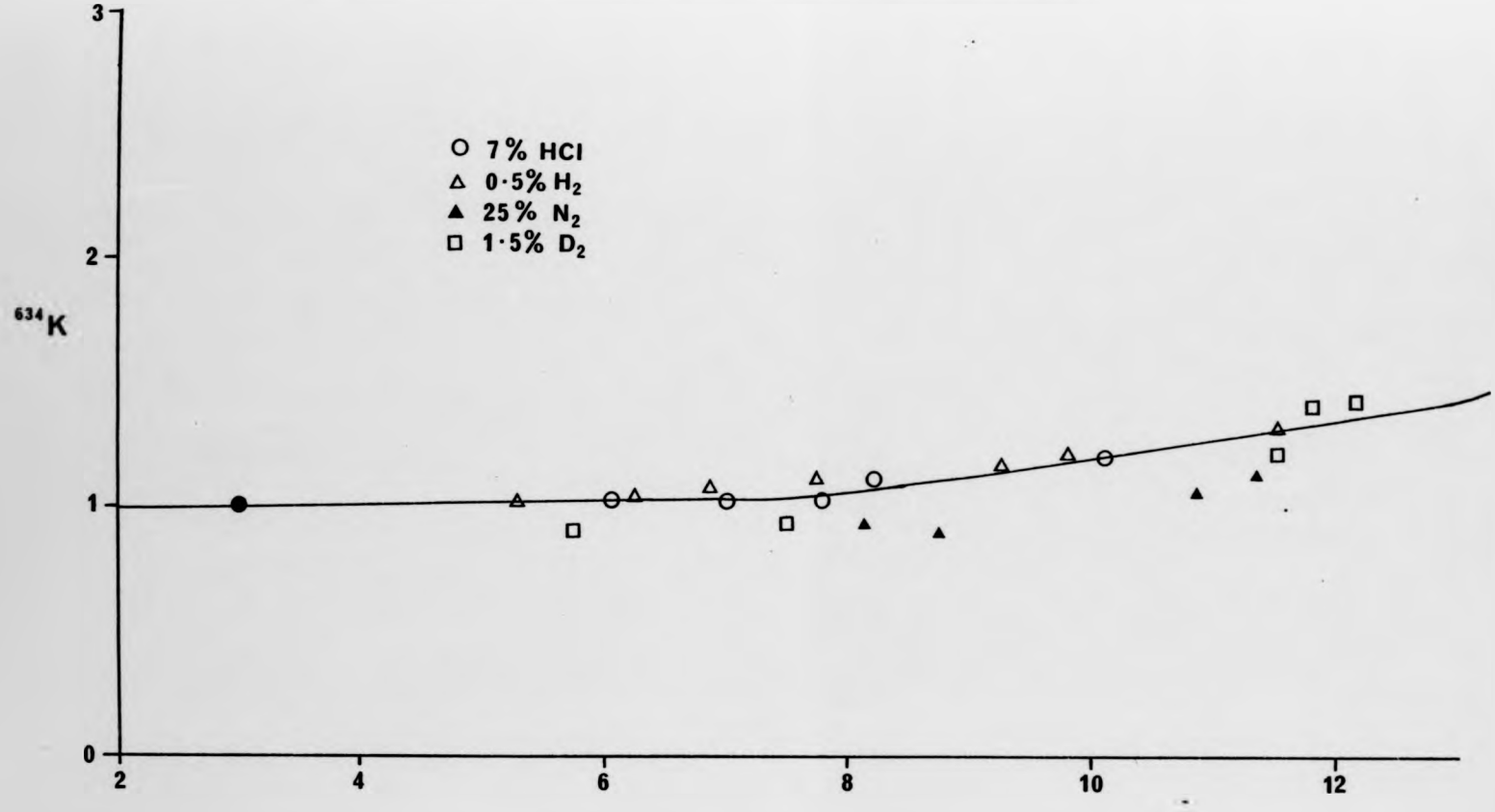

versus temperature for mixtures of various deactivating species with excited oxygen studied in this work. A selection of points has been plotted; other points were omitted for clarity. The value of ^{634}K is approximately equal to unity at temperatures up to 800K, as predicted by a simple collisional approach to the enhancement of the emission intensity. However, above 800K there is a systematic increase in ^{634}K. This increase is due to hot bands in the dimol emission of singlet oxygen and has been studied by Boodaghians and co-workers [73].

The line on figure 5.15 indicates the calculated value of ^{634}K allowing for hot bands. The agreement of the experimental data with the calculated ^{634}K - temperature plot is good evidence that the fitting of the 634nm Kinetic Model (equation 4.35) to the data is behaving as expected and that the model is a good representation of the real conditions. The enhancement factors obtained for all of the runs are given in tables 5.5 to 5.9.

5.4 Additional Emissions

An additional emission was observed at high temperatures in mixtures of O_2 with HCl, H_2 or D_2. This emission appeared at temperatures above 900K. In each case, the form of the emission intensity - time profile changed, so that the emission intensity at 634nm began to rise again. Run DSR126A (figure 5.16) is shown as an example. The emission shows an induction period of about 250 μs in this case. In general, the induction period reduces and the intensity of the additional emission increases with increasing temperature for all three additives.

The induction period and the presence of hydrogen (deuterium) in each additive suggests that the emission may be a by-product of the H + O_2 system. Washida, Akimoto and Okuda [74] have studied the system at 295K and found that $O_2(a^1\Delta_g)$ is a product of the reaction:

$$HO_2 + H \longrightarrow H_2 + O_2\ (a^1\Delta_g \text{ or } X^3\Sigma^-_g) \qquad (5.2)$$

The extra emission, therefore, could be due to this reaction, initiated by hydrogen atoms generated at high temperatures in the discharge flow - shock tube.

The experiments carried out in this work were designed to study the deactivation of $O_2(a^1\Delta_g)$ by HCl, H_2 and D_2, and, as a result, the temperature range in which the additional emission is present was avoided. Spectroscopic studies were not possible because of the short duration of the high temperature experiment (1000 μs) and the short persistence of the additional emission (200 μs).

In the studies involving HCl and HBr, further emissions were observed, which did not appear in the post-shock regime at either

Figure 5.16 Additional emission

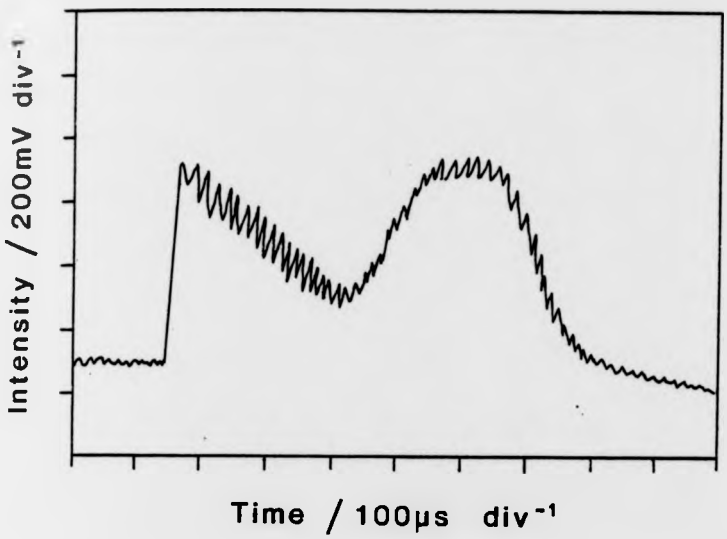

Run DSR126A:

1·5% D_2 in pure Oxygen at 922 Kelvin

634nm or 762nm. These green emissions were observed when pure oxygen was passed through the microwave discharge and into the flow tube at room temperature, immediately after a shock tube experiment had been performed. They had sufficient intensity to be visible to the naked eye (plate 5.1) and persisted for about 15 minutes.

Attempts were made to record the spectra of these emissions using a Hilger Prism Spectrograph but a useful result was not obtained due to poor resolution. It was suspected that either mercury in the oxygen stream or aluminium from the diaphragm may be involved in a reaction with these compounds. However, experiments intended to reproduce the glow artificially by passing discharged O_2 over chlorides and bromides of mercury and aluminium were unsuccessful.

One possible origin of the green glow in the HBr/O_2 experiments is the emission from the $HgBr(B^2\Sigma)$ radical which is blue/green in colour. The $HgBr/HgBr_2$ dissociation laser, which relies on this emission, has been described by Erlandson and Cool [75].

The existence of a similar system for $HgCl/HgCl_2$ would explain the glow in the HCl/O_2 experiments, although no reference to such a system has been found in the literature.

Plate 5.1

A photograph of the green emission observed after shock heating HCl/O_2 mixtures, followed by passing discharged O_2 along the flow tube.

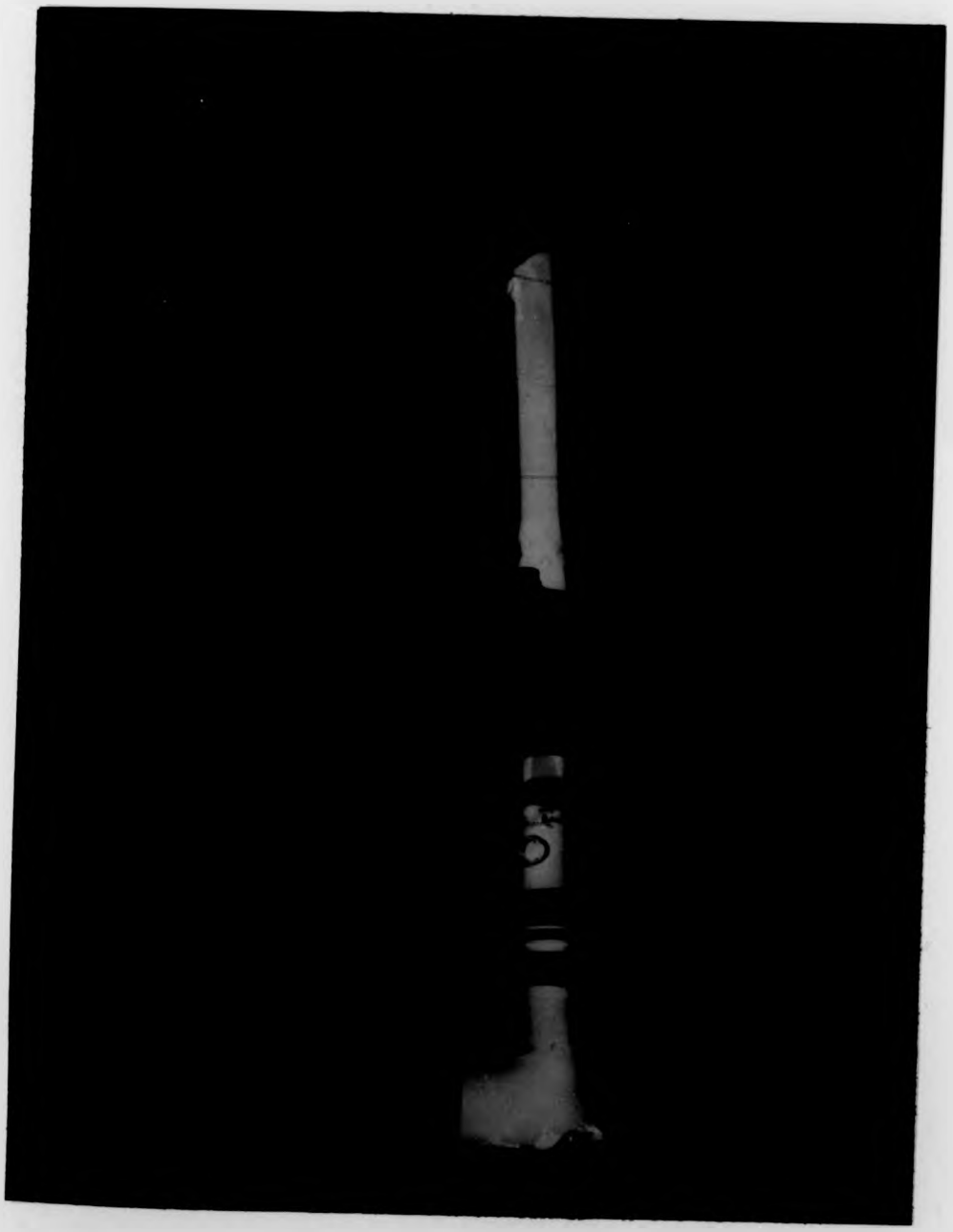

Plate 5.1

A photograph of the green emission observed after shock heating HCl/O_2 mixtures, followed by passing discharged O_2 along the flow tube.

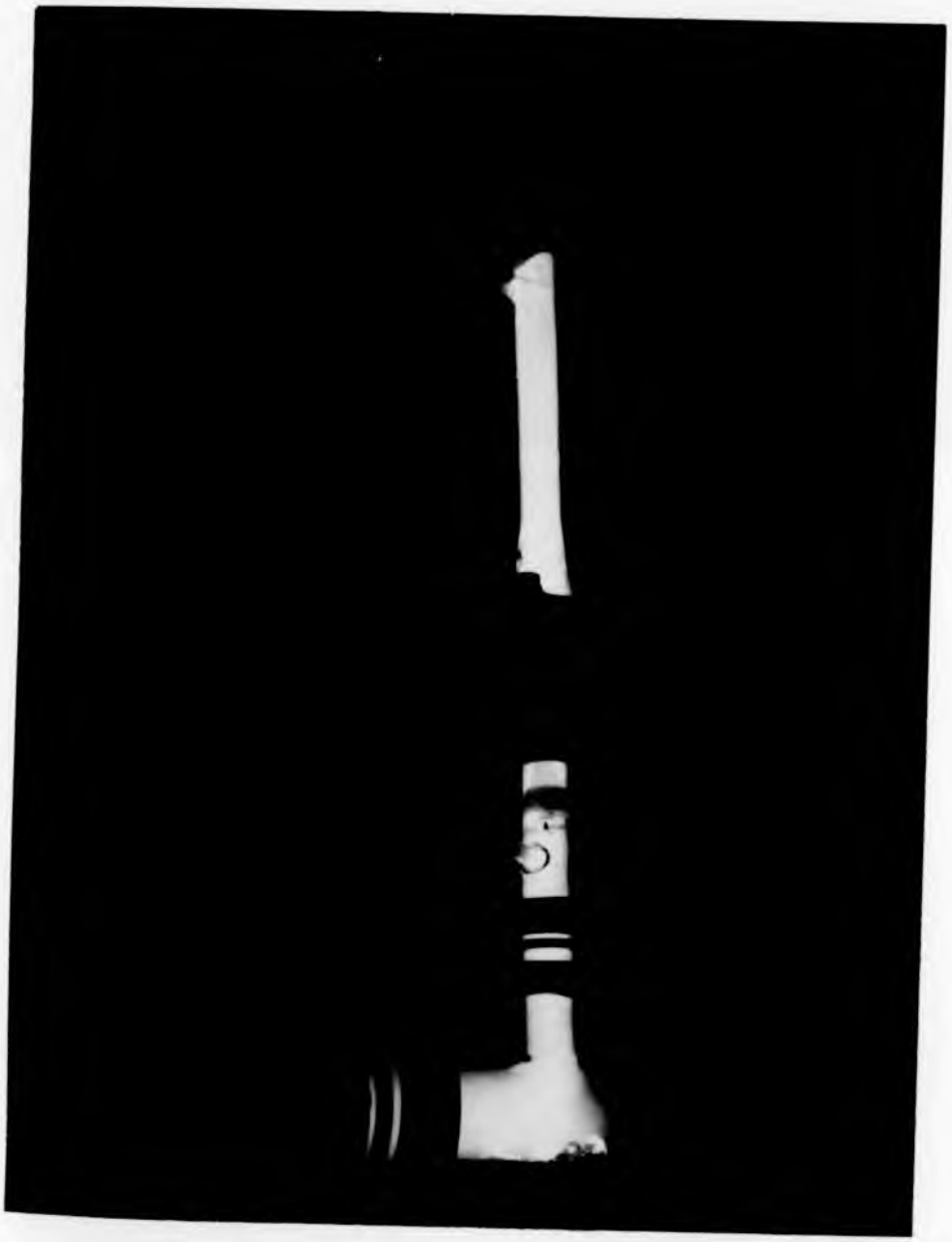

THE COLLISIONAL DEACTIVATION OF $O_2(b^1\Sigma^+_g)$

6.1 Introduction

The results of the temperature dependence study of the deactivation of $O_2(b^1\Sigma^+_g)$ by HCl, HBr, H_2 and D_2 are presented in this chapter. The room temperature deactivation of $O_2(b^1\Sigma^+_g)$ by these species is discussed first and then the high temperature results obtained by shock heating are considered.

As in the study of the deactivation of $O_2(a^1\Delta_g)$ reported in the previous chapter, additional emissions were observed. These emissions are considered in the final section.

This chapter serves only to present the results and comment upon their validity. A detailed discussion of these results is given in the next chapter.

6.2 Studies of the Collisional Deactivation of $O_2(b^1\Sigma^+_g)$ at 295K

The determination of the room temperature (295K) rate constants for the deactivation of $O_2(b^1\Sigma^+_g)$ by HCl, HBr, H_2 and D_2 was carried out by the method described in section 4.4.

The emission intensities at 634nm and 762nm were measured in the absence and then in the presence of the additive, M. A pseudo-first order deactivation rate constant, $k_q^m[M]$, for the additive was then determined from equation (4.52). The value of $k_q^{O_2}$ was taken as 1×10^5 mol^{-1} dm^3 s^{-1} [46] and the wall deactivation rate constants were calculated using equation (4.52). The procedure was repeated many times over the total pressure range 3 - 10 torr, adding between 0.5 and 9.0 percent of the deactivator to pure O_2.

Plots of $f(\Phi_m, \Phi_o)$ versus [M] were constructed to give the second order rate constant k_q^m as the gradient. The following rate constants were evaluated at 295K by least squares analysis.

$$k_q^{HCl} = (1.60 \pm 0.20) \times 10^7 \text{ mol}^{-1} \text{ dm}^3 \text{ s}^{-1}$$

$$k_q^{HBr} = (1.42 \pm 0.07) \times 10^8 \text{ mol}^{-1} \text{ dm}^3 \text{ s}^{-1}$$

$$k_q^{H_2} = (2.76 \pm 0.06) \times 10^8 \text{ mol}^{-1} \text{ dm}^3 \text{ s}^{-1}$$

$$k_q^{D_2} = (5.27 \pm 0.18) \times 10^6 \text{ mol}^{-1} \text{ dm}^3 \text{ s}^{-1}$$

The error limits are 2σ.

6.2.1 Deactivation of $O_2(b^1\Sigma^+_g)$ by HCl at 295K

The determination of the deactivation of $O_2(b^1\Sigma^+_g)$ by HCl was carried out in collaboration with Boodaghians [44,68]. The

experimental results are listed in table 6.1. Figure 6.1 shows the plot of $f(\Phi_{HCl}, \Phi_o)$ versus [HCl]. The gradient is the second order rate constant k_q^{HCl} for the deactivation of $O_2(b^1\Sigma^+_g)$ by HCl.

$$k_q^{HCl} = (1.60 \pm 0.20) \times 10^7 \text{ mol}^{-1} \text{ dm}^3 \text{ s}^{-1}$$

The error limits are 2σ.

This result is lower than previous estimates by Kohse-Hoinghaus and Stuhl [85], Thomas and Thrush [77] and Gauthier and Snelling [86].

$$k_q^{HCl} = (7.8 \pm 2.4) \times 10^7 \text{ mol}^{-1} \text{ dm}^3 \text{ s}^{-1} \quad [85]$$

$$k_q^{HCl} = (4.4 \pm 1.0) \times 10^7 \text{ mol}^{-1} \text{ dm}^3 \text{ s}^{-1} \quad [77]$$

$$k_q^{HCl} = (4.0 \pm 2.0) \times 10^7 \text{ mol}^{-1} \text{ dm}^3 \text{ s}^{-1} \quad [86]$$

but agrees well with the shortly-to-be-published result by Singh and Setser [87].

$$k_q^{HCl} = (2.4 \pm 1.2) \times 10^7 \text{ mol}^{-1} \text{ dm}^3 \text{ s}^{-1} \quad [87]$$

Although HCl is an awkward gas to handle, consistent results were obtained for several different mixtures of HCl and O_2. Since the plot is linear and has its intercept at the origin (0,0), no indication of a wall modification is observed in this case. Small amounts of impurities with a lower deactivation rate constant would have a negligible diluent effect upon an efficient deactivator, such as HCl, and impurities with a higher deactivation rate constant would increase the value of the observed rate constant. One may conclude

Table 6.1 The Deactivation of $O_2(b^1\Sigma_g^+)$ by HCl at 295 K

HCl %	PRESSURE /torr	ΦHCl $/10^{-3}$	ΦO_2 $/10^{-3}$	$f(\Phi HCl, \Phi O_2)$ $/s^{-1}$	[HCl] $/x\ 10^{-5}$ mol dm^{-3}
	4.26		3.94		
3	4.34	12.28		112	0.71
	4.76		3.98		
3	4.80	12.77		118	0.79
	5.25		4.00		
3	5.30	13.68		132	0.87
	5.71		3.97		
3	5.84	14.50		147	0.96
	6.37		4.16		
3	6.45	15.58		157	1.06
	6.87		4.34		
3	6.95	16.41		163	1.14
	7.38		4.38		
3	7.50	17.62		182	1.23
	7.95		4.63		
3	8.07	18.63		189	1.32
	8.48		4.71		
3	8.61	20.10		210	1.41
	10.22		5.34		
3	10.43	25.33		267	1.71
	9.39		5.07		
3	9.48	22.78		237	1.55
	4.43		4.36		

Table 6.1 continued

HCl %	PRESSURE /torr	ΦHCl $/10^{-3}$	ΦO_2 $/10^{-3}$	$f(\Phi HCl, \Phi O_2)$ $/s^{-1}$	[HCl] $/x\ 10^{-5}$ mol dm^{-3}
5	4.55	22.38		220	1.24
	3.89		4.21		
5	4.06	17.30		165	1.11
	4.92		4.45		
5	5.09	19.56		184	1.39
	4.84		4.97		
7	5.01	28.00		249	1.92
	5.38		5.10		
7	5.51	31.64		285	2.11
	5.88		5.15		
7	6.08	35.62		331	2.73
	6.74		5.07		
7	6.87	40.73		410	2.63
	7.04		5.17		
7	7.28	42.12		423	2.79
	7.41		4.88		
7	7.70	45.11		498	2.95
	7.74		5.03		
7	8.07	44.66		486	3.09
	8.36		4.95		
7	8.69	45.40		522	3.22
	9.35		5.46		
7	9.68	52.83		588	3.71
	10.10		5.00		

Table 6.1 continued

HCl %	PRESSURE /torr	ΦHCl $/10^{-3}$	ΦO_2 $/10^{-3}$	$f(\Phi HCl, \Phi O_2)$ $/s^{-1}$	[HCl] $/x\ 10^{-5}$ mol dm^{-3}
7	10.15	51.25		657	4.03
	4.05		4.61		
9	4.22	32.79		323	2.08
	4.43		4.50		
9	4.59	32.54		331	2.26
	5.05		4.52		
9	5.25	36.94		388	2.59
	6.66		4.34		
9	6.95	45.04		544	3.42
	5.51		4.32		
9	5.71	39.26		445	2.81
	7.32		4.66		
9	7.66	48.72		596	3.77

Figure 6.1 R.T. Quenching of $O_2(b\ ^1\Sigma_g^+)$ by HCl

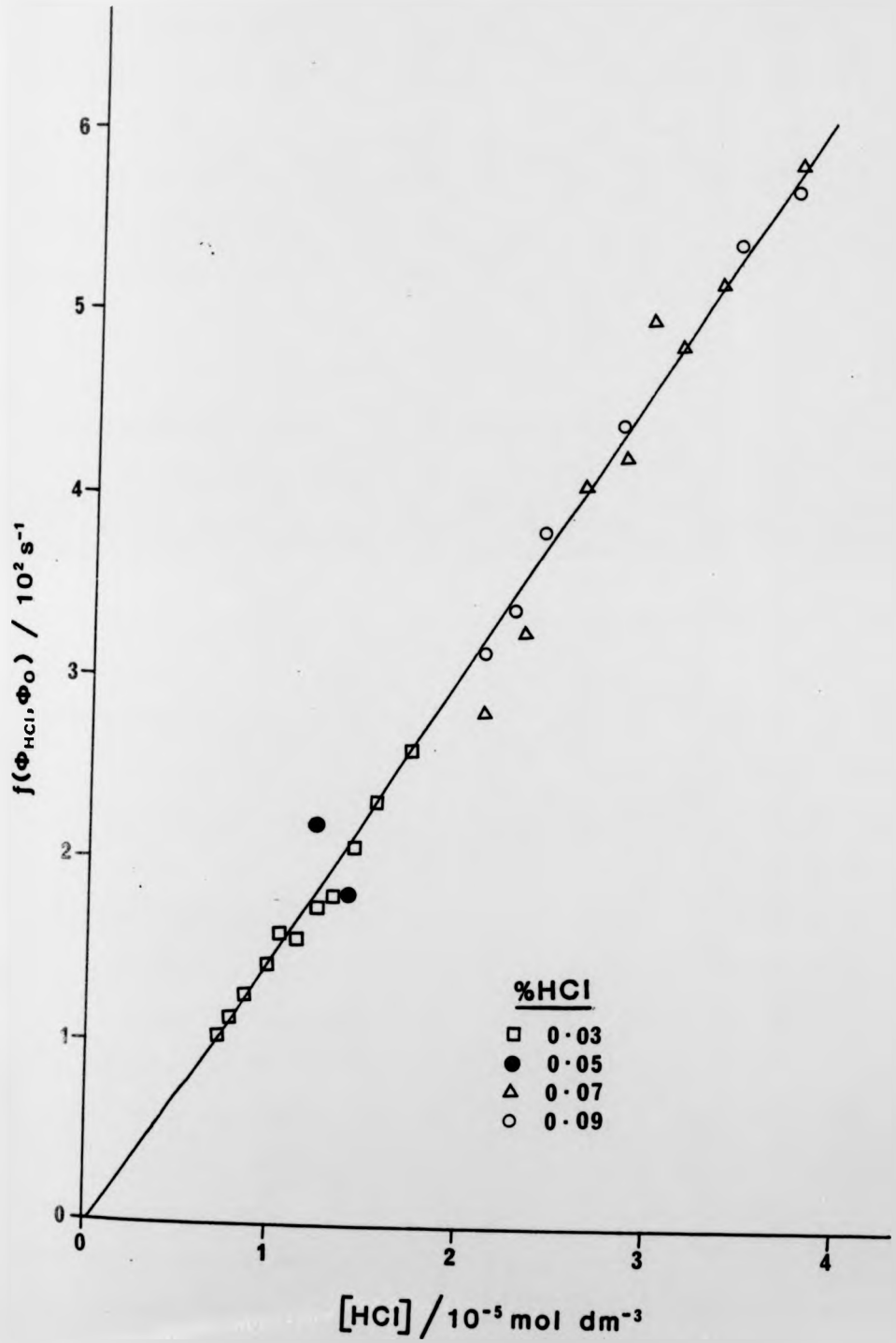

that the lower rate constant reported here is not the result of impurities in the system. In view of these facts, it is believed that the rate constant determined in this work is reliable and it is preferred to those reported by other workers.

The absence of a wall modification in these experiments supports the observation that there was no wall modification during the $HCl/O_2(a^1\Delta_g)$ experiments (section 5.2.1) and strengthens the view that a good value was obtained for k_d^{HCl} at 295K.

6.2.2 Deactivation of $O_2(b^1\Sigma^+_g)$ by HBr at 295K

In order to obtain a good estimate of k_q^{HBr} and to minimize the errors, a series of experiments was carried out which gave a total of 100 separate data points. The results are given in table 6.2. Figure 6.2 shows the plot of $f(\Phi_{HBr}, \Phi_o)$ versus [HBr]. The gradient is the second order rate constant for the collisional deactivation of $O_2(b^1\Sigma^+_g)$ by HBr.

$$k_q^{HBr} = (1.42 \pm 0.07) \times 10^8 \text{ mol}^{-1} \text{ dm}^3 \text{ s}^{-1}$$

The error limits are 2σ.

The plot is linear and has an intercept close to the origin (0,0), indicating that there is no significant modification of the wall deactivation in this case.

The contrast between the wall effect observed in the $HBr/O_2(a^1\Delta_g)$ experiments and the absence of a wall modification in this work may be explained by the difference in the nature of the wall deactivation processes. In the $HBr/O_2(a^1\Delta_g)$ experiments, the rate of deactivation at the wall is controlled by the efficiency of the wall with respect to $O_2(a^1\Delta_g)$. Therefore, an increase in the wall

Table 6.2 The Deactivation of $O_2(b^1\Sigma_g^+)$ by HBr at 295 K

HBr %	PRESSURE /torr	ϕHBr /x 10^{-3}	ϕO_2 /x 10^{-3}	$f(\phi HBr, \phi O_2)$ /s^{-1}	[HBr] /x 10^{-5} mol dm^{-3}
	3.71		4.21		
3	3.80	57		665	0.62
	4.09		3.83		
3	4.13	50		634	0.68
	4.25		3.97		
3	4.29	65		816	0.71
	4.37		4.03		
3	4.46	71		880	0.73
	4.62		4.01		
3	4.70	82		1042	0.77
	5.12		4.02		
3	5.24	86		1106	0.86
	5.61		4.05		
3	5.78	112		1480	0.95
	6.60		4.05		
3	6.27	113		1431	1.03
	6.68		4.07		
3	6.97	124		1781	1.15
	7.88		4.15		
3	7.96	133		1935	1.31
	3.80		4.38		
3	4.00	60		676	0.66
	4.00		4.20		
3	4.25	76		902	0.70

Table 6.2 continued

HBr %	PRESSURE /torr	ΦHBr /x 10^{-3}	ΦO_2 /x 10^{-3}	$f(\Phi HBr, \Phi O_2)$ /s^{-1}	[HBr] /x 10^{-5} mol dm^{-3}
	4.14		4.17		
3	4.33	89		1078	0.71
	4.58		4.08		
3	4.79	94		1179	0.79
	4.95		4.08		
3	5.28	105		1338	0.87
	5.49		3.94		
3	5.78	110		1480	0.95
	5.86		3.99		
3	6.19	128		1736	1.02
	6.35		4.00		
3	6.77	131		1820	1.11
	7.14		4.01		
3	7.67	158		2290	1.26
	7.76		4.09		
3	8.25	163		2401	1.36
	3.80		3.96		
3	3.96	87		1108	0.65
	3.84		3.99		
3	4.25	93		1177	0.70
	4.04		3.93		
3	4.25	93		1192	0.70
	4.41		3.96		
3	4.54	96		1232	0.75

Table 6.2 continued

HBr %	PRESSURE /torr	ΦHBr /x 10^{-3}	ΦO_2 /x 10^{-3}	$f(\Phi HBr, \Phi O_2)$ /s^{-1}	[HBr] /x 10^{-5} mol dm^{-3}
	4.70		3.96		
3	4.95	113		1467	0.81
	5.24		3.97		
3	5.45	122		1616	0.90
	5.57		3.94		
3	5.98	135		1831	0.98
	5.86		3.93		
3	6.23	136		1876	1.02
	6.39		3.93		
3	6.81	146		2070	1.19
	7.26		4.05		
3	7.71	159		2299	1.27
	3.80		3.98		
3	3.96	57		703	0.65
	3.96		3.98		
3	4.13	75		941	0.68
	4.08		3.96		
3	4.25	91		1165	0.70
	4.25		3.92		
3	4.46	85		1096	0.74
	4.54		3.88		
3	4.79	93		1224	0.79
	4.87		3.88		
3	5.12	98		1305	0.84

Table 6.2 continued

HBr %	PRESSURE /torr	ΦHBr /x 10^{-3}	ΦO_2 /x 10^{-3}	$f(\Phi HBr, \Phi O_2)$ /s^{-1}	[HBr] /x 10^{-5} mol dm^{-3}
	5.20		3.86		
3	5.53	108		1467	0.91
	5.69		3.85		
3	5.90	115		1601	0.97
	6.12		3.85		
3	6.52	131		1869	1.08
	7.14		3.93		
3	7.26	129		1902	1.20
	4.04		3.72		
5	4.25	150		2071	1.16
	4.91		3.71		
5	5.28	170		2406	1.45
	5.76		3.74		
5	6.15	210		3065	1.69
	6.81		3.80		
5	7.22	240		3634	1.99
	3.84		4.06		
5	4.04	140		1780	1.11
	4.54		4.07		
5	4.58	163		2080	1.25
	4.91		4.16		
5	5.03	162		2044	1.38
	5.53		4.12		
5	5.86	182		2381	1.61

Table 6.2 continued

HBr %	PRESSURE /torr	ΦHBr /x 10^{-3}	ΦO_2 /x 10^{-3}	f(ΦHBr, ΦO_2) /s^{-1}	[HBr] /x 10^{-5} mol dm^3
	5.98		4.18		
5	6.35	200		2637	1.74
	6.44		3.96		
5	7.10	214		3042	1.95
	7.59		4.05		
5	8.00	214		3172	2.19
	8.00		4.05		
5	8.50	250		3863	2.33
	3.96		4.20		
5	4.17	138		1685	1.15
	4.62		4.17		
5	4.79	157		1934	1.32
	5.12		4.11		
5	5.36	190		2461	1.47
	5.82		4.07		
5	6.15	226		3042	1.69
	6.56		4.27		
5	7.01	225		3000	1.93
	7.80		4.11		
5	8.21	214		3169	2.26
	8.91		4.23		
5	9.49	250		3854	2.61
	3.75				
5	3.88	132	4.20	1608	

Table 6.2 continued

HBr %	PRESSURE /torr	ΦHBr /x 10^{-3}	ΦO_2 /x 10^{-3}	f(ΦHBr, ΦO_2) /s^{-1}	[HBr] /x 10^{-5} mol dm^{-3}
	4.29		4.20		
5	4.46	146		1789	1.22
	4.95		4.11		
5	5.28	167		2137	1.45
	5.45		4.16		
5	5.78	188		2428	1.58
	5.86		4.18		
5	6.27	196		2562	1.72
	6.27		4.24		
5	6.60	192		2526	1.81
	7.18		4.10		
5	7.26	217		3105	1.99
	7.55		4.28		
5	7.67	231		3233	2.10
	3.92		3.95		
5	4.08	118		1527	1.12
	4.04		3.88		
5	4.29	124		1636	1.18
	4.46		3.82		
5	4.62	146		1980	1.27
	4.79		3.88		
5	4.99	155		2090	1.37
	5.28		3.85		
5	5.69	167		2311	1.57

Table 6.2 continued

HBr %	PRESSURE /torr	ΦHBr /x 10^{-3}	ΦO_2 /x 10^{-3}	$f(\Phi HBr, \Phi O_2)$ /s^{-1}	[HBr] /x 10^{-5} mol dm^{-3}
	5.69		3.83		
5	6.15	168		2381	1.68
	6.19		3.82		
5	6.68	186		2705	1.83
	6.72		3.93		
5	7.26	194		2822	2.00
	7.38				
5	8.04	215	3.91	3274	2.21
	8.13				
5	8.66	217	3.99	3365	2.38
	3.67				
7	3.92	136	4.18	1670	1.51
	3.96				
7	4.08	147	4.11	1849	1.57
	4.25				
7	4.58	163	4.06	2083	1.76
	4.58				
7	4.87	188	4.04	2431	1.87
	4.95				
7	5.32	192	4.01	2534	2.05
	5.45				
7	5.86	219	3.99	2966	2.26
	5.61				
7	6.11	216	3.96	2960	2.35

Table 6.2 continued

HBr %	PRESSURE /torr	ΦHBr /x 10^{-3}	ΦO_2 /x 10^{-3}	$f(\Phi HBr, \Phi O_2)$ /s^{-1}	[HBr] /x 10^{-5} mol dm^{-3}
	5.94				
7	6.44	235	3.95	3289	2.48
	6.44				
7	7.18	257	3.98	3640	2.76
	7.10				
7	7.76	258	4.01	3774	2.99
	3.71				
7	3.96	165	4.04	2104	1.52
	3.96				
7	4.21	170	4.03	2171	1.61
	4.25				
7	4.54	186	4.00	2413	1.74
	4.62		3.99		
7	4.99	200		2623	1.91
	4.99		4.00		
7	5.40	216		2858	2.07
	5.61		3.97		
7	5.98	232		3164	2.29
	6.52		4.03		
7	7.14	273		3850	2.74
	7.01		4.05		
7	7.67	277		3991	2.94
	3.71		4.18		
7	3.96	164		2020	1.52

Table 6.2 continued

HBr %	PRESSURE /torr	ΦHBr /x 10^{-3}	ΦO_2 /x 10^{-3}	$f(\Phi HBr, \Phi O_2)$ /s^{-1}	[HBr] /x 10^{-5} mol dm^{-3}
	3.96		4.10		
7	4.17	169		2120	1.60
	4.29		4.10		
7	4.54	193		2444	1.74
	4.91		4.05		
7	5.03	217		2830	1.93
	5.16		4.03		
7	5.61	237		3141	2.15
	5.94		4.02		
7	6.44	263		3616	2.47
	6.35		4.03		
7	6.93	264		3692	2.66
	6.72		4.03		
7	7.26	277		3951	2.78
	7.43		4.06		
7	8.09	273		4016	3.10

Figure 6.2 Deactivation of $O_2(b\ ^1\Sigma_g^+)$ by HBr at 295K

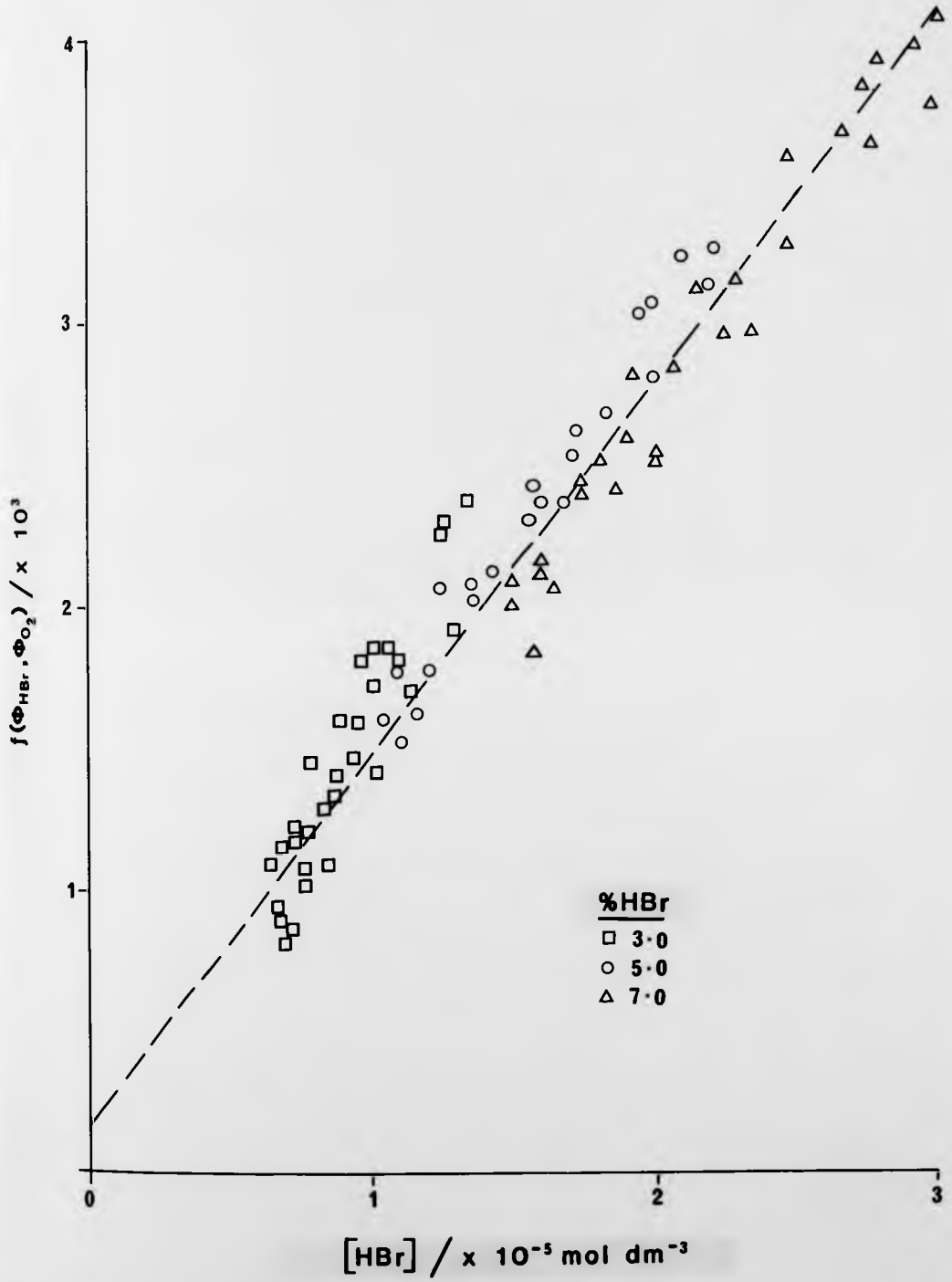

efficiency due to the adsorption of HBr will result in an increase in the wall deactivation rate for $O_2(a^1\Delta_g)$. In contrast, the efficiency of the wall with respect to $O_2(b^1\Sigma^+_g)$ is so great that the wall deactivation rate is diffusion controlled. Therefore, an increase in the wall efficiency with respect to $O_2(b^1\Sigma^+_g)$ will have no effect upon the wall deactivation rate for $O_2(b^1\Sigma^+_g)$.

The rate constant given here agrees very well with the work of Braithwaite and co-workers [42] and the forthcoming publication of Singh and Setser [87], who obtained:

$$k_q^{HBr} = (2.3 \pm 0.5) \times 10^8 \text{ mol}^{-1} \text{ dm}^3 \text{ s}^{-1} \quad [42]$$

$$k_q^{HBr} = (1.20 \pm 0.36) \times 10^8 \text{ mol}^{-1} \text{ dm}^3 \text{ s}^{-1} \quad [87]$$

6.2.3 Deactivation of $O_2(b^1\Sigma^+_g)$ by H_2 at 295K

In order to obtain a good estimate of $k_q^{H_2}$ and to minimize errors, a series of experiments was performed which gave a total of 100 separate data points. The results are presented in table 6.3. Figure 6.3 shows the plot of $f(\Phi_{H_2}, \Phi_o)$ versus $[H_2]$. The gradient is the second order rate constant for the collisional deactivation of $O_2(b^1\Sigma^+_g)$ by H_2.

$$k_q^{H_2} = (2.76 \pm 0.06) \times 10^8 \text{ mol}^{-1} \text{ dm}^3 \text{ s}^{-1}$$

The error limits are 2σ.

The plot is linear and has an intercept close to the origin (0,0), indicating that there is no significant change in the wall deactivation in this case.

Previously determined rate constants fall into two groups, an

Table 6.3 The Deactivation of $O_2(b^1\Sigma_g^+)$ by H_2 at 295 K

H_2 %	PRESSURE /torr	ΦH_2 /x 10^{-3}	ΦO_2 /x 10^{-3}	$f(\Phi H_2, \Phi O_2)$ /s^{-1}	$[H_2]$ /x 10^{-6} mol dm^{-3}
	5.03		5.08		
0.5	5.03	45		421	1.36
	5.20		5.25		
0.5	5.20	46		420	1.40
	5.45		5.28		
0.5	5.45	47		431	1.47
	5.69		5.35		
0.5	5.69	49		450	1.53
	6.02		5.32		
0.5	6.02	52		491	1.62
	6.44		5.47		
0.5	6.44	56		528	1.73
	6.93		6.05		
0.5	6.93	60		519	1.87
	7.34		5.64		
0.5	7.34	62		590	1.98
	7.84		5.72		
0.5	7.84	66		641	2.11
	8.09		5.75		
0.5	8.09	70		690	2.18
	5.07		5.21		
0.5	5.07	49		450	1.37
	5.28		5.34		
0.5	5.28	48		435	1.43

Table 6.3 continued

H_2 %	PRESSURE /torr	ΦH_2 /x 10^{-3}	ΦO_2 /x 10^{-3}	$f(\Phi H_2, \Phi O_2)$ /s^{-1}	$[H_2]$ /x 10^{-6} mol dm^{-3}
	5.61		5.36		
0.5	5.61	49		449	1.52
	5.78		5.37		
0.5	5.82	51		472	1.57
	6.06		5.40		
0.5	6.11	53		496	1.65
	6.44		5.46		
0.5	6.44	55		520	1.74
	6.77		5.51		
0.5	6.81	58		545	1.84
	7.14		5.58		
0.5	7.14	61		582	1.93
	7.59		5.65		
0.5	7.59	64		620	2.05
	7.88		5.74		
0.5	7.88	68		663	2.13
	8.46		5.84		
0.5	8.50	73		728	2.30
	5.03		5.33		
0.5	5.03	47		422	1.36
	5.20		5.45		
0.5	5.24	50		445	1.42
	5.53		5.48		

Table 6.3 continued

H_2 %	PRESSURE /torr	ΦH_2 /x 10^{-3}	ΦO_2 /x 10^{-3}	$f(\Phi H_2, \Phi O_2)$ /s^{-1}	$[H_2]$ /x 10^{-6} mol dm^{-3}
0.5	5.53	51		457	1.49
	5.86		5.55		
0.5	5.86	53		468	1.58
	6.19		5.57		
0.5	6.19	56		504	1.67
	6.44		5.65		
0.5	6.44	57		513	1.73
	6.77		5.70		
0.5	6.81	62		567	1.84
	6.97		5.70		
0.5	6.97	63		584	1.88
	7.10		5.77		
0.5	7.10	63		581	1.92
	7.43		5.85		
0.5	7.43	66		614	2.01
	5.07		5.23		
0.5	5.07	45		412	1.38
	5.24		5.32		
0.5	5.28	45		407	1.44
	5.45		5.36		
0.5	5.49	50		458	1.49
	5.69		5.35		
0.5	5.69	51		474	1.55
	5.86		5.36		

Table 6.3 continued

H_2 %	PRESSURE /torr	ΦH_2 /x 10^{-3}	ΦO_2 /x 10^{-3}	$f(\Phi H_2, \Phi O_2)$ /s^{-1}	$[H_2]$ /x 10^{-6} mol dm^{-3}
0.5	5.90	53		496	1.61
	6.19		5.38		
0.5	6.19	56		534	1.68
	6.52		5.43		
0.5	6.56	58		558	1.78
	6.93		5.54		
0.5	6.93	61		581	1.89
	7.47		5.61		
0.5	7.51	65		634	2.04
	8.00		5.74		
0.5	8.00	69		682	2.18
	5.03		5.11		
0.5	5.03	46		428	1.36
	5.20		5.31		
0.5	5.20	47		425	1.41
	5.32		5.32		
0.5	5.36	48		435	1.45
	5.53		5.36		
0.5	5.53	50		457	1.50
	5.86		5.41		
0.5	5.86	53		488	1.59
	6.23		5.52		
0.5	6.27	55		497	1.70
	6.60		5.50		

Table 6.3 continued

H_2 %	PRESSURE /torr	ΦH_2 /x 10^{-3}	ΦO_2 /x 10^{-3}	$f(\Phi H_2, \Phi O_2)$ /s^{-1}	$[H_2]$ /x 10^{-6} mol dm^{-3}
0.5	6.60	58		539	1.79
	6.97		5.60		
0.5	6.97	62		581	1.89
	7.10		5.63		
0.5	7.14	62		582	1.94
	7.59		5.77		
0.5	7.63	67		635	2.07
	5.12		5.21		
0.5	5.16	46		424	1.40
	5.36		5.22		
0.5	5.36	47		433	1.46
	5.53		5.25		
0.5	5.53	50		469	1.50
	5.69		5.27		
0.5	5.73	51		481	1.56
	5.86		5.29		
0.5	5.86	52		492	1.59
	6.23		5.32		
0.5	6.23	55		530	1.70
	6.68		5.43		
0.5	6.68	58		564	1.82
	6.85		5.46		
0.5	6.85	59		577	1.86

Table 6.3 continued

H_2 %	PRESSURE /torr	ΦH_2 /x 10^{-3}	ΦO_2 /x 10^{-3}	$f(\Phi H_2, \Phi O_2)$ /s^{-1}	$[H_2]$ /x 10^{-6} mol dm^{-3}
	7.26		5.51		
0.5	7.30	62		605	1.99
	7.47		5.62		
0.5	7.51	64		628	2.04
	4.58		5.37		
1.0	4.62	76		701	2.54
	4.95		5.34		
1.0	4.95	77		725	2.72
	5.20		5.31		
1.0	5.20	79		753	2.86
	5.40		5.36		
1.0	5.40	82		786	2.97
	5.78		5.41		
1.0	5.78	93		905	3.18
	6.27		5.48		
1.0	6.27	95		930	3.45
	6.56		5.54		
1.0	6.60	102		995	3.63
	7.22		5.68		
1.0	7.22	109		1079	3.97
	7.84		5.84		
1.0	7.84	121		1217	4.31
	8.09		5.94		
1.0	8.09	122		1221	4.45

Table 6.3 continued

H_2 %	PRESSURE /torr	ΦH_2 /x 10^{-3}	ΦO_2 /x 10^{-3}	$f(\Phi H_2, \Phi O_2)$ /s^{-1}	$[H_2]$ /x 10^{-6} mol dm^{-3}
	4.99		5.57		
1.0	5.03	82		729	2.75
	5.34		5.52		
1.0	5.34	83		755	2.92
	5.49		5.56		
1.0	5.49	88		804	2.99
	5.86		5.56		
1.0	5.90	92		859	3.22
	6.27		5.67		
1.0	6.31	97		904	3.45
	6.77		5.76		
1.0	6.77	105		996	3.70
	7.26		5.88		
1.0	7.34	113		1081	4.01
	7.84		5.94		
1.0	7.84	121		1193	4.28
	8.42		6.13		
1.0	8.46	131		1295	4.62
	8.91		6.19		
1.0	8.91	141		1426	4.87
	4.87		5.37		
1.0	4.87	79		738	2.67
	5.03		5.32		
1.0	5.07	79		748	2.78

Table 6.3 continued

H_2 %	PRESSURE /torr	ΦH_2 /x 10^{-3}	ΦO_2 /x 10^{-3}	$f(\Phi H_2, \Phi O_2)$ /s^{-1}	$[H_2]$ /x 10^{-6} mol dm^{-3}
	5.28		5.36		
1.0	5.28	84		797	2.89
	5.49		5.38		
1.0	5.53	86		826	3.03
	6.11		5.44		
1.0	6.11	96		937	3.35
	6.44		5.54		
1.0	6.48	101		976	3.55
	6.85		5.58		
1.0	6.93	108		1069	3.80
	7.51		5.77		
1.0	7.59	117		1167	4.12
	8.50		5.93		
1.0	8.58	136		1402	4.70
	9.08		6.11		
1.0	9.12	143		1485	5.00
	4.66		5.44		
1.0	4.70	80		731	2.54
	5.03		5.42		
1.0	5.03	83		772	2.74
	5.53		5.47		
1.0	5.57	89		841	3.03
	5.94		5.57		
1.0	5.98	93		869	3.25

Table 6.3 continued

H_2 %	PRESSURE /torr	ΦH_2 /x 10^{-3}	ΦO_2 /x 10^{-3}	$f(\Phi H_2, \Phi O_2)$ /s^{-1}	$[H_2]$ /x 10^{-6} mol dm^{-3}
	6.52		5.64		
1.0	6.56	102		971	3.57
	7.10		5.73		
1.0	7.14	112		1090	3.89
	7.67		5.89		
1.0	7.71	125		1226	4.20
	8.25		5.98		
1.0	8.25	135		1356	4.49
	8.54		6.07		
1.0	8.58	139		1397	4.62
	8.99		6.18		
1.0	9.08	141		1428	4.94

Figure 6.3 Deactivation of $O_2(b\ ^1\Sigma_g^+)$ by H_2 at 295K

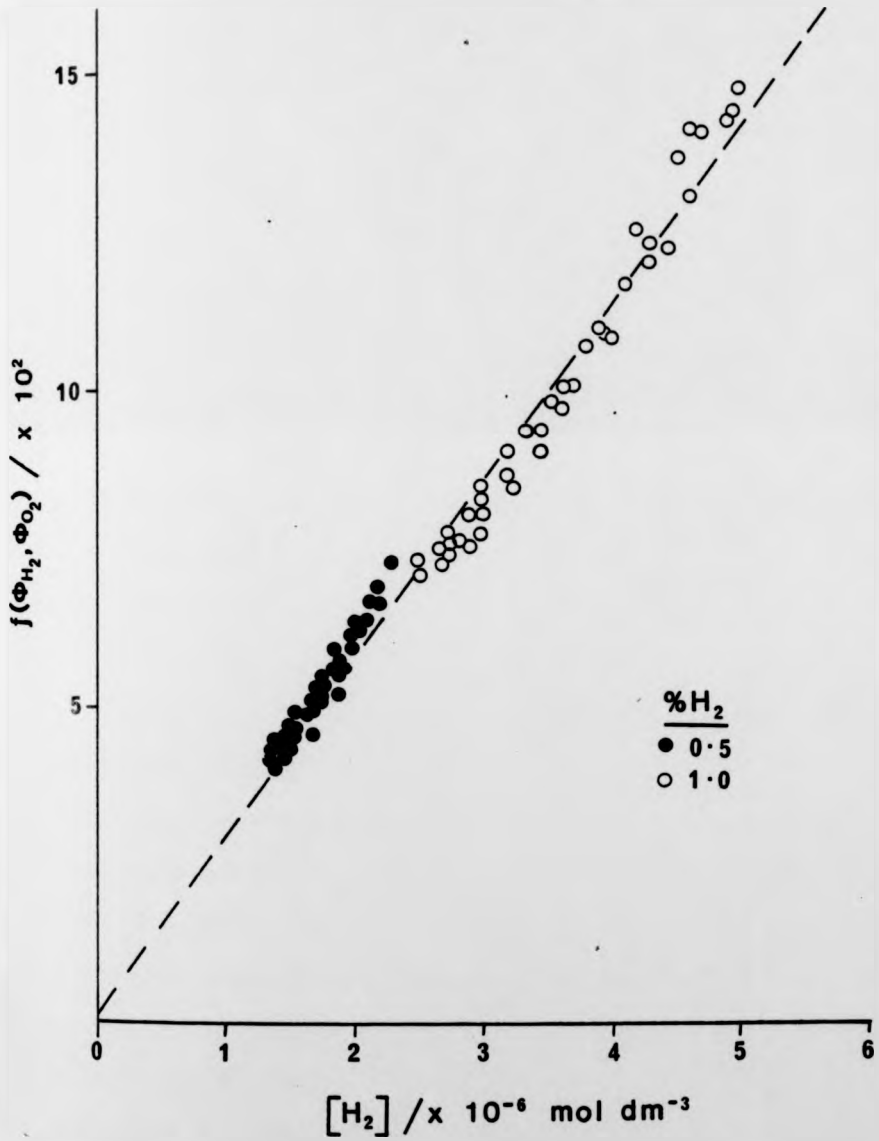

upper group of values around 5 x 10^8 mol^{-1} dm^3 s^{-1} [85,86,42] and a lower group of values around 2.5 x 10^8 mol^{-1} dm^3 s^{-1} [87,89,90]. Since the effect of impurities tends to increase rather than decrease the observed rate constant, the lower group of values is preferred. The rate constant determined in this work lies within the lower group, consisting of results by Becker, Groth and Schurath [89], Singh and Setser [87] and O'Brien and Myers [90], who obtained:

$$k_q^{H_2} = (2.71 \pm 1.20) \times 10^8 \text{ mol}^{-1} \text{ dm}^3 \text{ s}^{-1} \quad [87]$$

$$k_q^{H_2} = (2.41 \pm 0.72) \times 10^8 \text{ mol}^{-1} \text{ dm}^3 \text{ s}^{-1} \quad [89]$$

$$k_q^{H_2} = (2.41 \pm 0.36) \times 10^8 \text{ mol}^{-1} \text{ dm}^3 \text{ s}^{-1} \quad [90]$$

All four results lie within the same error limits. However, the value of the rate constant determined here is preferred because of the large number of data points.

6.2.4 Deactivation of $O_2(b^1\Sigma^+_g)$ by D_2 at 295K

Since only a small quantity of D_2 was available, a series of experiments was carried out which gave only 40 separate data points. It is felt that 40 data points are sufficient to give a good estimate of the rate constant for the deactivation of $O_2(b^1\Sigma^+_g)$ by D_2 with reasonably small errors and still conserve D_2 for high temperature experiments. The results of this determination are given in table 6.4. Figure 6.4 shows the plot of $f(\Phi_{D_2}, \Phi_o)$ versus $[D_2]$ which has the rate constant $k_q^{D_2}$ as its gradient.

Table 6.4 The Deactivation of $O_2(b^1\Sigma_g^+)$ by D_2 at 295 K

D_2 %	PRESSURE /torr	ΦD_2 /x 10^{-3}	ΦO_2 /x 10^{-3}	$f(\Phi D_2, \Phi O_2)$ $/s^{-1}$	$[D_2]$ /x 10^{-6} mol dm^{-3}
	4.17		5.58		
1.47	4.17	7.94		22.4	3.37
	4.29		5.46		
1.47	4.33	7.87		23.4	3.50
	4.66		5.48		
1.47	4.70	7.94		23.8	3.80
	4.95		5.48		
1.47	4.99	7.85		23.3	4.03
	5.40		5.53		
1.47	5.49	8.20		26.5	4.44
	5.57		5.34		
1.47	5.65	8.10		28.5	4.57
	6.11		5.66		
1.47	6.19	8.52		28.6	5.00
	6.72		5.73		
1.47	6.84	8.58		29.0	5.53
	7.38		5.84		
1.47	7.47	9.14		34.2	6.04
	8.00		5.98		
1.47	8.09	9.99		42.1	6.54
	4.41		5.64		
1.47	4.46	8.16		23.6	3.57
	4.66		5.65		
1.47	4.74	8.03		22.4	3.79

Table 6.4 continued

D_2 %	PRESSURE /torr	ΦD_2 /x 10^{-3}	ΦO_2 /x 10^{-3}	$f(\Phi D_2, \Phi O_2)$ /s^{-1}	$[D_2]$ /x 10^{-6} mol dm^{-3}
	4.99		5.51		
1.47	5.07	7.99		24.2	4.06
	5.45		5.73		
1.47	5.53	8.48		26.3	4.42
	5.82		5.78		
1.47	5.94	8.45		25.7	4.75
	6.19		5.85		
1.47	6.27	8.95		29.9	5.02
	7.14		6.02		
1.47	7.22	8.95		29.0	5.71
	7.84		6.25		
1.47	7.92	9.54		32.5	6.34
	8.09		5.27		
1.47	8.17	9.64		38.7	6.47
	4.21		5.21		
3.45	4.25	9.77		45.2	8.01
	4.46		5.24		
3.45	4.54	9.83		46.5	8.55
	4.70		5.27		
3.45	4.79	10.2		49.9	9.02
	4.12		5.48		
3.45	5.20	10.2		46.6	9.80
	5.57		5.37		
3.45	5.90	10.7		54.6	10.7

Table 6.4 continued

D_2 %	PRESSURE /torr	ΦD_2 /x 10^{-3}	ΦO_2 /x 10^{-3}	$f(\Phi D_2, \Phi O_2)$ /s^{-1}	$[D_2]$ /x 10^{-6} mol dm^{-3}
	6.31		5.42		
3.45	6.39	12.0		67.7	12.0
	7.05		5.53		
3.45	7.18	13.5		70.3	13.5
	8.09		5.68		
3.45	8.25	15.5		74.3	15.5
	8.66		5.77		
3.45	8.91	16.8		88.1	16.8
	4.13		5.52		
4.55	4.21	11.7		59.1	10.5
	4.29		5.69		
4.55	4.37	11.2		51.2	10.9
	4.62		5.72		
4.55	4.74	11.9		57.6	11.8
	4.95		5.56		
4.55	5.07	12.3		65.2	12.6
	5.45		5.59		
4.55	5.61	12.8		70.7	13.9
	5.82		5.61		
4.55	5.94	13.2		75.4	14.8
	6.44		5.72		
4.55	6.64	14.1		84.1	16.5
	7.10		5.82		

Table 6.4 continued

D_2 %	PRESSURE /torr	ΦD_2 /x 10^{-3}	ΦO_2 /x 10^{-3}	$f(\Phi D_2, \Phi O_2)$ /s^{-1}	$[D_2]$ /x 10^{-6} mol dm^{-3}
4.55	7.30	14.8		91.7	18.1
	7.63		6.20		
4.55	7.84	16.6		102.6	19.5
	8.46		6.44		
4.55	8.66	17.6		111.3	21.0

Figure 6.4 Deactivation of $O_2(b\ ^1\Sigma_g^+)$ by D_2 at 295 K

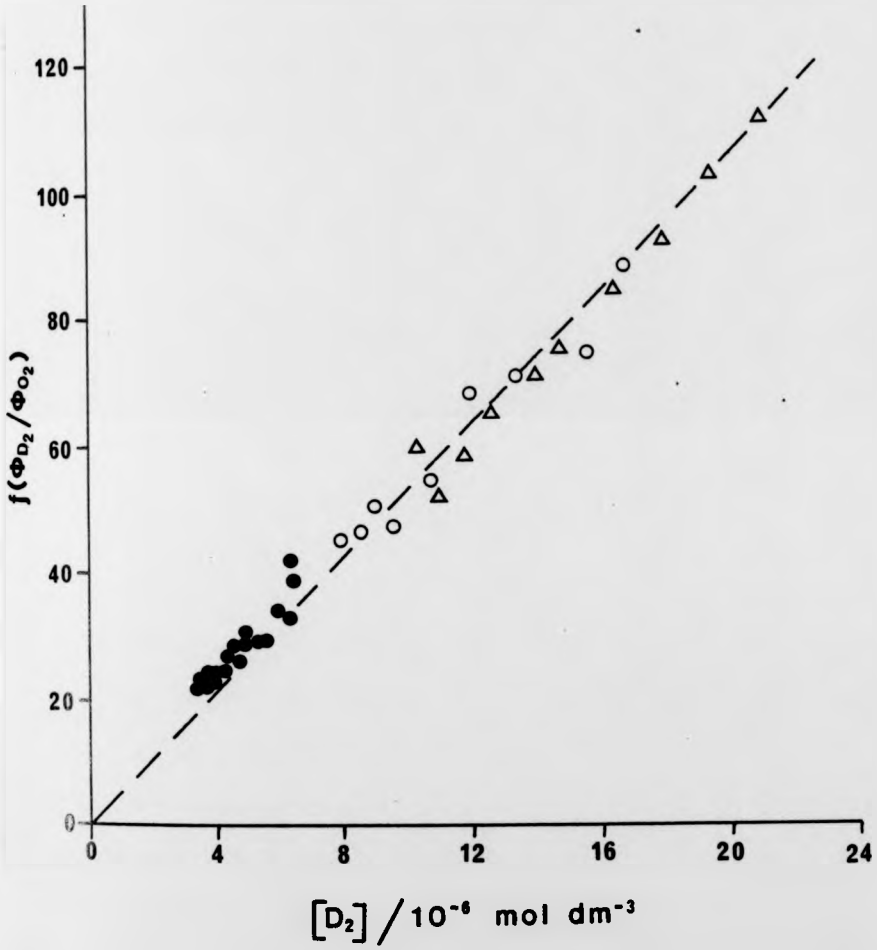

$$k_q^{D_2} = (5.27 \pm 0.18) \times 10^6 \text{ mol}^{-1} \text{ dm}^3 \text{ s}^{-1}$$

The error limits are 2σ.

Again, a linear plot is obtained with an intercept at the origin (0,0), indicating that there is no change in the wall reaction.

The rate constant given here is lower than those reported by O'Brien and Myers [90] and Davidson, Kear and Abrahamson [39].

$$k_q^{D_2} = (1.20 \pm 0.30) \times 10^7 \text{ mol}^{-1} \text{ dm}^3 \text{ s}^{-1} \quad [90]$$

$$k_q^{D_2} = (1.02 \pm 0.20) \times 10^7 \text{ mol}^{-1} \text{ dm}^3 \text{ s}^{-1} \quad [39]$$

It is nearer to that reported by Kohse-Hoinghaus and Stuhl [85].

$$k_q^{D_2} = (8.43 \pm 1.20) \times 10^6 \text{ mol}^{-1} \text{ dm}^3 \text{ s}^{-1} \quad [85]$$

However, they estimate that the rate constant may be 10 - 20 percent too large because of an unquantified H_2 impurity in their D_2 supply. The presence of H_2, which is 20 times more efficient as a deactivator of $O_2(b^1\Sigma^+_g)$, is a possible reason why the other two values are also larger than the value reported in this work. The value reported here is preferred to the above values [85,90,36] as it is lower and therefore may be less affected by an H_2 impurity.

Kohse-Hoinghaus and Stuhl [85] report that Becker, Groth and Schurath [92] determined the ratio $k_q^{D_2}:k_q^{H_2}$ to be 0.0168:1. Taking their value for $k_q^{H_2}$, which agrees well with that determined in the previous section, a value of

$$k_q^{D_2} = 4.03 \times 10^6 \text{ mol}^{-1} \text{ dm}^3 \text{ s}^{-1}$$

is obtained.

Although this value is the lowest, the value determined here is preferred because it was obtained independently of the $k_q^{H_2}$ value.

6.3 High Temperature Studies of the Collisional Deactivation of $O_2(b^1\Sigma^+_g)$

The determination of the rate constants for the deactivation of $O_2(b^1\Sigma^+_g)$ at temperatures between 500 and 1200 Kelvin was carried out by the method described in section 4.5. As with the $O_2(a^1\Delta_g)$ studies, it was not possible to make high temperature measurements of the deactivation of $O_2(b^1\Sigma^+_g)$ by HBr, for the reasons outlined in section 5.3.1.

In studies with HCl, H_2 and D_2, experiments were performed with mixtures of between 0.5 and 7.0 percent of these deactivators in pure O_2. The total volume flow rate at s.t.p. was 28.0 $cm^3\ s^{-1}$, at total pressures of approximately 6 torr, giving a typical linear flow velocity of about 1.6 $m\ s^{-1}$.

Before shock heating, the pre-shock decay of the $O_2(b^1\Sigma^+_g)$ emission (762nm) along the flow tube was measured using a movable photomultiplier.

Since the determination of the deactivation of $O_2(a^1\Delta_g)$ by each of these additives showed a significant increase in k_d^m at high temperatures, the analysis of the $O_2(b^1\Sigma^+_g)$ data was carried out using the 762nm Kinetic Model (equation 4.80) which takes the simultaneous deactivation of $O_2(a^1\Delta_g)$ into account.

6.3.1 Deactivation of $O_2(b^1\Sigma^+_g)$ by HCl at High Temperatures

This experimental work was carried out in collaboration with Boodaghians [44]. However, the data have been reanalysed here in view of the corrections to the $O_2(b^1\Sigma^+_g)$ deactivation rate constants discussed in section 4.5.2. The corrections arise from the participation of the reaction:

$$O_2(a^1\Delta_g) + M \text{ ----> } O_2(b^1\Sigma^+_g) + M \qquad (4.45)$$

and gain significance at temperatures above 1000K. Previous results for the temperature dependence of the deactivation of $O_2(b^1\Sigma^+_g)$ by NH_3, NO and HCl have shown a 'fall off' in the rate constant for the process at high temperatures. By allowing for reaction (4.45), it was hoped to determine whether the 'fall off' is a true representation of the temperature dependence or the result of using an incomplete kinetic scheme to describe the reactions in the shock heated gas.

Fixed integration times, t_s, calculated for the single slit mechanism (table 2.3) were used, together with fixed values of the energy pooling reaction rate constant, k_p, which were obtained in several previous studies [13,44,46,60] and are independent of the additive. The relaxation time of $O_2(b^1\Sigma^+_g)$, τ_{rel}, is very short in the presence of HCl (k_q^m is large) and becomes comparable to the integration time at higher temperatures so that the fitting of the two parameters would be interdependent. Therefore t_s is fixed to reduce the errors in the k_q^m value. The fixing of k_p allows ^{762}K to be established from the value of k_q^m obtained by fitting the 762nm Kinetic Model to the data. The value of ^{762}K is well defined as it is determined by the fit of equation (4.80) without influence from errors in t_s.

The device of fixing t_s and k_p allows the fitting of k_q^m and $k_d^{m'}$ to be carried out more accurately and more rapidly. The sensitivity analysis discussed in section 4.5.1 shows the wisdom of fixing these parameters in the $O_2(b^1\Sigma^+_g)$ analysis.

The results of the analysis are given in table 5.5, and the input parameters for each run are listed in Appendix 3. Figure 6.5 shows the temperature dependence of k_q^{HCl}. The dashed line has been

Table 6.5 Deactivation of $O_2(^1\Sigma_g^+)$ by HCl

HCl %	Run no	T_2 /Kelvin	^{762}K	k_q^{HCl} /x 10^7 mol^{-1} dm^3 s^{-1}	T_{rel} μs	k_p /x 10^4 mol^{-1} dm^3 s^{-1}
3	RA346	599	1.22	3.1	116	4.06
3	RA348	630	1.25	3.3	96	4.49
3	RA345	707	1.22	6.3	56	6.92
3	RA337	804	1.13	11.0	28	10.57
3	RA340	893	1.61	7.3	28	12.57
3	RA342	1038	2.25	3.8	26	17.08
5	RA334	725	1.42	6.3	36	7.95
5	RA350	736	1.12	4.3	29	7.98
5	RA332	825	2.05	5.1	33	10.94
5	RA330	891	2.29	5.1	29	13.09
5	RA331	944	2.14	5.6	22	14.09
5	RA351	947	1.82	7.8	19	14.46
5	RA353	1032	3.53	6.6	18	16.64
5	RA352	1046	2.77	3.9	21	17.31
7	RA362	701	1.69	3.6	40	5.85
7	RA361	743	1.49	5.9	27	7.78
7	RA360	778	1.56	6.5	24	9.08
7	RA359	818	1.63	6.8	21	10.21
7	RA358	880	1.51	9.1	16	12.20
7	RA357	958	1.66	9.1	14	14.11

Figure 6.5 Deactivation of $O_2(b\ ^1\Sigma_g^+)$ by HCl

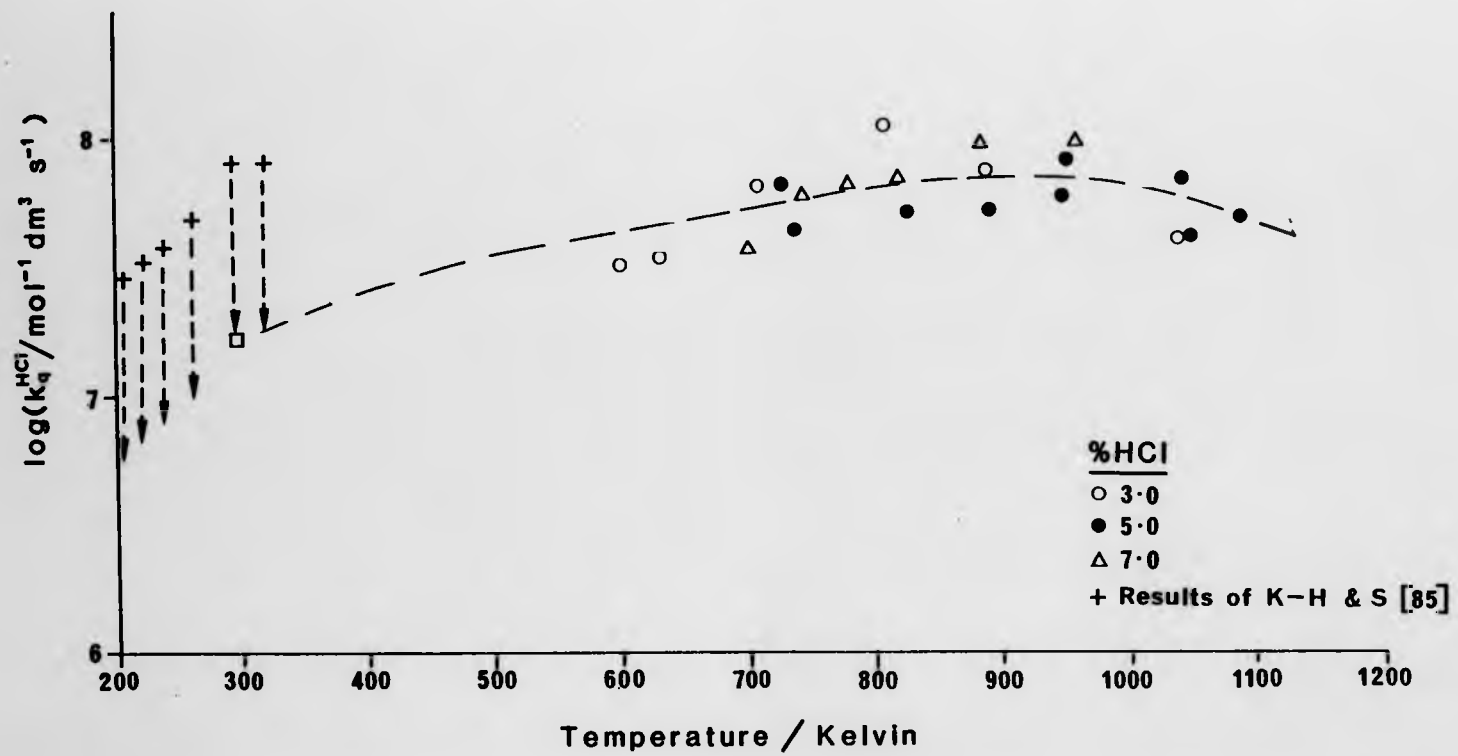

drawn by eye to show the general trend. The plot shows a slight positive temperature dependence which 'falls off' at higher temperatures.

The scatter in the results is typical of shock tube results. The large signal to noise ratio, however, aids the reduction of the scatter in these $O_2(b^1\Sigma^+_g)$ studies carried out with the discharge flow - shock tube.

One may conclude from the reanalysis that the model used by Boodaghians (equation 4.80 without corrections) is as appropriate as the one used in this work, which allows for $O_2(a^1\Delta_g)$ as a source of $O_2(b^1\Sigma^+_g)$, over the temperature range 295 to 1200 Kelvin. The observation that k_q^{HCl} 'falls off' at high temperatures must, therefore, be a result of the physical chemistry of the interaction.

The only other temperature dependence study of the deactivation of $O_2(b^1\Sigma^+_g)$ by HCl found in the literature is that of Kohse-Hoinghaus and Stuhl [85] who also obtained a small positive temperature dependence over the range 205 to 311 Kelvin. Their data have been added to figure 6.5. Taken together the two sets of data indicate that the deactivation of $O_2(a^1\Delta_g)$ by HCl is nearly independent of temperature. However, if the results were scaled down so that their value at 295K coincides with the one determined in this work, as indicated by the arrows on figure 6.5, they would follow the same trend as the results obtained here. That is to say, a small positive temperature dependence would be observed overall.

6.3.2 Deactivation of $O_2(b^1\Sigma^+_g)$ by H_2 at High Temperature

A series of determinations was carried out on mixtures containing 0.5 and 1.0 percent H_2 in pure O_2. The data were analysed by fitting the 762nm Kinetic Model in the same way as described in

the previous section. The results of the analysis are given in table 6.6(a). The input parameters for each run may be found in Appendix 4.

As with the $O_2(a^1\Delta_g)$ studies, an additional emission was seen at the monitoring wavelength (762nm in this case) which prevented analysis of the data above 1000K. This additional emission is discussed in section 6.4. A series of experiments was carried out using a $1\%H_2/24\%N_2/75\%O_2$ mixture, in an attempt to extend the temperature range.

Rather than use previously determined values of $k_q^{N_2}$ [46] to calculate the deactivation due to N_2 in the $H_2/N_2/O_2$ mixtures, it was decided to measure the deactivation of $O_2(b^1\Sigma^+_g)$ due to N_2/O_2 mixtures before proceeding with the $H_2/N_2/O_2$ experiments. Mixtures of 10, 25 and 50 percent N_2 in pure O_2 were tested in the same manner as the H_2/O_2 mixtures, except that k_p was also fitted since k_q^m is small (τ_{rel} is large) in this case. Results for these mixtures are given in table 6.7. Run parameters may be found in Appendix 5. For each mixture, k_q^m was plotted against temperature (figure 6.6). The scatter is sufficiently great, and the difference in deactivation sufficiently small, that it is not possible to draw three distinct curves through the points with any degree of accuracy.

An attempt was made to determine $k_q^{O_2}$ and $k_q^{N_2}$ by solving simultaneous equations at various temperatures. This was unsuccessful since the third set of results (50% N_2) did not agree with predicted values for this composition made from values of $k_q^{O_2}$ and $k_q^{N_2}$, calculated from the other two sets of results (10 and 25% N_2).

Although it would be possible to improve the scatter statistically by producing much more data, this would be a side track from the intended investigation. Since $k_q^{O_2}$ and $k_q^{N_2}$ could not be accurately obtained from this work, the overall constant k_q^m for the N_2/O_2 mixture was used when analysing the $H_2/N_2/O_2$ mixture.

Table 6.6(a) Deactivation of $O_2(b^1\Sigma_g^+)$ by H_2 in pure O_2

H_2 %	Run No	T_2 /Kelvin	^{762}K	$k_q^{H_2}$ /x 10^8 mol^{-1} dm^3 s^{-1}	k_p /x 10^4 mol^{-1} dm^3 s^{-1}
0.5	DSR61B	516	1.89	2.66	2.95
0.5	DSR30B	609	2.67	2.44	4.37
0.5	DSR29B	613	2.82	2.22	4.41
0.5	DSR27B	617	2.85	2.20	4.47
0.5	DSR32B	625	2.60	2.76	4.68
0.5	DSR31B	628	2.78	2.54	4.75
0.5	DSR33B	633	3.11	2.06	4.79
0.5	DSR35B	649	2.91	2.64	5.25
0.5	DSR36B	676	3.33	2.42	5.89
0.5	DSR38B	684	3.59	2.70	6.03
0.5	DSR34B	685	3.25	2.58	6.03
0.5	DSR39B	689	3.36	2.48	6.17
0.5	DSR40B	691	3.28	2.64	6.24
0.5	DSR37B	706	3.57	2.44	6.61
0.5	DSR42B	735	3.39	3.10	7.50
0.5	DSR43B	769	3.43	3.62	8.71
0.5	DSR44B	769	3.54	3.44	8.71
0.5	DSR41B	775	3.71	3.22	8.91
0.5	DSR46B	887	3.76	5.60	14.13
0.5	DSR45B	911	3.84	6.18	15.85
0.5	DSR47B	923	4.14	5.86	16.79
0.5	DSR49B	950	4.11	6.74	18.62
0.5	DSR48B	979	4.44	7.00	21.13
1.0	DSR60B	521	2.06	2.86	3.00

Table 6.6(a)

H_2 %	Run No	T_2 /Kelvin	^{762}K	$k_q^{H_2}$ /x 10^8 mol^{-1} dm^3 s^{-1}	k_p /x 10^4 mol^{-1} dm^3 s^{-1}
1.0	DSR59B	532	2.12	2.93	3.16
1.0	DSR52B	555	2.31	2.89	3.47
1.0	DSR51B	557	2.01	3.49	3.50
1.0	DSR53B	564	2.15	3.67	3.63
1.0	DSR54B	591	2.47	3.06	3.98
1.0	DSR55B	603	2.58	3.13	4.27
1.0	DSR5B	610	3.14	2.54	4.37
1.0	DSR7B	621	3.21	2.58	4.57
1.0	DSR6B	625	3.30	2.55	4.68
1.0	DSR4B	627	2.90	3.07	4.73
1.0	DSR50B	633	2.71	3.32	4.79
1.0	DSR9B	644	2.93	3.28	5.13
1.0	DSR10B	668	3.34	3.12	5.62
1.0	DSR8B	693	3.84	2.96	6.31
1.0	DSR18B	701	3.35	3.51	6.46
1.0	DSR11B	750	3.95	3.61	7.94
1.0	DSR15B	765	3.59	4.26	8.41
1.0	DSR12B	767	3.73	4.17	8.51
1.0	DSR24B	783	3.71	4.44	9.16
1.0	DSR17B	814	4.08	4.62	10.47
1.0	DSR19B	818	3.59	5.46	10.59
1.0	DSR23B	810	4.20	5.63	13.18
1.0	DSR20B	879	4.42	5.55	13.80
1.0	DSR21B	883	4.42	5.59	13.96

Table 6.6(a) continued

H_2 %	Run No	T_2 /Kelvin	^{762}K	$k_q^{H_2}$ /x 10^8 mol^{-1} dm^3 s^{-1}	k_p /x 10^4 mol^{-1} dm^3 s^{-1}
1.0	DSR25B	946	5.15	6.54	19.05
1.0	DSR22B	978	5.36	6.77	20.89

Table 6.6(b) Deactivation of $O_2(b^1\Sigma_g^+)$ by H_2 in O_2/N_2 mixtures

H_2 %	N_2 %	Run No	T_2 /Kelvin	^{762}K	$k_q^{H_2}$ /x 10^8 mol^{-1} dm^3 s^{-1}	T_{rel} /μs	k_p /x 10^4 mol^{-1} dm^3 s^{-1}
1.0	24.0	DSR420B	514	2.93	1.53	131	2.19
1.0	24.0	DSR422B	525	2.93	1.79	107	2.48
1.0	24.0	DSR421B	535	3.60	1.48	155	2.65
1.0	24.0	DSR423B	557	3.44	1.85	101	3.05
1.0	24.0	DSR424B	601	3.64	3.27	72	3.81
1.0	24.0	DSR416B	616	3.20	2.99	55	4.29
1.0	24.0	DSR419B	620	3.49	2.79	67	4.37
1.0	24.0	DSR418B	627	3.74	2.79	59	4.72
1.0	24.0	DSR415B	644	3.62	2.99	52	4.91
1.0	24.0	DSR412B	682	3.55	3.71	42	5.76
1.0	24.0	DSR410B	691	4.29	3.05	48	5.89
1.0	24.0	DSR414B	704	4.51	3.00	47	6.10
1.0	24.0	DSR413B	730	3.65	4.46	33	6.94
1.0	24.0	DSR411B	738	4.58	3.49	44	6.98

Table 6.6(b) continued

H_2 %	N_2 %	Run No	T_2 /Kelvin	^{762}K	$k_q^{H_2}$ /x 10^8 mol^{-1} dm^3 s^{-1}	τ_{rel} /μs	k_p /x 10^4 mol^{-1} dm^3 s^{-1}
1.0	24.0	DSR404B	807	4.05	4.92	29	8.61
1.0	24.0	DSR405B	849	3.46	6.06	21	8.92
1.0	24.0	DSR402B	858	4.38	4.69	22	9.18
1.0	24.0	DSR401B	877	3.62	5.74	21	9.03
1.0	24.0	DSR409B	877	3.48	6.02	22	9.02
1.0	24.0	DSR407B	968	1.40	8.27	16	4.84
1.0	24.0	DSR406B	978	2.98	5.72	17	7.52

Figure 6.6 Deactivation of $O_2(b\ ^1\Sigma_g^+)$ by O_2 / N_2 mixtures

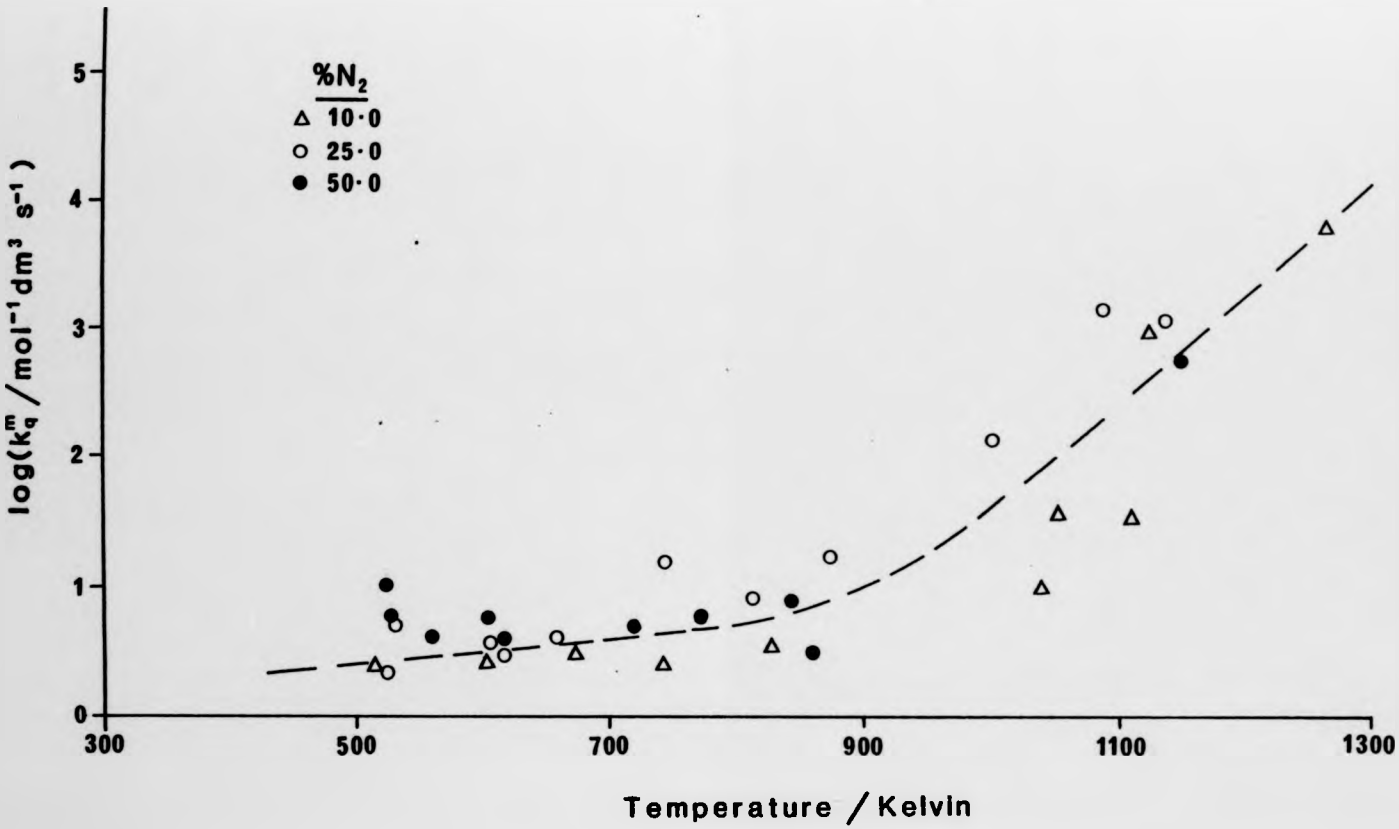

Table 6.7 Deactivation of $O_2(b^1\Sigma_g^+)$ by N_2/O_2 mixtures

N_2 %	Run No	T_2 /Kelvin	^{762}K	k_q^m /x 10^5	τ_{rel} /μs	k_p /x 10^4 mol^{-1} dm^3 s^{-1}
10	DSR234B	519	1.49	3.97	781	2.49
10	DSR229B	604	1.89	4.70	473	3.78
10	DSR228B	676	2.07	5.90	364	4.46
10	DSR227B	742	2.12	3.96	441	3.45
10	DSR225B	829	2.26	5.51	275	5.16
10	DSR232B	1040	2.23	9.95	118	9.33
10	DSR226B	1053	1.63	15.77	80	10.41
10	DSR224B	1110	1.49	15.49	69	9.83
10	DSR223B	1124	1.43	30.22	41	17.22
10	DSR233B	1263	1.66	38.62	24	10.98
25	DSR239B	525	1.74	3.68	755	1.71
25	DSR238B	527	2.00	6.89	486	3.50
25	DSR216B	609	2.67	6.41	354	4.47
25	DSR222B	612	2.83	4.55	509	3.33
25	DSR221B	656	2.97	5.94	345	4.58
25	DSR218B	742	2.54	11.89	142	7.80
25	DSR220B	814	3.53	8.14	194	7.44
25	DSR219B	874	2.74	12.49	109	8.97
25	DSR211B	1001	2.67	21.44	57	14.91
25	DSR212B	1087	2.41	31.38	36	19.66
25	DSR215B	1135	2.20	30.57	39	17.10
50	DSR208B	523	2.28	10.20	330	3.67
50	DSR209B	526	2.64	7.15	484	2.97
50	DSR210B	561	3.26	6.19	431	3.23

Table 6.7 continued

N_2 %	Run No	T_2 /Kelvin	^{762}K	k_q^m /x 10^5	τ_{rel} /μs	k_p /x 10^4 mol^{-1} dm^3 s^{-1}
50	DSR207B	606	3.03	8.24	285	3.94
50	DSR206B	614	3.82	6.24	351	3.82
50	DSR205B	718	4.94	7.06	273	5.50
50	DSR203B	769	4.83	7.46	243	5.67
50	DSR204B	843	5.74	9.13	176	8.26
50	DSR201B	858	9.00	4.99	43	7.10
50	DSR202B	1147	4.18	27.6	304	18.2

The results of the temperature dependence study of the deactivation of $O_2(b^1\Sigma^+_g)$ by H_2 in $H_2/N_2/O_2$ mixtures are given in table 6.6(b) and the run parameters are also given in Appendix 4.

Figure 6.7 shows the temperature dependence of $k_q^{H_2}$. The dashed line has been drawn by eye to show the general trend. The plot shows an increase in $k_q^{H_2}$ with temperature which, unlike that for the deactivation of $O_2(b^1\Sigma^+_g)$ by HCl and other efficient deactivators [44], does not 'fall off' at higher temperatures. The scatter is good for shock tube results which is due in part to the large signal to noise ratio and to the fact that H_2 is easier to handle than HCl.

The only other temperature dependence study of the deactivation of $O_2(b^1\Sigma^+_g)$ by H_2 was carried out by Kohse-Hoinghaus and Stuhl [85], who obtained a positive temperature dependence in the range 202 to 344 Kelvin. Their data are also shown on figure 6.7. If the two sets of results were taken together, the rate constant for the deactivation of $O_2(b^1\Sigma^+_g)$ by H_2 might seem to be independent of temperature. However, if their results are scaled down (indicated by arrows in figure 6.7) as suggested in the previous section, they agree with the positive temperature dependence observed in this work.

6.3.3 Deactivation of $O_2(b^1\Sigma^+_g)$ by D_2 at High temperature

A series of experiments was carried out on mixtures of 1.5 and 3.0 percent D_2 in pure O_2. The data were analysed by fitting the 762nm Kinetic Model in the same manner as in the H_2 and HCl studies. The results of the analysis are given in table 6.8(a). The run parameters may be found in Appendix 6. The experiments using a 1.5 percent D_2 mixture did not show any deactivation of $O_2(b^1\Sigma^+_g)$ due to the addition of D_2 at the high temperatures. In the experiments using 3.0 percent D_2, there was enough additional deactivation of $O_2(b^1\Sigma^+_g)$ to

Table 6.8(a) Deactivation of $O_2(b^1\Sigma_g^+)$ by D_2 in pure O_2

D_2 %	Run No	T_2 /Kelvin	^{762}K	$k_q^{D_2}$ /x 10^6 mol^{-1} dm^3 s^{-2}	T_{rel} μs	k_p /x 10^4 mol^{-1} dm^3 s^{-1}
1.5	DSR121B	533	0.84	-3.3	522	2.70
1.5	DSR119B	537	0.86	-2.0	533	2.84
1.5	DSR120B	545	1.62	-28.7	1067	1.87
1.5	DSR118B	554	2.46	-26.0	1609	3.14
1.5	DSR122B	575	1.05	-8.7	514	3.09
1.5	DSR124B	602	0.83	9.3	303	3.98
1.5	DSR123B	634	1.00	-4.7	272	4.25
1.5	DSR108B	661	1.25	-15.3	312	4.26
1.5	DSR107B	670	1.19	-5.3	280	4.76
1.5	DSR106B	681	1.10	1.3	237	5.16
1.5	DSR103B	706	0.78	72.0	156	7.29
1.5	DSR114B	746	1.11	-0.7	125	7.35
1.5	DSR113B	758	1.31	-12.7	152	7.23
1.5	DSR109B	798	1.29	-3.3	123	8.61
1.5	DSR115B	802	1.40	-14.0	131	8.62
1.5	DSR125B	844	1.38	-14.0	98	10.50
1.5	DSR105B	850	1.28	+8.0	93	10.90
1.5	DSR126B	955	1.13	29.3	57	15.00
3.0	DSR129B	536	0.92	1.3	405	2.55
3.0	DSR127B	541	0.93	2.7	409	2.67
3.0	DSR128B	547	0.95	6.3	490	2.60
3.0	DSR130B	572	0.78	15.7	287	3.40
3.0	DSR131B	612	0.82	17.3	210	4.07
3.0	DSR132B	627	0.74	24.0	152	4.47

Table 6.8(a) continued

D_2	Run No	T_2 /Kelvin	762_K	$k_q^{D_2}$ /x 10^6 mol^{-1} dm^3 s^{-1}	T_{rel} μs	k_p /x 10^4 mol^{-1} dm^3 s^{-1}
3.0	DSR134B	628	0.86	19.7	191	4.36
3.0	DSR133B	630	0.75	26.7	167	4.62
3.0	DSR136B	630	0.75	27.3	167	4.76
3.0	DSR141BX	631	0.75	24.7	153	4.69
3.0	DSR135B	637	0.81	20.3	172	4.54
3.0	DSR142B	651	0.75	29.3	137	5.13
3.0	DSR140B	700	0.96	23.3	129	6.16
3.0	DSR138B	721	0.94	26.0	109	6.65
3.0	DSR143B	731	0.96	24.0	92	7.00
3.0	DSR139B	763	0.85	43.7	67	8.54
3.0	DSR147B	763	0.79	46.3	60	8.61
3.0	DSR146B	768	0.96	30.7	70	8.48
3.0	DSR145B	785	0.96	37.0	82	8.63
3.0	DSR144B	792	1.01	35.7	74	9.12
3.0	DSR137B	846	1.06	40.0	62	10.9

Table 6.8(b) Deactivation of $O_2(b^1\Sigma_g^+)$ by D_2 in N_2/O_2 mixtures

D_2 %	N_2 %	Run No	T_2 /Kelvin	762 K	$k_q^{D_2}$ /x 10^6 mol^{-1} dm^3 s^{-1}	τ_{rel} /μs	k_p /x 10^4 mol^{-1} dm^3 s^{-1}
3.0	22.0	DSR316B	513	1.11	2.6	680	1.17
3.0	22.0	DSR317B	514	1.06	0.5	663	1.00
3.0	22.0	DSR314B	547	1.43	12.7	331	2.45
3.0	22.0	DSR310B	596	1.92	-9.1	639	1.08
3.0	22.0	DSR315B	610	1.64	8.7	249	2.66
3.0	22.0	DSR311B	617	1.61	7.0	269	2.39
3.0	22.0	DSR312B	618	1.46	4.4	315	1.96
3.0	22.0	DSR309B	627	1.38	3.3	187	3.36
3.0	22.0	DSR308B	703	1.55	23.3	135	3.95
3.0	22.0	DSR307B	749	2.58	-5.2	245	2.49
3.0	22.0	DSR313B	758	1.73	-6.1	365	1.80
3.0	22.0	DSR305B	767	2.07	2.4	194	3.09
3.0	22.0	DSR306B	786	2.29	1.3	179	3.33
3.0	22.0	DSR302B	833	1.74	9.0	119	3.59
3.0	47.0	DSR330B	511	1.76	5.6	460	1.49

Table 6.8 (b) continued

D_2	N_2	Run No	T_2 /Kelvin	^{762}K	$k_q^{D_2}$ /x 10^6 mol^{-1} dm^3 s^{-1}	T_{rel} /μs	k_p /x 10^4 mol^{-1} dm^3 s^{-1}
3.0	47.0	DSR331B	511	3.08	-7.0	796	1.01
3.0	47.0	DSR332B	537	2.24	-0.3	437	1.50
3.0	47.0	DSR333B	610	2.38	0.4	374	1.76
3.0	47.0	DSR327B	614	1.98	5.4	285	1.91
3.0	47.0	DSR320B	617	2.11	9.0	255	2.29
3.0	47.0	DSR326B	657	5.42	-14.0	506	1.31
3.0	47.0	DSR324B	692	1.88	-14.8	114	3.93
3.0	47.0	DSR325B	717	1.86	31.3	107	3.90
3.0	47.0	DSR323B	734	2.05	24.0	117	3.80
3.0	47.0	DSR328B	817	2.18	25.3	94	4.41
3.0	47.0	DSR329B	852	1.58	88.0	40	7.52
3.0	47.0	DSR319B	864	1.65	100.6	45	8.29

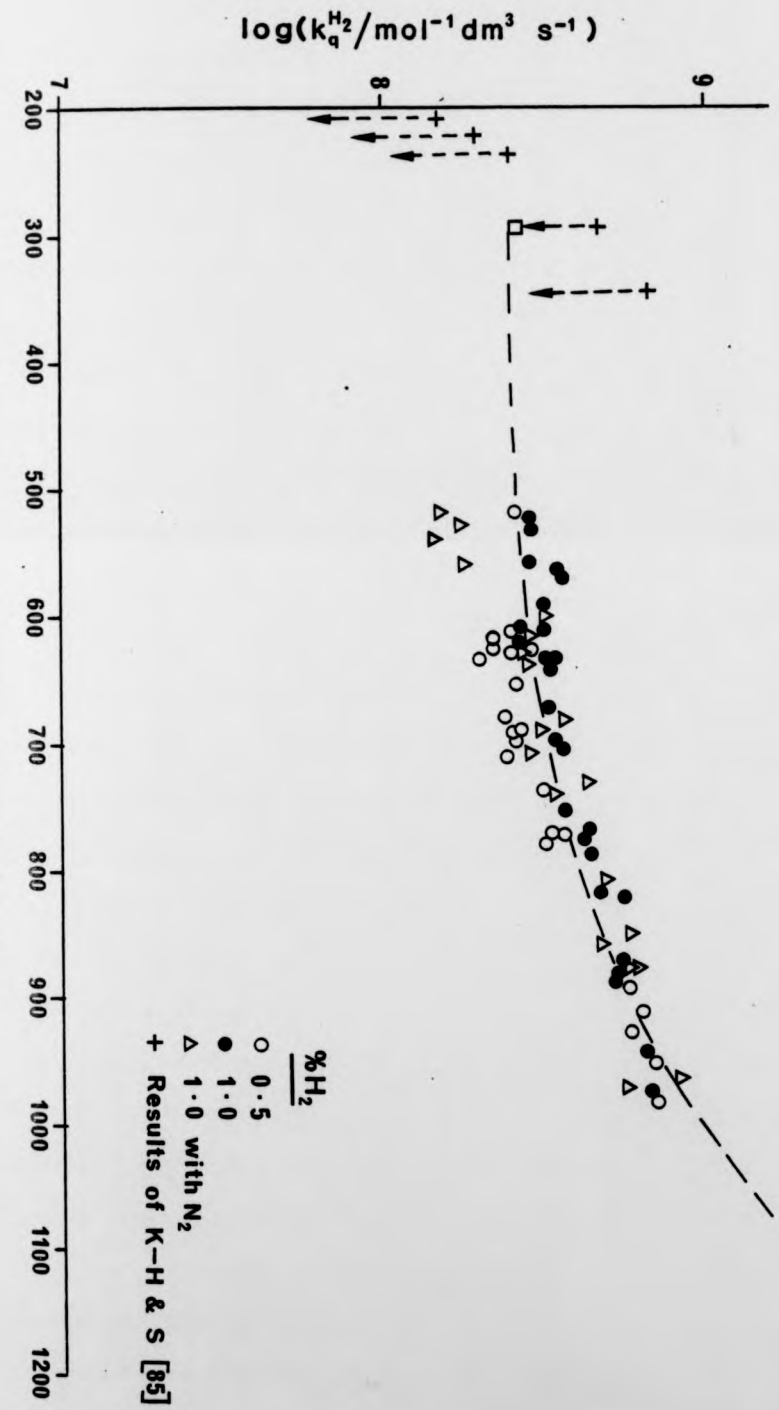

Figure 6.7 Deactivation of $O_2(b\ ^1\Sigma_g^+)$ by H_2

determine $k_q^{D_2}$.

As with the H_2 studies, an additional emission was observed at 762nm (see section 6.4) which prevented analysis above 900 Kelvin. A series of experiments was carried out using $3\%D_2/22\%N_2/75\%O_2$ and $3\%D_2/47\%N_2/50\%O_2$ mixtures in an attempt to extend the temperature range. The results of these experiments are given in table 6.8(b) and the run parameters are also in Appendix 6. The value of k_q^m for the N_2/O_2 mixtures determined in the previous section was used in the analysis of these data.

Since the N_2/O_2 results are scattered (not giving a precise value for k_q^m in N_2/O_2 mixtures), the subtraction of k_q^m for N_2/O_2 from the overall constant k_q^m in the $D_2/N_2/O_2$ experiments produces more scattered results than in the D_2/O_2 experiments. This situation was worse than in the $H_2/N_2/O_2$ work because the deactivation of $O_2(b^1\Sigma^+_g)$ by D_2 is less efficient than by H_2 and closer to the value for O_2 at high temperatures. The obvious remedy to this situation is to increase the mole fraction of D_2 in the mixture to obtain a greater difference between k_q^m $(D_2/N_2/O_2)$ and k_q^m (N_2/O_2). In doing so, however, one is faced with the fact that the additional emission will appear at lower temperatures which will reduce the temperature range even further.

The results for both D_2/O_2 and $D_2/N_2/O_2$ experiments are plotted against temperature on figure 6.8. The dashed line has been drawn by eye to show the general trend. The plot shows a slight increase in $k_q^{D_2}$ with temperature, but the scatter in the $D_2/N_2/O_2$ results is so great that little else can be said.

Kohse-Hoinghaus and Stuhl [85] have also investigated the temperature dependence of the deactivation of $O_2(b^1\Sigma^+_g)$ by D_2. Again they obtained a positive temperature dependence over the range 202 to 344 Kelvin. Their data are also shown on figure 6.8. Taken together

Figure 6.8 Deactivation of $O_2(b\ ^1\Sigma_g^+)$ by D_2

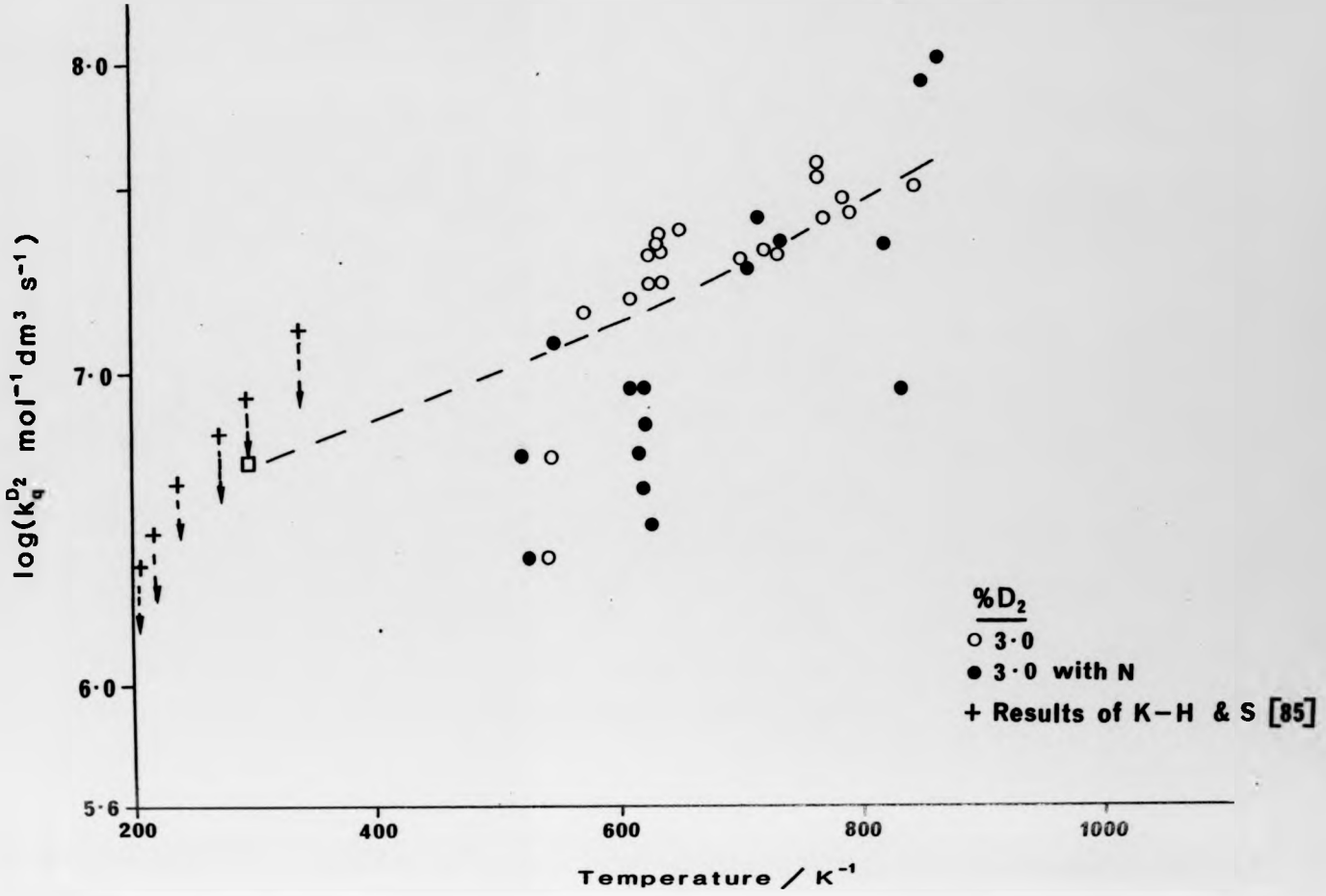

the two sets of results show a positive temperature dependence for the deactivation of $O_2(a^1\Delta_g)$ by $O_2(b^1\Sigma^+_g)$. The agreement is even better if the Kohse-Hoinghaus and Stuhl results are scaled down (indicated by arrows on figure 6.8) to make the 295K rate constants equal, as suggested in section 6.3.2.

6.4 Additional Emissions at 762nm

An additional emission was observed at high temperatures in mixtures of O_2 with HCl, H_2 and D_2. The emission showed the same characteristics as that observed at 634nm (section 5.4) but appeared at temperatures as low as 750K. Since the $O_2(a^1\Delta_g)$ and $O_2(b^1\Sigma^+_g)$ studies were carried out simultaneously, many 762nm data were recorded in the range 750 to 1000 Kelvin which contained the additional emission.

The time elapsed between shock heating and the maximum intensity of this emission was recorded (table 6.9). This time is known as the induction time for the phenomenon. Plots were made of the induction time versus temperature observed in both the H_2 and the D_2 work (figures 6.9 and 6.10). The plots show that the induction time decreases with temperature and that the appearance temperature (temperature at which the emission is first observed) decreases with increasing concentration of H_2 or D_2.

Since these characteristics are the same as those of the additional emission at 634nm, it is thought that the emission at 762nm may be produced from a similar process to that suggested in section 5.4 (equation 5.2).

Indeed Hislop and Wayne [93] and Washida, Akimoto and Okuda [74] report that $O_2(b^1\Sigma^+_g)$ is also a product of the reaction (6.2) in the scheme:

$$H + O_2 + M \longrightarrow HO_2 + M \qquad (6.1)$$

$$H + HO_2 \longrightarrow H_2 + O_2(b^1\Sigma^+_g,\ a^1\Delta_g \text{ or } X^3\Sigma^-_g) \qquad (6.2)$$

The mole fractions of $O_2(X^3\Sigma^-_g)$, $O_2(a^1\Delta_g)$ and $O_2(b^1\Sigma^+_g)$ in the products of reaction (6.2) are 0.60, 0.015 and 0.00028 respectively.

Table 6.9(a) Induction Times of Additional Emission with H_2

H_2 %	Run No	Temperature /Kelvin	Induction /μs
0.5	DSR47B	923	330
0.5	DSR49B	950	250
0.5	DSR48B	979	240
1.0	DSR24B	783	470
1.0	DSR14B	815	530
1.0	DSR19B	818	470
1.0	DSR23B	870	310
1.0	DSR20B	883	300
1.0	DSR21B	879	270
1.0	DSR25B	946	220
1.0	DSR22B	978	180
1.0*	DSR404B	807	570
1.0*	DSR405B	849	480
1.0*	DSR402B	858	370
1.0*	DSR401B	877	370
1.0*	DSR409B	877	390
1.0*	DSR407B	968	280
1.0*	DSR406B	978	170
1.0*	DSR403B	1157	50

* with N_2

Table 6.9(b) Induction Times of Additional Emission with D_2

D_2 %	Run No	Temperature /Kelvin	Induction /μs
1.5	DSR125B	816	540
1.5	DSR126B	922	320
1.5	DSR102B	1130	120
1.5	DSR110B	1123	130
1.5	DSR111B	1151	120
1.5	DSR101B	1201	140
3.0	DSR145B	754	640
3.0	DSR144B	769	630
3.0*	DSR322B	798	620
3.0*	DSR328B	817	610
3.0*	DSR329B	852	400
3.0*	DSR319B	864	440
3.0*	DSR304B	912	240
3.0*	DSR321B	952	280
3.0*	DSR318B	978	170
3.0*	DSR303B	1035	100
3.0*	DSR301B	1164	50

* With N_2

Figure 6.9 Induction times of additional emission with H_2

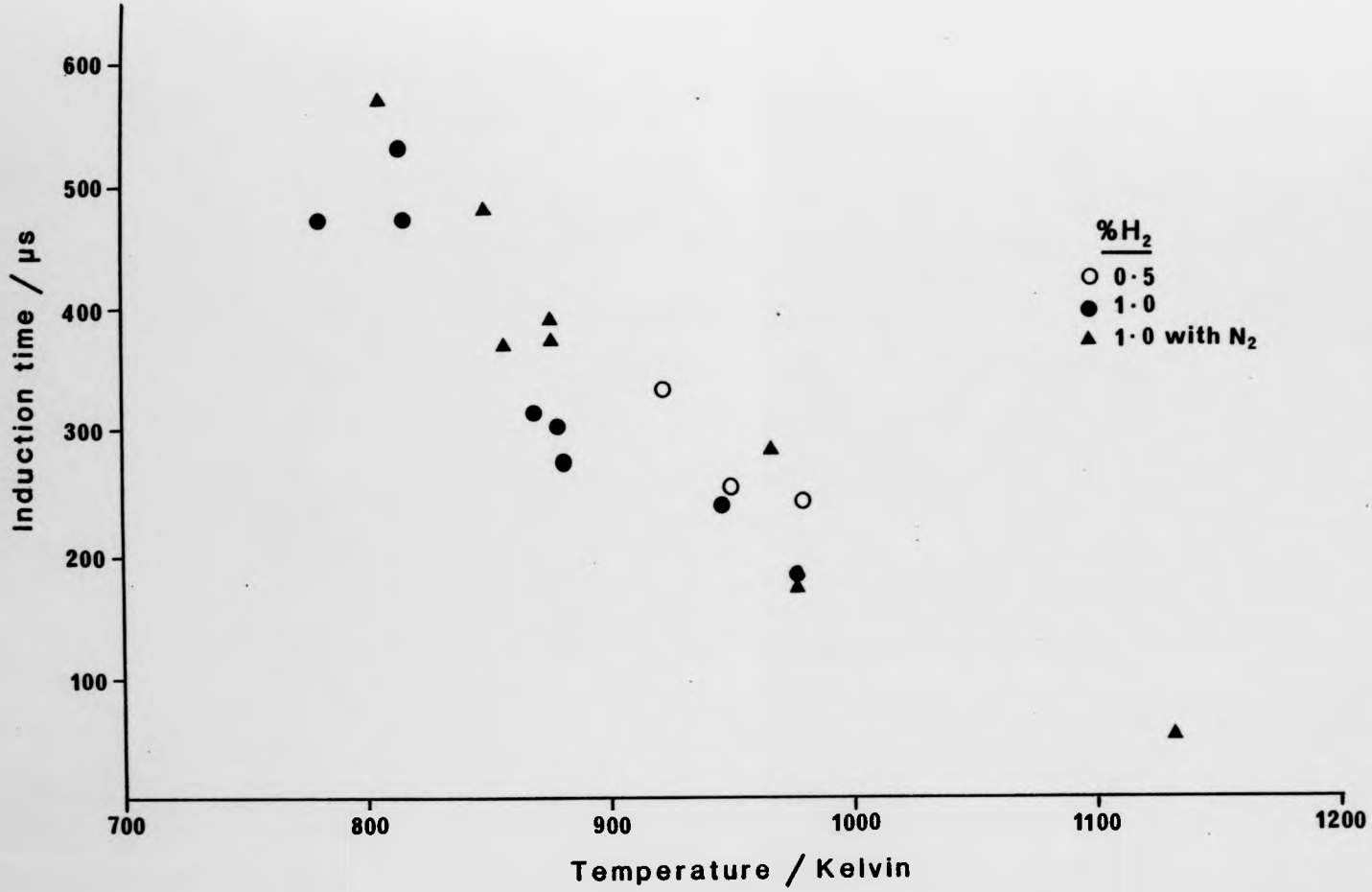

Figure 6.10 Induction times of additional emission with D_2

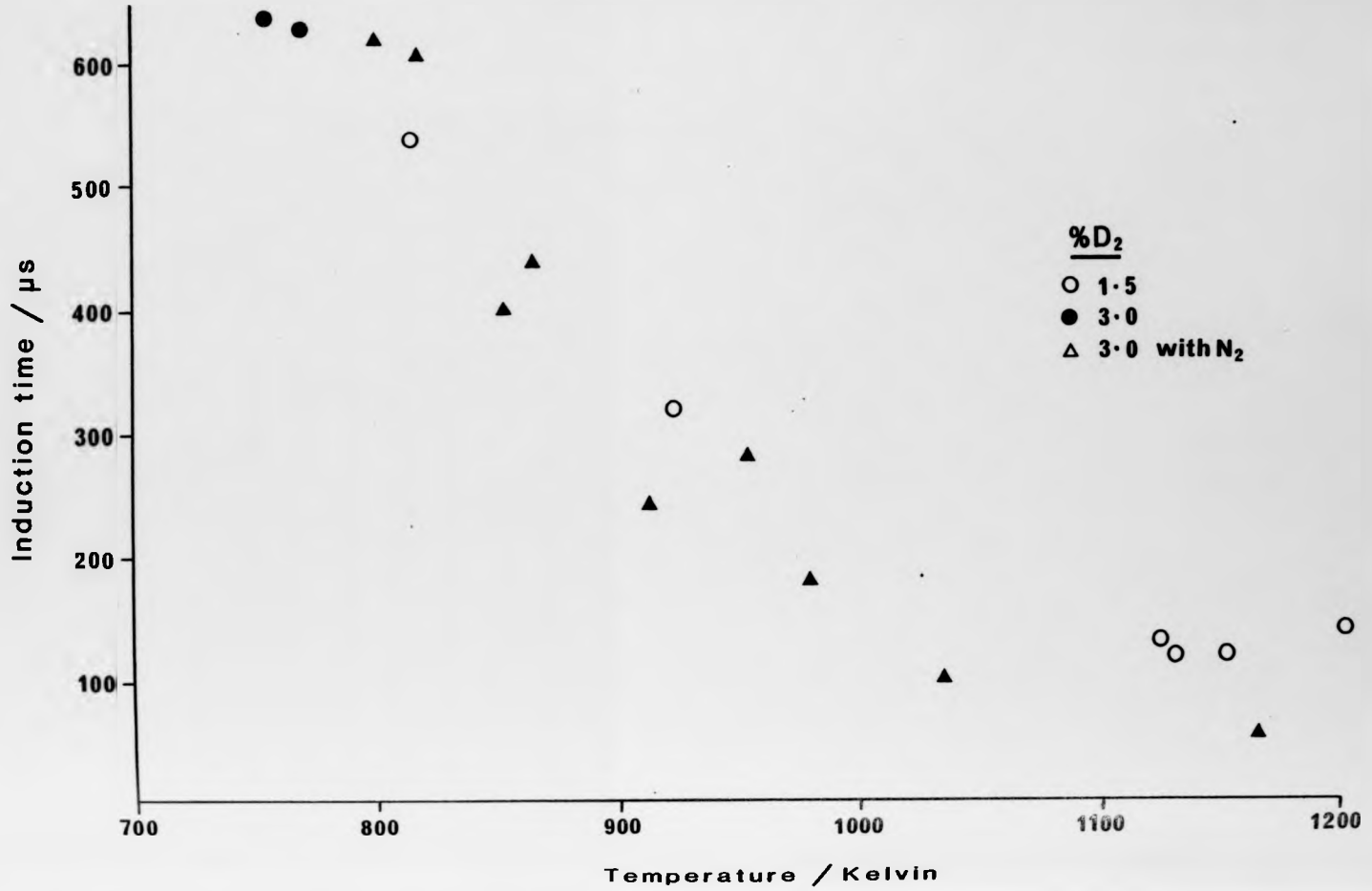

The remaining product is the OH radical. The observation that concentration of $O_2(b^1\Sigma^+_g)$ is not added to significantly by the $O_2(a^1\Delta_g)$ energy pooling reaction was also made by Hislop and Wayne.

The observation in this work that the 762nm emission appears at lower temperatures than the 634nm emission can be accounted for by the fact that the emission from $O_2(b^1\Sigma^+_g)$ is much stronger than that from $O_2(a^1\Delta_g)$ and hence it can be seen at much lower concentrations.

In view of the reaction scheme given above, and the characteristics of the emission, one may conclude that the source of both the additional 762nm and 634nm emissions is due to additional $O_2(b^1\Sigma^+_g)$ and $O_2(a^1\Delta_g)$, produced from reactions (6.1) and (6.2). Reaction (6.1) may be initiated by hydrogen atoms generated at high temperatures in the discharge flow - shock tube.

DISCUSSION OF THE COLLISIONAL DEACTIVATION OF SINGLET MOLECULAR OXYGEN

7.1 Introduction

In this chapter, the rate constants for the collisional deactivation of singlet molecular oxygen and their temperature dependences are discussed. The information which these results yield is considered in an attempt to gain some knowledge of the mechanisms involved in the transfer of energy.

There have been several theoretical approaches to the elucidation of a mechanism for the deactivation of singlet molecular oxygen. These calculations have concentrated on the deactivation of $O_2(b^1\Sigma^+_g)$, where there is a large amount of experimental data, particularly at room temperature. The literature does not contain any quantitative attempts to calculate rate constants for the deactivation of $O_2(a^1\Delta_g)$. Some empirical and quantitative studies, however, have been carried out.

The chapter begins with a discussion of the deactivation of $O_2(a^1\Delta_g)$ and then considers the deactivation of $O_2(b^1\Sigma^+_g)$. The final section summarises the features of the deactivation processes.

7.2 Discussion of the Collisional Deactivation of $O_2(a^1\Delta_g)$

A relatively large excitation energy, 94.3 kJ mol^{-1}, has to be converted to vibrational or translational energy in the deactivation process. The deactivation of $O_2(a^1\Delta_g)$ to $O_2(X^3\Sigma^-_g)$ requires a spin inversion (forbidden process) to take place, unless the deactivator has a triplet state lying below the $O_2(a^1\Delta_g)$ energy. The deactivators studied in this work, HCl, HBr, H_2 and D_2 do not have triplet states with energies in this region. Consequently, the low deactivation rate constants ($< 1 \times 10^5$ mol^{-1} dm^3 s^{-1}) which are observed are not unexpected. These deactivation rate constants agree well with those determined for other molecular species [28], which fall in the range 4.8 mol^{-1} dm^3 s^{-1} for helium to 2.1×10^6 mol^{-1} dm^3 s^{-1} for ozone.

The probability of the deactivation of $O_2(a^1\Delta_g)$ taking place upon collision with a deactivator at 295K may be calculated using equations (7.1) and (7.2).

$$k_{\Delta M} = 2.751 \times 10^9 \, (\sigma_{\Delta M})^2 \, (T/\mu)^{1/2} \quad mol^{-1} \, dm^3 \, s^{-1} \qquad (7.1)$$

$$P_{\Delta M} = k_d{}^m / k_{\Delta M} \qquad (7.2)$$

where $k_{\Delta M}$ is the rate constant predicted if deactivation takes place upon every collision, $\sigma_{\Delta M}$ is the 'hard sphere' collision diameter in Å, and μ is the reduced mass. The probabilities for the deactivation of $O_2(a^1\Delta_g)$ by the deactivators studied in this work, and those from previous work carried out in this laboratory [13,44,46,60], are given in table 7.1.

The deactivation probabilities inform us that only one in two million collisions will be successful when the most efficient

Table 7.1 Deactivation Probabilities for $O_2(a^1\Delta_g)$ at 295 K

M	σ_{MM} A°	$\sigma_{\Delta M}$ A°	μ g mol^{-1}	$k_{\Delta M}$ mol^{-1} dm^3 s^{-1}	k_d^M mol^{-1} dm^3 s^{-1}	$P_{\Delta M}$
H_2	2.915	3.228	1.88	3.59×10^{11}	2.22×10^4	6.1×10^{-8}
D_2	2.948	3.245	3.56	3.34×10^{11}	2.56×10^3	7.7×10^{-9}
HCl	3.305	3.423	14.9	1.43×10^{11}	8.00×10^4	5.6×10^{-7}
HBr	3.3	3.4	23.1	1.15×10^{11}	4.2×10^4	3.7×10^{-7}
O_2	3.541	3.541	16.0	1.48×10^{11}	9.40×10^2	6.4×10^{-9}
N_2	3.749	3.654	14.9	1.63×10^{11}	<40*	$<2.5 \times 10^{-12}$
NO	3.599	3.570	15.5	1.53×10^{11}	2.10×10^4	1.4×10^{-7}
N_2O	3.816	3.679	20.9	1.40×10^{11}	$<3 \times 10^3$	$<2.1 \times 10^{-8}$
SO_2	4.404	3.973	21.3	1.85×10^{11}	3×10^3	1.6×10^{-8}
CO_2	3.897	3.719	18.5	1.87×10^{11}	$<3 \times 10^3$	$<1.6 \times 10^{-8}$
NH_3	2.58	3.06	11.1	1.33×10^{11}	5.37×10^3	4.0×10^{-8}

* From reference [28]

σ_{MM} values are obtained from Hirschfelder, Curtiss and Bird [94] and also Lambert [12], $\sigma_{\Delta\Delta}$ is taken to be that for $O_2(X^3\Sigma_g^-)$

Figure 7.1 Collision theory plot for the deactivation of $O_2(a\,^1\Delta g)$ by H_2

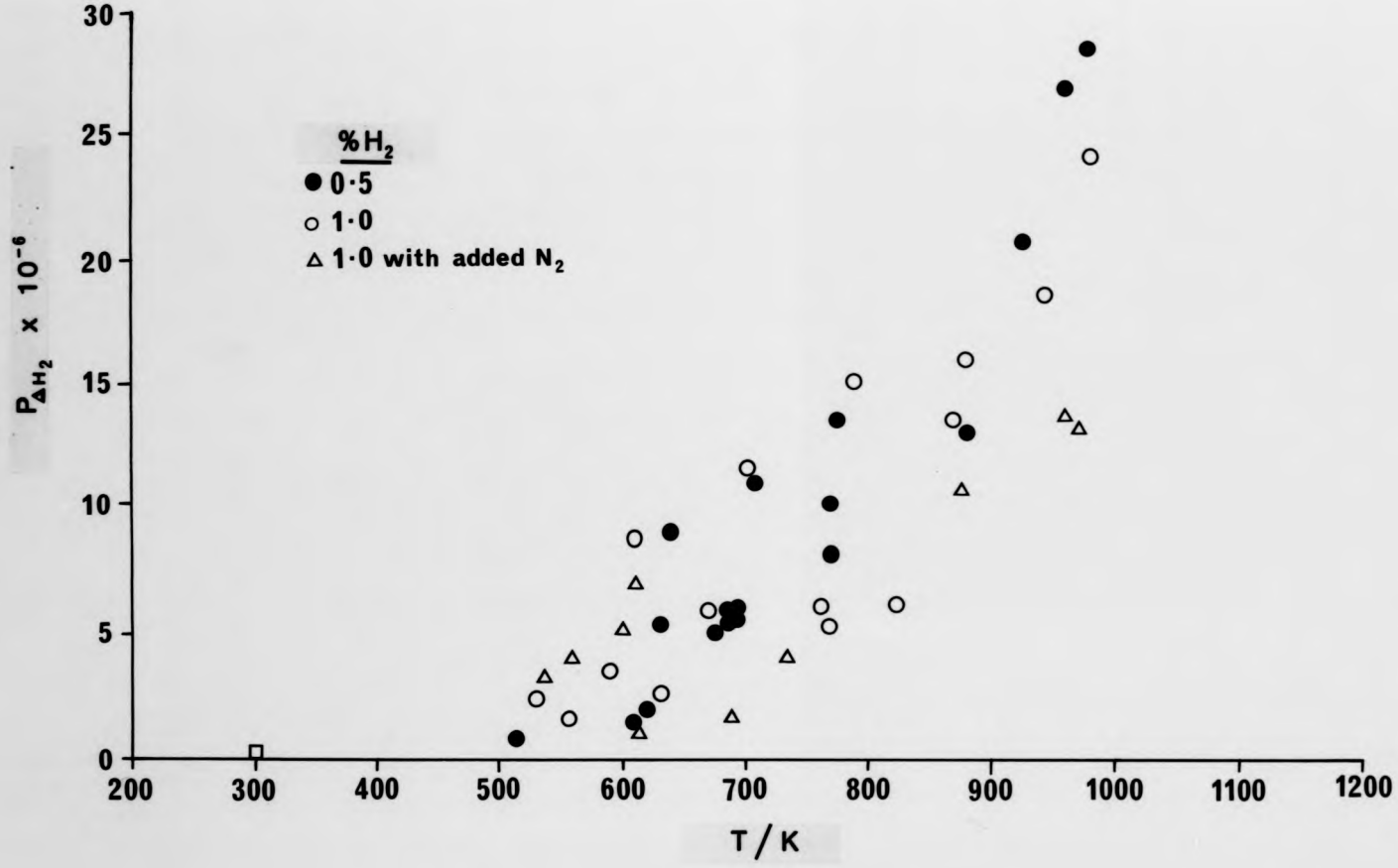

deactivator, HCl, is a collision partner. This figure falls to one in two hundred million when a poor deactivator such as O_2 is employed. The small probabilities indicate that most collisions (grazing collisions involving long range attractive forces) are too weak to result in energy transfer and that only a few collisions ('head on' collisions involving short range repulsive forces) are strong enough to influence energy transfer.

In order to determine whether the temperature dependence of the deactivation of $O_2(a^1\Delta_g)$ by the deactivators studied in this work reflects the $T^{1/2}$ temperature dependence predicted by simple collision theory, a plot was constructed of $P_{\Delta H_2}$ versus T (figure 7.1). The deactivation due to H_2 was chosen because the results have the least scatter and cover the greatest temperature range. The probability, $P_{\Delta H_2}$, is obviously not constant over the temperature range studied, which indicates that the deactivation of $O_2(a^1\Delta_g)$ by H_2 is not simply influenced by the collision rate.

Several theoretical approaches to the electronic to vibrational energy transfer in the deactivation of $O_2(a^1\Delta_g)$ in solution [96,97,98] have been based on the well established theories of vibrational relaxation [12,88,99].

The classical Landau-Teller theory of vibrational relaxation is based on the assumption that only short range repulsive forces influence the energy transfer process. The theory works well for non-polar diatomic molecules, but it does not take into account the angle dependent dipole interaction involved when the collision partners are polar diatomic molecules.

Since the consideration of deactivation probabilities and the positive temperature dependence give experimental evidence of the participation of short range repulsive forces, it was thought worthwhile to examine the dependence of the deactivation of $O_2(a^1\Delta_g)$

Figure 7.2 Landau-Teller plot for the deactivation of $O_2(a\,^1\Delta_g)$ by HCl

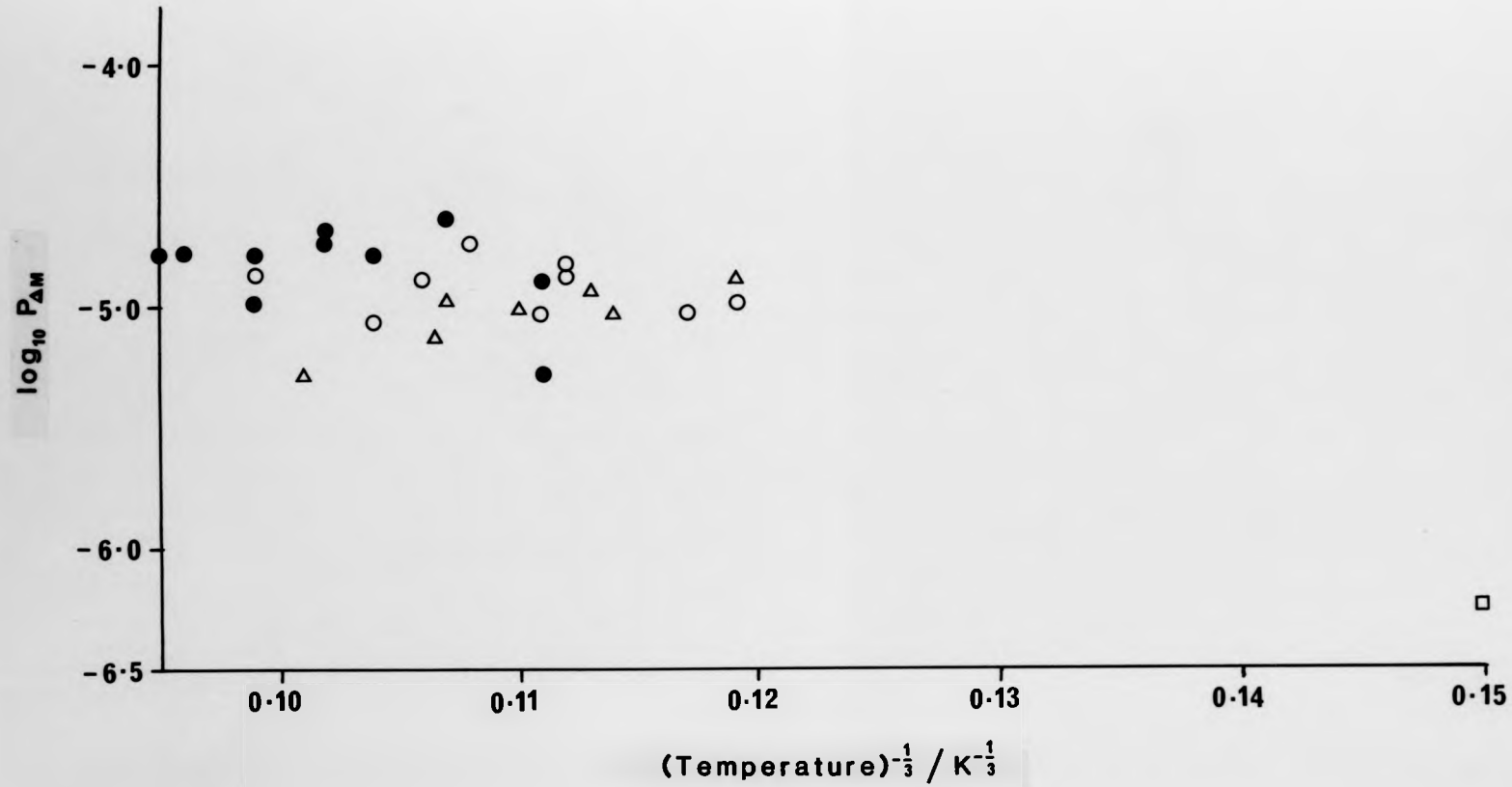

Figure 7.3 Landau–Teller plot for the deactivation of $O_2(a\,^1\Delta_g)$ by H_2

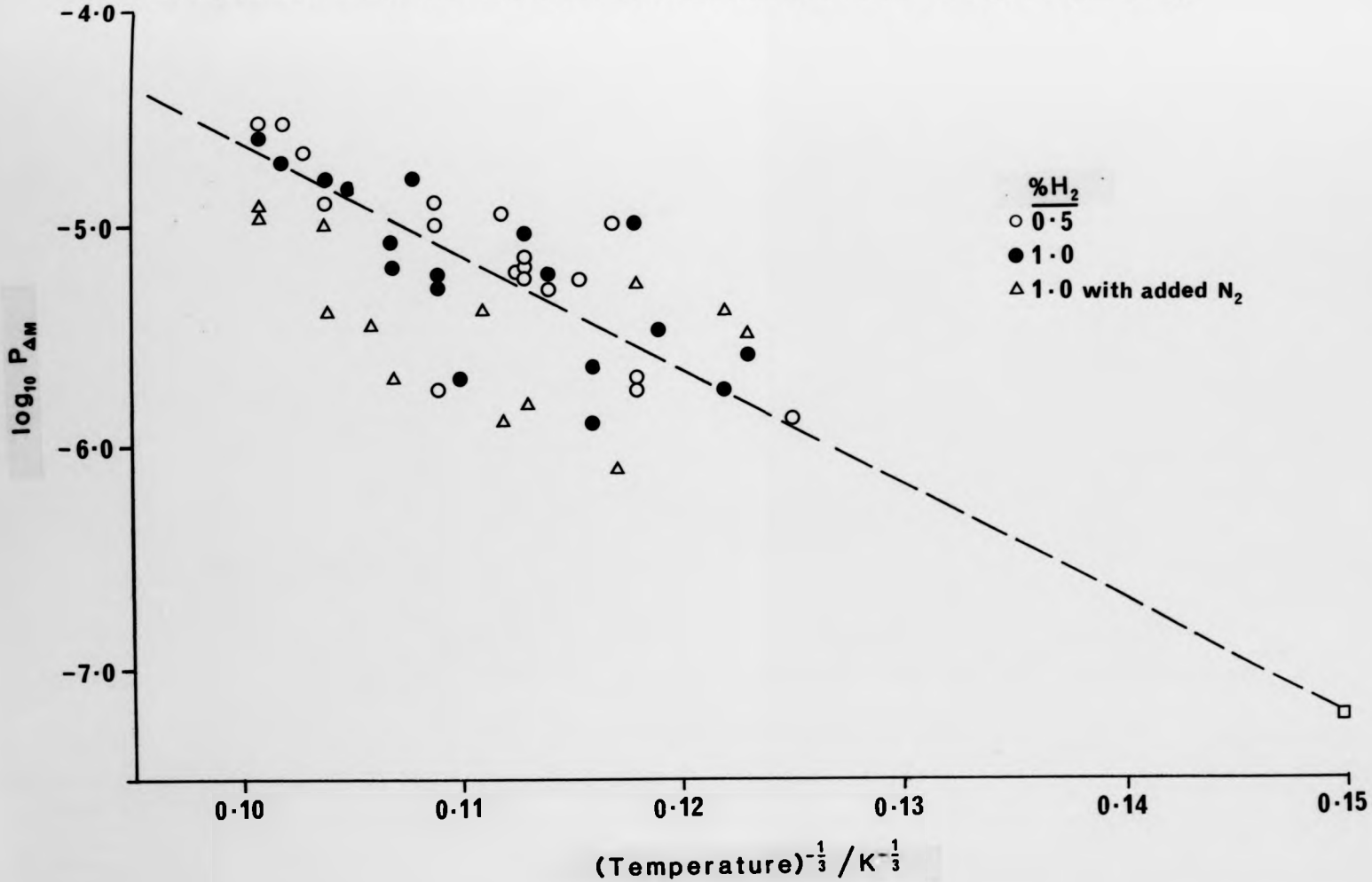

Figure 7.4 Landau–Teller plot for the deactivation of $O_2(a\,^1\Delta_g)$ by D_2

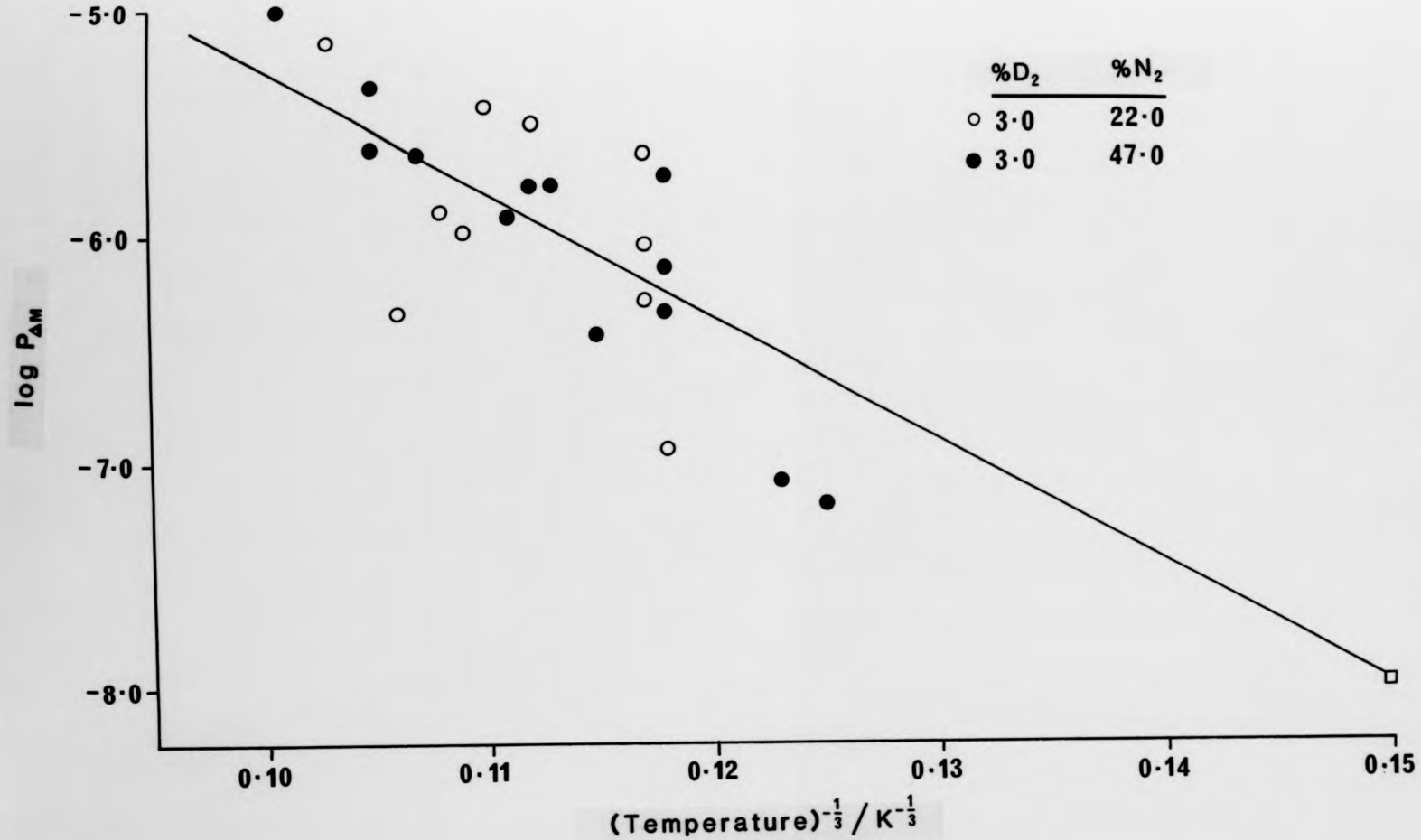

upon $T^{-1/3}$ for each of the additives. Plots were made of the logarithm of the deactivation probability, log $P_{\Delta M}$, versus the temperature function, $T^{-1/3}$, (figures 7.2 to 7.4) to test the relationship:

$$\text{Log } P_{\Delta M} = A - BT^{-1/3} \qquad (7.3)$$

which is predicted by the Landau-Teller theory.

A linear dependence between the logarithm of the deactivation probability and the term $T^{-1/3}$ is observed for the deactivation by H_2 and D_2, but not for the deactivation by HCl. It is not surprising that the deactivation of $O_2(a^1\Delta_g)$ by HCl does not fit the Landau-Teller model since HCl is a polar molecule. However, it is interesting that the deactivation of $O_2(a^1\Delta_g)$ by H_2 and D_2, which is an electronic to vibrational energy transfer process, shows the same temperature dependence as predicted by this theory of vibrational relaxation. If vibrational relaxation is involved in the overall deactivation of $O_2(a^1\Delta_g)$, it will follow the forbidden electronic to vibrational energy transfer step and will be a much more rapid process. Therefore, it is unlikely that the vibrational relaxation is the rate determining step which influences the temperature dependence.

This view is supported by the work of Wild, Klingshirn and Maier [96] which suggests that the deactivation of $O_2(a^1\Delta_g)$ by $O_2(X^3\Sigma^-_g)$, in the liquid phase, is a three step process:

(i) Electronic to vibrational intersystem crossing which is rate determining and is dominated by pathways involving $O_2(X^3\Sigma^-_g)_{v=2}$ and $O_2(X^3\Sigma^-_g)_{v=3}$.

(ii) Vibrational relaxation of the v>1 levels of $O_2(X^3\Sigma^-_g)$

to the v=1 level, primarily by near-resonant vibrational to vibrational energy transfer, which is a very rapid process.

(iii) Collisional deactivation of $O_2(X^3\Sigma^-_g)_{v=1}$ by slow vibrational to translational energy transfer.

One conclusion which may be drawn from the Landau-Teller relationship is that the factors which affect vibrational relaxation are also important in electronic to vibrational energy transfer.

The temperature dependences of the rate constants for the deactivation of $O_2(a^1\Delta_g)$ by HCl, H_2 and D_2 have also been shown to fit simple Arrhenius functions.

$$k_d^{HCl} = (2.75 \pm 1.70) \times 10^7 \exp[-(1750 \pm 190)/T]$$

$$k_d^{H_2} = (1.32 \pm 1.08) \times 10^8 \exp[-(2600 \pm 180)/T]$$

$$k_d^{D_2} = (2.75 \pm 0.75) \times 10^7 \exp[-(2740 \pm 90)/T]$$

These Arrhenius expressions predict activation energies of 14.5, 21.6 and 22.8 kJ mol^{-1} respectively.

There are no studies of the temperature dependence of the deactivation of $O_2(a^1\Delta_g)$, other than those reported by Boodaghians [44], with which to compare these expressions. However, both the pre-exponential and exponential factors are similar to those reported by Boodaghians and also to those found in the temperature dependence studies of the chemical reaction of $O_2(a^1\Delta_g)$ with various alkenes [76].

The activation energies are quite large, considering that the deactivation process involves the dissipation of energy and that these activation energies are insufficient to allow access to the

triplet states of the deactivators.

By analogy with vibrational to vibrational energy transfer one would expect resonant channels to be most important. Where resonant channels are not available, 'down hill' processes should dominate the transfer of energy, unless there is an 'up hill' channel which is nearer to resonance than the available 'down hill' channels and requires a small activation energy.

Table 7.2 shows the possible products of energy transfer between $O_2(a^1\Delta_g)_{v=0}$ and $HCl(X^1\Sigma^+_g)_{v=0}$ which would require an activation energy. While the observed activation energy for the deactivation of $O_2(a^1\Delta_g)$ by HCl agrees, within experimental error, with that required for the energy transfer process:

$$O_2(a^1\Delta_g)_{v=0} + HCl(X^1\Sigma^+_g)_{v=0} \longrightarrow O_2(X^3\Sigma^-_g)_{v=4} + HCl(X^1\Sigma^+_g)_{v=1} \qquad (7.4)$$

(13.0 kJ mol^{-1}), there are two other pathways which involve a lower activation energy.

There are also six 'down hill' pathways which do not require an activation energy, two of which are nearer to resonance than the 'up hill' pathway suggested. Although the excitation of HCl to higher vibrational levels will be less favoured than excitation to v=1 in a single collision, it is difficult to understand why the pathway described by equation (7.4) should dominate the energy transfer process.

Table 7.3 shows that there is also a good correspondence between the observed activation energy for the deactivation of $O_2(a^1\Delta_g)$ by H_2 and that required for the following process,

Table 7.2 Potential Products of the Deactivation of $O_2(a^1\Delta_g)$ by HCl

Deactivation Products		Energy Released	
$HCl(X^1\Sigma_g^+)$ vibrational level	$O_2(X^3\Sigma_g^-)$ vibrational level	cm^{-1} molecule^{-1}	kJ mole^{-1}
1	0	-4997	-59.7
1	1	-3440	-41.1
1	2	-1908	-22.8
1	3	- 399	- 4.8
1	4	1088	13.0
1	5	2550	30.5
2	0	-2215	-26.5
2	1	- 658	- 7.9
2	2	874	10.4
2	3	2383	28.5
2	4	3870	46.2
2	5	5332	63.7
3	0	465	5.6
3	1	2022	24.2
3	2	3554	42.5
3	3	5063	60.5
3	4	6556	78.3
3	5	8012	95.7

Table 7.3 Potential Products of the Deactivation of $O_2(a^1\Delta_g)$ by H_2

Deactivation Products		Energy Released	
$H_2(X^1\Sigma_g^+)$ vibrational level	$O_2(X^3\Sigma_g^-)$ vibrational level	cm^{-1} $molecule^{-1}$	kJ $mole^{-1}$
1	0	-3723	-44.7
1	1	-2166	-26.0
1	2	-634	- 7.6
1	3	875	10.5
1	4	2362	28.2
1	5	4160	49.7
2	0	204	2.4
2	1	1761	21.0
2	2	3293	39.3
2	3	4874	58.3
2	4	6199	74.1
2	5	7751	92.6
3	0	3899	46.6
3	1	5454	65.2
3	2	6988	83.5

$$O_2(a^1\Delta_g)_{v=0} + H_2(X^1\Sigma^+_g)_{v=0} \longrightarrow O_2(X^3\Sigma^-_g)_{v=1} + H_2(X^1\Sigma^+_g)_{v=2} \quad (7.5)$$

which is 21.0 kJ mol^{-1}. This suggests a favoured pathway in the deactivation of $O_2(a^1\Delta_g)$ by H_2. Again, there are also pathways (both exothermic and endothermic) which are nearer to resonance than the one suggested above.

However, table 7.4 shows that in the less efficient deactivation of $O_2(a^1\Delta_g)$ by D_2, there is not an energy requirement for an electronic to vibrational energy transfer process which corresponds to the observed activation energy. The closest comparison is for the process,

$$O_2(a^1\Delta_g)_{v=0} + D_2(X^1\Sigma^+_g)_{v=0} \longrightarrow O_2(X^3\Sigma^-_g)_{v=1} + D_2(X^1\Sigma^+_g)_{v=3} \quad (7.6)$$

which requires an activation energy of 27.6 kJ mol^{-1}. The difference in the required and observed activation energies is too great to claim a correspondence with this process. It is also noted that there are three deactivation pathways which would require an activation energy lower than that observed and six exothermic channels, two of which are much nearer to resonance.

The preference for endothermic pathways over exothermic and resonant pathways raises doubts about the validity of these Arrhenius dependences.

A consequence of accepting that the activation energies are 'real', and not simply fortuitous, is a dramatic change in the deactivation probabilities. If there is an additional energy requirement then the probability that two colliding molecules have sufficient energy is given by:

Table 7.4 Potential Products of the Deactivation of $O_2(^1\Delta_g)$ by D_2

Deactivation Products		Energy Released	
$D_2(X^1\Sigma_g^+)$ vibrational level	$O_2(X^1\Sigma_g^-)$ vibrational level	cm^{-1} $molecule^{-1}$	kJ $mole^{-1}$
1	0	-4888	−58.4
1	1	-3331	−39.8
1	2	-1799	−21.5
1	3	- 290	−3.5
1	4	1197	14.3
1	5	2659	31.8
2	0	-2010	-24.0
2	1	- 453	- 5.4
2	2	1079	12.9
2	3	2588	30.9
2	4	4075	48.7
2	5	5537	66.2
3	0	757	9.0
3	1	2314	27.6
3	2	3846	46.0
3	3	5355	64.0
3	4	6842	81.8
3	5	8304	99.2

$$P_E = \exp(-Ea/RT) \qquad (7.7)$$

where Ea is the activation energy in J mol^{-1}. Allowing for such a factor would increase the deactivation probabilities for some deactivators (NO, SO_2, HCl, H_2 and D_2) by 3 - 4 orders of magnitude. Such revised probabilities would be approximately the same as those for the deactivation of $O_2(b^1\Sigma^+_g)$ (section 7.3). This seems unlikely since the deactivation of $O_2(a^1\Delta_g)$ is a spin forbidden process, whereas the deactivation of $O_2(b^1\Sigma^+_g)$ is a spin allowed process and, therefore, more favourable.

In view of the inconsistencies involved in assuming that the observed activation energies are 'real', one must regard them with some degree of caution and, perhaps, some scepticism. Temperature dependence experiments performed by a technique which involves less scatter would be of great assistance in confirming or rejecting the validity of Arrhenius activation energies for the deactivation of $O_2(a^1\Delta_g)$ by the deactivators studied here.

Thomas and Thrush [77,78] studied the deactivation of $O_2(a^1\Delta_g)$ by various additives at 295K. They determined the fraction of deactivating steps, q_v, which result in the population of a particular vibrational level in the deactivator. Then they took a statistical approach to predict the probability, P_v, of populating a particular level of the deactivator molecule during the deactivation process. A surprisal plot was made of $\ln(q_v/P_v)$ versus the fraction of electronic energy which is transferred into vibrational energy and a linear relationship was observed. It was estimated from these calculations that approximately 25% of the electronic energy dissipated is transferred into translational and rotational energy.

Thomas and Thrush concluded that resonant deactivation

pathways were not particularly favoured and that the deactivation mechanism is not specific. The failure to favour strongly the resonant processes indicates that the deactivation occurs on the repulsive part of the intermolecular potential, which is in agreement with the implications of the positive temperature dependence observed in this thesis. They pointed out an exception to this general conclusion, the deactivation of $O_2(a^1\Delta_g)$ by NO, which results in the preferential population of both the v=2 and the v=4 levels of ground state NO, although the v=3 level is populated to a lesser extent. This observation is supported by the detection of $NO(X^2\Pi_g)_{v=4}$ in the products of the deactivation, by Ogryzlo and Thrush [79].

Davidson and Ogryzlo [80] attempted to relate log k_q^m and the highest fundamental vibrational frequency of the deactivator. A good correlation was found for the deactivation of $O_2(b^1\Sigma^+_g)$ by diatomic molecules. The trend is that log k_q^m increases as the highest fundamental vibrational frequency of the deactivator increases. They concluded that the process involves electronic to vibrational energy transfer from $O_2(b^1\Sigma^+_g)$ to the deactivator.

A plot of log k_d^m for the deactivation of $O_2(a^1\Delta_g)$ at 295K versus the highest fundamental vibrational frequency of the deactivator has been constructed from the results reported here and those previously obtained in this laboratory, (figure 7.5). A correlation coefficient of 0.35 was obtained, which indicates that there is very little correlation between the deactivation rate constant and the highest fundamental vibrational frequency of the deactivator.

Parmenter and co-workers [81,82] have developed a theory which relates the collisional cross-section, σ, to the potential energy well depth, ε, of a complex A*-M, where A* is the excited species and M is a deactivator.

Figure 7.5 Dependence of the logarithm of the deactivation constant for $O_2(a\,^1\Delta_g)$ upon the highest fundamental vibrational frequency of the deactivator

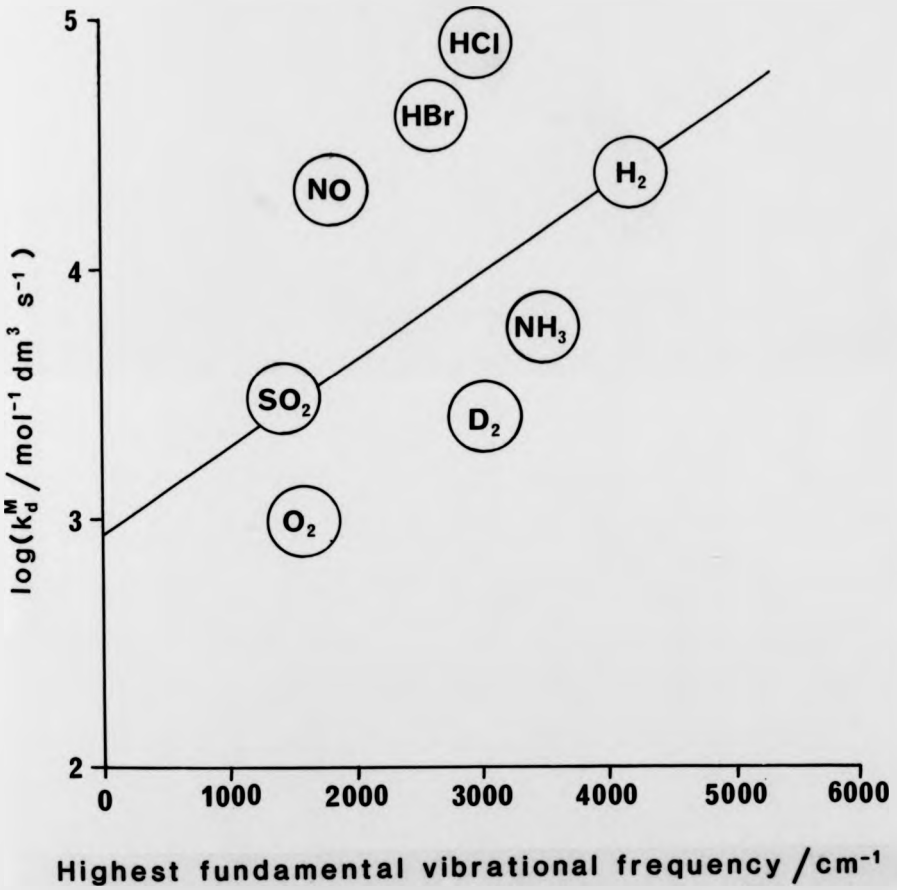

$$\ln \sigma_m = C + \varepsilon_{A^*M}/kT \qquad (7.8)$$

They observed that the experimental data can also be described by the related correlation:

$$\ln \sigma_m = C' + \beta(\varepsilon_{mm}/k)^{1/2} \qquad (7.9)$$

at a given temperature, where β and C' are constants and ε_{mm} is the well depth between pairs of M molecules.

This theory is only appropriate when attractive forces dominate the interaction, and has been shown to hold for electronic deactivation, predissociation, and vibrational and rotational relaxation processes by Parmenter and co-workers.

Since equation (7.8) predicts a negative temperature dependence, which is contrary to the experimental observations for the deactivation of $O_2(a^1\Delta_g)$, and there is already evidence for the participation of repulsive forces, it would be inappropriate to try to correlate the experimental data with equations (7.8) and (7.9).

One may conclude that there is a general, non-specific mechanism for the deactivation of $O_2(a^1\Delta_g)$, for which the first and rate determining step is electronic to vibrational energy transfer. There is strong evidence, from the work of Thomas and Thrush, Maier and co-workers and this thesis that short range repulsive forces dominate the deactivation process. The work of Maier and co-Workers and the Landau-Teller relationship found here, point to electronic to vibrational energy transfer being influenced by the same factors as vibrational to vibrational energy transfer. This is in agreement with

the findings of Thomas and Thrush that most of the energy from $O_2(a^1\Delta_g)$ is transferred into vibration although as much as 25% may be transferred into translation and rotation in this process.

There is evidence for specific pathways being preferred in the case of the efficient deactivator, NO, and there is a suggestion from this work that specific pathways may also be favoured in the deactivation by HCl and H_2.

7.3 Discussion of the Collisional Deactivation of $O_2(b^1\Sigma^+_g)$

The deactivation of $O_2(b^1\Sigma^+_g)$ to $O_2(X^3\Sigma^-_g)$ would require 156.9 kJ mol^{-1} of excitation energy to be transferred into vibrational or translational energy. Furthermore, such a transition would require spin inversion (forbidden process) to take place, unless the deactivator has a triplet state lying below the $O_2(b^1\Sigma^+_g)$ energy. Since the deactivators studied in this work do not have triplet states with energies in this region, one might expect the deactivation rate constants to compare with those for $O_2(a^1\Delta_g)$, which are less than 1×10^5 mol^{-1} dm^3 s^{-1}. In fact, the rate constants for the deactivation of $O_2(b^1\Sigma^+_g)$ are three or four orders of magnitude greater. The reason for such a difference [28] lies not in the fact that the transition from $O_2(b^1\Sigma^+_g)$ to $O_2(X^3\Sigma^-_g)$ is not orbitally forbidden as it is for $O_2(a^1\Delta_g)$, but in the fact that $O_2(b^1\Sigma^+_g)$ may be deactivated to the $O_2(a^1\Delta_g)$ state. A transition from $O_2(b^1\Sigma^+_g)$ to $O_2(a^1\Delta_g)$ requires only 62.6 kJ mol^{-1} of energy to be dissipated and is a spin allowed process.

The deactivation rate constants determined here agree well with those determined by other workers [39,42,77,85-90] and lie within the range of deactivation rate constants determined for other molecular deactivators [28] of 3.5×10^3 mol^{-1} dm^3 s^{-1} for argon to 1.1×10^{10} mol^{-1} dm^3 s^{-1} for ozone.

In order to determine whether the temperature dependence of the deactivation of $O_2(a^1\Delta_g)$ by the deactivators studied in this work is simply a result of the increase in collision rate with temperature, a plot of $P_{\Sigma H_2}$ versus T was made (figure 7.7). The deactivation due to H_2 was chosen because the results have least scatter and cover the greatest temperature range. Clearly, $P_{\Sigma H_2}$ does not remain constant over the temperature range studied here.

The probability of the deactivation of $O_2(b^1\Sigma^+_g)$ taking place

upon a single collision at 295K with the deactivators studied in this work and previous studies in this laboratory [13,44,46,60] are given in table 7.5. The probabilities inform us that one in 200 collisions will be successful when the most efficient deactivator, NH_3, is a collision partner, which is considerably more probable than the figure of one in 25 million obtained for the deactivation of $O_2(a^1\Delta_g)$ by this molecule. The less efficient deactivator, O_2, is successful only once in 1.5 million collisions with $O_2(b^1\Sigma^+_g)$, a figure which is comparable to the one in 2 million obtained for the efficient deactivation of $O_2(a^1\Delta_g)$ by HCl.

The small probabilities (< 1 in 60,000) for the deactivation of $O_2(b^1\Sigma^+_g)$ by D_2, N_2, O_2 and SO_2 indicate that the successful interactions involve 'head on' collisions and that short range repulsive forces are involved. Molecules such as H_2, HBr, CO_2 and NH_3 have relatively large deactivation probabilities (> 1 in 1,300), indicating that weaker interactions may also result in deactivation when these molecules collide with $O_2(b^1\Sigma^+_g)$.

Kear and Abrahamson [91] devised a method to calculate the deactivation rate constants for $O_2(b^1\Sigma^+_g)$ at 295K. Their method is similar to the Schwartz, Slawsky and Herzfeld (SSH) theory [88] of vibrational energy transfer and assumes that the transfer takes place entirely under the influence of short range repulsive forces. The participation of long range attractive forces is not taken into account. In each case (table 7.6), their calculated values were at least a factor of ten lower than experimental values. The failure of these calculations to predict rate constants as high as those obtained experimentally suggests that short range repulsive forces are not solely responsible for the transfer of energy.

Later, Braithwaite, Davidson and Ogryzlo [42,95] attempted to calculate the same rate constants using a model which allows for only

upon a single collision at 295K with the deactivators studied in this work and previous studies in this laboratory [13,44,46,60] are given in table 7.5. The probabilities inform us that one in 200 collisions will be successful when the most efficient deactivator, NH_3, is a collision partner, which is considerably more probable than the figure of one in 25 million obtained for the deactivation of $O_2(a^1\Delta_g)$ by this molecule. The less efficient deactivator, O_2, is successful only once in 1.5 million collisions with $O_2(b^1\Sigma^+_g)$, a figure which is comparable to the one in 2 million obtained for the efficient deactivation of $O_2(a^1\Delta_g)$ by HCl.

The small probabilities (< 1 in 60,000) for the deactivation of $O_2(b^1\Sigma^+_g)$ by D_2, N_2, O_2 and SO_2 indicate that the successful interactions involve 'head on' collisions and that short range repulsive forces are involved. Molecules such as H_2, HBr, CO_2 and NH_3 have relatively large deactivation probabilities (> 1 in 1,300), indicating that weaker interactions may also result in deactivation when these molecules collide with $O_2(b^1\Sigma^+_g)$.

Kear and Abrahamson [91] devised a method to calculate the deactivation rate constants for $O_2(b^1\Sigma^+_g)$ at 295K. Their method is similar to the Schwartz, Slawsky and Herzfeld (SSH) theory [88] of vibrational energy transfer and assumes that the transfer takes place entirely under the influence of short range repulsive forces. The participation of long range attractive forces is not taken into account. In each case (table 7.6), their calculated values were at least a factor of ten lower than experimental values. The failure of these calculations to predict rate constants as high as those obtained experimentally suggests that short range repulsive forces are not solely responsible for the transfer of energy.

Later, Braithwaite, Davidson and Ogryzlo [42,95] attempted to calculate the same rate constants using a model which allows for only

Table 7.5 Deactivation Probabilities for $O_2(b^1\Sigma_g^+)$ at 295 K

M	$k_{\Sigma M}$ x 10^{11} mol^{-1} dm^3 s^{-1}	k_q^M mol^{-1} dm^3 s^{-1}	$P_{\Sigma M}$
H_2	3.59	2.76×10^8	7.7×10^{-4}
D_2	3.34	5.27×10^6	1.6×10^{-5}
HCl	1.43	1.60×10^7	1.1×10^{-4}
HBr	1.15	1.42×10^8	1.2×10^{-3}
O_2	1.48	1.00×10^5	6.8×10^{-7}
N_2	1.63	1.20×10^6	7.4×10^{-6}
NO	1.53	1.70×10^7	1.1×10^{-4}
N_2O	1.40	$4.2 \times 10^{7*}$	3.0×10^{-4}
SO_2	1.85	2.50×10^5	1.4×10^{-5}
CO_2	1.87	2.20×10^8	1.2×10^{-3}
NH_3	1.33	7.05×10^8	5.3×10^{-3}

* from reference [28]

$\sigma_{\Sigma M}$ values and therefore $k_{\Sigma M}$ values are assumed to be equal to those in table 7.1.

Table 7.6 Calculated and Observed Values for the Deactivation of $O_2(b^1\Sigma_g^+)$ at 295 K

M	EXPERIMENT $mol^{-1}\ dm^3\ s^{-1}$	SRIT $mol^{-1}\ dm^3\ s^{-1}$	LRIT $mol^{-1}\ dm^3\ s^{-1}$	SRIT + LRIT $mol^{-1}\ dm^3\ s^{-1}$
H_2	2.76×10^8	4.3×10^7	4.6×10^8	5.0×10^8
D_2	5.27×10^6	9.2×10^5	1.2×10^7	1.1×10^7
HCl	1.60×10^7	-	5.3×10^6	$>5.3 \times 10^6$
HBr	1.42×10^8	1.2×10^8	3.4×10^8	4.6×10^8
O_2	1.00×10^5	34	$\sim$10	$\sim$44
N_2	1.20×10^6	1.0×10^4	9.1×10^5	9.2×10^5
NO	1.70×10^7	-	9.3×10^6	$>9.3 \times 10^6$

SRIT - Kear and Abrahamson [91]

LRIT - Braithwaite, Davidson and Ogryzlo [42, 95]

long range attractive forces and their results are also given in table 7.6. A better correspondence between these calculations and the experimental values is noted. They conclude that in the deactivation of $O_2(b^1\Sigma^+_g)$ by the diatomic molecules studied, energy transfer can take place under the influence of long range attractive forces. It is also suggested that their calculations and those of Kear and Abrahamson are complementary and therefore additive.

It appears from these calculations that both short and long range interactions are involved in the deactivation of $O_2(b^1\Sigma^+_g)$. Since long range interaction theory (LRIT) values are greater than short range interaction theory (SRIT) values in each case, domination of the deactivation by long range attractive forces is implied. This is contrary to the interpretation of the small deactivation probabilities as an indication that short range interactions dominate the deactivation of $O_2(b^1\Sigma^+_g)$.

The work of Braithwaite, Ogryzlo, Davidson and Schiff [42] predicts a temperature dependence for the deactivation $O_2(b^1\Sigma^+_g)$ by HBr which is positive if the interactions are wholly short range and negative if the interactions are wholly long range.

Since HCl is a similar molecular species to HBr, one might expect the predictions of LRIT and SRIT for the deactivation of $O_2(b^1\Sigma^+_g)$ by HCl to be similar to those for deactivation by HBr. In contrast to the 'u' shaped plot predicted by Braithwaite and co-workers for the deactivation by HBr versus temperature, the observed behaviour of the temperature dependence of the deactivation of $O_2(a^1\Delta_g)$ by HCl shows a maximum (figure 6.5).

Braithwaite and co-workers have also calculated the rate constants for the deactivation of $O_2(b^1\Sigma^+_g)$ by H_2, based on LRIT and SRIT. Their predictions are shown on figure 7.6, along with the experimental results obtained in this work and from previous work

Figure 7.6 Deactivation of $O_2(b\,^1\Sigma_g^+)$ by H_2

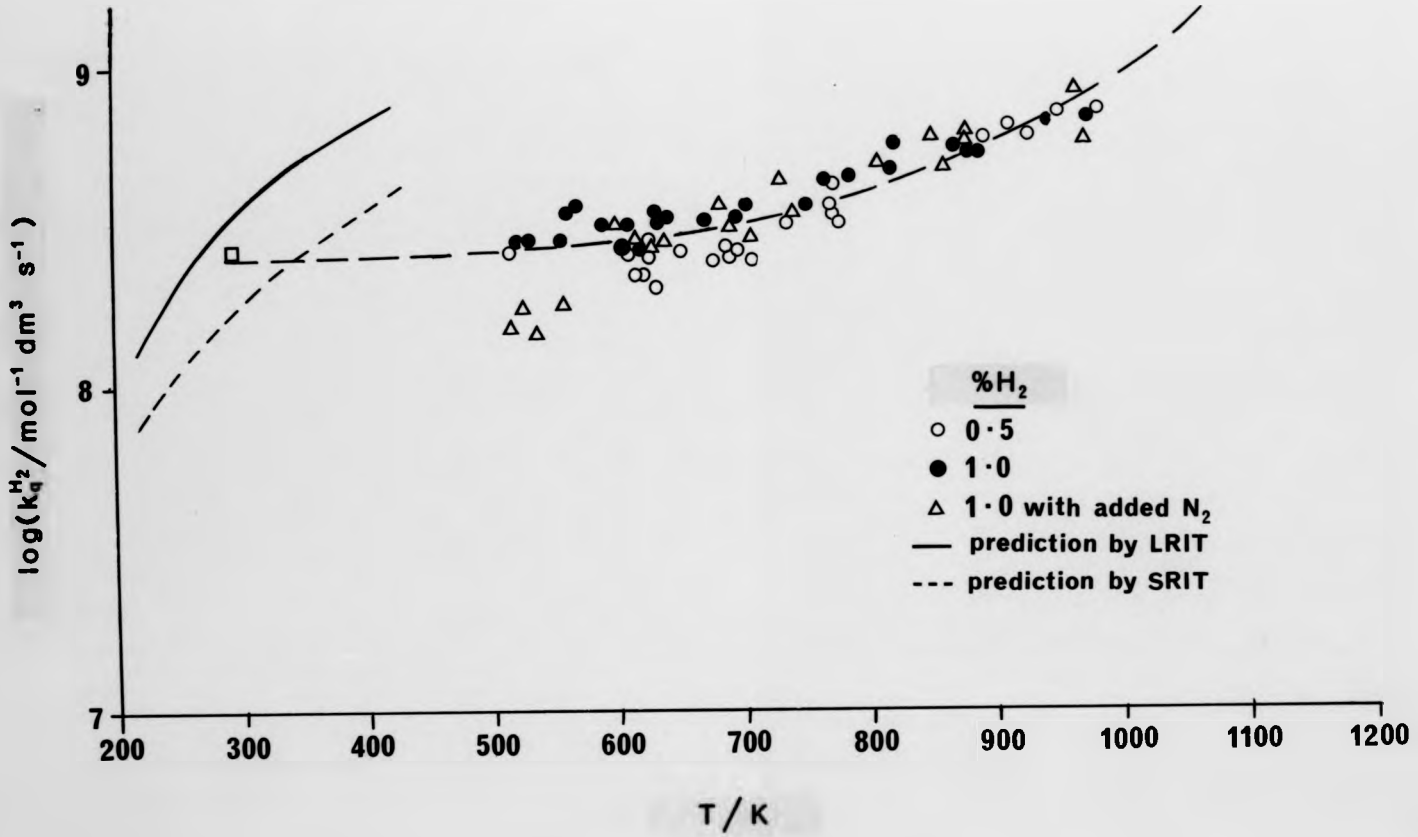

Figure 7.7 Collision theory plot for the deactivation of $O_2(b\,^1\Sigma_g^+)$ by H_2

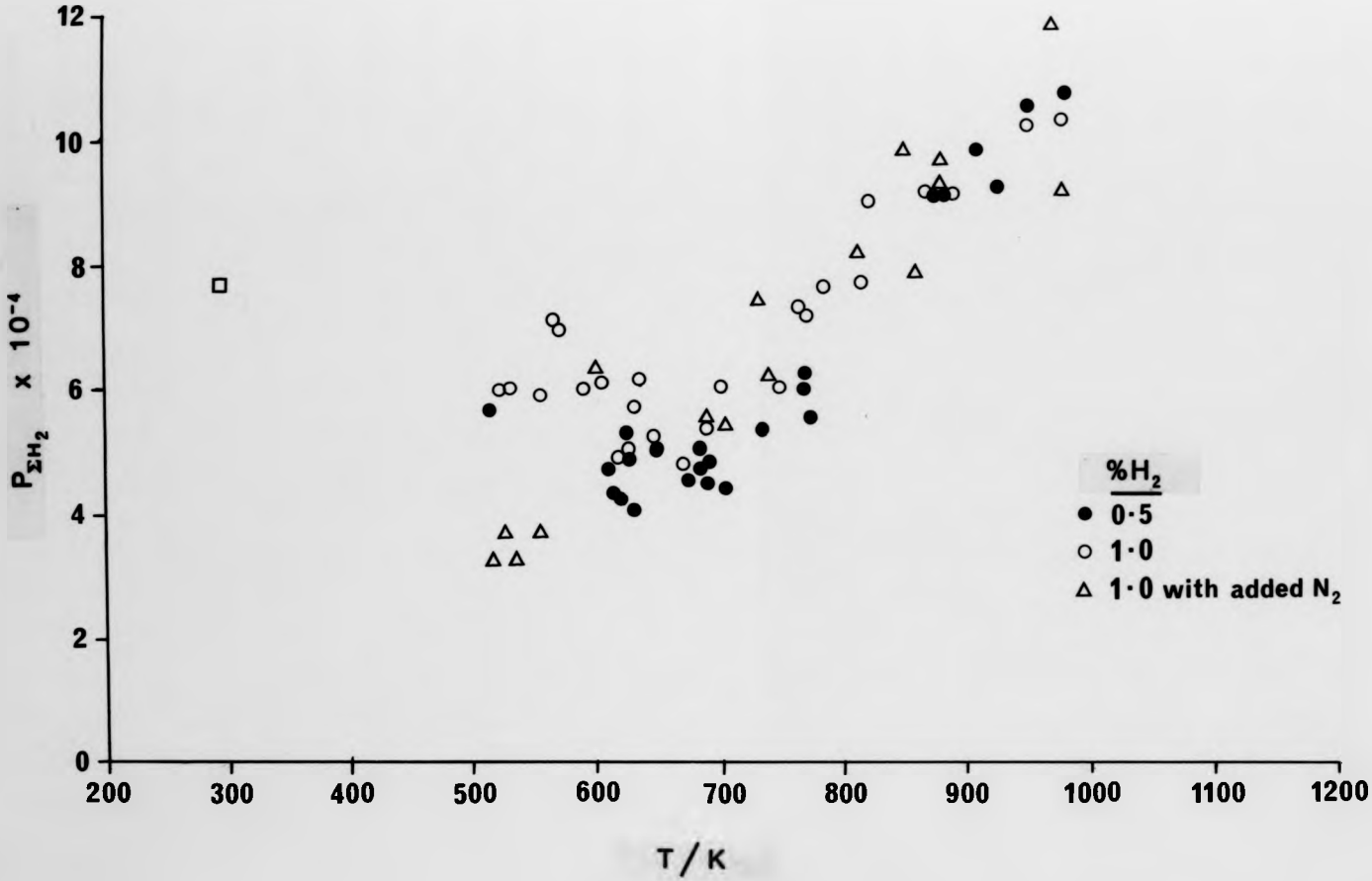

carried out in this laboratory. In contrast to the predictions for the deactivation by HBr, the temperature dependence of both SRIT and LRIT do not predict a 'fall off' in the value of the rate constant, k_q^{H2}, at high temperatures.

While the predictions of Braithwaite and co-workers do not extrapolate well to the higher temperatures studied in this work, the general trend and order of magnitude are in agreement. Their work is the only one which offers an explanation of the 'fall off' in the rate constant observed for HCl and other polar species, but not for H_2, D_2 and O_2 at higher temperatures.

In order to determine whether the temperature dependence of the deactivation of $O_2(b^1\Sigma^+_g)$ by the deactivators studied in this work is simply a result of the increase in collision rate with temperature, a plot of $P_{\Sigma H_2}$ versus T was made (figure 7.7). The deactivation due to H_2 was chosen because the results have least scatter and cover the greatest temperature range. Clearly, $P_{\Sigma H_2}$ does not remain constant over the temperature range studied here.

Since the deactivation of $O_2(a^1\Delta_g)$ showed Landau-Teller behaviour (equation 7.3) and there is also evidence for the participation of short range repulsive forces in the deactivation of $O_2(b^1\Sigma^+_g)$, it was thought worthwhile to examine the relationship between log $P_{\Sigma M}$ and $T^{-1/3}$. In contrast to the temperature dependence of the $O_2(a^1\Delta_g)$ deactivation, none of the deactivators studied here showed a Landau-Teller type dependence upon temperature. The results for the deactivation of $O_2(b^1\Sigma^+_g)$ by H_2 are given as an example of the type of plot obtained (figure 7.8).

Arrhenius plots were also tried for the deactivation of $O_2(b^1\Sigma^+_g)$ by HCl, H_2 and D_2. In each case, it was impossible to fit the data to an Arrhenius expression.

An empirical correlation has been made, by Davidson and

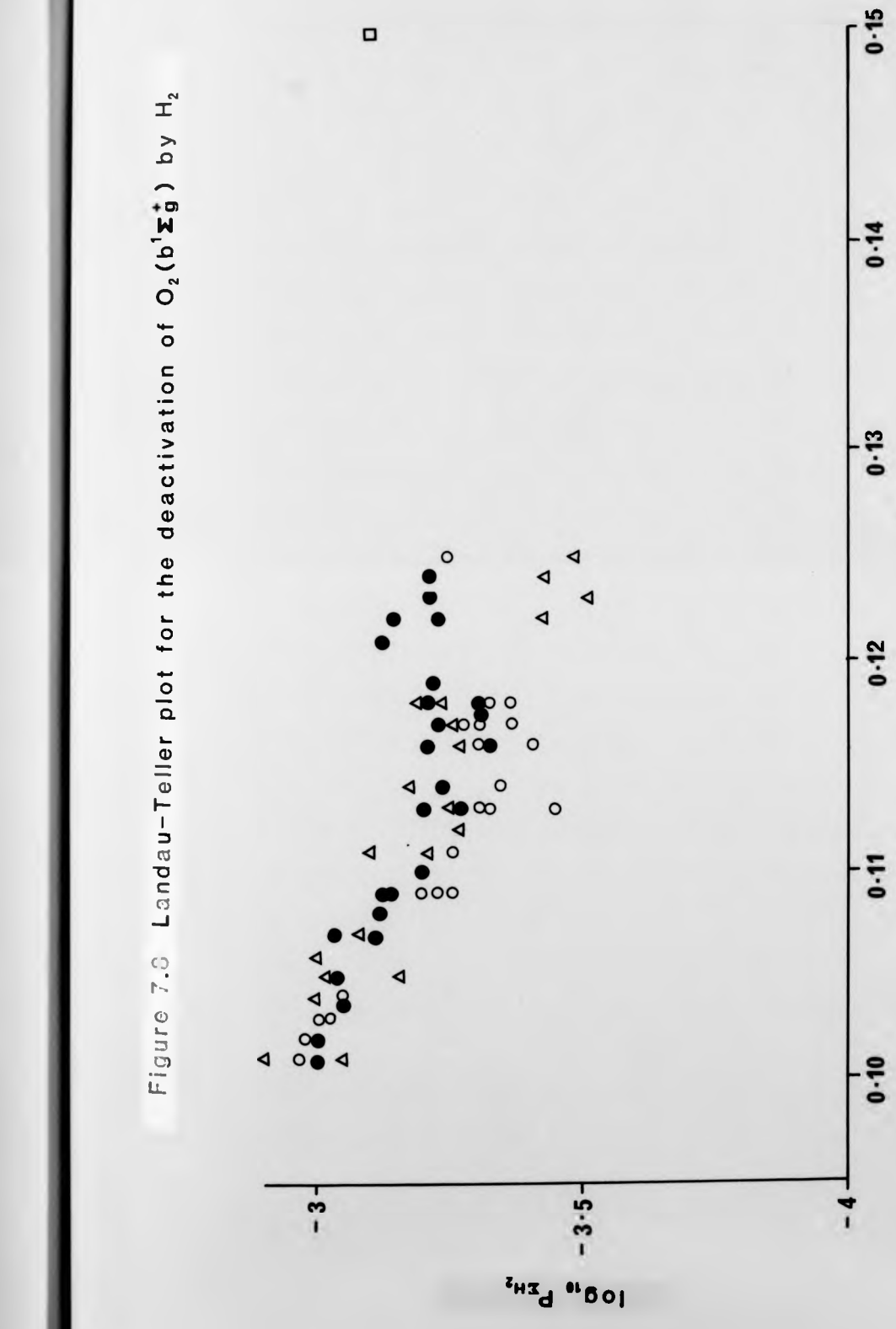

Figure 7.8 Landau–Teller plot for the deactivation of $O_2(b^1\Sigma_g^+)$ by H_2

Ogryzlo [80], between log k_q^m and the highest fundamental vibrational frequency of the deactivator. A very good correlation was found for the deactivation of $O_2(b^1\Sigma^+_g)$ by homonuclear diatomics. They concluded that such a correlation may be interpreted as evidence that the deactivation process involves the transfer of the electronic energy of $O_2(b^1\Sigma^+_g)$ to vibrational energy in the deactivator. Figure 7.9 is a plot of log k_q^m versus the highest fundamental vibrational frequency of the deactivator for the deactivators studied in this work and those studied previously in this laboratory. The dashed line shows the general correlation for which the correlation coefficient is 0.78. This indicates that there is a reasonable correlation in the general case.

The full line shows the correlation for deactivation by the homonuclear diatomics alone. The correlation coefficient for these molecules alone is 0.999 which is an excellent correlation.

The correlation between the logarithm of the rate constant and the highest fundamental vibrational frequency of the deactivator is evidence that the ability of the deactivator to accept large quantities of vibrational energy is important in the deactivation of $O_2(b^1\Sigma^+_g)$ in general and particularly important in the deactivation of $O_2(b^1\Sigma^+_g)$ by homonuclear diatomic molecules.

Thomas and Thrush [78] have observed vibrational excitation in several deactivators during the deactivation of both $O_2(a^1\Delta_g)$ and $O_2(b^1\Sigma^+_g)$.

In the deactivation of $O_2(b^1\Sigma^+_g)$ by HCl, they observed the strong infra-red emissions of the (1,0) and (2,1) bands of HCl together with the weaker emissions from the (2,0) band. This corresponds to the process:

Figure 7.9 Dependence of the logarithm of the deactivation constant for $O_2(b\,^1\Sigma_g^+)$ upon the highest fundamental vibrational frequency of the deactivator

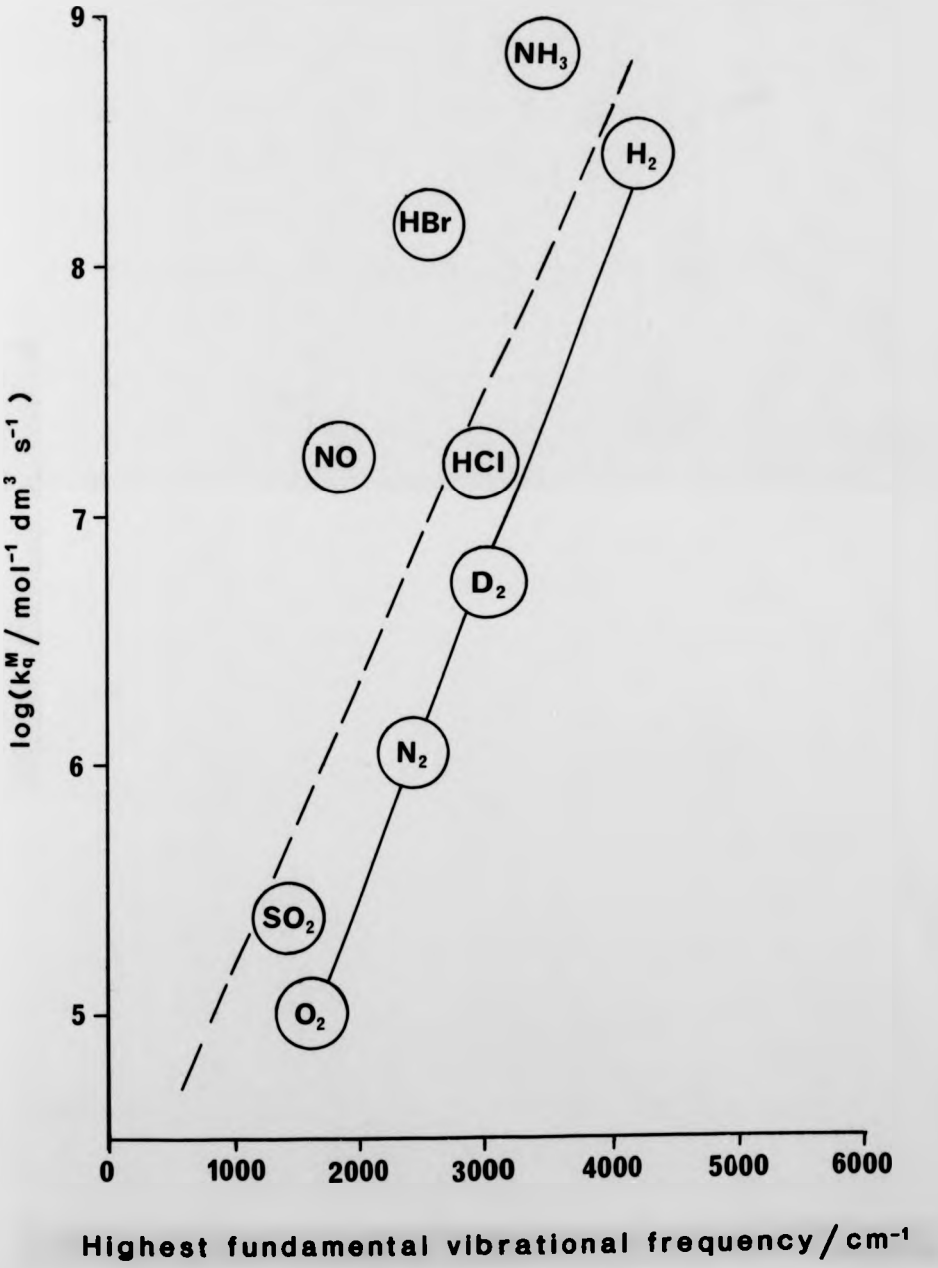

$$O_2(b^1\Sigma^+_g)_{v=0} + HCl(X^1\Sigma_g^+)_{v=0} \text{ ----> } O_2(a^1\Delta_g)_{v=0} + HCl(X^1\Sigma_g^+)_{v=2} \quad (7.10)$$

which is endothermic by 5.1 kJ mol^{-1}. Surprisal analysis [79] showed that the observed rate of excitation of $HCl(X^1\Sigma_g^+)_{v=2}$ is consistent with equation (7.10). It was also shown that the vibrational relaxation of $HCl(X^1\Sigma_g^+)_{v=2}$ to $HCl(X^1\Sigma_g^+)_{v=1}$ could account for the entire population of $HCl(X^1\Sigma_g^+)_{v=1}$.

Thomas and Thrush also obtained indirect evidence that the $H_2(X^1\Sigma_g^+)_{v=1}$ is excited in the deactivation of $O_2(b^1\Sigma^+_g)$ by H_2. This was done by adding H_2 to the experiments with $O_2(b^1\Sigma^+_g)$ and HCl. The emission of the (2,0) and (2,1) bands of HCl was extinguished, leaving only the (1,0) band in the infra-red spectrum, which shows that the deactivation of $O_2(b^1\Sigma^+_g)$ by H_2 yields a species with sufficient energy to excite HCl to the first vibrational level but not to the second. The only species which fits this requirement is $H_2(X^1\Sigma_g^+)_{v=1}$.

The surprisal plot for the deactivation of $O_2(b^1\Sigma^+_g)$ was found to be the same as that for $O_2(a^1\Delta_g)$, which suggests a common non-specific mechanism. Although it shows that the electronic energy goes preferentially into vibrational energy in the products, their work suggests that resonant energy transfer is not important. It was found that, in general, about 75 - 80 percent of the excitation energy is taken up by the deactivator, while the remaining 20 - 25 percent is accommodated by the rotational and translational modes of the deactivator and the deactivated. The endothermicity of the deactivation of $O_2(b^1\Sigma^+_g)$ by HCl indicates that it is also possible to transfer energy from translation to vibration during the deactivation process.

One may conclude from this discussion of the collisional deactivation of $O_2(b^1\Sigma^+_g)$ that the temperature dependence of the process is slightly positive but does not depend upon a simple function of temperature. The evidence from the deactivation probabilities, together with the predictions of SRIT and LRIT, indicate that the deactivation of $O_2(b^1\Sigma^+_g)$ may take place under the influence of both short and long range forces. The correlation between the logarithm of the rate constant and the highest fundamental vibrational frequency of the deactivator, and the product analyses and surprisal analysis of Thomas and Thrush, show that electronic to vibrational energy transfer is important, although energy differences may be made up from rotational and translational involvement.

7.4 Concluding Remarks

While it is not yet possible to elucidate a detailed mechanism for the deactivation of $O_2(a^1\Delta_g)$ or $O_2(b^1\Sigma^+_g)$, the experimental and theoretical studies have provided useful information about the types of processes involved. There are both similarities and differences in the deactivation of $O_2(a^1\Delta_g)$ and $O_2(b^1\Sigma^+_g)$.

The mechanisms of deactivation are similar in that they both appear to involve short range repulsive forces. In both cases, the energy transferred from the electronically excited species goes mainly into vibrational modes of the deactivator, although resonant pathways are not required for the deactivation of either $O_2(a^1\Delta_g)$ or $O_2(b^1\Sigma^+_g)$.

The contrasts between the two processes are, however, more numerous and more striking. The room temperature (295K) rate constants for the deactivation of $O_2(b^1\Sigma^+_g)$ are 3 - 4 orders of magnitude greater than those for $O_2(a^1\Delta_g)$ because $O_2(b^1\Sigma^+_g)$ may be deactivated to $O_2(a^1\Delta_g)$ via a spin allowed process while $O_2(a^1\Delta_g)$ is deactivated to $O_2(X^3\Sigma^-_g)$ via a spin forbidden process. The temperature dependence of the deactivation of $O_2(a^1\Delta_g)$ is always positive, presumably because deactivation occurs wholly as a result of short range interactions. In contrast to the deactivation of $O_2(a^1\Delta_g)$, the deactivation of $O_2(b^1\Sigma^+_g)$ shows an initial increase in the rate constant with temperature followed in some cases by a 'fall off' at higher temperatures. The variability of the overall temperature dependence of the deactivation rate of $O_2(b^1\Sigma^+_g)$ seems to depend upon whether the temperature dependence of the deactivation through long range interactions (significant at higher temperatures) is positive or negative.

Further experiments are needed to establish the temperature dependence of the deactivation of both of these singlet molecular

oxygen species, particularly over the temperature range from 295 to 500K, where there is a large gap in the work presented here. It would also be useful if calculations based on LRIT and SRIT could be performed to predict both the room temperature (295K) rate constants and the temperature dependence of the deactivation of $O_2(a^1\Delta_g)$ by some of the deactivators studied here.

SUGGESTIONS FOR FURTHER WORK

8.1 Introduction

This chapter outlines some potentially rewarding studies which could be carried out using the discharge flow - shock tube technique. There are suggestions for the continued study of singlet molecular oxygen and also for the study of complementary chemical systems, which are expected to exhibit similar behaviour to singlet molecular oxygen.

8.2 Studies Involving Singlet Molecular Oxygen

As already mentioned in chapter 7, the determination of the rate constants for the deactivation of singlet molecular oxygen in the temperature range 295 to 500K, by the deactivators studied in this work, would be most useful. At present, Billington [83] is investigating the deactivation and energy pooling reactions of singlet molecular oxygen in the temperature range 100 to 450K, using a thermally jacketed flow tube.

A study of the temperature dependence of the deactivation of singlet molecular oxygen by hydrogen deuteride (HD) would be a useful addition to the work carried out here. It would be interesting to compare HD to H_2 and D_2, which have different deactivation efficiencies. Since sufficient high purity HD to perform a series of discharge flow - shock tube experiments would be extremely expensive, it would be sensible to prepare and purify the gas in the laboratory. A method for the preparation of HD from $LiAlH_4$ and D_2O has been described by Wender, Friedel and Orchin [100]. The method involves the use of an apparatus described by Dibeler [101] and results in 99% HD after purification at liquid hydrogen temperatures.

Fookson, Pomerants and Rich [102] have also prepared this gas and report a purification method which allows a purity of 99.8% HD; the remaining 0.2% is H_2. Since H_2 is an efficient deactivator, it would be important to arrange for each batch of gas to be assayed.

A Bentham M300 monochromator is now available in this laboratory and would be of great assistance in identifying the green emission observed during the HCl and HBr studies, if for some reason the work is repeated. In order to record the spectra of the additional emissions at high temperatures, a portable, rapid scan spectrometer would be required, although one is not yet available in this laboratory.

If the explanation of the additional emissions at 634nm and 762nm, given in sections 5.4 and 6.4, is correct, then the discharge flow - shock tube technique is well suited to study the production of $O_2(b^1\Sigma^+_g)$ and $O_2(a^1\Delta_g)$ at high temperatures in mixtures of O_2 with HCl, H_2, D_2 and probably HD.

Slanger [103, 104, 105] has reported the formation of six different bound electronic states of O_2 by oxygen atom recombination. The species observed were $O_2(X^3\Sigma^-_g)$, $O_2(a^1\Delta_g)$, $O_2(b^1\Sigma^+_g)$ and the three upper O_2 states, $O_2(A^3\Sigma_u^+)$, $O_2(C^3\Delta_u)$ and $O_2(c^1\Sigma_u^-)$. The upper states are reported to have long lifetimes, which are estimated [105] to be about 0.2 seconds for $O_2(A^3\Sigma_u^+)$ and about 40 seconds for $O_2(c^1\Sigma_u^-)$ and $O_2(C^3\Delta_u)$. The emissions, many of which are in the visible region of the spectrum, should be intense enough to study with our system.

Already, a second discharge flow - shock tube has been constructed and preliminary experiments are being carried out on the production of oxygen atoms, via the reaction:

$$N + NO \longrightarrow N_2 + O \qquad (8.1)$$

The reactions of atomic nitrogen are well understood at room temperature [106]. The use of the NO - O glow, as a standard method for determining oxygen atom concentrations, has been investigated by Schiff and co-workers [107,108] and shown to be reliable.

8.3 Studies of Other Electronically Excited Molecules

In recent years, Fink and co-workers [109,110,111] have been engaged in studies of the metastable states of group VI diatomic molecules. Molecular species such as SO, S_2, SeO, SeS, Se_2 and TeSe have $^1\Delta_g$ and $^1\Sigma_g^+$ electronically excited states equivalent to those of O_2.

These species may be produced in electronically excited states by first passing chlorides of these species (for example, S_2Cl_2 and $SeOCl_2$) in helium through a microwave discharge to produce the appropriate ground state radicals. The products of the discharge are then added to a flow of $O_2(a^1\Delta_g)$ to produce the excited states.

The radiative lifetimes of these species are expected to be long, although they have not actually been measured. Studies by Fink and co-workers have concentrated on the spectroscopy of these molecules and the observation of several energy pooling reactions which may be compared to those of singlet molecular oxygen.

The discharge flow - shock tube technique would be particularly suited to the investigation of the excitation of the ground state species by $O_2(a^1\Delta_g)$. Studies of the energy pooling reactions and deactivation of these species may prove valuable to the study of electronic to vibrational energy transfer in general, and would be a useful comparison with the study of the deactivation of singlet molecular oxygen.

Lin and Setser [112] have recently studied the deactivation of $NF(b^1\Sigma_g^+)$ which is isoelectronic with O_2 and also has a comparatively long radiative lifetime of 23 milliseconds. The temperature dependence of the deactivation of $NF(b^1\Sigma_g^+)$ with a variety of deactivators could be studied by the discharge flow - shock tube technique. This chemical system might be attractive to study because of the direct comparisons which could be made with $O_2(b^1\Sigma^+_g)$. It

might also be interesting to search for energy pooling reactions analogous to those for O_2, SO and SeO.

APPENDIX 1

```
      PROGRAM SENDEL
C
      EXTERNAL FFUNC
      DIMENSION AV (1000)
      DIMENSION AV1 (1000)
      DIMENSION TPAV (1000)
      DIMENSION RES (1000)
C
      PRINT*,'This is a program to calculate the ANALYSIS EQUATION ',
     *'for the 634nm emission under CHANGED DECAY conditions; ',
     *'INTEGRATE it with respect to time; and DIFFERENTIATE it ',
     *'with respect to another parameter.'
C
    5 OPEN(5,FILE='.RSEND')
      OPEN(7,FILE='.RES')
      REWIND 5
      REWIND 7
      DK=0.0025
      TS=10.0
      PSG=1.00
      RO21=5.00
      T21=2.50
      AK=1.00
      PRINT*
      PRINT*,'Total decay value (DK)=',DK,'per microsec.'
      PRINT*,'Integration time (TS)=',TS,'microsec.'
      PRINT*,'Pre-shock glow (PSG)=',PSG,'millivolts.'
```

```
      PRINT*,'Density ratio (RO21)=',RO21
      PRINT*,'Temperature ratio (T21)=',T21
      PRINT*,'Molecular enhancement factor (AK)=',AK
      PRINT*
      PRINT*,'Do you wish to use alternative values? (answer 1 for ',
     *'yes, 0 for no).'
      READ*,ANS
      IF (ANS.EQ.0) GOTO 10
      PRINT*,'Input DK, TS, PSG, RO21, T21, AK,'
      READ*,DK,TS,PSG,RO21,T21,AK
C
   10 DO 20, TP=0,TS,1
      WRITE(5,*)TP,FFUNC(DK,PSG,RO21,T21,AK,TP)
      PRINT*,TP,FFUNC(DK,PSG,RO21,T21,AK,TP)
   20 CONTINUE
C
      DO 30, TP=TS,1000,50
      WRITE(5,*)TP,FFUNC(DK,PSG,RO21,T21,AK,TP)
      PRINT*,TP,FFUNC(DK,PSG,RO21,T21,AK,TP)
   30 CONTINUE
C
      PRINT*,'Do you wish to INTEGRATE with respect to time?'
      PRINT*,'Answer 1 for yes, 0 for no!'
      READ*,INT
      IF (INT.EQ.0) GOTO 40
      CALL FINT(FFUNC,DK,PSG,RO21,T21,AK,TP,TS,AV,TPAV)
      PRINT*,'Which parameter do you wish to differentiate'
      PRINT*,'with respect to ?'
      PRINT*,'Enhancement factor, AK ?'
      PRINT*,'Total decay value, DK ?'
```

```
      PRINT*,'Integration time, TS ?'
      PRINT*
      PRINT*,'Type 1, 2, or 3 for AK, DK, TS.'
      READ*,PAR
      B=1.0001
      IF(PAR.EQ.1) THEN
      DIV=AK*(B-1.0)
      AK=AK*B
      ENDIF
      IF(PAR.EQ.2) THEN
      DIV=DK*(B-1.0)
      DK=DK*B
      ENDIF
      IF(PAR.EQ.3) THEN
       DIV=TS*(B-1.0)
      TS=TS*B
      ENDIF
      CALL FINT(FFUNC,DK,PSG,RO21,T21,AK,TP,TS,AV1,TPAV)
      DO 40, I=1,500
      RES(I)=(AV1(I)-AV(I))/DIV
      WRITE(7,*)TPAV(I),RES(I)
      PRINT*,TPAV(I),RES(I)
C
   40 CONTINUE
  111 PRINT*,'Type 1 to run again, 0 to finish.'
      READ*,GO
      IF(GO.EQ.1) GOTO 5
      STOP
      END
```

```
C     **********************FUNCTION FFUNC*********************
C     This function calculates the post-shock glow.
      FUNCTION FFUNC(DK,PSG,RO21,T21,AK,TP)
      FFUNC=PSG*(RO21**2)*(T21**0.5)*AK*(EXP(-DK*TP))
      RETURN
      END
C     ******************SUBROUTINE FINT************************
C     This subroutine integrates the ANALYSIS EQUATION with respect
C     to time.
      SUBROUTINE FINT(FFUNC,DK,PSG,RO21,T21,AK,TP,TS,AV,TPAV)
      DIMENSION Y (1000),AV(1000),TPAV(1000)
      TP=-TS
      DO 10,I=1,500
      IF (TP.LT.0) GOTO 11
      IF (TP.GE.0) GOTO 12
   11 F1=PSG
      GOTO 13
   12 F1=FFUNC(DK,PSG,RO21,T21,AK,TP)
   13 TP=TP+(0.2*TS)
      IF (TP.LT.0) GOTO 14
      IF (TP.GE.0) GOTO 15
   14 F2=PSG
      GOTO 16
   15 F2=FFUNC(DK,PSG,RO21,T21,AK,TP)
   16 Y(I)=((F1+F2)/2)*0.2*TS
C
   10 CONTINUE
      DO 20,I=1,500
      AV(I)=(Y(I)+Y(I+1)+Y(I+2)+Y(I+3)+Y(I+4))/TS
      TPAV(I)=(((I-6)*0.2)+0.5)*TS
```

```
20 CONTINUE
   RETURN
   END
```

APPENDIX 2

```
      PROGRAM SENSIG
C
      EXTERNAL FFUNC
      DIMENSION AV (1000)
      DIMENSION AV1 (1000)
      DIMENSION TPAV (1000)
      DIMENSION RESULT (1000)
C
      PRINT*,'This is a program to calculate the ANALYSIS EQUATION '
      PRINT*,'for the 762nm emission under CHANGED DECAY conditions;'
      PRINT*,'INTEGRATE with respect to time; and DIFFERENTIATE it'
      PRINT*,'it with respect to another parameter.'
C
    5 OPEN(5,FILE='.RSIG')
      OPEN(7,FILE='.RESULT')
      REWIND 5
      REWIND 7
      PSG=1.00
      RO21=5.00
      TS=10.0
      AK=3.60
      DDK=0.00083
      SDK=0.104
      RDK=0.00322
      PRINT*
      PRINT*,'Preshock glow (PSG)=',PSG,'millivolts.'
      PRINT*,'Density ratio (RO21)=',RO21
```

```
      PRINT*,'Integration time (TS)=',TS,'microsec.'
      PRINT*,'Molecular enhancement factor (AK)=',AK
      PRINT*,'Increase in delta decay (DDK)=',DDK,'per microsec.'
      PRINT*,'Increase in sigma decay (SDK)=',SDK,'per microsec.'
      PRINT*,'Room temp. decay (RDK)=',RDK,'per microsec.'
      PRINT*
      PRINT*,'Do you wish to use alternative values? (answer 1 for ',
     *'yes, 0 for no).'
      READ*,ANS
      IF (ANS.EQ.0) GOTO 10
      PRINT*,'Input PSG, RO21, TS, AK, DDK, SDK, RDK'
      READ*,PSG,RO21,TS,AK,DDK,SDK,RDK
C
   10 DO 20, TP=0,TS,1
      WRITE(5,*)TP,FFUNC(PSG,RO21,AK,TP,DDK,SDK,RDK)
      PRINT*,TP,FFUNC(PSG,RO21,AK,TP,DDK,SDK,RDK)
   20 CONTINUE
C
      DO 30, TP=TS,1000,50
      WRITE(5,*)TP,FFUNC(PSG,RO21,AK,TP,DDK,SDK,RDK)
      PRINT*,TP,FFUNC(PSG,RO21,AK,TP,DDK,SDK,RDK)
   30 CONTINUE
C
      PRINT*,'Do you wish to INTEGRATE with respect to time?'
      PRINT*,'Answer 1 for yes, 0 for no!'
      READ*,INT
      IF (INT.EQ.0) GOTO 40
      CALL FINT(FFUNC,PSG,RO21,AK,TP,DDK,SDK,RDK,TS,AV,TPAV)
```

```
PRINT*,'Which parameter do you wish to differentiate'
PRINT*,'with respect to ?'
PRINT*,'Enhancement factor, AK ?'
PRINT*,'Delta decay increment,DDK ?'
PRINT*,'Sigma decay increment,SDK ?'
PRINT*,'Room temp. decay, RDK ?'
PRINT*,'Integration time, TS ?'
PRINT*
PRINT*,'Type 1, 2, 3, 4, or 5 for AK, DDK,SDK,RDK, TS.'
READ*,KNO
B=1.0001
IF(KNO.EQ.1) THEN
DIV=AK*(B-1.0)
AK=AK*B
ENDIF
IF(KNO.EQ.2) THEN
DIV=DDK*(B-1.0)
DDK=DDK*B
ENDIF
IF(KNO.EQ.3) THEN
DIV=SDK*(B-1.0)
SDK=SDK*B
ENDIF
IF(KNO.EQ.4)THEN
DIV=RDK*(B-1.0)
RDK=RDK*B
ENDIF
IF(KNO.EQ.5) THEN
 DIV=TS*(B-1.0)
TS=TS*B
```

```
      ENDIF
      CALL FINT(FFUNC,PSG,RO21,AK,TP,DDK,SDK,RDK,TS,AV1,TPAV)
      DO 40, I=1,500
      RESULT(I)=(AV1(I)-AV(I))/DIV
      WRITE(7,*)TPAV(I),RESULT(I)
      PRINT*,TPAV(I),RESULT(I)
C
   40 CONTINUE
  111 PRINT*,'Type 1 to run again, 0 to finish.'
      READ*,GO
      IF(GO.EQ.1) GOTO 5
      STOP
      END
C     **********************FUNCTION FFUNC*********************
C     This function calculates the post-shock glow.
      FUNCTION FFUNC(PSG,RO21,AK,TP,DDK,SDK,RDK)
      FFUNC=PSG*RO21*((AK*EXP(-DDK*TP))+((1-AK)*EXP(-SDK*TP)))
     **(EXP(-RDK*TP))
      RETURN
      END
C     ********************SUBROUTINE FINT************************
C     This subroutine integrates the ANALYSIS EQUATION with respect
C     to time.
      SUBROUTINE FINT(FFUNC,PSG,RO21,AK,TP,DDK,SDK,RDK,TS,AV,TPAV)
      DIMENSION Y (1000),AV(1000),TPAV(1000)
      TP=-TS
      DO 10,I=1,500
      IF (TP.LT.0) GOTO 11
      IF (TP.GE.0) GOTO 12
   11 F1=PSG
```

```
      GOTO 13
   12 F1=FFUNC(PSG,RO21,AK,TP,DDK,SDK,RDK)
   13 TP=TP+(0.2*TS)
      IF (TP.LT.0) GOTO 14
      IF (TP.GE.0) GOTO 15
   14 F2=PSG
      GOTO 16
   15 F2=FFUNC(PSG,RO21,AK,TP,DDK,SDK,RDK)
   16 Y(I)=((F1+F2)/2)*0.2*TS
C
   10 CONTINUE
      DO 20,I=1,500
      AV(I)=(Y(I)+Y(I+1)+Y(I+2)+Y(I+3)+Y(I+4))/TS
      TPAV(I)=(((I-6)*0.2)+0.5)*TS
   20 CONTINUE
      RETURN
      END
```

APPENDIX 3

Input Parameters for HCl/O_2

Run No	I^{762} /mV	I^{634} /mV	P_1 /torr	V_s /km s^{-1}	α_L /x 10^{-3} μs^{-1}	ρ_{21}
R(A)330	243	6.5	6.12	1.138	5.50	4.77
R(A)331	217	6.2	6.50	1.199	8.25	4.91
R(A)332	224	7.0	6.29	1.074	4.15	4.58
R(A)334	174	4.9	6.62	0.975	4.43	4.25
R(A)337	297	5.3	6.87	1.054	6.16	4.52
R(A)339	390	6.6	6.08	1.210	6.83	4.98
R(A)340	406	8.5	6.58	1.143	4.85	4.79
R(A)341	448	7.3	6.21	1.090	4.83	4.63
R(A)342	467	7.3	6.21	1.276	7.41	5.15
R(A)343	388	5.8	5.92	1.041	4.48	4.47
R(A)344	391	6.5	6.17	0.972	4.37	4.24
R(A)345	356	6.1	6.72	0.952	4.16	4.17
R(A)346	364	5.9	6.21	0.950	4.50	4.16
R(A)347	437	7.2	6.41	0.823	3.32	3.65
R(A)348	436	7.2	6.29	0.862	3.54	3.82
R(A)350	250	5.6	6.25	0.981	4.55	4.27
R(A)351	237	5.6	6.33	1.191	8.13	4.92
R(A)352	173	4.8	6.45	1.278	8.39	5.15
R(A)353	192	5.1	6.54	1.267	8.04	5.12
R(A)354	186	5.5	6.00	1.384	8.28	5.40
R(A)355	189	5.6	6.37	1.257	6.80	5.09
R(A)356	203	5.9	6.08	1.335	7.33	5.29

Appendix 3 continued

Run No	I^{762} /mV	I^{634} /mV	P_1 /torr	V_s /km s^{-1}	α_L /x 10^{-3} μs^{-1}	ρ_{21}
R(A)357	189	5.7	6.29	1.189	6.36	4.94
R(A)358	153	4.9	6.37	1.125	6.58	4.73
R(A)359	134	4.7	6.54	1.064	5.73	4.54
R(A)360	131	4.9	6.54	1.024	5.94	4.41
R(A)361	142	5.1	6.58	0.987	5.12	4.29
R(A)362	142	5.5	6.66	0.940	4.33	4.12
R(A)363	158	6.0	6.71	0.920	3.97	4.04
R(A)364	136	6.0	6.58	0.837	3.22	3.67

APPENDIX 4

Input Parameters for H_2/O_2 and $H_2/N_2/O_2$

Run No	I^{762} /mV	I^{634} /mV	P_1 /torr	V_s /km s^{-1}	α_L /x 10^{-3} μs^{-1}	ρ_{21}
DSR4A(B)	138	15	4.70	0.836	2.10	3.81
DSR5A(B)	138	17	4.91	0.842	1.87	3.72
DSR6A(B)	136	17	4.79	0.860	2.22	3.80
DSR7A(B)	121	14	5.12	0.855	2.24	3.78
DSR8A(B)	138	14	5.37	0.941	2.31	4.12
DSR9A(B)	95	13	5.36	0.884	1.94	3.89
DSR10A(B)	117	14	4.21	0.912	2.08	4.00
DSR11A(B)	107	14	4.21	1.004	2.52	4.34
DSR12A(B)	100	14	4.66	1.022	2.81	4.40
DSR13A(B)	168	13	4.21	1.426	4.68	5.39
DSR15A(B)	128	14	5.94	1.012	2.41	4.39
DSR17A(B)	152	15	5.28	1.072	2.39	4.55
DSR18A(B)	118	13	6.52	0.950	2.19	4.15
DSR19A(B)	113	12	7.01	1.077	3.08	4.57
DSR20A(B)	120	12	6.19	1.137	3.24	4.75
DSR21A(B)	110	11	6.58	1.141	3.26	4.76
DSR22A(B)	129	12	6.35	1.230	3.44	5.01
DSR23A(B)	119	11	6.52	1.128	2.90	4.72
DSR24A(B)	159	15	6.19	1.040	2.59	4.45
DSR25A(B)	114	11	6.19	1.200	3.68	4.93
DSR27A(B)	241	13	6.68	0.850	1.80	3.76

Appendix 4 continued

Run No	I^{762} /mV	I^{634} /mV	P_1 /torr	V_s /km s^{-1}	α_L /x 10^{-3} μs^{-1}	ρ_{21}
DSR29A(B)	138	14	6.39	0.846	1.87	3.74
DSR30A(B)	127	14	6.27	0.841	2.00	3.72
DSR31A(B)	187	17	6.35	0.864	2.00	3.81
DSR32A(B)	182	16	6.44	0.860	1.89	3.80
DSR34A(B)	162	15	6.27	0.870	1.84	3.84
DSR34A(B)	190	18	6.11	0.932	2.21	4.08
DSR35A(B)	174	18	6.27	0.889	2.13	4.91
DSR36A(B)	160	16	6.19	0.921	2.06	4.04
DSR37A(B)	169	16	6.11	0.956	2.22	4.17
DSR38A(B)	197	16	5.69	0.930	2.05	4.07
DSR39A(B)	185	16	6.11	0.936	2.27	4.10
DSR40A(B)	163	15	6.27	0.939	2.39	4.11
DSR41A(B)	174	16	6.31	1.030	2.59	4.43
DSR42A(B)	184	16	6.23	0.987	2.54	4.28
DSR43A(B)	159	15	6.11	1.024	2.63	4.41
DSR44A(B)	187	15	5.89	1.024	2.67	4.41
DSR45A(B)	147	14	6.35	1.166	3.60	4.85
DSR46A(B)	138	13	6.27	1.143	3.22	4.78
DSR47A(B)	165	15	5.98	1.177	3.15	4.88
DSR48A(B)	155	14	5.94	1.229	3.26	5.02
DSR49A(B)	142	13	6.11	1.202	3.01	5.95
DSR50A(B)	283	13	6.27	0.871	1.95	3.83
DSR51A(B)	201	10	5.65	0.773	1.58	3.42

Appendix 4 continued

Run No	I^{762} /mV	I^{634} /mV	P_1 /torr	V_s /km s^{-1}	α_L /x 10^{-3} μs^{-1}	ρ_{21}
DSR52A(B)	220	11	6.60	0.771	1.49	3.42
DSR53A(B)	229	10	6.72	0.784	1.60	3.46
DSR54A(B)	243	11	6.27	0.819	1.56	3.61
DSR55A(B)	265	12	6.02	0.834	1.56	3.68
DSR56A(B)	244	10	7.18	0.766	1.71	3.39
DSR57A(B)	447	11	5.78	0.802	1.51	3.55
DSR59A(B)	325	13	5.78	0.740	1.14	3.25
DSR60A(B)	209	10	7.05	0.725	1.32	3.18
DSR61A(B)	349	9	6.89	0.716	1.32	3.15
DSR401A(B)	49	13.0	5.86	1.141	2.71	4.63
DSR402B	37	-	6.77	1.122	2.90	4.57
DSR404A(B)	50	12.0	5.36	1.071	2.20	4.42
DSR405A(B)	44	11.6	5.94	1.113	2.49	4.54
DSR406A(B)	42	11.2	6.35	1.236	3.18	4.89
DSR407A(B)	49	12.1	5.57	1.164	2.60	4.69
DSR409A(B)	46	12.1	5.61	1.141	2.34	4.63
DSR410A(B)	43	11.3	6.06	0.945	1.75	3.99
DSR411A(B)	48	11.8	5.28	0.997	1.58	4.18
DSR412A(B)	32	8.9	6.06	0.936	1.73	3.95
DSR413A(B)	31	9.3	5.90	0.988	2.00	4.14
DSR414A(B)	31	9.3	5.98	0.959	1.90	4.04
DSR415A(B)	28	8.9	6.35	0.889	1.66	3.78
DSR416A(B)	34	10.0	6.68	0.854	1.71	3.64

Appendix 4 continued

Run No	I^{762} /mV	I^{634} /mV	P_1 /torr	V_s /km s^{-1}	α_L /x 10^{-3} μs^{-1}	ρ_{21}
DSR417A(B)	45	11.0	5.73	0.857	1.35	3.66
DSR418A(B)	41	10.3	6.60	0.868	1.83	3.70
DSR419A(B)	47	10.9	5.73	0.859	1.44	3.66
DSR420A(B)	44	10.9	6.52	0.718	1.01	3.05
DSR421A(B)	50	11.4	5.24	0.747	0.86	3.18
DSR422A(B)	33	9.8	7.01	0.733	1.26	3.12
DSR423A(B)	44	11.3	6.27	0.778	1.30	3.32
DSR424A(B)	37	10.4	6.44	0.836	1.62	3.57

APPENDIX 5

Input Parameters for N_2/O_2

Run No	I^{762} /mV	I^{634} /mV	P_1 /torr	V_s /km s^{-1}	α_L /x 10^{-3} μs^{-1}	ρ_{21}
DSR201A(B)	120	7.4	5.94	1.129	1.64	4.40
DSR202A(B)	123	7.9	5.86	1.392	2.59	5.00
DSR203A(B)	104	6.6	5.82	1.033	0.97	4.13
DSR204A(B)	112	7.0	5.90	1.112	1.43	4.36
DSR205A(B)	103	7.0	5.82	0.981	1.17	3.97
DSR206A(B)	98	6.5	6.60	0.856	1.00	3.53
DSR207A(B)	129	7.8	5.86	0.846	0.85	3.49
DSR208A(B)	125	7.7	6.02	0.732	0.61	3.02
DSR209A(B)	135	8.2	5.78	0.735	0.60	3.04
DSR210A(B)	115	7.2	6.52	0.784	0.81	3.25
DSR211A(B)	339	17.3	6.06	1.257	2.88	4.93
DSR212A(B)	359	15.5	6.06	1.331	3.21	5.09
DSR215A(B)	278	12.8	5.57	1.371	3.69	5.18
DSR216A(B)	238	11.7	6.23	0.842	1.51	3.61
DSR217A	-	13.2	6.02	1.039	2.15	4.31
DSR218A(B)	326	14.9	5.86	1.001	2.16	4.19
DSR219A(B)	336	15.2	6.27	1.136	2.65	4.60
DSR220A(B)	362	15.8	5.86	1.075	2.18	5.54
DSR221A(B)	363	15.7	6.06	0.901	1.56	3.84
DSR222A(B)	364	15.6	6.02	0.846	1.34	3.62
DSR223A(B)	733	22.8	5.28	1.358	3.54	5.26

Appendix 5 continued

Run No	I^{762} /mV	I^{634} /mV	P_1 /torr	V_s /km s^{-1}	α_L /x 10^{-3} μs^{-1}	ρ_{21}
DSR224A(B)	634	20.5	6.23	1.346	4.02	5.24
DSR225A(B)	687	21.5	5.78	1.087	2.47	4.56
DSR226A(B)	709	22.2	5.49	1.296	3.33	5.125
DSR227A(B)	673	21.1	5.69	0.997	2.09	4.270
DSR228A(B)	656	20.5	6.11	0.926	1.70	4.016
DSR229A(B)	680	20.6	6.15	0.835	1.36	3.66
DSR230A(B)	710	21.3	5.90	0.844	1.54	3.69
DSR232A(B)	655	19.6	6.02	1.282	3.71	5.09
DSR233A(B)	613	18.4	6.44	1.467	5.03	5.51
DSR234A(B)	622	19.4	5.98	0.721	1.11	3.15
DSR235A	-	20.4	5.98	0.720	1.10	3.14
DSR236A	-	213	5.82	0.743	1.18	3.25
DSR237A(B)	676	20.3	6.31	0.743	1.27	3.14
DSR238A(B)	432	17.1	5.58	0.734	0.92	3.14
DSR239A(B)	337	14.5	6.77	0.731	1.06	3.12

APPENDIX 6

Input Parameters for D_2/O_2 and $D_2/N_2/O_2$

Run No	I^{762} /mV	I^{634} /mV	P_1 /torr	V_s /km s^{-1}	α_L /x 10^{-3} μs^{-1}	ρ_{21}
DSR101A	-	17	4.91	1.423	2.17	5.47
DSR102A	-	25	5.78	1.365	2.58	5.34
DSR103A(B)	1075	25	4.74	0.915	1.13	3.99
DSR104A(B)	636	25	5.20	0.930	1.21	4.06
DSR105A(B)	622	25	5.28	1.084	1.65	4.59
DSR106A(B)	686	25	4.99	0.894	1.06	3.92
DSR107A(B)	597	24	4.95	0.881	1.11	3.87
DSR108B	619	-	5.03	0.872	1.07	3.83
DSR109A(B)	699	27	5.36	1.029	1.87	4.42
DSR110A(B)	532	37	5.07	1.368	2.91	5.35
DSR111A(B)	561	34	5.40	1.383	3.23	5.38
DSR112A	-	33	6.27	0.910	1.69	3.98
DSR113A(B)	582	34	5.94	0.986	2.01	4.26
DSR114A(B)	503	29	6.93	0.975	2.49	4.22
DSR115A(B)	603	34	5.57	1.032	2.17	4.42
DSR116A	-	36	5.78	1.129	1.90	4.72
DSR116B	-	36	5.78	1.129	1.90	4.72
DSR117A	-	19	5.69	0.978	1.43	4.23
DSR117B	-	20	5.69	0.978	1.43	4.23
DSR118A(B)	659	19	4.21	0.737	0.77	3.24
DSR119A(B)	501	17	6.64	0.719	1.24	3.14
DSR120A(B)	749	23	4.87	0.730	0.91	3.20

Appendix 6 continued

Run No	I^{762} /mV	I^{634} /mV	P_1 /torr	V_s /km s^{-1}	α_L /x 10^{-3} μs^{-1}	ρ_{21}
DSR121A(B)	545	19	7.10	0.713	1.45	3.12
DSR122A(B)	803	24	5.20	0.766	1.20	3.37
DSR123A(B)	746	21	5.31	0.842	1.86	3.71
DSR124A(B)	682	21	5.86	0.801	1.43	3.54
DSR125A(B)	404	21	6.11	1.078	3.32	4.57
DSR126A(B)	415	19	5.57	1.181	3.37	4.87
DSR127A(B)	349	15	6.44	0.732	1.23	3.19
DSR128A(B)	488	19	4.66	0.737	0.89	3.22
DSR129A(B)	332	15	7.10	0.723	1.34	3.14
DSR130A(B)	450	18	5.53	0.769	1.14	3.36
DSR131A(B)	433	18	5.69	0.820	1.41	3.59
DSR132A(B)	376	16	6.44	0.841	1.75	3.68
DSR133A(B)	399	18	5.61	0.845	1.57	3.69
DSR134A(B)	435	18	5.53	0.841	1.56	3.68
DSR135A(B)	435	18	5.82	0.851	1.74	3.72
DSR136A(B)	410	20	5.82	0.842	1.75	3.71
DSR137A(B)	473	20	5.45	1.082	2.78	4.55
DSR138A(B)	470	20	5.65	0.951	2.16	4.11
DSR139A(B)	400	18	6.31	1.005	2.85	4.31
DSR140A(B)	484	21	5.45	0.927	2.05	4.02
DSR141A(B)	405	18	6.48	0.844	2.00	3.69
DSR142A(B)	441	19	6.19	0.867	1.94	3.79
DSR143A(B)	412	18	6.35	0.968	2.55	4.17
DSR144A(B)	440	20	5.40	1.035	2.43	4.40

Appendix 6 continued

Run No	I^{762} /mV	I^{634} /mV	P_1 /torr	V_s /km s^{-1}	α_L /x 10^{-3} μs^{-1}	ρ_{21}
DSR145A(B)	487	20	5.16	1.019	2.30	4.35
DSR146A(B)	355	17	6.77	1.009	3.01	4.32
DSR147A(B)	347	17	6.72	1.004	2.99	4.30
DSR302A(B)	270	16	6.52	1.107	2.48	4.51
DSR304A(B)	281	15	6.06	1.185	2.48	4.73
DSR305A(B)	302	16	5.57	1.037	1.90	4.29
DSR306A(B)	262	14	5.86	1.058	2.00	4.36
DSR307A(B)	273	14	5.65	1.018	1.40	4.23
DSR308A(B)	258	13	5.78	0.966	1.54	4.05
DSR309A(B)	270	14	5.69	0.876	1.18	3.71
DSR310A(B)	229	13	6.44	0.836	1.28	3.55
DSR311A(B)	285	15	5.69	0.863	1.16	3.66
DSR312A(B)	281	14	5.78	0.864	1.28	3.66
DSR313A(B)	252	13	6.39	0.856	1.36	3.63
DSR314A(B)	308	15	5.63	0.770	0.97	3.27
DSR315A(B)	309	15	6.15	0.854	1.31	3.62
DSR316A(B)	309	15	6.11	0.722	0.88	3.05
DSR317A(B)	270	14	6.77	0.724	1.01	3.06
DSR318A	-	5.8	6.81	1.255	1.98	4.78
DSR319A(B)	124	7.4	5.32	1.145	1.31	4.48
DSR320A(B)	101	6.6	5.94	0.868	0.78	3.56
DSR323A(B)	90	6.5	6.52	1.007	1.37	4.06
DSR324A(B)	96	6.5	6.35	0.959	0.97	3.90

Appendix 6 continued

Run No	I^{762} /mV	I^{634} /mV	P_1 /torr	V_s /km s^{-1}	α_L /x 10^{-3} μs^{-1}	ρ_{21}
DSR325A(B)	97	6.6	6.56	0.988	1.24	4.00
DSR326A(B)	100	6.5	6.35	0.917	1.03	3.74
DSR327A(B)	107	6.8	6.11	0.864	0.82	3.54
DSR328A(B)	93	6.2	6.35	1.097	1.46	4.34
DSR329A(B)	91	6.1	6.77	1.133	1.72	4.45
DSR330A(B)	84	5.7	6.85	0.724	0.66	2.95
DSR331A(B)	91	5.7	6.72	0.724	6.10	2.95
DSR332A(B)	94	6.3	6.85	0.761	0.76	3.12
DSR333A(B)	126	7.1	5.69	0.834	0.72	3.43

REFERENCES

1. J. W. Chamberlain,
Physics of the Aurora and Airglow, (Academic Press, New York 1961).
2. M. Bantle, E. J. Llewellyn and B. H. Solheim,
Journal of Atmospheric and Terrestrial Physics, 1984, 46 (3), 265.
3. W. F. J. Evans, D. M. Hunten, E. J. Llewellyn and A. Vallance Jones,
Journal of Geophysical Research, 1968, 73, 2285.
4. K. G. Vohra,
Proceedings of the Symposium on Singlet Molecular Oxygen, (Bombay 1976).
5. J. Bland,
Journal of Chemical Education, 1976, 53, 274.
6. W. E. McDermott, N. R. Pchelkin, D. J. Bernard and R. R. Bousek
Applied Physics Letters, 1978, 32, 469.
7. J. B. Koffend, C. E. Gardner and R. F. Heidner,
Journal of Chemical Physics, 1984, 32 (5), 1861.
8. L. Mallet,
Comptes Rendus Hebdomadaires des Seances de L'Academie des Sciences, 1927, 185 352.
9. L. Torchin, R. Jegou and H. Brunet,
Journal of Chemical Physics, 1983, 79 (4), 2100.
10. J. Nicholas,
Chemical Kinetics, (Harper and Row, 1976).
11. W. J. Moore,
Physical Chemistry, (Longman, 1978).
12. J. D. Lambert,
Vibrational and Rotational Relaxation in Gases, (Clarendon Press Oxford, 1977).
13. K. R. Grant,
Thesis, (Keele University, 1981).
14. J. N. Bradley,
Shock Tubes in Chemistry and Physics, (Methuen, 1962)
15. R. A. Hartunian, W. P. Thompson and E. W. Hewitt,
Journal of Chemical Physics, 1966, 44, 1765.

16. R. W. F. Gross and N. Cohen,
Journal of Chemical Physics, 1968, **48**, 2582.

17. P. Borrell, P. M. Borrell and A. Brittain,
U. S. Clearing-House, Federal Scientific and Technical Information, AD1969, 702808.

18. R. A. Young and G. Black,
Journal of Chemical Physics, 1965, **42**, 3740.

19. P. Borrell, P. M. Borrell and M. D. Pedley,
Chemical Physics Letters, 1977, **51** (2), 300.

20. H. Katayama, S. Ogawa, M. Ogawa and Y. Tanaka,
Journal of Chemical Physics, 1977, **67**, 2132.

21. G. Herzberg,
Spectra of Diatomic Molecules, (Van Nostrand, New York, 1945).

22. R. M. Badger, A. C. Wright and R. F. Whitlock,
Journal of Chemical Physics, 1965, **43**, 4345.

23. L. Wallace and D. M. Hunten,
Journal of Geophysical Research, 1968, **73**, 4813.

24. A. U. Kahn and M. Kasha,
Journal of the American Chemical Society, 1970, **92**, 3293.

25. L. Elias, E. A. Ogryzlo and H. I. Schiff,
Canadian Journal of Chemistry, 1959, **37**, 1680.

26. R. L. Brown,
Journal of Physical Chemistry, 1967, **71**, 2492.

27. M. Yaron and A. von Engel,
Chemical Physics Letters, 1975, **33**, 316.

28. R. P. Wayne,
Singlet Oxygen Vol. 1, (Ed. A. A. Frimer, Chem. Rubber Publishing Company, 1985)

29. I. D. Clark and R. P. Wayne,
Chemical Physics Letters, 1969, **3**, 93.

30. G. Black and T. G. Slanger,
Journal of Chemical Physics, 1981, **74**, 6517.

31. I. B. C. Matheson, J. Lee, B. S. Yamanashi and N. L. Wohlbarsht,
Chemical Physics Letters, 1974, **27**, 355.

32. J. G. Parker and D. N. Ritke,
Journal of Chemical Physics, 1973, **59**, 3713.

33. L. R. Martin, R. B. Cohen and J. F. Schatz,
Chemical Physics Letters, 1976, **41**, 394.

34. S. A. Lawton, S. E. Novick, H. P. Broida and A. V. Phelps.
Journal of Chemical Physics, 1977, **66**, 1381.

35. R. P. Wayne,
Quarterly Journal of the Royal Meteorological Society, 1967,
93, 395.

36. E. J. Bowen,
Advanced Photochemistry, 1963, **1**, 23.

37. F. D. Findlay and D. R. Snelling,
Journal of Chemical Physics, 1971, **55**, 545.

38. T. C. Frankiewicz and R. S. Berry,
Journal of Chemical Physics, 1973, **58**, 1787.

39. J. A. Davidson, K. Kear and E. W. Abrahamson,
Journal of Photochemistry, 1972/3, **1** 307.

40. R. W. Murray and M. L. Kaplan,
Journal of the American Chemical Society, 1969, **91**, 5358.

41. M. Braithwaite, E. A. Ogryzlo, J. A. Davidson and H. I. Schiff,
Journal of the Chemical Society, Faraday II, 1976, **72**, 2075.

42. M. Braithwaite, E. A. Ogryzlo, J. A. Davidson and H. I. Schiff,
Chemical Physics Letters, 1976, **42**, 158.

43. K. Kohse-Hoinghaus and F. Stuhl,
Journal of Chemical Physics, 1980, **72**, 3720.

44. R. B. Boodaghians,
Thesis, (Keele University, 1983).

45. C. J. Smith,
The General Properties of Matter, (Edward Arnold, London, 1953).

46. M. D. Pedley,
Thesis, (Keele University, 1978).

47. R. J. Richardson, J. D. Kelley and C. E. Wiswall,
Journal of Applied Physics, 1981, **52** (2), 1066.

48. E. A. Ogryzlo,
Photophysiology Vol. 5 1970, 35.

49. R. M. Badger, A. C. Wright and R. F. Whitlock,
Journal of Chemical Physics, 1965, **43** (12), 4345.

50. W. S. Gleason, A. D. Broadbent, E. Whittle and J. N. Pitts,
Journal of the American Chemical Society, 1970, **92** (7), 2068.

51. R. E. Huie and J. T. Herron,
International Journal of Chemical Kinetics V, 1973, 197.

52. K. Furukawa and E. A. Ogryzlo,
Chemical Physics Letters, 1971, **12** (2), 370.

53. Selected Values of Physical and Thermodynamic Properties of Hydrocarbons and Related Compounds, (American Petroleum Institute Research Project **44**, 1952)

54. J. N. Bradley,
Shock Tubes in Chemistry and Physics, (Methuen, London, 1962).

55. J.K. Wright,
Shock Tubes, (Methuen, London, 1961)

56. A. G. Gaydon and I. R. Hurle,
The Shock Tube in High Temperature Chemical Physics, (Chapman and Hall, London, 1963).

57. C. T. Bowman and R. K. Hanson,
Journal of Physical Chemistry, 1978, **83**, 757.

58. J. A. N. A. F. Thermochemical Tables, (Dow Chemical Company, Michigan, 1965).

59. R. C. Millikan,
General Electric Research Report, 1964, 64-RL-3700C.

60. P. M. Borrell,
Thesis, (Keele University, 1980).

61. P. Borrell,
Computers in Chemistry, 1980, **4**, 131.

62. G. Burns and D. F. Hornig,
Canadian Journal of Chemistry, 1960, **38**, 1702.

63. J. N. Bradley and R. Tuffnell,
Proceedings of the Royal Society, (London), 1964, **A280**, 198.

64. H. Hartridge and F. J. W. Roughton,
Proceedings of the Royal Society A, 1923, **104**, 376.

65. R. L. Belford and R. A. Strehlow,
American Review of Physical Chemistry, 1969, 247.

66. E. F. Greene and J. P. Toennies,
Chemical Reactions in Shock Waves, (Edward Arnold, London, 1964)

67. R. G. Derwent and B. A. Thrush,
Transactions of the Faraday Society, 1971, **67**, 2036.

68. R. Boodaghians, P. Borrell, P. M. Borrell and D. S. Richards,
Bulletin des Societés Chimiques Belges, 1983, **92** (6/7), 651.

69. J. P. Singh, J. Bachar and D. W. Setser,
To be published in Journal of Physical Chemistry.

70. F. D. Findlay and D. R. Snelling,
Journal of Chemical Physics, 1971, 55 (2), 545.

71. K. H. Becker, W. Groth and U. Schurath,
Chemical Physics Letters, 1971, 8 (3), 259.

72. P. Borrell, P. M. Borrell, M. D. Pedley, K. R. Grant
and R. B. Boodaghians,
Proceedings of the 13th International Symposium on Shock Tubes,
(State University of New York Press, Albany, 1982), 541.

73. R. Boodaghians, P. Borrell, P. M. Borrell and
K. R. Grant,
Journal of the Chemical Society, Faraday Transactions II,
1981, 78, 1195.

74. N. Washida, H. Akimoto and M. Okuda,
Journal of Physical Chemistry, 1978, 82 (1), 18.

75. A. C. Erlandson and T. A. Cool,
Chemical Physics Letters, 1983, 96 (6), 685.

76. R. D. Ashford and E. A. Ogryzlo,
Journal of the American Chemical Society, 1975, 97, 3604.

77. R. G. O. Thomas and B. A. Thrush,
Proceedings of the Royal Society, (London), 1977, A356, 295.

78. R. G. O. Thomas and B. A. Thrush,
Proceedings of the Royal Society, (London), 1977, A356, 307.

79. E. A. Ogryzlo and B. A. Thrush,
Chemical Physics Letters, 1973, 32, 34.

80. J. A. Davidson and E. A. Ogryzlo,
Chemiluminescence and Bioluminescence, Eds. M. J. Cormier,
D. M. Hercules and J. Lee (Plenum Press, New York, 1973).

81. H. M. Lin, M. Seaver, K. Y. Tons, A. E. W. Knight and
C. S. Parmenter.
Journal of Chemical Physics, 1979, 70, 5442.

82. C. S. Parmenter and M. Seaver,
Journal of Chemical Physics, 1979, 70, 5458.

83. A. P. Billington,
Unpublished work, Keele University.

84. A. Leiss, U. Schurath, K. H. Becker and E. H. Fink,
Journal of Photochemistry, 1978, 8, 211.

69. J. P. Singh, J. Bachar and D. W. Setser,
To be published in Journal of Physical Chemistry.

70. F. D. Findlay and D. R. Snelling,
Journal of Chemical Physics, 1971, 55 (2), 545.

71. K. H. Becker, W. Groth and U. Schurath,
Chemical Physics Letters, 1971, 8 (3), 259.

72. P. Borrell, P. M. Borrell, M. D. Pedley, K. R. Grant
and R. B. Boodaghians,
Proceedings of the 13th International Symposium on Shock Tubes,
(State University of New York Press, Albany, 1982), 541.

73. R. Boodaghians, P. Borrell, P. M. Borrell and
K. R. Grant,
Journal of the Chemical Society, Faraday Transactions II,
1981, 78, 1195.

74. N. Washida, H. Akimoto and M. Okuda,
Journal of Physical Chemistry, 1978, 82 (1), 18.

75. A. C. Erlandson and T. A. Cool,
Chemical Physics Letters, 1983, 96 (6), 685.

76. R. D. Ashford and E. A. Ogryzlo,
Journal of the American Chemical Society, 1975, 97, 3604.

77. R. G. O. Thomas and B. A. Thrush,
Proceedings of the Royal Society, (London), 1977, A356, 295.

78. R. G. O. Thomas and B. A. Thrush,
Proceedings of the Royal Society, (London), 1977, A356, 307.

79. E. A. Ogryzlo and B. A. Thrush,
Chemical Physics Letters, 1973, 32, 34.

80. J. A. Davidson and E. A. Ogryzlo,
Chemiluminescence and Bioluminescence, Eds. M. J. Cormier,
D. M. Hercules and J. Lee (Plenum Press, New York, 1973).

81. H. M. Lin, M. Seaver, K. Y. Tons, A. E. W. Knight and
C. S. Parmenter.
Journal of Chemical Physics, 1979, 70, 5442.

82. C. S. Parmenter and M. Seaver,
Journal of Chemical Physics, 1979, 70, 5458.

83. A. P. Billington,
Unpublished work, Keele University.

84. A. Leiss, U. Schurath, K. H. Becker and E. H. Fink,
Journal of Photochemistry, 1978, 8, 211.